Dynamic modelling of incidents for the protection of helium cryostats against excessive pressure

Zur Erlangung des akademischen Grades einer

DOKTORIN DER INGENIEURWISSENSCHAFTEN (DR.-ING.)

von der KIT-Fakultät für Chemieingenieurwesen und Verfahrenstechnik des Karlsruher Instituts für Technologie (KIT)

genehmigte

DISSERTATION

von

Christina Weber M. Sc.

aus Arnsberg

Erstgutachter: Prof. Dr.-Ing. Steffen Grohmann

Zweitgutachter: Prof. Dr.-Ing. Thomas Schulenberg

Tag der mündlichen Prüfung: 23. April 2021

Danksagung

Die vorliegende Arbeit entstand während meiner Tätigkeit als Doktorandin am Institut für Technische Physik (ITEP) des Karlsruher Instituts für Technologie (KIT).

Die Forschung lebt von der Begeisterung für ein Thema. Der Bereich der kryogenen Sicherheitstechnik hat diese Begeisterung in mir geweckt. Auch wenn ich die Arbeit alleine schreiben musste, waren an ihrem Gelingen die mir nahestehenden Menschen beteiligt. Daher möchte ich zu allererst meinem Doktorvater Herrn Prof. Dr.-Ing. Steffen Grohmann für die Möglichkeit, das mir entgegengebrachte Vertrauen und das Interesse an meiner Arbeit bedanken. Herrn Prof. Dr.-Ing. Thomas Schulenberg danke ich für die Übernahme des Korreferats.

Für die technische Unterstützung und die große Hilfsbereitschaft bedanke ich mich ganz herzlich bei den Kollegen am ITEP. Ein ganz besonderer Dank gilt hier Eugen Specht und Ingeborg Meyer, die mir stets ohne zu zögern mit Rat und Tat zur Seite standen und mich nicht nur bei technischen Fragen großartig unterstützt haben.

Meinen Doktorandenkollegen David Gomse und Carolin Zoller danke ich für die vielen konstruktiven Diskussionen, die mich stets weitergebracht haben. Aber auch bei allen anderen Doktoranden möchte ich mich vor allem für die tolle Atmosphäre und den Zusammenhalt bedanken. In dieser Zeit haben sich viele neue starke Freundschaften entwickelt und bestehende sich vertieft. Wegen euch werde ich gerne an die Zeit zurückdenken.

Auch den von mir betreuten Studenten Jonas Schwenzer, Dorothea Groß, Sebastian Knott und Sabrina Schirle möchte ich für ihre Beiträge zu meiner Arbeit danken. Alexander Scholz, dir danke ich für die sprachliche Durchsicht der schriftlichen Ausarbeitung.

Ganz besonders möchte ich mich aber auch bei meiner Familie und meinen Freunden bedanken, die mich mit ihrer unermüdlichen Unterstützung und ihrem Rückhalt dem Ziel näher gebracht haben. Ohne euch wäre diese Arbeit nicht möglich gewesen. Danke Mama und Papa, dass ihr auf so viel Zeit mit mir verzichtet habt.

Lieber Yannick, zuletzt danke ich dir von ganzem Herzen. Ohne deine Aufmunterungen, deine konstruktiven Einwände und deine unendliche Geduld wäre der Weg so viel schwerer gewesen.

Abstract

Helium cryostats are commonly vacuum-insulated, pressurised systems that fall under the scope of the *European Pressure Equipment Directive 2014/68/EU* (PED). Operated at temperatures of typically $T < 10\,\mathrm{K}$, helium cryostats are often related to technical applications of superconductivity. This includes, for example, superconducting magnet systems used in magnetic resonance imaging (MRI), nuclear magnetic resonance spectroscopy (NMR), particle physics and nuclear fusion, superconducting radio-frequency cavities, squids and quantum computing. The technology to provide low temperature operation in the form of helium refrigerators, liquefiers and transfer systems is also included in the applications of helium cryostats.

Under the PED, all pressure equipment must be protected against excessive pressure. In the context of helium cryostats, several risks for pressure increase exist, whereby loss of insulating vacuum (LIV) often constitutes a maximum credible incident (MCI). In case of LIV, the latent and sensible heat of the de-sublimation airflow is predominantly transferred to the helium system. Additional heat loads may arise from the energy stored in superconducting components, which become resistive at increasing temperature. Established standards for the protection of cryogenic storage vessels against excessive pressure do not cover the conditions in helium cryostats as active internal components significantly influence the risk potential.

Due to the low operating temperature, incidental heat fluxes are large and the low vaporisation enthalpy of liquid helium causes large pressure rise rates in the order of ($\mathrm{bar\,s^{-1}}$). Therefore, the protection of helium cryostats against excessive pressure requires a detailed understanding of the process dynamics. A dimensioning procedure for pressure relief devices (PRDs) under such conditions, however, does not yet exist. Currently, dimensioning of PRDs is often based on a small number of constant heat flux values, resulting in potentially oversized PRDs. In the case of pressure relief valves (PRV), over-sizing can result in unstable operation with reduced discharge capacity, inadmissible overpressure and damage of the PRV.

In this document, the LIV scenario as a typical MCI is investigated with a focus on the heat transfer mechanism. More specifically, different models for the dimensioning of PRDs are compared and their applicability for helium cryostats is evaluated. As a further development of an existing basic dynamic model, the heat transfer from the vacuum space to the helium system is modelled by a transient heat transfer equation. The resulting one-dimensional differential equation system considers the heat transfer, both from the air to the wall and from the wall to the helium, the heat conduction in the cryogenic vessel wall and a thermal resistance due to thermal insulation.

Abstract

The transient heat transfer model and the dimensioning procedure are validated with experiments performed in the cryogenic safety test facility PICARD at the Institute of Technical Physics at KIT. In the experimental study, parameters such as the venting diameter, the initial liquid helium level, the set pressure of the PRV and the type of PRV are varied. Additionally, the influence of multi-layer insulation (MLI) on the heat flux is investigated.

Beside novel experiments and modelling, this dissertation provided substantial contributions to the development of the new European Standard EN 17527 *"Helium cryostats – protection against excessive pressure"* (Publication by CEN/TC 268/WG6 forthcoming).

Kurzfassung

Heliumkryostate sind meist vakuumisolierte Druckbehälter, die in den Anwendungsbereich der Druckgeräterichtline (*European Pressure Equipment Directive 2014/68/EU*, PED) fallen. Heliumkryostate werden bei Temperaturen von typischerweise $T < 10\,\mathrm{K}$ betrieben und sind oft mit technischen Anwendungen der Supraleitung verbunden. Dazu gehören zum Beispiel supraleitende Magnetsysteme für die Magnetresonanztomographie (MRT), die Kernspinresonanzspektroskopie (NMR), die Teilchenphysik und Kernfusion, supraleitende hochfrequente Kavitäten, Squids und Quantencomputer. Die Technologie für den Niedertemperaturbetrieb in Form von Helium-Kälteanlagen, Verflüssigern und Transfersystemen ist ebenfalls enthalten.

Nach der PED müssen Druckgeräte vor Überdruck geschützt werden. Bei Heliumkryostaten bestehen mehrere Risiken für einen Druckanstieg, wobei der Verlust des Isolationsvakuums (engl.: Loss of insulating vacuum, LIV) oft die maximal zu erwartende Störung (engl.: Maximum credible incident, MCI) darstellt. In diesem Fall wird hauptsächlich die latente und sensible Wärme des desublimierenden Luftstroms auf das Heliumsystem übertragen. Zusätzliche Wärmelasten können durch die in supraleitenden Komponenten gespeicherte Energie entstehen. Bei steigender Temperatur werden Supraleiter resistiv und die gespeicherte Energie wird als Wärme dissipiert. Etablierte Standards für den Schutz von kryogenen Lagerbehältern gegen Überdruck decken die Bedingungen in Heliumkryostaten nicht vollständig ab, da die aktiven internen Komponenten das Risikopotenzial maßgeblich beeinflussen.

Aufgrund der niedrigen Betriebstemperatur sind die Wärmeströme im Fall von Störungen groß und die geringe Verdampfungsenthalpie des flüssigen Heliums verursacht große Druckanstiegsgeschwindigkeiten in der Größenordnung von $(\mathrm{bar\,s^{-1}})$. Die Absicherung von Heliumkryostaten gegen unzulässigen Überdruck erfordert daher ein detailliertes Verständnis der Prozessdynamik. Ein Dimensionierungsverfahren für Druckentlastungseinrichtungen (engl.: Pressure relief device PRD) unter solchen Bedingungen existiert jedoch noch nicht. Bisher basiert die Dimensionierung von PRDs oft auf einigen wenigen konstanten Wärmestromwerten, was zu potenziell überdimensionierten PRDs führt. Bei Druckentlastungsventilen (engl.: Pressure relief valves PRV) kann die Überdimensionierung zu instabilem Betrieb mit reduzierter Abblasekapazität, unzulässigem Überdruck und Beschädigung des PRV führen.

Das LIV-Szenario als typisches MCI wird in dieser Arbeit mit Schwerpunkt auf dem Wärmeübertragungsmechanismus untersucht. Verschiedene Modelle für die Dimensionierung von PRDs werden verglichen und ihre Anwendbarkeit für Heliumkryostate bewertet.

Kurzfassung

Als Weiterentwicklung eines bestehenden dynamischen Grundmodells wird der Wärmeübergang vom Vakuumraum zum Heliumsystem durch eine transiente Wärmeübergangsgleichung modelliert. Die resultierenden eindimensionalen Differentialgleichungssysteme berücksichtigen die konvektive Wärmeübertragung sowohl von der Luft als auch auf das Helium, die Wärmeleitung in der kryogenen Behälterwand und einen Wärmewiderstand durch thermische Isolierung.

Das transiente Wärmeübergangsmodell und das Dimensionierungsverfahren werden durch Experimente im kryogenen Sicherheitsprüfstand PICARD am Institut für Technische Physik des KIT validiert. Vor den Experimenten wurde die Anlage modifiziert und das Messsystem erweitert. In der experimentellen Studie werden Parameter wie der Belüftungsdurchmesser, der Füllstand des flüssigen Heliums, der Einstelldruck des PRV und die Art des PRV variiert. Zusätzlich wird der Einfluss von Superisolation (engl.: Multi-Layer-Insulation MLI), auf die Wärmeübertragung untersucht.

Neben Experimenten und Modellierung leistete diese Arbeit wesentliche Beiträge zur Entwicklung der neuen Europäischen Norm EN 17527 *"Heliumkryostate – Schutz vor unzulässigem Überdruck"*, die in Kürze von CEN/TC 268/WG6 veröffentlicht wird.

Contents

Symbols and abbreviations

Latin symbols

Symbol	Description	Unit
A	area	m^2
a	liquid level	-
c	velocity	$\mathrm{m\,s^{-1}}$
c	specific heat capacity	$\mathrm{kJ\,kg^{-1}\,K^{-1}}$
c_p	isobaric specific heat capacity	$\mathrm{kJ\,kg^{-1}\,K^{-1}}$
C	discharge function	-
C_A	orifice calibration factor	$\mathrm{Pa}^{0.5}$
C_B	orifice calibration factor	Pa
C_E	orifice calibration factor	$\mathrm{Pa}^{2.5}$
C_C	orifice calibration factor	$\mathrm{Pa}^{1.5}$
C_Orifice	flow coefficient of orifices	-
C_D	orifice calibration factor	Pa^2
C_Venturi	flow coefficient of classical venturi tubes	-
d	diameter	m
D	pipe diameter of flow measurement devices	m
g	gravitational acceleration	$\mathrm{m\,s^{-2}}$
h	specific enthalpy	$\mathrm{kJ\,kg^{-1}}$
k	overall heat transfer coefficient	$\mathrm{W\,m^{-2}\,K^{-1}}$
K_d	discharge coefficient	-
K_dr	certified discharge coefficient	-
L	length	m
L_1	geometry factor of standardized orifice sections	-
$L_2{}'$	geometry factor of standardized orifice sections	-
M	mass	kg
$\dot{M}$	mass flow	$\mathrm{kg\,s^{-1}}$
$\dot{m}$	mass flux	$\mathrm{kg\,s^{-1}\,m^{-2}}$
$\tilde{M}$	molar mass	$\mathrm{g\,mol^{-1}}$
N_Layer	number of insulation layer	-
P	perimeter	m

Symbol	Description	Unit
p	pressure	bar
p_0	relieving pressure	bar(a)
p_S	maximum allowable pressure	bar(g)
p_{set}	set pressure	bar(g)
$\dot{Q}$	heat flow	W
$\dot{q}$	heat flux	$W\,m^{-2}$
R	universal gas constant	$kJ\,kmol^{-1}\,K^{-1}$
R_{spec}	specific gas constant	$kJ\,kg^{-1}\,K^{-1}$
s	specific entropy	$kJ\,kg^{-1}\,K^{-1}$
T	temperature	K
t	time	s
u	internal energy	$kJ\,kg^{-1}$
v	specific volume	$m^3\,kg^{-1}$
x	coordinate in flow direction	m
Y_{H_2O}	water loading of air	$kg\,kg^{-1}$
Y_S	water loading of air under saturation	$kg\,kg^{-1}$
z	coordinate in altitude	m

Greek symbols

Symbol	Description	Unit
Δh_{melt}	melting enthalpy	$kJ\,kg^{-1}$
Δh_{sub}	sublimation enthalpy	$kJ\,kg^{-1}$
Δh_V	vaporisation enthalpy	$kJ\,kg^{-1}$
Δp	pressure difference	bar
Ψ	discharge function	-
α	heat transfer coefficient	$W\,m^{-2}\,K^{-1}$
α_C	condensation coefficient Hertz-Knudsen	-
α_E	evaporation coefficient Hertz-Knudsen	-
α_T	transmission coefficient Hertz-Knudsen	-
β	volume expansivity	K^{-1}
$\beta_{Orifice}$	diameter ratio of orifices	-
$\beta_{Venturi}$	diameter ratio of venturi tubes	-
χ	bulk compressibility	bar^{-1}
$\epsilon_{Orifice}$	expansion coefficient of orifices	-
$\epsilon_{Venturi}$	expansion coefficient of venturi tubes	-
ϵ	emissivity	-
η	dynamic viscosity	Pa s
λ	thermal conductivity	$W\,m^{-1}\,K^{-1}$

Symbol	Description	Unit
μ	isenthalpic joule thomson coefficient	$\mathrm{K\,bar^{-1}}$
ω	compressibility factor	-
ρ	density	$\mathrm{kg\,m^{-3}}$
σ	Stefan-Boltzmann-constant	$\mathrm{W\,m^{-1}\,K^{-4}}$
φ	humidity	-
ξ	mass fraction	-
ζ	darcy friction factor	-

Subscripts

Subscript	Description
0,x	conditions at the relieving state in upstream piping
0	conditions at the relieving state of the pressure vessel
amb	ambient conditions
b	conditions in the downstream pipe
Cond	conduction
Conv	convection
Cr	conditions of the cryogenic vessel wall
crit	conditions at critical point
Dep	deposition
He	conditions of helium
liq	saturated liquid
melt	melting point
Rad	radiation
operate	normal operation conditions
sat	saturation
sub	sublimation point
th	conditions at the throat of the pressure relief device
trip	triple point
V	conditions of the vacuum vessel
vap	saturated vapor
vent	conditions of venting fluid
W,i	conditions at the inner surface of the cryogenic vessel
W,o	conditions at the outer surface of the cryogenic vessel

Abbreviations

Abbreviation	Description
BD	bursting disc
CSM	case-specific model
DEB	di-electric breakdown
E	experiment
HEM	homogeneous equilibrium model
ITEP	Institute for Technical Physics
KIT	Karlsruhe Institute of Technology
LBV	loss of beamline vacuum
LCF	leak of cryogenic fluid
LHe	liquid helium
LIV	loss of insulating vacuum
MCI	maximum credible incident
MLI	multi-layer insulation
ODE	ordinary differential equation
P&ID	piping and instrumentation diagram
PED	pressure equipment directive
PICARD	pressure increase in cryostats and analysis of relief devices
PRD	pressure relief device
PRV	pressure relief valve
QSD	quench of superconducting device
SCD	superconducting device

List of Figures

List of Tables

1 Introduction

Helium cryostats are commonly designed as vacuum-insulated pressurised systems with a maximum allowable pressure of $p_S \geq 0.5\,\mathrm{bar(g)}$. Hence, they fall under the scope of the European Pressure Equipment Directive 2014/68/EU (PED) [27]. Usually operated at temperatures of $T < 10\,\mathrm{K}$, helium cryostats are often related to technical applications of superconductivity, particle physics and nuclear fusion, squids and quantum computing in industry and research institutions. Technical applications in research institutions typically require unique and complex design solutions, often exploiting small design margins for cutting-edge performance.

Under the PED, an individual risk assessment has to be carried out for each cryostat in its specific environment. The open handling of cryogenic fluids bears several risks, such as eye injury, asphyxiation and tissue damage (cold burns). This type of risks must be prevented by appropriate measures such as educating staff, providing personal protective equipment or putting up warning labels [1, 59]. In helium cryostats, evaporation of liquid coolant involves the risk of excessive pressure increase. This risk is particular in the case of helium due to its low vaporization enthalpy ($20.6\,\mathrm{kJ\,kg^{-1}}$ at $1\,\mathrm{bar(a)}$ [53]). Even a small heat input may cause an evaporation of liquid, followed by a rapid pressure increase. Since a heat input into helium cannot be prevented completely, de-pressurisation of the helium system must be guaranteed. According to the PED, helium cryostats have to be equipped with a pressure relief device (PRD) to protect them against excessive pressure in case of an incident. Incidents are characterised by heat loads that may cause an increase in pressure beyond the maximum allowable pressure of the pressure equipment. For the dimensioning of PRDs, an exact prediction of the relieving mass flow rate and from this of the minimum cross-section required to protect the system against excessive pressure based on the heat input is crucial. Established standards [31, 45] for the protection of cryogenic storage vessels against excessive pressure, however, do not entirely cover the conditions in helium cryostats due to the unique design solutions and the specific properties of helium. Thus, PRDs for helium cryostats are often not satisfactorily dimensioned bearing risks for the equipment and the user.

Depending on the application in which helium cryostats are used, the following incidents can be relevant for the dimensioning of PRDs (cf. [30]): loss of insulating vacuum (LIV), loss of beamline vacuum (LBV), quench of superconducting device (QSD), leak of cryogenic fluid (LCF) and di-electric breakdown (DEB). Out of these five incidents, risk assessments often define LIV as the maximum credible incident (MCI) that can affect a helium cryostat independently of its application due to highest heat loads to helium. Consequently, this work focuses on LIV.

In the case of LIV, the latent and sensible heat of the de-sublimation airflow is predominantly transferred to the helium system. Several experimental studies that deal with the heat input to helium cryostats following LIV have been published in the literature. Previous publications [17, 24, 52] quantify the heat flow to helium as the main design criterion of PRDs, but use only constant heat flux values for the dimensioning. More recent publications [39, 40, 81, 85] have pointed out that the use of these constant heat flux values neglects the process dynamics and thus may result in over-sized PRDs with implications on costs, space, risk of helium leakage and operation. Specifically, over-sized PRVs are prone to unstable release where the PRV periodically opens and closes at a characteristic frequency. This phenomenon is commonly referred to as *pumping* or *chattering*. Instabilities cause reduced discharge capacities and over-pressures and can damage the valve seat. The latter may result in a risk of helium leaks after the response of the PRV.

To take the process dynamics into account, a first dynamic modelling approach of LIV has been developed in [38] and refined in [85]. However, none of the resulting heat flux profiles is generally applicable due to the implementation of a facility-specific empirical temperature fitting.

Against this background, the present work focuses on a dimensioning procedure of PRDs for helium cryostats that is universally applicable for all flow conditions and set pressures only depending on the dimensions and the operating conditions of the cryostat. Specifically, the LIV-scenario is investigated with a focus on the heat transfer from the vacuum space to the helium system, implementing a transient heat transfer equation. In Chapter 2, the general approach of the PRD dimensioning process is introduced. Subsequently, different models for the dimensioning of PRDs are compared and their applicability to helium cryostats is evaluated. A new helium-specific dimensioning procedure is introduced in Chapter 3. In Chapter 4, the dynamic modelling of LIV is described. This includes the implementation of the applied fluid properties and of the derived system of ordinary differential equations (ODEs) into a numerical solver. Chapter 5 provides a brief overview of the safety test facility that is used for experimental validation. Design and functionality of PRVs in helium cryostats, instrumentation of the test facility and data evaluation are also covered. In Chapter 6, the general applicability of the LIV-model is discussed by a thorough experimental model investigation, analysing the influence of insulation, leak size and relieving pressure on the dynamic venting process. In addition, the use of spring-loaded PRVs with different characteristics is discussed. Finally, Chapter 7 summarises the key results of the present work and concludes with suggestions for future studies.

2 PRD dimensioning - State-of-the-art

This chapter covers the state-of-the-art of pressure relief device (PRD) dimensioning, including the definition of systems that commonly require PRDs. An overview of the established standardised procedure with a focus on cryogenic applications is presented and the limitations on the applicability to helium cryostats are discussed.

2.1 General approach

The European Pressure Equipment Directive 2014/68/EU (PED) [27] requires the installation of PRDs in pressure equipment with a maximum allowable pressure of $p_S \geq 0.5\,\text{bar}\,(\text{g})$ to ensure that the pressure inside the equipment does not permanently exceed p_S. Helium cryostats are mostly vacuum-insulated pressurised systems that meet this condition and thus fall under the scope of the PED. The PED allows a pressure increase of up to $1.1 \cdot p_S$ for a short period of time, resulting in the following definition of the relieving pressure p_0 of PRDs

$$p_0 \leq 1.1 \cdot p_S \tag{2.1}$$

Figure 2.1 schematically illustrates the flow path through a PRD with the fluid states that are relevant for dimensioning. The following conditions are distinguished

(0) relieving state in the pressure vessel,

(0,x) relieving state in the piping upstream of the PRD, influenced by the heat input and pressure drop in the piping,

(th) fluid state in the narrowest cross section of the PRD, commonly referred to as "*throat*",

(b) fluid state in the piping downstream of the PRD, commonly referred to as "*back*" conditions, influenced by the pressure drop in the downstream piping.

The main objective of the dimensioning process is to define the minimum discharge area A_{th} of the PRD that is required to protect the system against excessive pressure in case of an incident. A_{th} is calculated based on the continuity equation as

$$A_{th} = \frac{\dot{M}_0}{\dot{m}_{th} \cdot K_{dr}} \tag{2.2}$$

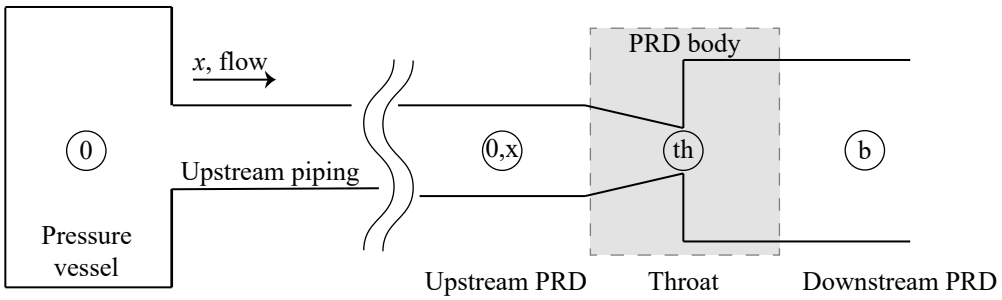

Figure 2.1: Schematic depiction of the fluid states that are relevant for the dimensioning of PRDs with a focus on the application to helium cryostats.

where $\dot{M}_0$ is the required relieving mass flow rate as a function of the relieving pressure p_0 and the specific volume v_0 at pressure vessel relieving conditions. $\dot{m}_{\mathrm{th}}$ is the mass flux that can be released through A_{th} under ideal flow conditions, given as

$$\dot{m}_{\mathrm{th}} = \frac{c_{\mathrm{th}}}{v_{\mathrm{th}}} \tag{2.3}$$

where v_{th} is the specific volume and c_{th} the fluid velocity, both at the throat of the PRD.

c_{th} is derived by applying the mass-specific energy conservation in one-dimensional, compressible, frictionless, steady-state and adiabatic fluid flow (i.e. isentropic flow $s = \text{const.}$) through short nozzles between state "0" and "th"

$$g \cdot z_0 + \frac{{c_0}^2}{2} + h_0 = g \cdot z_{\mathrm{th}} + \frac{{c_{\mathrm{th}}}^2}{2} + h_{\mathrm{th}} \tag{2.4}$$

where g is the gravitational acceleration, z is the height, c is the velocity and h is the enthalpy. The potential energies $g \cdot z$ are mostly neglected. The velocity in the piping upstream of the PRD c_0 is usually neglected as well, since it is small compared to the velocity at the throat of the PRD c_{th}. [68]

Solving Equation 2.4 for c_{th} yields

$$c_{\mathrm{th}} = \sqrt{2 \cdot (h_0 - h_{\mathrm{th}})} \tag{2.5}$$

Combining Equation 2.5 and 2.3 results in the commonly applied mass flux definition

$$\dot{m}_{\mathrm{th}} = \frac{\sqrt{2 \cdot (h_0 - h_{\mathrm{th}})}}{v_{\mathrm{th}}} \tag{2.6}$$

K_{dr} is an experimentally derived, dimensionless, certified discharge coefficient that corrects the deviation of PRDs from an ideal nozzle

$$K_{\mathrm{dr}} = \underbrace{\frac{\dot{M}_{0,\mathrm{measured}}}{\dot{M}_{0,\mathrm{ideal}}}}_{K_{\mathrm{d}}} \cdot \begin{cases} 0.9 & \text{PRV} \\ 1 & \text{BD} \end{cases} \tag{2.7}$$

where $\dot{M}_{0,\text{measured}}$ is the mass flow rate measured for a specific device and $\dot{M}_{0,\text{ideal}}$ is the mass flow rate that could be released through an ideal nozzle with the respective discharge area. The mass flow ratio is referred to as the discharge coefficient K_d[1]. In Equation 2.7, two types of PRDs are distinguished, re-closable devices, such as pressure relief valves (PRVs) and non re-closable devices, such as bursting discs (BDs). For PRVs, the factor 0.9 adds an additional safety margin to A_th. For gaseous and liquid flow with air and water, respectively, manufacturers provide measured K_d values only for one specific PRD. In case of two-phase flow, neither measured values are available nor does the literature provide a general calculation rule for the definition of the discharge coefficient. Various correlations are available in the literature [20, 55, 56, 65] depending on either thermodynamical or fluiddynamical properties as well as the single phase K_d values, but are not validated for helium. Specifically, the supercritical state is not considered separately. Since a supercritical fluid, as well as a gas, is compressible, the value for gaseous flow is assumed.

Different models exist in the literature for the calculation of both the relieving mass flow rate $\dot{M}_0$ and the enthalpy difference $(h_0 - h_\text{th})$. Those applied in established standards for the dimensioning of PRDs are introduced in the following.

2.2 Standardised procedures in ISO 4146 and ISO 21013

ISO 4126[2] is the internationally established product standard of PRDs for protection against excessive pressure, consisting of 10 parts [2–6, 43–46]. The calculation of the minimum discharge area A_th, including the definition of the mass flux and the discharge coefficient, is described in Part 7 for single-phase flow and in Part 10 for two-phase flow. ISO 4126 specifies general requirements for PRDs, independent of the medium for which they are designed. Low-temperature applications as relevant in helium cryostats are not considered.

The established standard for the dimensioning of PRDs in cryogenic storage vessels is ISO 21013. Conditions in cryostats that are more complex than those in storage vessels are not covered in ISO 21013. Due to this lack of data, the state-of-the-art calculation of the mass flow rate $\dot{M}_0$ to be released from cryogenic storage vessels and cryostats is based on the approach introduced in ISO 21013-3:2016 [31]. The calculation procedure of A_th in ISO 21013-3:2016 [31] is the same as the one presented in ISO 4126-7:2013 [45].

The standardised mass flux calculation for single-phase flow requires dimension-dependent input parameters, which leads to the introduction of different conversion factors. For more clarity, the model presented in this work strictly uses SI units. The unit conversions to ISO 4126 and ISO 21013 are explained in Appendix A.1.

[1] In the literature, the discharge coefficient is also referred to as α_W.

[2] On national levels standards vary by country, e.g. AD2000 Information Sheet A1 & A2 [7,8] in Germany and API520 [10] in America. However, for single-phase relieving all standards all are based on the same approach.

2.2.1 Calculation of the relieving mass flow rate

According to ISO 21013-3:2016 [31], the mass flow rate $\dot{M}_0$ to be released from vacuum-insulated cryogenic vessels is calculated as

$$\dot{M}_0 = \frac{\dot{Q}}{v_0 \cdot \left(\frac{\partial h}{\partial v}\right)_{p_0}} \tag{2.8}$$

where $\dot{Q}$ is the heat load to the fluid and the expression in the denominator is the specific enthalpy change. The heat load to a cryogenic system is defined for the following cases:

- Vacuum insulated vessels with intact insulation system, with and without pressure built-up systems (e.g. vaporizer).
- loss of insulating vacuum (LIV) in cryostats containing cryogenic fluids with a normal saturation temperature $T_{\mathrm{sat}} \geq 75\,\mathrm{K}$.
- LIV in cryostats containing cryogenic fluids with a normal saturation temperature $T_{\mathrm{sat}} \leq 75\,\mathrm{K}$ considering air condensation on cold surfaces.
- LIV in combination with fire.

As helium has a normal saturation temperature $T_{\mathrm{sat}} = 4.2\,\mathrm{K}$, the last two cases are relevant for the dimensioning of PRDs in helium cryostats. Here, the heat load $\dot{Q}$ is calculated as a function of the number of insulation layers N_{Layer} as

$$\frac{\dot{Q}}{\mathrm{W}} = \begin{cases} A_{\mathrm{Cr}} \cdot \frac{38400+420 \cdot N_{\mathrm{Layer}}^{0.73}}{0.96+N_{\mathrm{Layer}}^{0.73}} & \text{without fire} \\ 1.95 \cdot A_{\mathrm{Cr}}^{0.82} \cdot \frac{92160+1000 \cdot N_{\mathrm{Layer}}^{0.73}}{0.96+N_{\mathrm{Layer}}^{0.73}} & \text{with fire} \end{cases} \tag{2.9}$$

where A_{Cr} is the surface of the cryogenic circuit affected by LIV in m^2. Table 2.1 summarizes heat flux values calculated with Equation 2.9 for commonly applied insulation configurations. A maximum value of $4\,\mathrm{W\,cm^{-2}}$ is calculated for a bare cryogenic vessel and without the consideration of fire and $0.64\,\mathrm{W\,cm^{-2}}$ for 10 layers of MLI and without fire. However, two aspects related to Equation 2.9 have to be discussed. First, the fire case does not have to be considered in risk assessments according to the pressure equipment directive (PED) [27] as this often yields over-sized PRDs, causing e.g. leaks and unstable operation with reduced discharge capacities. The risk of fire, however, has to be excluded by appropriate measures, such as fire prevention, fire protection and fire-fighting measures [27]. If the risk of fire cannot be excluded by these or other methods, Equation 2.9 shall be used. Second, the origin of Equation 2.9 is not traceable in the standard. Based on an E-mail exchange [64] between the Standardisation Committee responsible for ISO 21013 and for the new EN 17527 - introduced in the next chapter - it could be clarified that Equation 2.9 for the non-fire case is based on an inter- and extrapolation of four values from the literature

- $3.8\,\mathrm{W\,cm^{-2}}$ for a bare surface at sub-critical p_0 and normal helium [52]

Table 2.1: Heat flux transferred to helium following loss of insulation vacuum with and without consideration of fire for different numbers of insulation layers according to ISO 21013-3:2016 (cf. Equation 2.9).

N_{Layer}	$\dot{q}$ in $\mathrm{W\,cm^{-2}}$	
	Fire	No fire
0	9.6	4.0
12	1.4	0.6
24	0.9	0.4
36	0.7	0.3

- $0.6\,\mathrm{W\,cm^{-2}}$ for 10 layers of MLI at sub-critical p_0 and normal helium [52]
- $3.1\,\mathrm{W\,cm^{-2}}$ for a bare surface at sub-critical p_0 and superfluid helium [37]
- $0.44\,\mathrm{W\,cm^{-2}}$ for 3 mm of lightweight composite insulation at sub-critical p_0 and superfluid helium [37]

As this shows that Equation 2.9 is derived based on values that are measured under totally different conditions without taking into account the type of insulation, its general applicability to helium cryostats can be doubted.

The calculation of the specific enthalpy change depends on the relieving pressure. For sub-critical relieving pressure, i.e. $p_0 < p_{\mathrm{crit}}$, the dominator in Equation 2.8 can be simplified to

$$v_0 \cdot \left(\frac{\partial h}{\partial v}\right)_{p_0} = v_{\mathrm{vap}} \cdot \left(\frac{h_{\mathrm{vap}} - h_{\mathrm{liq}}}{v_{\mathrm{vap}} - v_{\mathrm{liq}}}\right) \tag{2.10}$$

where h_{vap} and v_{vap} are the specific enthalpy respectively specific volume of saturated vapour and h_{liq} and v_{liq} are the specific enthalpy respectively specific volume of saturated liquid, all at p_0. The relieving temperature T_0 at sub-critical pressure equals the saturation temperature at p_0. Sub-critical relieving pressures, however, rarely occur in helium cryostats due to helium's low critical pressure of $p_{\mathrm{crit}} = 2.3\,\mathrm{bar(a)}$.

At critical and supercritical relieving pressure, the specific volume and the specific enthalpy in Equation 2.8 are calculated as

$$v_0 = f\left(p_0, T_0\right) \tag{2.11}$$

$$h_0 = f\left(p_0, T_0\right) \tag{2.12}$$

The relieving temperature T_0 is defined, where the coefficient

$$\frac{\sqrt{v}}{v \cdot \left(\frac{\partial h}{\partial v}\right)_{p_0}} \tag{2.13}$$

reaches its maximum [77]. Equation 2.13 is derived based on the assumption that in a system at constant pressure and volume, the mass of fluid which would occupy additional space due to expansion has to be released through a PRD. At supercritical pressure, the

specific enthalpy change is temperature dependent. In order to receive the maximum possible relieving mass flow rate, the maximum value of Equation 2.13, i.e. the minimum specific enthalpy change, is considered.

2.2.2 Calculation of the mass flux

The mass flux is derived applying the fundamental equation of the enthalpy change for a single fluid system at constant entropy, cf. [49, 68],

$$\int_{h_{\mathrm{th}}}^{h_0} \mathrm{d}h = \int_{p_{\mathrm{th}}}^{p_0} v \cdot \mathrm{d}p \tag{2.14}$$

For liquid flow, with $v = \text{const.}$ and $p_{\mathrm{th}} = p_{\mathrm{b}}$, the mass flux yields

$$\dot{m}_{\mathrm{th,liq}} = \sqrt{\frac{2 \cdot (p_0 - p_{\mathrm{b}})}{v}} \tag{2.15}$$

where p_0 and p_{b} are the relieving pressure in the pressure vessel and the back pressure in the piping downstream of the PRD, respectively. For liquid flow, an empirical viscosity correction factor K_{V} as a function of the Reynolds-Number[3] Re is applied.

$$K_{\mathrm{V}} = \left(2.9935 + \frac{2.878}{Re^{0.5}} + \frac{342.75}{Re^{1.5}}\right)^{-1} \tag{2.16}$$

For ideal gaseous flow, the specific volume is a function of pressure according to the isentropic relation $p \cdot v^{\kappa} = \text{const.}$

$$v = v_0 \cdot p_0^{\frac{1}{\kappa}} \cdot p^{-\frac{1}{\kappa}} \tag{2.17}$$

$$v_{\mathrm{th}} = v_{\mathrm{b}} \cdot p_{\mathrm{b}}^{\frac{1}{\kappa}} \cdot p_{\mathrm{th}}^{-\frac{1}{\kappa}} \tag{2.18}$$

where κ is the dimensionless isentropic expansion exponent. Solving Equation 2.14 by applying Equation 2.17 and 2.18 results in the mass flux for gaseous flow as function of the pressure vessel relieving conditions and the dimensionless discharge function C[4]

$$\dot{m}_{\mathrm{th,gas}} = \sqrt{2 \cdot \frac{p_0}{v_0}} \cdot C \tag{2.19}$$

The discharge function C is characterised by the isentropic expansion coefficient and the pressure ratio p_{b}/p_0 as

$$C = \begin{cases} \sqrt{\frac{\kappa}{\kappa-1}} \cdot \sqrt{\left(\frac{p_{\mathrm{b}}}{p_0}\right)^{\frac{2}{\kappa}} - \left(\frac{p_{\mathrm{b}}}{p_0}\right)^{\frac{\kappa+1}{\kappa}}} & \frac{p_{\mathrm{b}}}{p_0} > \Delta p_{\mathrm{crit}} \\ \left(\frac{2}{\kappa+1}\right)^{\frac{1}{\kappa-1}} \cdot \sqrt{\frac{\kappa}{\kappa+1}} & \frac{p_{\mathrm{b}}}{p_0} \leq \Delta p_{\mathrm{crit}} \end{cases} \tag{2.20}$$

[3] The Reynolds-Number Re is a dimensionless number in fluid dynamics that describes the ratio of inertial to viscous forces.

[4] In the literature C is also referred to as ψ.

It has a parabolic profile with a maximum at the so-called fluid-dynamical critical pressure ratio

$$\Delta p_{\mathrm{crit}} = \left(\frac{p_{\mathrm{b}}}{p_0}\right)_{\mathrm{crit}} = \left(\frac{2}{\kappa+1}\right)^{\frac{\kappa}{\kappa-1}} \tag{2.21}$$

A further decrease of p_{b}/p_0 does not influence the mass flux any more, as the flow velocity is at sonic speed and the discharge function constantly assumes its maximum value.

The form of the discharge function is presented differently in ISO 4126-7:2013 and ISO 21013-3:2016, however, it delivers the same results. The conversion between the two forms is presented in Appendix A.2.

For two-phase flow, the specific volume is a function of the compressibility factor ω

$$v_{\mathrm{2ph}} = v_0 \cdot \left(\omega \cdot \left(\frac{p_0}{p} - 1\right) + 1\right) \tag{2.22}$$

where ω is defined for flashing and non-flashing flow at pressure vessel relieving conditions, e.g. saturated liquid, two-phase or gas vapour. The mass flux for two phase flow is thus defined as

$$\dot{m}_{\mathrm{th,2ph}} = \sqrt{2 \cdot \frac{p_0}{v_0}} \cdot \frac{\sqrt{\omega \cdot \ln\left(\frac{p_{\mathrm{b}}}{p_0}\right)^{-1} - (\omega - 1) \cdot \left(1 - \frac{p_{\mathrm{b}}}{p_0}\right)}}{\omega \cdot \left(\left(\frac{p_{\mathrm{b}}}{p_0}\right)^{-1} - 1\right) + 1} \tag{2.23}$$

The two-phase flow is at sonic speed if p_{b}/p_0 takes the critical value according to

$$0 = \Delta p_{\mathrm{crit}}^2 + \left(\omega^2 - 2 \cdot \omega\right) \cdot (1 - \Delta p_{\mathrm{crit}})^2 + 2 \cdot \omega^2 \cdot \ln \Delta p_{\mathrm{crit}} + 2 \cdot \omega^2 \cdot (1 - \Delta p_{\mathrm{crit}}) \tag{2.24}$$

2.2.3 Influence of piping up- and downstream of PRDs

Pressure drops and heat inputs in the piping up- and downstream of PRDs influence the density at the throat and thus the relieving capacity, cf. Equation 2.15 and 2.19.

When using PRVs, it is recommended to limit the pressure drop in the up- and downstream piping to 3 % and 10 % of the set pressure p_{set}, respectively. The set pressure is the predefined gauge pressure, at which a PRV commences to open. Depending on the PRV type,

$$p_{\mathrm{set}} = \frac{p_0}{(1.05 \ldots 1.10)} \tag{2.25}$$

where p_0 is the relieving pressure at which the PRV is fully open.[5]

The heat input upstream of PRDs in piping longer than 0.6 m shall be considered, while the heat input in the downstream piping can be neglected. The temperature increase in the pipe is calculated for convective heat transfer of internal single-phase flow through a pipe of fixed surface temperature. For vacuum insulated vessels, the heat transfer surface

[5] Or reversely, the relieving pressure is the set pressure plus overpressure, where the latter depends on the opening characteristics.

is divided into two parts: the area inside the vacuum vessel A_{PV} with a lower impact on the heat transfer, and the area A_{amb} outside of the cryostat. The first part is weighted by the average temperature in the annular space, resulting in the following formula for the calculation of the adjusted relieving temperature $T_{0,x}$ at the outlet of the pipe

$$T_{0,x} = T_{\mathrm{amb}} - \frac{T_{\mathrm{amb}} - T_0}{e^{\frac{\alpha}{M_0 \cdot c_p} \cdot \left(\frac{T_{\mathrm{amb}} + T_0}{2 \cdot T_{\mathrm{amb}}} \cdot A_{\mathrm{PV}} + A_{\mathrm{amb}} \right)}} \tag{2.26}$$

where T_{amb} is the ambient temperature, T_0 is the relieving temperature of the cryogenic vessel according to Equation 2.10 or 2.13, c_p is the isobaric specific heat capacity of the cryogenic fluid and α is the convective heat transfer coefficient. For α, different values are given in ISO 21013 dependent on ambient temperature and relieving temperature of the cryogenic fluid. In case of helium with relieving temperatures $T_0 \leq 75\,\mathrm{K}$, $\alpha = 78.5\,\mathrm{W\,m^{-2}\,K^{-1}}$ is assumed. In case of fire, $\alpha = 105\,\mathrm{W\,m^{-2}\,K^{-1}}$. The mass flux calculation is performed iteratively, using $p_0 = p_{0,\mathrm{x}}$ and $T_0 = T_{0,\mathrm{x}}$.

2.2.4 Limitations of ISO 4126 and ISO 21013 in case of helium cryostats

The mass flux calculations in ISO 4126 Part 7 and 10 for both single-phase and two-phase flow are only applicable for

$$T_0 \leq 0.9 \cdot T_{\mathrm{crit}} \tag{2.27}$$

$$p_0 \leq 0.5 \cdot p_{\mathrm{crit}} \tag{2.28}$$

Considering the low critical pressure of helium of $p_{\mathrm{crit}} = 2.3\,\mathrm{bar(a)}$, a relieving pressure of $p_0 \leq 1.15\,\mathrm{bar(a)}$ is within the possible range. Since the maximum allowable pressure of helium cryostats is often higher than the critical pressure, the procedure in ISO 4126-7:2013 is not generally applicable to helium cryostats.

The fixed heat transfer coefficient α in Equation 2.26 is originally deduced from a bare liquid hydrogen pipe around which air flows at a velocity of about $6.7\,\mathrm{m\,s^{-1}}$ [64]. This datum value over-simplifies the conditions in helium cryostat applications, covering a wide range of relieving mass flow rates.

Further, helium cryostats are commonly used in technical applications of superconductivity, including specific components such as superconducting magnets or radio-frequency cavities, squids and quantum computing. These components add additional risks to the cryostat, which are potentially relevant for the dimensioning of the PRDs.

As the vacuum vessel in vacuum-insulated cryostats is directly attached to pressure retaining components, the vacuum vessel is part of the pressure equipment according to the PED [27], although its maximum allowable pressure is $p_{\mathrm{S}} < 0.5\,\mathrm{bar\,(g)}$. Hence, it has to be equipped with a safety related PRD. Scenarios for the dimensioning of PRDs for the vacuum vessel, however, are not covered in established standards.

Due to these limitations of ISO 4126 and ISO 21013, the new European Standard EN 17527 *"Helium cryostats – Protection against excessive pressure"* has been developed, addressing all specific helium-related risks and the dimensioning of PRDs for helium cryostats. The new approach is presented in the next chapter.

3 PRD dimensioning in the new European Standard EN 17527

The detailed analysis of the dimensioning of cryogenic PRDs presented in this chapter has been performed within the Standardization Committee CEN TC268/WG6. The working group has developed the first European Standard on *"Helium Cryostats - Protection against excessive pressure"* [30]. This dissertation project provided substantial contributions to this development.

The new Standard deals not only with the dimensioning process of PRDs, but also provides an overall approach on how to achieve a save design solution for the protection of helium cryostat against excessive pressure. This includes the definition of possible incidental scenarios, the risk assessment, the development of protection concepts and the substance release from the helium cryostat.

Figure 3.1 illustrates the procedure of the risk assessment and the development of protection concepts. The resulting relieving pressure for a specific incidental scenario is the input into a four step PRD dimensioning procedure, which is depicted in Figure 3.2. In the first step, the specific volume and the temperature at pressure vessel relieving conditions are calculated (red). Both are required for the definition of the relieving mass flow rate in step 2 (blue). Then, the mass flux is calculated in step 3 (yellow). Steps 1 to 3 deliver the input for the final calculation of the minimum discharge area in step 4 (green). Both flow charts have been developed by the author in the course of the standardisation work. In the following sections, the four step dimensioning procedure is described in detail.

3.1 Calculation of the relieving specific volume and the relieving temperature

Other than in ISO 21013-3:2016 [31], where $v_0 = v_{\mathrm{vap}}$ at sub-critical pressure, the specific volume at relieving conditions v_0 for sub-critical relieving pressure is calculated iteratively to

$$v_0 = v \mid \max_{v \geq v_{\mathrm{i}}} \left[A_{\mathrm{th}} \left(v \right) \right] \tag{3.1}$$

signifying the particular fluid state v_0 during the relieving process with $v \geq v_{\mathrm{i}}$, where A_{th} reaches its maximum. The initial specific volume v_{i} is calculated according to

$$v_{\mathrm{i}} = \frac{V_{\mathrm{He}}}{M_{\mathrm{He}}} \tag{3.2}$$

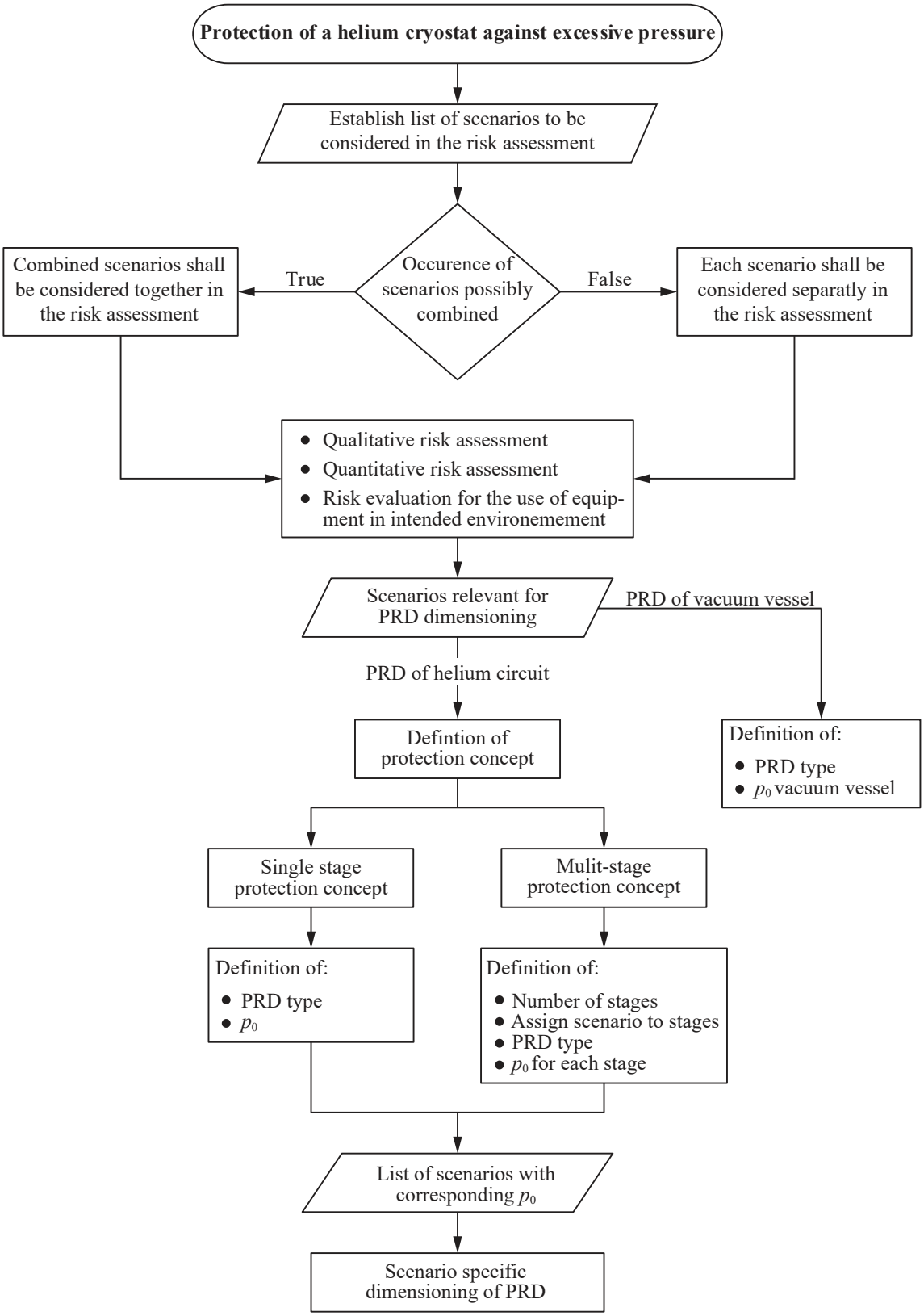

Figure 3.1: Flow chart of the risk assessment and the development of the protection concepts resulting in the definition of the relieving pressures p_0. Developed by the author in the course of the standardisation work [30].

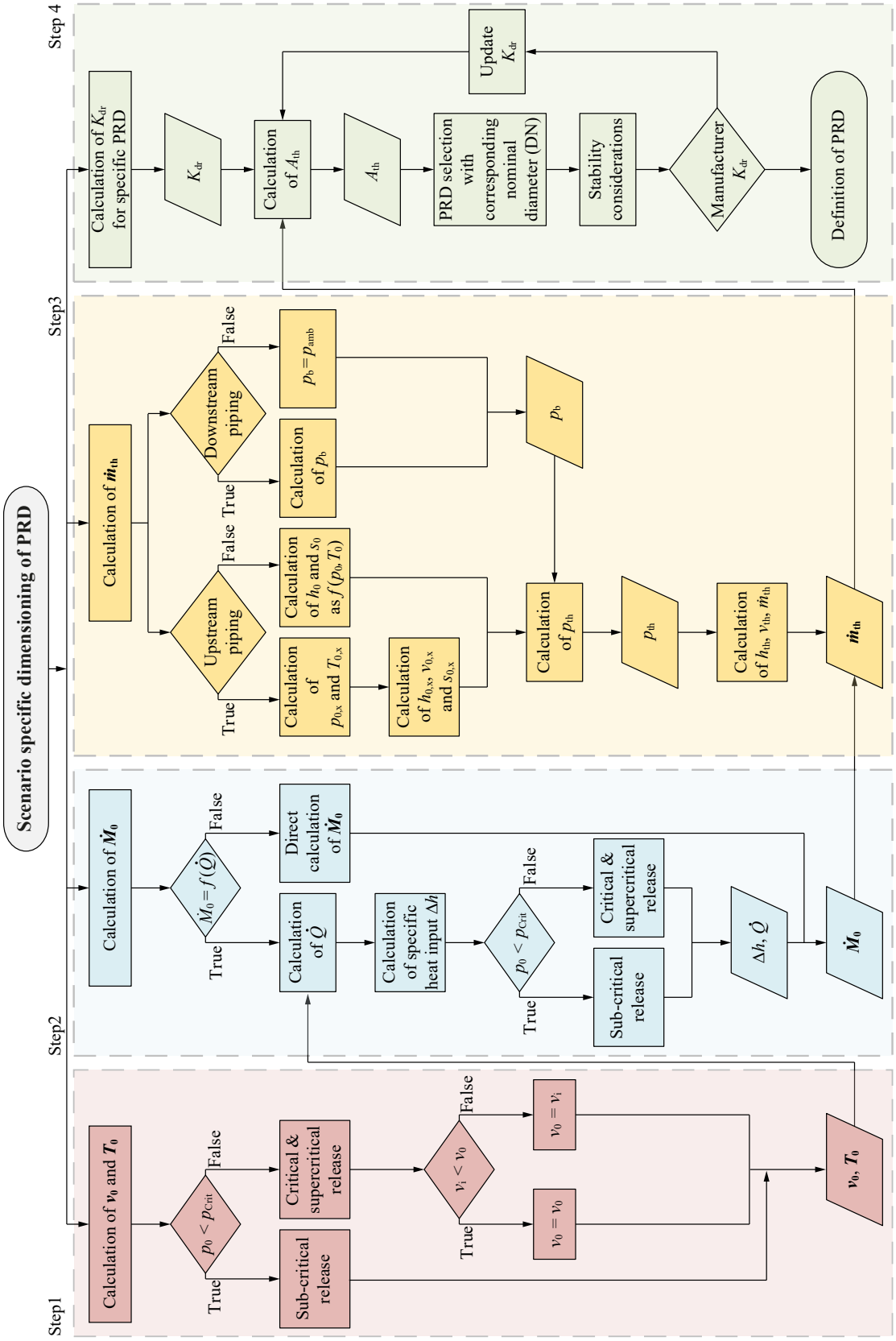

Figure 3.2: Flow chart of the four step PRD dimensioning procedure for helium cryostat. Developed by the author in the course of the standardisation work [30].

where V_{He} is the volume of the cryogenic circuit and M_{He} the initial helium mass inside the system. This definition of v_0 in Equation 3.1 considers the possibility of liquid or two-phase inlet conditions at small initial specific volumes v_{i}, i.e. at large initial filling quantities. Exemplary calculations have shown that a PRD dimensioned at these conditions following ISO 21013-3:2016 [31] would be under-sized. Thus, a safe calculation of v_0 at sub-critical relieving pressure in the entire field of application is provided by Equation 3.1.

The relieving temperature at sub-critical pressure is defined to

$$T_0 = T_{\mathrm{sat}}\left(p_0\right) \tag{3.3}$$

where T_{sat} is the saturation temperature. At critical and supercritical relieving pressure, v_0 is defined to

$$v_0 = \begin{cases} v\left(p_0, T_0\right) & v_{\mathrm{i}} < v\left(p_0, T_0\right) \\ v_{\mathrm{i}} & v_{\mathrm{i}} \geq v\left(p_0, T_0\right) \end{cases} \tag{3.4}$$

where T_0 is calculated according to Equation 2.13. This distinction ensures that the specific volume at relieving conditions in the pressure vessel does not assume values lower than the initial specific volume during pressure increase. After activation of a PRD the specific volume always increases, i.e. the amount/mass of fluid is reduced at constant volume. Note that Equation 2.13 might result in $v_0 < v_{\mathrm{i}}$, which is physically impossible.

3.2 Calculation of the relieving mass flow rate

The calculation of the relieving mass flow rate $\dot{M}_0$ is separated into two cases. In the first case relevant for the dimensioning of PRDs of the cryogenic circuit, $\dot{M}_0$ is a function of the heat flow $\dot{Q}$ to the cryogenic fluid according to Equation 2.8. In the second case relevant for the dimensioning of PRDs of the vacuum vessel, $\dot{M}_0$ is a function of the leak size A_{Leak}. The heat load $\dot{Q}$ transferred to helium, required in the first case, is defined for the following incidental scenarios:

- loss of insulating vacuum (LIV)
- loss of beamline vacuum (LBV)
- quench of superconducting device (QSD)

Fire is not considered as an incidental scenario in the EN 17527 as discussed in Subsection 2.2.1. A reference to ISO 21013-3:2016 is given if fire cannot be excluded.

The heat input following LIV and LBV is predominantly caused by the desublimation or condensation of the venting fluid on the cold surface, whereas in a QSD, the heat is induced by the transition of the superconductor from a superconducting to a resistive state, yielding a heat dissipation according to Ohm's law of $\dot{Q} = RI^2$, where R is the resistance and I is the current.

In the second case, for the dimensioning of the PRD of the vacuum vessel, the following incidental scenarios are taken into account

- leak of cryogenic fluid (LCF),
- di-electric breakdown (DEB).

For both scenarios, $\dot{M}_0$ is directly calculated applying the Bernoulli-equation for short nozzles

$$\dot{M}_0 = A_{\mathrm{Leak}} \cdot K_{\mathrm{d}} \cdot \sqrt{2 \cdot \frac{p_{\mathrm{Cr}}}{v_{\mathrm{Cr}}}} \cdot \begin{cases} \sqrt{\frac{\kappa}{\kappa-1}} \cdot \sqrt{\left(\frac{p_{\mathrm{V}}}{p_{\mathrm{Cr}}}\right)^{\frac{2}{\kappa}} - \left(\frac{p_{\mathrm{V}}}{p_{\mathrm{Cr}}}\right)^{\frac{\kappa+1}{\kappa}}} & \frac{p_{\mathrm{V}}}{p_{\mathrm{Cr}}} > \Delta p_{\mathrm{Crit}} \\ \left(\frac{2}{\kappa+1}\right)^{\frac{1}{\kappa-1}} \cdot \sqrt{\frac{\kappa}{\kappa+1}} & \frac{p_{\mathrm{V}}}{p_{\mathrm{Cr}}} \leq \Delta p_{\mathrm{Crit}} \end{cases} \tag{3.5}$$

Due to the variety of specific applications and design solutions of helium cryostats, in addition to the application of the presented formulas, EN 17527 allows to define the heat load based on one of the following methods including detailed documentation

- published experimental data that show a good correspondence to the considered design. A summary of literature data is given in Table 3.1, or
- unpublished experimental data obtained for the particular cryostat design, or
- numerical modelling of the processes during the incidental scenario.

In the following subsection, the calculation rules for each incidental scenario are presented in detail.

3.2.1 Loss of insulating vacuum (LIV)

For LIV with atmospheric air, the heat load is defined as

$$\dot{Q}_{\mathrm{LIV}} = \dot{q}_{\mathrm{LIV}} \cdot A_{\mathrm{Cr}} \tag{3.6}$$

where $\dot{q}_{\mathrm{LIV}}$ is the heat flux transferred to helium dependent on the number of insulation layers N_{Layer} and A_{Cr} is the surface of the cryogenic circuit. Based on the literature data summarized in Table 3.1, the maximum heat flux $\dot{q}_{\mathrm{LIV}}$ transferred to helium following LIV with a bare cryogenic surface is defined for sub- and supercritical relieving pressures p_0 as

$$\dot{q}_{\mathrm{LIV}} = \begin{cases} 3.8\,\mathrm{W\,cm^{-2}} & p_0 \leq p_{\mathrm{Crit}} \\ 2.0\,\mathrm{W\,cm^{-2}} & p_0 > p_{\mathrm{Crit}} \end{cases} \tag{3.7}$$

This distinction is a significant advancement for helium cryostat design. Recent studies [39, 81] have shown that the use of $3.8\,\mathrm{W\,cm^{-2}}$ for supercritical relieving pressure results in over-sized PRVs with unstable operation and reduced discharge capacities. Due to lack of data for insulated surfaces, the heat flux calculation according to Equation 2.9 without consideration of fire is presently recommended.

The heat flux following LIV can be limited by the leak size, specifically by the ratio of the leak area to the cryogenic surface ${}^{A_{\mathrm{Leak}}}/_{A_{\mathrm{Cr}}}$. Hence, if

$$\frac{A_{\mathrm{Leak}}}{A_{\mathrm{Cr}}} < 8 \cdot 10^{-4} \tag{3.8}$$

$\dot{q}_{\mathrm{LIV}}$ is calculated according to the LBV scenario presented in the next subsection.

Table 3.1: Literature values for the heat flux caused by LIV with atmospheric air into a helium (He) cryostat, depending on the number of insulation layers N_{Layer} with the respective relative venting area ${}^{A_{\mathrm{Orifice}}}/_{A_{\mathrm{Cr}}}$ and the specific measurement conditions.

Reference	N_{Layer}	$\dot{q}$ ($\mathrm{W\,cm^{-2}}$)	Remarks and conditions	${}^{A_{\mathrm{Orifice}}}/_{A_{\mathrm{Cr}}}$
Dhuley & VanSciver [24]	0	3.0	Max. value at sub-critical p_0	$5.65 \cdot 10^{-4}$
Lehmann & Zahn [52]	0	3.8	Max. value at sub-critical p_0	
Ercolani et al. [32]	0	4.5 1.9	Max. value at sub-critical p_0 Max. value at supercritical p_0	$9.5 \cdot 10^{-3}$
Zoller [85]	0	0.9 . . . 1.3	Value at fist opening of PRV Supercritical p_0	$9.82 \cdot 10^{-5}$ . . . $5.65 \cdot 10^{-4}$
Weber [79, 80]	0	1.4 . . . 1.9	Value at fist opening of PRV Supercritical p_0	$8.8 \cdot 10^{-4}$
Lehmann & Zahn [52]	1 10	2.0 0.6	Max. value at sub-critical p_0 Max. value at sub-critical p_0	

3.2.2 Loss of beamline vacuum (LBV)

The heat load $\dot{Q}_{\mathrm{LBV}}$ in case of LBV with atmospheric air depends on the expected leak size A_{Leak} that results from the risk assessment.

$$\dot{Q}_{\mathrm{LBV}} = \begin{cases} \dot{q}_{\mathrm{LIV}} \cdot A_{\mathrm{Cr}} & \frac{A_{\mathrm{Leak}}}{A_{\mathrm{Cr}}} \geq 8 \cdot 10^{-4} \\ \dot{M}_{\mathrm{LBV}} \cdot \Delta h_{\mathrm{air}} & \frac{A_{\mathrm{Leak}}}{A_{\mathrm{Cr}}} < 8 \cdot 10^{-4} \end{cases} \tag{3.9}$$

where $\dot{M}_{\mathrm{LBV}}$ is the mass flow rate through a specific leak area and Δh_{air} is the enthalpy difference of air from ambient to wall conditions, considering the latent and sensible heat of the air components nitrogen, argon, oxygen and water. If Equation 3.8 applies, the heat transfer mechanism is limited by the mass flow rate entering the vacuum space, and the air is deposited completely on the cold surface at constant vacuum pressure p_{V}. Under these conditions and the assumption of the leak as an ideal short nozzle according to Equation 2.19, $\dot{M}_{\mathrm{LBV}}$ is calculated as

$$\dot{M}_{\mathrm{LBV}} = A_{\mathrm{Leak}} \cdot \sqrt{2 \cdot \frac{p_{\mathrm{amb}}}{v_{\mathrm{amb}}}} \cdot \begin{cases} \sqrt{\frac{\kappa}{\kappa-1}} \cdot \sqrt{\left(\frac{p_{\mathrm{V}}}{p_{\mathrm{amb}}}\right)^{\frac{2}{\kappa}} - \left(\frac{p_{\mathrm{V}}}{p_{\mathrm{amb}}}\right)^{\frac{\kappa+1}{\kappa}}} & \frac{p_{\mathrm{V}}}{p_{\mathrm{amb}}} > \Delta p_{\mathrm{Crit}} \\ \left(\frac{2}{\kappa+1}\right)^{\frac{1}{\kappa-1}} \cdot \sqrt{\frac{\kappa}{\kappa+1}} & \frac{p_{\mathrm{V}}}{p_{\mathrm{amb}}} \leq \Delta p_{\mathrm{Crit}} \end{cases} \tag{3.10}$$

3.2.3 Quench of superconducting device (QSD)

The heat load $\dot{Q}_{\text{Quench}}$ transferred to helium following a QSD is calculated according to

$$\dot{Q}_{\text{Quench}} = \dot{q}_{\text{Quench}} \cdot A_{\text{SCD}} \tag{3.11}$$

where the heat flux $\dot{q}_{\text{Quench}}$ following a quench is calculated applying heat transfer correlations and A_{SCD} is the surface of the superconducting device (SCD) affected by the quench. The heat transfer correlations are a function of the temperature difference between the surface temperature of the SCD and the helium relieving temperature $T_{\text{SCD}} - T_0$ according to [16, 51]. The surface temperature, however, is to be considered as input from the magnet design, as it is dependent on many parameters, such as the material, the current and the voltage used.

Besides the definition of the heat load, the specific heat input required for the calculation of the relieving mass flow rate is calculated based on Equation 2.10 with v_0 according to Equation 3.1 and Equation 2.11 to 2.13 at sub- and supercritical pressure, respectively.

3.2.4 Leak of cryogenic fluid (LCF)

LCF can either be a helium leak from the helium circuit, or a helium-cooled thermal shield, or a nitrogen leak from a nitrogen-cooled thermal shield. The possible leak area A_{Leak} required in Equation 3.5 is a result of the risk assessment. However, LCF can only cause an excessive pressure increase if the pressure inside the vacuum vessel p_{V} exceeds the maximum allowable pressure of the vacuum vessel $p_{\text{S,V}}$ assuming that the total amount of cryogenic fluid in the system evaporates in the vacuum vessel and is warmed up to ambient temperature.

3.2.5 Di-electric breakdown (DEB)

In case of DEB, the leak size that refers to the size of the perforation following an electrical arc is estimated by considering a conservative scenario, where the thermal energy is entirely transferred into a single point on the cryogenic surface, causing the melting of a hole in the wall of a vessel or a pipe.

3.3 Calculation of the mass flux

As the density of the fluid and consequently the relieving capacity of the PRD is affected by the increase in temperature and the pressure drop in the upstream piping, the impact of these two influences on the relieving capacity is evaluated first. The temperature increase in the piping upstream of the PRD is calculated similar to the approach in ISO 21013-3. However, it is recommended to calculate the heat transfer coefficient using common

engineering correlations instead of one constant value, as the variety of applications and conditions cannot be covered by one constant value. Furthermore, the heat transfer surface inside the vacuum vessel might be affected by LIV. Due to this, it is recommended to calculate the helium and the wall temperature section-wise considering the local boundary conditions according to

$$T_{0,x,i} = T_{\mathrm{W},i} - \frac{T_{\mathrm{W},i} - T_{0,\mathrm{in},i}}{e^{\frac{k_i \cdot P_i \cdot L_i}{\dot{M} \cdot c_{p,i}}}} \tag{3.12}$$

where $T_{0,x,i}$ is the outlet temperature of a pipe section i, $T_{0,\mathrm{in},i}$ is the inlet temperature, $T_{\mathrm{W},i}$ is the wall temperature, k_i is the average overall heat transfer coefficient, P_i is the perimeter, L_i is the length and $c_{p,i}$ is the isobaric specific heat capacity of helium at $T_{0,x,i}$ and $p_{0,x,i}$. The pressure drop in both the upstream and the downstream piping system is calculated according to common engineering correlations.

The mass flux is calculated applying the homogeneous equilibrium model (HEM) according to [72]. Typically, the HEM is applied only in case of two phase flow. In EN 17527, however, the mass flux also for single phase flow is calculated according to the HEM with the advantages that there are no limits regarding the relieving pressure and the flow type does not have to be distinguished. This leads to a single formula to solve, which is less error-prone compared to the calculations in Section 2.2. The mass flux at the throat $\dot{m}_{\mathrm{th}}$ is calculated by searching the maximum value of Equation 2.6, dependent on the relieving state upstream of the PRD and the throat conditions assuming an isentropic expansion

$$\dot{m}_{\mathrm{th,HEM}} = \max_{p_{\mathrm{b}} \leq p \leq p_0} \left(\frac{\sqrt{2 \cdot \left(h_{0,x}\left(s_{0,x}, p_{0,x}\right) - h\left(s_{0,x}, p\right)\right)}}{v\left(s_{0,x}, p\right)} \right) \tag{3.13}$$

where $s_{0,x}$ is the specific entropy in the piping upstream of the PRD. The pressure at the throat is the one corresponding to the maximum value of $\dot{m}_{\mathrm{th,HEM}}$. For liquid and sub-sonic flow $p_{\mathrm{th}} = p_{\mathrm{b}}$, for sonic flow $p_{\mathrm{th}} = p_{\mathrm{Laval}}$, where p_{Laval} is the Laval pressure [68], which always occurs in sonic flow conditions independently of the downstream pressure. Supercritical flow is compressible, as is gaseous flow, so that sonic flow can occur.

3.4 Definition of the certified discharge coefficient

For preliminary dimensioning, the following values of the certified discharge coefficient K_{dr} are defined

- 0.95 for PRVs with single-phase vapour flow both upstream and in the throat
- 0.85 for PRVs with two-phase flow both upstream and in the throat
- 0.65 for PRVs with single-phase liquid flow both upstream and in the throat
- 0.65 for BDs with single-phase vapour flow both upstream and in the throat

After the selection of a specific PRD, the K_{dr} has to be updated with the value provided by the manufacturer as it depends on the particular throat shape.

PRVs are available only in a grid of nominal sizes (e.g. DN20, DN25, etc.). After dimensioning of the PRV, a particular device with the next larger nominal size will be selected, which bears the risk of over-sizing. In systems prone to unstable operation, the minimum discharge area can be adapted to the required conditions by adjusting the discharge coefficient through a lift restriction. According to [45], the lift shall be restricted to not more than 30 % of the nominal lift or 1 mm, whichever is larger.

3.5 Summary

The new European Standard covers the specific requirements for the protection of helium cryostats against excessive pressure based on a list of heat flux data for specific conditions. However, recent publications [32, 81, 85] have shown that the dimensioning of PRVs for helium cryostats based on those heat flux data often results in over-sizing with reduced discharge capacities, unstable operation and overpressure. So far, a freely available possibility of PRD dimensioning based on dynamic modelling of incidents in helium cryostats does not yet exit although its application is allowed in the new European Standard EN 17527. The development of such a dynamic model is the central objective of this thesis. The result is presented in the next chapter.

4 Dynamic modelling of incidents

In this chapter, the dynamic model developed to describe the processes that are induced by loss of insulating vacuum (LIV), which is defined as the maximum credible incident (MCI) that can affect a helium cryostat, is presented in detail. This includes the introduction of the applied fluid properties and the implementation of the resulting systems of ordinary differential equations (ODEs) into a numerical solver.

4.1 Maximum credible incident

To be defined as the MCI in helium cryostat, the considered incident shall result in a heat flow transferred to helium that is higher compared to heat flows resulting from other incidents that might affect the cryostat in its environment. Since LIV often fulfils this requirement according to the risk assessment, this work focuses on the processes in a helium cryostat induced by LIV. Figure 4.1a schematically depicts the dynamic venting process with the basic time dependent variables and geometry parameters relevant for the modelling of LIV. The venting process works as follows: Ambient air flows through a leak into the vacuum space, causing a pressure increase inside the vacuum vessel. When the air reaches the cryogenic vessel wall, it deposits on the cold outer surface due to wall temperatures $T_{\mathrm{W,o}}$ below the condensation temperature of the air components. The resulting heat flux is transferred through the wall to the helium inside the cryogenic vessel, where it triggers an iso-choric pressure increase until the relieving pressure of the PRV is reached. The mass flow rate required to prevent the system from an excessive pressure increase is released through the PRV. Depending on the length of the piping upstream of the PRV, i.e. the length between the cryostat and the inlet of the PRV, an additional heat flow $\dot{Q}_{\mathrm{up}}$ is transferred to the discharging helium. Since $\dot{Q}_{\mathrm{up}}$ influences the density at the inlet of the PRV, and thus its minimum required discharge diameter, the consideration of $\dot{Q}_{\mathrm{up}}$ is essential for the dimensioning process.

Figure 4.1b shows the zoom into the schematic wall temperature profile at steady state conditions that combines the processes inside the vacuum space with those inside the cryogenic vessel, forming the basis for the initialisation of the heat transfer through the vessel wall.

The definition of the initial steady state conditions of a helium cryostat that are required to start the evaluation of the dynamic model is presented in Section 4.2. The set of equations describing the processes inside the vacuum vessel are introduced in Section 4.3. In Section 4.4, the dynamic heat transfer through the vessel wall is described, followed by

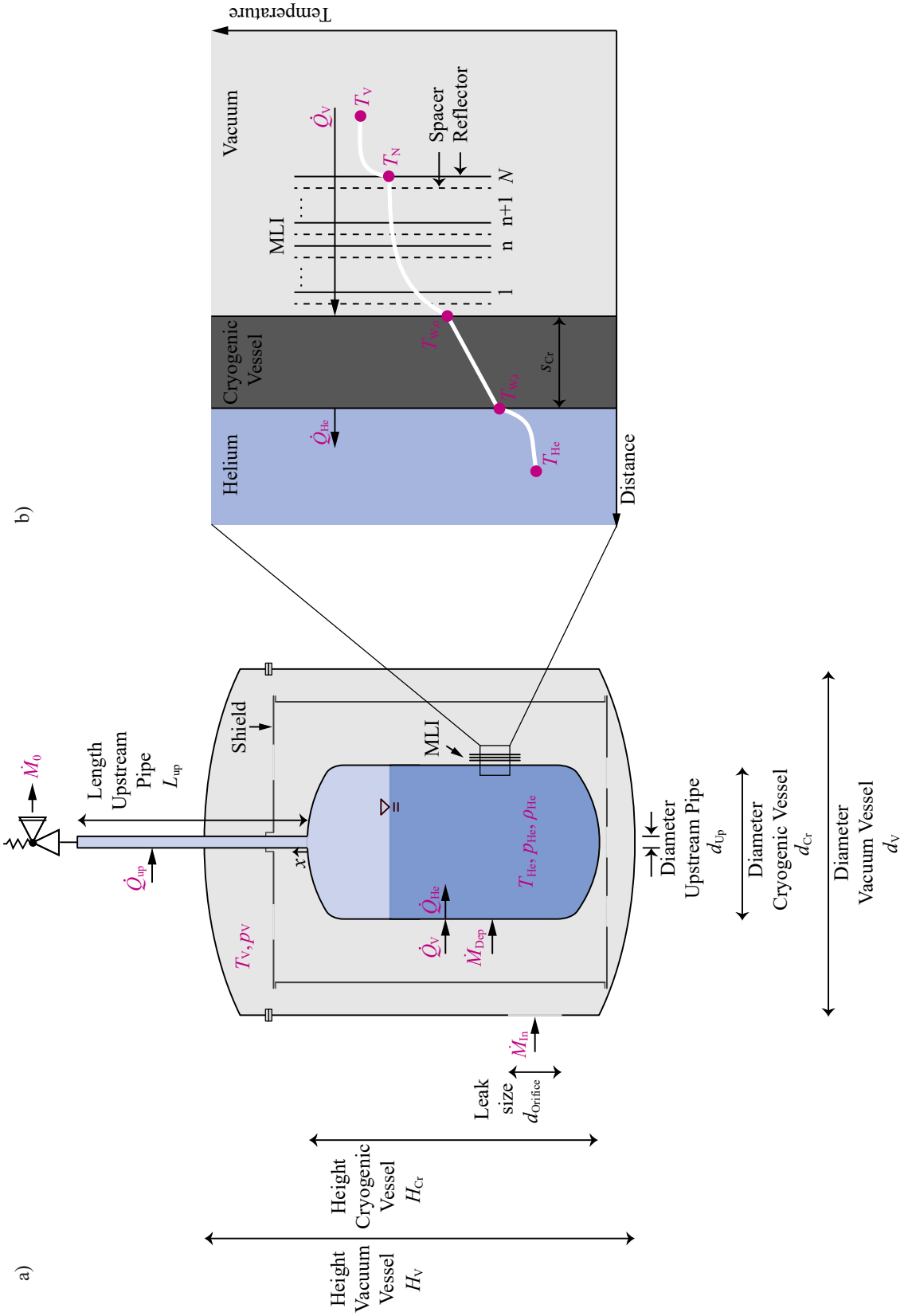

Figure 4.1: a) Schematic drawing of a helium cryostat with the basic time dependent variables and geometry parameters relevant for the modelling of LIV. b) Zoom into the schematic initial temperature profile between the vacuum space and the helium inside the cryogenic vessel.

the definition of the set of equations reflecting the processes inside the helium vessel in Section 4.5. The heat input to helium inside the piping upstream of the PRV is modelled in Section 4.6.

Although the main objective is to develop a generally applicable model for the dimensioning of PRDs for helium cryostats, some of the generally applicable equations presented in this chapter have been adapted with a focus on the model validation with experimental data obtained at the cryogenic safety test facility PICARD that is described in Chapter 6. The influence of the usage of generally applicable equations on the model validation is also discussed in Chapter 6. The derivation of the PICARD specific model equations is explained in Section 5.7. Furthermore, the experiments have been used to justify assumptions made in the model and to optimize the model if parameters cannot be described analytically.

4.2 Initial steady state conditions

In this section, the derivation of the initial parameters for the evaluation of the model are described based on the assumption of steady state conditions inside the cryostat during normal operation.

4.2.1 Initial values inside the vacuum and the helium vessel

Referring to the variables defined in Figure 4.1a, the initial vacuum pressure $p_{\mathrm{V}}(0)$, the initial vacuum temperature $T_{\mathrm{V}}(0)$, the initial helium pressure $p_{\mathrm{He}}(0)$, the initial helium temperature $T_{\mathrm{He}}(0)$ and the initial helium density $\rho_{\mathrm{He}}(0)$ can be easily defined by the normal operating conditions of the cryostat as

$$p_{\mathrm{V}}(0) \leqslant 10^{-6}\,\mathrm{mbar} \tag{4.1}$$

$$T_{\mathrm{V}}(0) = T_{\mathrm{amb}} \tag{4.2}$$

$$\varphi(0) = 0\ldots1 \tag{4.3}$$

$$p_{\mathrm{He}}(0) = p_{\mathrm{operate}} \tag{4.4}$$

$$T_{\mathrm{He}}(0) = \begin{cases} T_{\mathrm{sat}}\left(p_{\mathrm{He}}(0)\right) & p_{\mathrm{He}}(0) \leq p_{\mathrm{crit}} \\ T\left(p_{\mathrm{He}}(0), \rho_{\mathrm{He}}(0)\right) & p_{\mathrm{He}}(0) > p_{\mathrm{crit}} \end{cases} \tag{4.5}$$

$$\rho_{\mathrm{He}}(0) = \begin{cases} \rho\left(p_{\mathrm{He}}(0), T_{\mathrm{He}}(0), a_{\mathrm{He}}(0)\right) & p_{\mathrm{He}}(0) \leq p_{\mathrm{crit}} \\ M_{\mathrm{operate}}/V_{\mathrm{Cr}} & p_{\mathrm{He}}(0) > p_{\mathrm{crit}} \end{cases} \tag{4.6}$$

$$a_{\mathrm{He}}(0) = 0\ldots1 \tag{4.7}$$

where φ is the relative humidity of air, p_{operate} is the operating pressure of the cryostat, $T_{\mathrm{sat}}\left(p_{\mathrm{He}}\left(0\right)\right)$ the saturation temperature at $p_{\mathrm{He}}\left(0\right)$, V_{Cr} is the volume of the helium vessel, $a_{\mathrm{He}}\left(0\right)$ the liquid level during normal operation and M_{operate} is the helium mass during normal operation. The initial vacuum pressure of 10^{-6} mbar represents a pressure in the high vacuum regime that is typically used for insulation vacua of cryostat.

4.2.2 Initial wall temperatures

The definition of the initial average outer wall temperature $T_{\mathrm{W,o}}\left(0\right)$ and the initial average inner wall temperature $T_{\mathrm{W,i}}\left(0\right)$, however, is more complex. It requires the application of Fourier's equation for a steady state one dimensional heat transfer

$$\dot{q}_{\mathrm{V}} = \frac{\lambda_{\mathrm{Cr}}}{s_{\mathrm{Cr}}} \cdot \left(T_{\mathrm{W,o}} - T_{\mathrm{W,i}}\right) = \dot{q}_{\mathrm{He}} \tag{4.8}$$

where the heat flux transferred to the outer surface of the cryogenic vessel $\dot{q}_{\mathrm{V}}$ and the heat flux transferred to helium $\dot{q}_{\mathrm{He}}$ represent the boundary conditions. In case of steady state, $\dot{q}_{\mathrm{V}}$ is equal to $\dot{q}_{\mathrm{He}}$. λ_{Cr} is the thermal conductivity of the cryogenic vessel wall and s_{Cr} the wall thickness.

Due to sufficiently high insulation vacua, it is assumed that the heat flux transferred to the outer surface of the cryogenic vessel $\dot{q}_{\mathrm{V}}$ consists only of the heat flux due to thermal radiation $\dot{q}_{\mathrm{Rad}}$. Terms for thermal conduction and convection are neglected. The Stefan-Boltzmann equation for a concentric annular gap provides the thermal radiation heat flux on bare surfaces. If multi-layer insulation (MLI) is installed, the thermal radiation is calculated considering N reflective layers as grey emitters [13].

$$\dot{q}_{\mathrm{Rad}} = \begin{cases} \dfrac{\sigma \cdot \left(T_{\mathrm{V}}^4 - T_{\mathrm{W,o}}^4\right)}{\frac{1}{\epsilon_{\mathrm{V}}} + \frac{A_{\mathrm{V}}}{A_{\mathrm{Cr}}} \cdot \left(\frac{1}{\epsilon_{\mathrm{Cr}}} - 1\right)} & N = 0 \\ \dfrac{\sigma \cdot \left(T_{\mathrm{V}}^4 - T_{\mathrm{W,o}}^4\right)}{\left(\frac{1}{\epsilon_{\mathrm{Cr}}} + \frac{1}{\epsilon_{\mathrm{MLI}}} - 1\right) + (N-1) \cdot \left(\frac{2}{\epsilon_{\mathrm{MLI}}} - 1\right) + \left(\frac{1}{\epsilon_{\mathrm{MLI}}} + \frac{1}{\epsilon_{\mathrm{V}}} - 1\right)} & N > 0 \end{cases} \tag{4.9}$$

where σ is the Stefan-Boltzmann constant, $T_{\mathrm{V}} = T_{\mathrm{amb}}$ is either the temperature of the vacuum vessel surface, a thermal radiation shield or the N^{th} layer of MLI, whatever is relevant in the considered cryostat. Accordingly, A_{V} is either the inner surface of the vacuum vessel having an emissivity $\epsilon_{\mathrm{V}} = 0.8$ of oxidized stainless steel or of the thermal radiation shield, if installed, having an emissivity of $\epsilon_{\mathrm{Al}} = 0.1$ of polished aluminium [23], for example. For the emissivity of the cryogenic vessel $\epsilon_{\mathrm{Cr}} = 0.07$, a value for electro-polished stainless steel [23] can be assumed and the reflective layers could have an emissivity of $\epsilon_{\mathrm{MLI}} = 0.04$. The multiple reflection reduces the heat flux due to thermal radiation significantly.

The heat transfer inside the helium vessel at steady state conditions is dominated by convection due to helium's small thermal conductivity and large specific heat [76, p.140].

$$\dot{q}_{\mathrm{He}} = \alpha_{\mathrm{He}} \cdot \left(T_{\mathrm{W,i}} - T_{\mathrm{He}}\right) \tag{4.10}$$

where α_{He} is the average heat transfer coefficient to helium and T_{He} is the constant helium bulk temperature at normal operation. At two-phase conditions inside the cryostat, the heat transfer coefficient is calculated separately for the liquid ($\alpha_{\mathrm{He,liq}}$) and the gaseous ($\alpha_{\mathrm{He,gas}}$) phase. The calculation of the average heat transfer coefficient α_{He} requires the separation of the heat transfer surface A_{Cr} in a wetted and a dry part, using the initial liquid level $a_{\mathrm{He}}(0)$.

Depending on the heat flux, $\alpha_{\mathrm{He,liq}}$ is based on either free convection, nucleate boiling or film boiling. Since free convection in the liquid phase occurs only at heat fluxes below $1\,\mathrm{W\,m^{-2}}$, it has only limited technical relevance in helium cryostats [76, p.120] and is neglected in this work. At higher heat fluxes, the heat transfer is driven by either nucleate boiling or film boiling [76, p.115-123]. The transition between them occurs at the minimum film boiling heat flux of $300\,\mathrm{W\,m^{-2}}$. The correlation of Kutateladze [51] is used for the nucleate boiling regime and the correlation of Breen and Westwater [16] for the film boiling regime.

$$\alpha_{\mathrm{He,liq}} = \begin{cases} \alpha_{\mathrm{nb}} & \dot{q}_{\mathrm{He}} \leq 300\,\mathrm{W\,m^{-2}} \\ \alpha_{\mathrm{fb}} & \dot{q}_{\mathrm{He}} > 300\,\mathrm{W\,m^{-2}} \end{cases} \tag{4.11}$$

where the heat transfer coefficient for nucleate boiling α_{nb} is defined in Equation 4.12 and the one for film boiling α_{fb} in Equation 4.13.

$$\begin{aligned} \alpha_{\mathrm{nb}} = 1.90 \cdot & \left(g \cdot \left(\frac{\rho_{\mathrm{liq}}}{\eta_{\mathrm{liq}}} \right)^2 \cdot \left(\frac{\sigma}{g \cdot \rho_{\mathrm{liq}}} \right)^{1/2} \right)^{0.3125} \cdot \left(\frac{p_{\mathrm{He}}}{\sigma} \cdot \left(\frac{\sigma}{g \cdot \rho_{\mathrm{liq}}} \right)^{1/2} \right)^{1.75} \\ & \cdot \left(\frac{\rho_{\mathrm{liq}}}{\rho_{\mathrm{vap}}} \right)^{1.5} \cdot \left(\frac{c_{p,\mathrm{liq}}}{\Delta h_{\mathrm{v}}} \right)^{1.5} \cdot \left(\lambda_{\mathrm{liq}} \cdot \left(\frac{g \cdot \rho_{\mathrm{liq}}}{\sigma} \right)^{1/2} \right) \cdot (T_{\mathrm{W,i}} - T_{\mathrm{He}})^{1.5} \end{aligned} \tag{4.12}$$

$$\begin{aligned} \alpha_{\mathrm{fb}} = 0.37 \cdot & \left(\frac{g \cdot (\rho_{\mathrm{liq}} - \rho_{\mathrm{vap}})}{\sigma} \right)^{1/8} \\ & \cdot \left(\frac{\lambda_{\mathrm{vap}} \cdot \rho_{\mathrm{vap}} \cdot (\rho_{\mathrm{liq}} - \rho_{\mathrm{vap}}) \cdot g}{\eta_{\mathrm{vap}} \cdot (T_{\mathrm{W,i}} - T_{\mathrm{He}})} \cdot \frac{(\Delta h_{\mathrm{v}} + 0.34 \cdot c_{p,\mathrm{vap}} \cdot (T_{\mathrm{W,i}} - T_{\mathrm{He}}))^2}{\Delta h_{\mathrm{v}}} \right)^{1/4} \end{aligned} \tag{4.13}$$

where g is the gravitational acceleration, ρ is the density, η is the dynamic viscosity, σ is the surface tension, c_p is the specific heat capacity at constant pressure, λ is the thermal conductivity and Δh_{v} is the vaporisation enthalpy. The indices "vap" and "liq" refer to the conditions of saturated vapour and of saturated liquid, respectively.

In the gaseous phase, the heat transfer coefficient is implemented by a Nusselt-correlation[1] Nu for free convection to vertical plates according to [18], which is valid for the complete

[1] The Nusselt-number $Nu = {}^{\alpha \cdot L}/_{\lambda}$, where L is the characteristic length of heat transfer problem, is a dimensionless number to calculate the convective heat transfer between a solid surface and a fluid.

range of Prandl-numbers[2] Pr and Rayleigh-numbers[3] Ra [12, p.469]. In [18], it is stated that the correlation is also applicable to vertical cylinders if ${}^{d}/_{L} \geq 35 \cdot Gr^{-1/4}$, where Gr is the Grashof number[4]. With its application range, most cryostats should be covered by this correlation.

$$\alpha_{\mathrm{He,gas}} = \frac{\lambda_{\mathrm{He}}}{d_{\mathrm{Cr}}} \cdot \underbrace{\left(0.825 + \frac{0.387 \cdot Ra^{1/2}}{\left(1 + \left(\frac{0.492}{Pr} \right)^{9/16} \right)^{8/27}} \right)^{2}}_{Nu} \tag{4.14}$$

Solving Equations 4.8 to 4.14 simultaneously results in the required initial outer and inner wall temperatures $T_{\mathrm{W,o}}(0)$ and $T_{\mathrm{W,i}}(0)$, respectively.

4.2.3 Initial temperature distribution in MLI blankets

Figure 4.2 shows the initial temperature distribution in a MLI blanket for a total number of 12, 24 and 30 layers, which are typical values in technical helium cryostat applications. Layer 1 is the layer close to the cryogenic surface and layer N the layer close to the warm surface of the vacuum vessel. Based on the radiative equilibrium with vacuum vessel and the $N^{\mathrm{th}-1}$ layer, the temperature of the N^{th} layer takes the ambient temperature. At sufficiently high insulating vacua and a proper installation of the MLI, only a heat flux due to radiation is transferred through the MLI. At steady state conditions, the heat flux transferred between each layer is equal to the result of Equation 4.9.

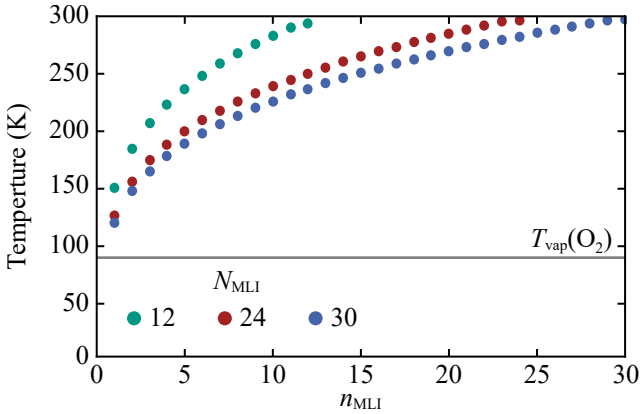

Figure 4.2: Initial temperature distribution in a MLI blanket for 12, 24 and 30 layers of MLI.

[2]The Prandl-number Pr is a dimensionless number of fluids describing the ratio of kinematic viscosity to thermal diffusivity.

[3]The Rayleigh-number Ra is a dimensionless number of fluids associated with buoyancy-driven flow. It is defined as product of the Grashof-number Gr and Prandl-number.

[4]The Grashof-number Gr is dimensionless number of fluid that describes the ratio of buoyancy to viscosity.

The evaluation of the temperature distribution in a MLI-blanket yields layer temperatures of $T_n \geq 100\,\mathrm{K}$. Thus, a deposition of the venting fluid on MLI layers can be neglected. However, this assumption is valid only for MLI blankets being installed without a thermal shield. In case of an installation together with a thermal shield actively cooled to temperatures below the condensation temperature of the venting fluid, the deposition on the shield and the MLI may have to be taken into account.

4.3 Dynamic processes inside the vacuum vessel

In this section, the set of equations for modelling the processes induced by LIV inside the vacuum vessel is presented. This includes the differential equations of the vacuum temperature and pressure as well as the algebraic equations of the venting and the deposited mass flow rate as a function of the time-dependent variables.

4.3.1 Vacuum temperature

The temperature inside the vacuum vessel T_V is assumed to correspond to the venting air temperature and hence to be constant

$$\frac{\mathrm{d}T_\mathrm{V}}{\mathrm{d}t} = 0 \tag{4.15}$$

The temperature decrease during the isenthalpic expansion of the venting fluid is in the order of 1 K and therefore negligible. Furthermore, gas molecules are observed to have a sticking probability close to unity on surfaces at cryogenic temperatures [36, 85]. As a result, heat and mass transfer from the cold cryogenic surface back to the vacuum space can be neglected as long as the wall temperatures are below the condensation temperature of the venting fluid.

4.3.2 Vacuum pressure

The pressure increase inside the vacuum vessel $\mathrm{d}p_\mathrm{V}/\mathrm{d}t$ following LIV is calculated based on the time-derivative of the ideal gas law [38]

$$\frac{\mathrm{d}p_\mathrm{V}}{\mathrm{d}t} = \frac{\left(\dot{M}_\mathrm{In}\left(p_\mathrm{V}\right) - \dot{M}_\mathrm{Dep}\left(T_\mathrm{W,o}, p_\mathrm{V}\right)\right) \cdot R_\mathrm{vent} \cdot T_\mathrm{V}}{V_\mathrm{V} - V_\mathrm{Cr}} \tag{4.16}$$

where $T_\mathrm{W,o}$ is the outer surface temperature of the cryogenic vessel, $\dot{M}_\mathrm{In}$ is the venting mass flow rate, $\dot{M}_\mathrm{Dep}$ is the mass flow rate deposited on the cryogenic surface, R_vent is the specific gas constant of the venting fluid and V_V and V_Cr are the volumes of the vacuum and cryogenic vessel, respectively.

4.3.3 Venting mass flow rate

The venting mass flow rate $\dot{M}_{\mathrm{In}}$ is modelled applying the Bernoulli-equation for short nozzles

$$\dot{M}_{\mathrm{In}} = A_{\mathrm{Leak}} \cdot \sqrt{2 \cdot \frac{p_{\mathrm{amb}}}{v_{\mathrm{amb}}}} \cdot \begin{cases} \sqrt{\frac{\kappa}{\kappa-1}} \cdot \sqrt{\left(\frac{p_{\mathrm{V}}}{p_{\mathrm{amb}}}\right)^{\frac{2}{\kappa}} - \left(\frac{p_{\mathrm{V}}}{p_{\mathrm{amb}}}\right)^{\frac{\kappa+1}{\kappa}}} & \frac{p_{\mathrm{V}}}{p_{\mathrm{amb}}} > \Delta p_{\mathrm{crit}} \\ \left(\frac{2}{\kappa+1}\right)^{\frac{1}{\kappa-1}} \cdot \sqrt{\frac{\kappa}{\kappa+1}} & \frac{p_{\mathrm{V}}}{p_{\mathrm{amb}}} \leq \Delta p_{\mathrm{crit}} \end{cases} \tag{4.17}$$

where A_{Leak} is the cross section of a leak that results from the risk assessment. With the application of the Bernoulli-equation, it is assumed that a leak inside the vacuum vessel has an ideal round shape. The influence of this assumption on the PRV dimensioning process is discussed in Subsection 6.4.4.

4.3.4 Deposited mass flow rate

The deposition process of the venting fluid on the cryogenic surface is already modelled in [85] applying the Hertz-Knudsen-Equation according to [36]

$$\dot{M}_{\mathrm{Dep}} = A_{\mathrm{Cr}} \cdot \alpha_{\mathrm{T}} \cdot \frac{1}{\sqrt{2 \cdot \pi \cdot R_{\mathrm{vent}}}} \cdot \left(\alpha_{\mathrm{C}}\left(T_{\mathrm{W,o}}\right) \cdot \frac{p_{\mathrm{V}}}{\sqrt{T_{\mathrm{V}}}} - \alpha_{\mathrm{E}}\left(T_{\mathrm{W,o}}\right) \cdot \frac{p_{\mathrm{V,sat}}\left(T_{\mathrm{W,o}}\right)}{\sqrt{T_{\mathrm{W,o}}}} \right) \tag{4.18}$$

where α_{T} is the transmission coefficient describing the probability of molecules passing through obstacles, α_{C} is the condensation coefficient defining the probability of molecules being deposited on the cold surface, α_{E} is the evaporation coefficient defining the probability of molecules leaving the cold surface and $p_{\mathrm{V,sat}}$ is the saturation pressure of the venting fluid at wall temperature.

The coefficients α_{T}, α_{C} and α_{E} are based on empirically derived functions. Due to a lack of data in the literature, especially α_{T} in case of multi-layer insulated cryogenic surfaces is derived based in experimental data obtained at the cryogenic safety test facility PICARD (cf. Subsection 6.3.4).

Definition of the transmission coefficient α_{T}

By comparison of literature data [36] and a parameter study based on measurement data obtained at PICARD, a constant transmission coefficient for bare cryogenic surfaces is defined in [85]. For multi-layer insulated surfaces, α_{T} is a function of the vacuum pressure and depends on the number of layers N and the type of MLI, specifically the thickness and the perforation of the reflective layers. In Equation 4.19, the interpolation functions of α_{T} for four different MLI configurations are summarized with pressures given in bar. The MLI configuration parameters are presented in detail in Section 5.3 and the derivation of the interpolating functions based on experimental data is explained in

Subsection 6.3.4. The resulting pressure dependent profiles of α_T for different exemplary insulation configurations are depicted in Figure 4.3b.

$$\alpha_\mathrm{T} = \begin{cases} 3 \cdot 10^{-2} & & N = 0 \\ & & \& \; N = 1 \text{ MLI2} \\ \begin{cases} 3 \cdot 10^{-2} & p_\mathrm{v} < 0.02\,\mathrm{bar} \\ 0.0401282 - 0.496382 \cdot \exp\left[p_\mathrm{v}\right] \cdot p_\mathrm{v} & 0.02\,\mathrm{bar} \leq p_\mathrm{v} < 0.075\,\mathrm{bar} \\ 0 & 0.075\,\mathrm{bar} \leq p_\mathrm{v} < 0.35\,\mathrm{bar} \\ 3.17 \cdot 10^{-4} - 3.02 \cdot 10^{-4} \cdot \log\left[p_\mathrm{v}\right] & 0.35\,\mathrm{bar} \leq p_\mathrm{v} < 0.8\,\mathrm{bar} \\ 2.5 \cdot 10^{-4} & p_\mathrm{v} > 0.8\,\mathrm{bar} \end{cases} & N = 12 \text{ MLI1} \\ \begin{cases} 3 \cdot 10^{-2} & p_\mathrm{v} < 0.02\,\mathrm{bar} \\ 0.0401282 - 0.496382 \cdot \exp\left[p_\mathrm{v}\right] \cdot p_\mathrm{v} & 0.02\,\mathrm{bar} \leq p_\mathrm{v} < 0.075\,\mathrm{bar} \\ 0 & 0.075\,\mathrm{bar} \leq p_\mathrm{v} < 0.7\,\mathrm{bar} \\ 2.13 \cdot 10^{-4} - 5.97 \cdot 10^{-4} \cdot \log\left[p_\mathrm{v}\right] & 0.7\,\mathrm{bar} \leq p_\mathrm{v} < 0.9\,\mathrm{bar} \\ 1.5 \cdot 10^{-4} & p_\mathrm{v} > 0.9\,\mathrm{bar} \end{cases} & \begin{matrix} N = 24 \text{ MLI1} \\ \& \; N = 10 \text{ MLI3} \end{matrix} \end{cases} \tag{4.19}$$

Definition of the condensation coefficient α_C and the evaporation coefficient α_E

α_C and α_E are defined in sections considering the literature data [15, 22, 36] for nitrogen and water at temperatures below 20 K and above 63 K, respectively.

$$\alpha_\mathrm{C}\left(20\,\mathrm{K}\right) = 1 \qquad \alpha_\mathrm{E}\left(20\,\mathrm{K}\right) = 0 \tag{4.20}$$

$$\alpha_\mathrm{C}\left(63\,\mathrm{K}\right) = 10^{-2} \qquad \alpha_\mathrm{E}\left(63\,\mathrm{K}\right) = 10^{-3} \tag{4.21}$$

Where [85] performed a linear fit for α_C and α_E in the temperature range of $20 \ldots 63\,\mathrm{K}$, this work uses the Clausius-Clapeyron-Equation to obtain both coefficients between 20 K and the triple point temperature of oxygen $T_{\mathrm{trip,O_2}} = 55\,\mathrm{K}$ as they are a function of the saturation pressure.

$$\left\{\alpha_\mathrm{C}, \alpha_\mathrm{E}\right\} = a + b \cdot \frac{\mathrm{d}p_\mathrm{sat}}{\mathrm{d}T} \cdot T \tag{4.22}$$

The triple point of oxygen is used since it has the lowest temperature of the air components, and thus initiates the deposition process. This procedure is repeated for temperatures above the triple point of oxygen $T_{\mathrm{trip,O_2}}$ and below the evaporation temperature of nitrogen $T_{\mathrm{vap,N_2}} = 77.3\,\mathrm{K}$ at ambient pressure.

The following boundary values of α_C and α_E at $T_{\mathrm{vap,N_2}}$ are applied

$$\alpha_\mathrm{C}\left(T_{\mathrm{vap,N_2}}\right) = 0 \qquad \alpha_\mathrm{E}\left(T_{\mathrm{vap,N_2}}\right) = 1 \tag{4.23}$$

since wall temperatures above the evaporation temperature of nitrogen $T_{\mathrm{vap,N_2}}$ cause the nitrogen to evaporate without further deposition. This results in the following distinction for the calculation of α_{C} and α_{E} with temperatures given in K and pressures in bar:

$$\alpha_{\mathrm{C}} = \begin{cases} 1 & T_{\mathrm{W,o}} < 20\,\mathrm{K} \\ 1 - 5.49709 \cdot \dfrac{\mathrm{d}p_{\mathrm{sub}}}{\mathrm{d}T} \cdot T_{\mathrm{W,o}} & 20\,\mathrm{K} \leq T_{\mathrm{W,o}} < T_{\mathrm{trip,O_2}} \\ 0.0102058 - 0.00169403 \cdot \dfrac{\mathrm{d}p_{\mathrm{vap}}}{\mathrm{d}T} \cdot T_{\mathrm{W,o}} & T_{\mathrm{trip,O_2}} \leq T_{\mathrm{W,o}} \leq T_{\mathrm{vap,N_2}} \\ 0 & T_{\mathrm{W,o}} > T_{\mathrm{vap,N_2}} \end{cases} \tag{4.24}$$

$$\alpha_{\mathrm{E}} = \begin{cases} 0 & T_{\mathrm{W,o}} < 20\,\mathrm{K} \\ 0 + 0.00555262 \cdot \dfrac{\mathrm{d}p_{\mathrm{sub}}}{\mathrm{d}T} \cdot T_{\mathrm{W,o}} & 20\,\mathrm{K} \leq T_{\mathrm{W,o}} < T_{\mathrm{trip,O_2}} \\ -0.0195573 + 0.169234 \cdot \dfrac{\mathrm{d}p_{\mathrm{vap}}}{\mathrm{d}T} \cdot T_{\mathrm{W,o}} & T_{\mathrm{trip,O_2}} \leq T_{\mathrm{W,o}} \leq T_{\mathrm{vap,N_2}} \\ 1 & T_{\mathrm{W,o}} > T_{\mathrm{vap,N_2}} \end{cases} \tag{4.25}$$

The resulting temperature dependent profiles of α_{C} and α_{E} are depicted in Figure 4.3a.

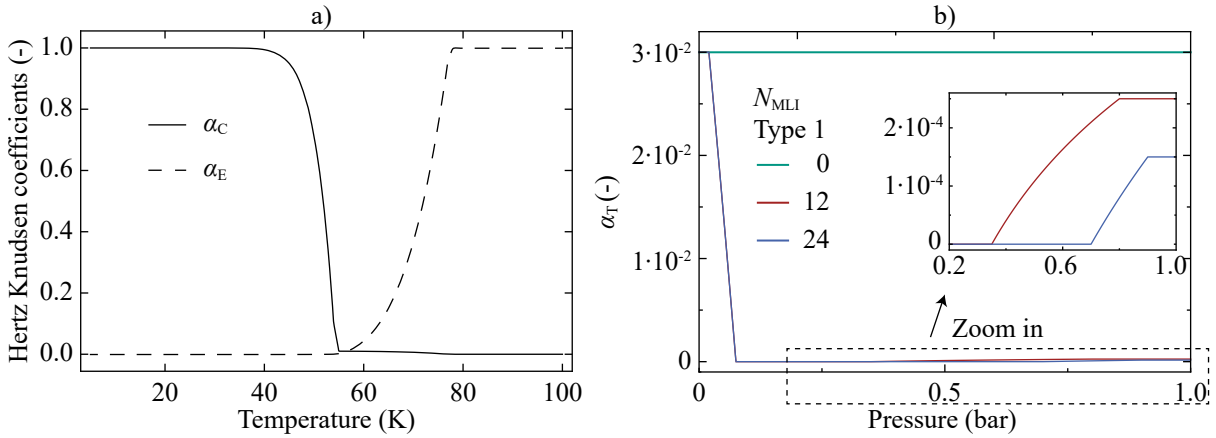

Figure 4.3: a) Profiles of the Hertz-Knudsen condensation α_{C} (full line) and evaporation coefficient α_{E} (dashed line) as a function of temperature following Equations 4.24 and 4.25. b) Profiles of the transmission coefficient for different insulation configurations as a function of pressure following Equation 4.19.

4.4 Dynamic heat transfer equation

The considered temperature profiles between the vacuum space and the helium are schematically depicted in Figure 4.4, including all heat fluxes relevant for modelling. The dotted-dashed line shows the temperature profile assumed in a first dynamic modelling approach of LIV according to [38], where the thermal resistance of the wall was neglected and the outer wall temperature was set equal to the helium bulk temperature. The dashed line represents the temperature profile in a refined dynamic model according to [85], where the thermal resistance of the wall is considered via an empirical fit of measured wall temperature data. In either case, only the deposited heat flux is transferred to the outer surface and the transient heat transfer process inside the cryogenic vessel and a convective resistance inside the helium has not been implemented. Therefore, the model in [85] is extended by the heat conduction in the vessel wall, the convective heat transfer to helium and the thermal radiation heat flux to the outer surface (cf. full line in Figure 4.1). In addition, the influence of MLI on the heat transfer process is implemented. An earlier state of the heat transfer model is already published by the author in [79].

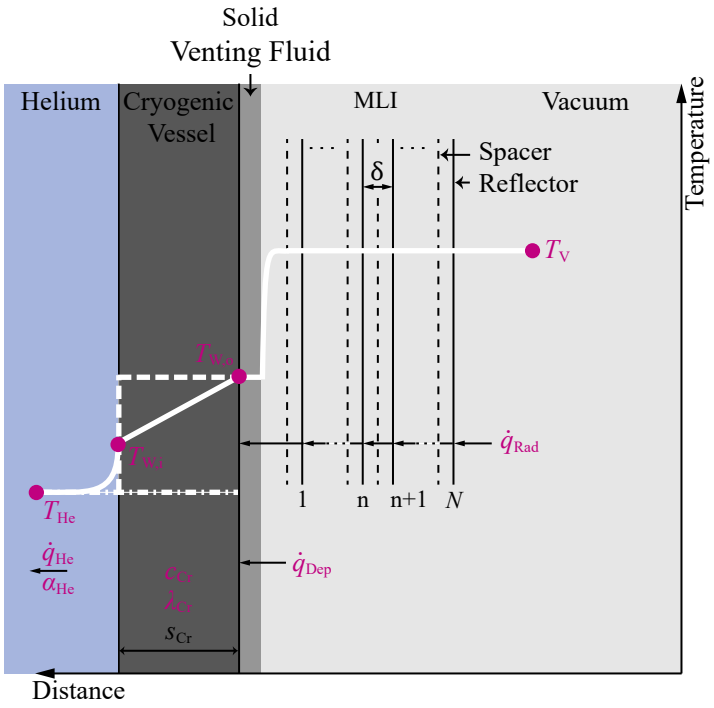

Figure 4.4: Schematic temperature profiles between the vacuum space and the helium inside the cryogenic vessel including all quantities relevant for the one-dimensional heat transfer equations. The *full* line depicts the temperature profile assumed in this work, compared to the *dashed* line considered in [85] and the *dotted-dashed* line according to [38].

4.4.1 Definition of the cryogenic wall temperatures

The time-dependent wall temperature profiles of the outer and the inner helium vessel surface, T_{W_o} and T_{W_i}, are calculated by one-dimensional transient heat transfer equations

$$\frac{dT_{W,o}}{dt} = \frac{A_{Cr}}{c_{Cr} \cdot M_{Cr}} \cdot (\dot{q}_V + \dot{q}_{Rad} - \dot{q}_{Cond}) \quad (4.26)$$

$$\frac{dT_{W,i}}{dt} = \frac{A_{Cr}}{c_{Cr} \cdot M_{Cr}} \cdot (\dot{q}_{Cond} - \dot{q}_{He}) \quad (4.27)$$

where A_{Cr} is the outer surface of the cryogenic vessel, c_{Cr} is the specific heat capacity of the vessel material (i.e. stainless steel) at the mean wall temperature $T_W = 1/2\,(T_{W,o} + T_{W,i})$ and M_{Cr} is the mass of the vessel. $\dot{q}_V$ is the heat flux transferred on the outer surface of the vacuum vessel caused by the venting fluid, $\dot{q}_{Rad}$ is the heat flux due to thermal radiation, $\dot{q}_{Cond}$ is the heat flux due to thermal conduction in the vessel wall and $\dot{q}_{He}$ is the heat flux transferred to helium.

4.4.2 Heat flux caused by the venting fluid

When the venting fluid reaches the cold outer surface of the cryogenic vessel, it deposits on the wall, i.e. sublimates and/or condensates, due to initial wall temperatures below the condensation temperature of the air components. Based on Nußelt's Wasserhauttheorie [12, p.502ff], the sequence of this heat transfer problem generally includes three subsequent resistances

1. the transport of the venting fluid to the phase boundary due to flow and diffusion
2. the deposition of the venting fluid at the phase boundary, including the release of sublimation and/or condensation enthalpy,
3. the transport of the released energy to the cryogenic surface through the deposited layer due to conduction.

The first resistance is included in Equation 4.18, where the mass flow rate is defined that reaches the phase boundary. The third resistance of the solid venting fluid layer is neglected due to its small thicknesses and missing knowledge of its properties. The second resistance has to be extended by the sensible heat of the gas and the deposited layer in the present model, due to both a superheated venting fluid and a sub-cooled solid layer with respect to the condensation and de-sublimation temperature.

Based on the aforementioned assumptions, at wall temperatures below the condensation temperature of the air components, the heat flux transferred to the outer surface of the cryogenic vessel caused by the venting fluid $\dot{q}_V$ is calculated by multiplying the deposited mass flow rate $\dot{M}_{Dep}$ according to Equation 4.18 with the enthalpy difference of the

venting fluid $\Delta h\left(T_{\mathrm{amb}} \rightarrow T_{\mathrm{W,o}}, p_{\mathrm{V}}, \varphi\right)$ from ambient to the outer wall surface conditions considering the relative humidity of air φ

$$\left(\dot{q}_{\mathrm{V}}\right)_{T_{\mathrm{W,o}} \leq T_{\mathrm{vap,O_2}}} = \frac{\dot{M}_{\mathrm{Dep}}\left(T_{\mathrm{W,o}}, p_{\mathrm{V}}\right)}{A_{\mathrm{Cr}}} \cdot \Delta h\left(T_{\mathrm{amb}} \rightarrow T_{\mathrm{W,o}}, p_{\mathrm{V}}, \varphi\right) \tag{4.28}$$

where $\Delta h\left(T_{\mathrm{amb}} \rightarrow T_{\mathrm{W,o}}, p_{\mathrm{V}}, \varphi\right)$ includes the sensible heat of the superheated gas Δh_{gas}, the sensible heat of sub-cooled liquid Δh_{liq} and the sensible heat of sub-cooled solid $\Delta h_{\mathrm{solid}}$ as well as the vaporization enthalpy Δh_{V} and melting enthalpy Δh_{melt} of the venting fluid

$$\begin{aligned} \Delta h\left(T_{\mathrm{amb}} \rightarrow T_{\mathrm{W,o}}, p_{\mathrm{V}}, \varphi\right) = {} & \Delta h_{\mathrm{gas}}\left(T_{\mathrm{amb}} \rightarrow T_{\mathrm{vap}}, p_{\mathrm{V}}, \varphi\right) + \Delta h_{\mathrm{V}} \\ & + \Delta h_{\mathrm{liq}}\left(T_{\mathrm{vap}} \rightarrow T_{\mathrm{melt}}, p_{\mathrm{V}}, \varphi\right) + \Delta h_{\mathrm{melt}} \\ & + \Delta h_{\mathrm{solid}}\left(T_{\mathrm{melt}} \rightarrow T_{\mathrm{W,o}}, p_{\mathrm{V}}, \varphi\right) \end{aligned} \tag{4.29}$$

Although the leak is localized, the deposition layer is assumed to be uniformly formed over the entire cryogenic surface. In a previous work [85], only the main component of the venting fluid - nitrogen - was considered in the enthalpy calculation. This model uses humid air instead. The derivation of the fluid property data, especially for solid humid air, is explained in Subsection 4.7.2.

If the wall temperature increases above the condensation temperature of the air components, the heat transfer process is mainly driven by either forced convection or natural convection. The heat flux due to natural convection $\dot{q}_{\mathrm{Conv}}$ between the venting fluid inside the vacuum space and the wall can be calculated according to

$$\left(\dot{q}_{\mathrm{V}}\right)_{T_{\mathrm{W,o}} > T_{\mathrm{vap,O_2}}} = \alpha_{\mathrm{V}} \cdot \left(T_{\mathrm{V}} - T_{\mathrm{W,o}}\right) \tag{4.30}$$

where α_{V} is the heat transfer inside the vacuum space according to Equation 4.14. For multi-layer insulated surfaces, natural convection to the N^{th} layer and among the layers can be neglected at Grashof numbers of $\mathrm{Gr} < 2860$ [84].

Forced convection is neglected due to the following reasons:

- At vacuum pressures $p_{\mathrm{V}} > 0.5\,\mathrm{bar}$, which corresponds to the fluid-dynamical critical pressure, the ratio between Grashof and Reynolds number $({}^{Gr}/_{Re^2} \gg 1)$[5] confirms that forced confection can be neglected [12, p.479].
- The flow conditions required for the calculation of a heat transfer coefficient due to forced convection cannot be defined, e.g. due to variable leak positions or the occurrence of a free jet at the hole in the vacuum vessel.

[5] $\gg 1$ is defined to a ratio of 10, which corresponds to one order of magnitude higher than 1.

4.4.3 Heat flux due to thermal conduction

In theory, a fully transient heat transfer through the cryogenic vessel wall would yield the most accurate heat flux profile due to thermal conduction. However, as the model shall be generally and easily applicable for the dimensioning of PRVs, the transient approach is substituted by a quasi-stationary approach, which represents a satisfactory compromise between accuracy and facilitated applicability. Based on the Fourier equation, the heat flux due to thermal conduction in the cryogenic vessel wall $\dot{q}_{\mathrm{Cond}}$ is calculated to

$$\dot{q}_{\mathrm{Cond}} = \frac{\lambda_{\mathrm{Cr}}}{s_{\mathrm{Cr}}} \cdot (T_{\mathrm{W,o}} - T_{\mathrm{W,i}}) \tag{4.31}$$

where λ_{Cr} is the thermal conductivity of stainless steel at mean wall temperature T_{W} and s_{Cr} is the thickness of the wall. This approach yields a slightly faster temperature increase only within the first second after the initiation of the venting process compared to a fully transient heat transfer. Since this time frame is, however, not in the safety relevant region, this deviation is acceptable.

4.4.4 Heat flux due to thermal radiation

Electromagnetic waves are exchanged between surfaces of different temperatures. In the case of cryostats, this is the cryogenic vessel surface at low temperature and the inner surface of the vacuum vessel or of the radiation shield, if installed, at high temperature. The Stefan-Boltzmann equation for a concentric annular gap provides the thermal radiation heat flux on cryogenic surfaces

$$\dot{q}_{\mathrm{Rad}} = \frac{\sigma \cdot \left(T_{\mathrm{V}}^4 - T_{\mathrm{W,o}}^4\right)}{\frac{1}{\epsilon_{\mathrm{V}}} + \frac{A_{\mathrm{V}}}{A_{\mathrm{Cr}}} \cdot \left(\frac{1}{\epsilon_{\mathrm{Cr}}} - 1\right)} \tag{4.32}$$

where σ is the Stefan-Boltzmann constant, $T_{\mathrm{V}} = T_{\mathrm{amb}}$ is the temperature inside the vacuum space and A_{V} is either the inner surface of the vacuum vessel. Exemplary values for the emissivity of the vacuum vessel, the helium vessel, a thermal shield and MLI are given in Subsection 4.2.2. The surface area of the inner MLI layer is calculated taking a gap of 1 mm between the cryogenic surface and the inner layer into account. A reduction of the thermal radiation heat flux through the reflective layers can no longer be assumed after venting of the insulation vacuum, since the venting fluid immediately warms the MLI blanket to room temperature due to its low mass and its low heat capacity.

4.4.5 Heat flux due to convection inside the helium

Inside the helium vessel, the helium temperature increases by contact with the wall due to convective heat transfer. The convective heat flux transferred to helium is calculated as

$$\dot{q}_{\mathrm{He}} = \alpha_{\mathrm{He}} \cdot (T_{\mathrm{W,i}} - T_{\mathrm{He}}) \tag{4.33}$$

where α_{He} is the heat transfer coefficient to helium and T_{He} is the helium bulk temperature. α_{He} depends on the thermodynamic state of helium. Before reaching the thermodynamic critical pressure, depending on the heat flux[6], either nucleate or film boiling occurs in the liquid phase [76], cf. Equation 4.11. In the gaseous phase, free convection is considered by a correlation for vertical cylinders according to Equation 4.14. The difference in the heat transfer coefficients of liquid and gaseous phase requires the separation of the heat transfer surface A_{Cr} in Equation 4.27 in a wetted and a dry part, using the liquid level a_{He} as a function of pressure according to

$$a_{\mathrm{He}} = \frac{\rho_{\mathrm{He}} \cdot (1 - x_{\mathrm{He}})}{\rho_{\mathrm{He,liq}}} \tag{4.34}$$

where $\rho_{\mathrm{He,liq}}$ is the density of the saturated liquid as a function of p_{He} and x_{He} is the quality of helium as a function of p_{He} and ρ_{He}. The helium bulk temperatures of the gaseous and the liquid phases are assumed to be equal.

At pressures above the thermodynamic critical pressure, a Nusselt-correlation for free convection on a semi-infinite plate of constant temperature in an infinite medium is used [41]

$$\alpha_{\mathrm{He,sc}} = \frac{\lambda_{\mathrm{He}}}{A_{\mathrm{Cr}}/P_{\mathrm{Cr}}} \cdot \underbrace{0.615 \cdot Ra^{0.258}}_{Nu} \tag{4.35}$$

where the ratio of the cryogenic surface area to the perimeter of the cryogenic vessel $A_{\mathrm{Cr}}/P_{\mathrm{Cr}}$ represents the characteristic length of the heat transfer problem.

4.5 Dynamic processes inside the helium vessel

For the modelling of the temperature and pressure increase inside the helium vessel and the relieving mass flow rate, three cases are distinguished depending on the relieving pressure p_0 of the PRV

1. closed helium vessel for pressures $p_{\mathrm{He}} < p_0$
2. open helium vessel for sub-critical relieving pressure $p_0 \leq p_{\mathrm{He}} \leq p_{\mathrm{crit}}$
3. open helium vessel for supercritical relieving pressure $p_{\mathrm{crit}} \leq p_0 \leq p_{\mathrm{He}}$

The corresponding state changes of helium inside the helium vessel are illustrated in a pv-diagram in Figure 4.5. Dependent on the initial specific volume, the liquid level can change in two ways:

A At low initial specific volumes, e.g. $v_{\mathrm{He,A}} = 0.0092\,\mathrm{m^3\,kg^{-1}}$ (A1), the isochoric heat input causes liquid expansion with a rising liquid level until the entire vessel is filled with liquid helium at the saturated liquid curve and above. In Figure 4.5 saturated liquid occurs at the opening of the PRV (A2). If the pressure increases beyond the supercritical pressure, a single supercritical phase occurs inside the helium vessel.

[6]The minimum film boiling heat flux of helium is assumed to be $0.3\,\mathrm{Wcm^{-2}}$ [76].

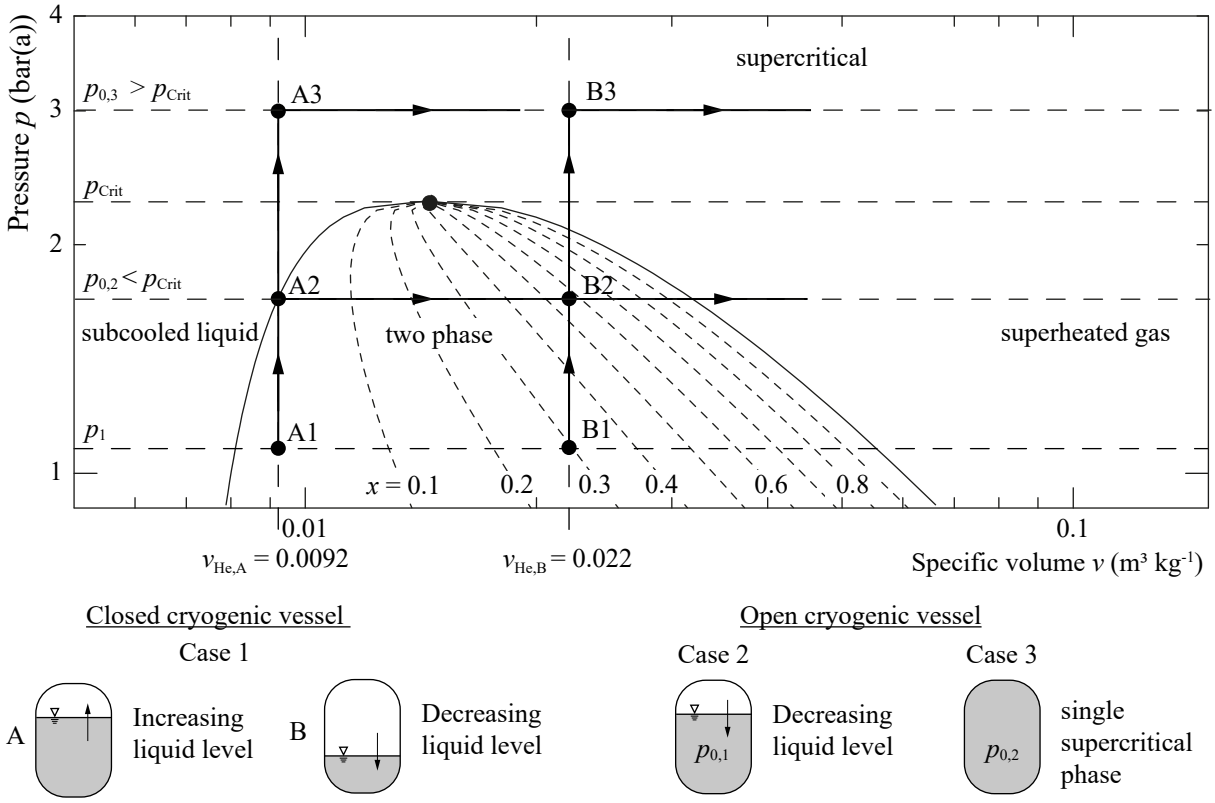

Figure 4.5: Process path of helium inside the helium vessel during LIV in a pv-diagram of helium for two different initial liquid levels and sub- and supercritical relieving pressure, respectively.

B At high initial specific volumes, e.g. $v_{\mathrm{He,B}} = 0.022\,\mathrm{m^3\,kg^{-1}}$ (B1), the isochoric heat input causes a decreasing liquid level up to the opening of the PRV (B2) or until the liquid disappears at the saturated vapour curve. Below the critical pressure, the helium vessel is completely filled with gas before a supercritical phase occurs at pressures above the critical one.

After the opening of the PRV, the process is assumed ideally as isobaric. The temperature stays constant at sub-critical pressure and as long as there is a liquid level, because of the latent heat of vaporization. It increases either at supercritical pressure or at sub-critical pressure if only gaseous helium is stored in the cryostat. At supercritical relieving pressure, only one phase is relevant for the heat transfer (A3 and B3 at $p_{0,3}$), while at sub-critical relieving pressure (A2 at $p_{0,2}$) both liquid and gaseous phase influence the heat transfer. The decrease of the liquid level due to the relieving mass flow rate must also be taken into account at sub-critical pressures.

4.5.1 Closed helium vessel

Applying the First Law of Thermodynamics according to common literature [11] to the closed helium vessel with a constant helium mass $\mathrm{d}M_{\mathrm{He}}/\mathrm{d}t = 0$ including liquid and gaseous

phases and under neglect of potential and kinetic energy as well as volume work yields

$$\frac{\mathrm{d}u_{\mathrm{He}}}{\mathrm{d}t} = \frac{\dot{Q}_{\mathrm{He}}}{M_{\mathrm{He}}} \tag{4.36}$$

where u_{He} is the specific internal energy of helium and $\dot{Q}_{\mathrm{He}}$ is the heat flow transferred to helium according to Section 4.4. However, due to the highly transient processes and the specific boundary conditions, also the energy due to the change of pressure $v\mathrm{d}p$ is considered in this work. Assuming an isochoric process due to a constant mass and volume inside the cryostat

$$\frac{\mathrm{d}\rho_{\mathrm{He}}}{\mathrm{d}t} = \frac{\mathrm{d}M_{\mathrm{He}}}{\mathrm{d}t} = 0 \tag{4.37}$$

Equation 4.36 is expressed to

$$\frac{\mathrm{d}h_{\mathrm{He}}}{\mathrm{d}t} = \frac{\mathrm{d}u_{\mathrm{He}} + v\mathrm{d}p}{\mathrm{d}t} = \frac{\dot{Q}_{\mathrm{He}}}{M_{\mathrm{He}}} \tag{4.38}$$

where h_{He} is the specific enthalpy of helium that is defined as $h = u + pv$ [11]. Based on the aforementioned assumptions, the time-derivative of the specific enthalpy ${}^{\mathrm{d}h_{\mathrm{He}}}/_{\mathrm{d}t}$ in Equation 4.38 is expressed using the total derivative of h_{He} as a function of temperature T_{He} and density ρ_{He} to

$$\frac{\mathrm{d}h_{\mathrm{He}}}{\mathrm{d}t} = \left(\frac{\mathrm{d}h_{\mathrm{He}}}{\mathrm{d}T_{\mathrm{He}}}\right)_{\rho} \cdot \frac{\mathrm{d}T_{\mathrm{He}}}{\mathrm{d}t} \tag{4.39}$$

Solving Equation 4.38 with 4.39 for ${}^{\mathrm{d}T_{\mathrm{He}}}/_{\mathrm{d}t}$ results in the following definition of the temperature increase of helium inside the closed helium vessel

$$\frac{\mathrm{d}T_{\mathrm{He}}}{\mathrm{d}t} = \frac{\dot{Q}_{\mathrm{He}}}{M_{\mathrm{He}} \cdot \left(\frac{\mathrm{d}h_{\mathrm{He}}}{\mathrm{d}T_{\mathrm{He}}}\right)_{\rho}} \tag{4.40}$$

The helium pressure increase ${}^{\mathrm{d}p_{\mathrm{He}}}/_{\mathrm{d}t}$ inside the closed vessel is calculated applying the total derivative of p_{He} as a function of T_{He} and ρ_{He} and Equation 4.37 to

$$\frac{\mathrm{d}p_{\mathrm{He}}}{\mathrm{d}t} = \left(\frac{\mathrm{d}p_{\mathrm{He}}}{\mathrm{d}T_{\mathrm{He}}}\right)_{\rho} \cdot \frac{\mathrm{d}T_{\mathrm{He}}}{\mathrm{d}t} \tag{4.41}$$

The influence of the use of the specific enthalpy at constant density instead of the specific internal energy in Equation 4.38 is discussed in Appendix D.1.

4.5.2 Open helium vessel

When the PRV opens, the helium vessel becomes an open vessel with decreasing helium mass. Applying the First Law of Thermodynamics neglecting both the potential and the kinetic energy yields

$$\frac{\mathrm{d}u_{\mathrm{He}}}{\mathrm{d}t} = \frac{\left(\dot{Q}_{\mathrm{He}} - \dot{M}_0 \cdot (h_{\mathrm{He}} - u_{\mathrm{He}})\right)}{M_{\mathrm{He}}} \tag{4.42}$$

where $\dot{M}_0$ is the mass flow rate out of the helium vessel. The helium pressure is assumed to be constant during the relieving process

$$\frac{\mathrm{d}p_{\mathrm{He}}}{\mathrm{d}t} = 0 \tag{4.43}$$

This open system can be transferred into a closed substitute system by assuming a movable piston that allows the system to expand reversibly. In the First Law of Thermodynamics for a closed system, the corresponding work due to volume change $p\mathrm{d}v$ is considered as

$$\frac{\mathrm{d}h_{\mathrm{He}}}{\mathrm{d}t} = \frac{\mathrm{d}u_{\mathrm{He}} + p\mathrm{d}v}{\mathrm{d}t} = \frac{\dot{Q}_{\mathrm{He}}}{M_{\mathrm{He}}} \tag{4.44}$$

This conversation simplifies the model evaluation since the same equation for the open and the closed system can be applied. Only the fluid property data have to be adapted according to the isobaric and the isochoric boundary conditions, respectively.

At sub-critical relieving pressure $p_0 \leq p_{\mathrm{crit}} = 2.28\,\mathrm{bar}$, the helium temperature also remains constant. Instead, the liquid level according to Equation 4.34 decreases since the average helium density decreases due to the released mass flow rate. At supercritical relieving pressure $p_0 \geq p_{\mathrm{crit}}$, the helium temperature increase inside the open helium vessel is calculated applying the total derivative for h_{He} as a function of temperature and pressure to express the time-derivative of the specific enthalpy in Equation 4.44. Solving for ${}^{\mathrm{d}T_{\mathrm{He}}}/_{\mathrm{d}t}$ yields the helium temperature increase at supercritical relieving pressure.

$$\left(\frac{\mathrm{d}T_{\mathrm{He}}}{\mathrm{d}t}\right) = \begin{cases} 0 & p_0 \leq p_{\mathrm{crit}} \\ \dfrac{\dot{Q}_{\mathrm{He}}}{M_{\mathrm{He}} \cdot \left(\frac{\mathrm{d}h_{\mathrm{He}}}{\mathrm{d}T_{\mathrm{He}}}\right)_p} & p_0 > p_{\mathrm{crit}} \end{cases} \tag{4.45}$$

where h_{He} is the specific enthalpy of helium as a function of temperature and pressure.

The calculation of the relieving mass flow rate $\dot{M}_0$ that equals the time-derivative of the helium mass ${}^{\mathrm{d}m_{\mathrm{He}}}/_{\mathrm{d}t}$ depends also on the relieving pressure. At sub-critical relieving pressure, $\dot{M}_0$ is calculated applying the total derivative for h_{He} as a function of temperature and density to express the time-derivative of the enthalpy in Equation 4.44, while at supercritical p_0, the relieving mass flow rate is defined via the density change of helium.

$$\left(\frac{\mathrm{d}M_{\mathrm{He}}}{\mathrm{d}t}\right) = \dot{M}_0 = \begin{cases} \dfrac{\dot{Q}_{\mathrm{He}}}{-\rho_{\mathrm{He}} \cdot \left(\frac{\mathrm{d}h_{\mathrm{He}}}{\mathrm{d}\rho_{\mathrm{He}}}\right)_{T,p}} & p_0 \leq p_{\mathrm{crit}} \\ \frac{\mathrm{d}\rho_{\mathrm{He}}}{\mathrm{d}t} \cdot V_{\mathrm{Cr}} & p_0 > p_{\mathrm{crit}} \end{cases} \tag{4.46}$$

where the time-derivative of the density at supercritical p_0 is calculated by applying the total derivative of ρ_{He} as a function of T_{He} and p_{He} and Equation 4.43. At sub-critical p_0, ρ_{He} is only dependent on the mass released, as temperature and pressure are constant as long as there is a liquid level inside the cryostat. Once all liquid evaporates, the model assumes the calculation rules of supercritical release since the remaining gas behaves

similar to the supercritical fluid.

$$\left(\frac{\mathrm{d}\rho_{\mathrm{He}}}{\mathrm{d}t}\right) = \begin{cases} \frac{1}{V_{\mathrm{Cr}}} \cdot \frac{\mathrm{d}M_{\mathrm{He}}}{\mathrm{d}t} & p_0 \leq p_{\mathrm{crit}} \\ \left(\frac{\mathrm{d}\rho_{\mathrm{He}}}{\mathrm{d}T_{\mathrm{He}}}\right)_p \cdot \frac{\mathrm{d}T_{\mathrm{He}}}{\mathrm{d}t} & p_0 > p_{\mathrm{crit}} \end{cases} \tag{4.47}$$

Clearly, the implementation of a time-dependent density is not necessary, since the system is already completely defined via temperature and pressure. However, during the numerical implementation of the ODE system, it was observed that the evaluation could be performed more stable when Equation 4.47 was included.

4.6 Heat transfer to piping upstream of PRD

As shown in Equation 3.13, the dimensioning of the PRD is heavily dependent on the helium density, which may change on the way between the helium vessel and the PRD. Especially if the connecting pipe is long and lacks insulation, the temperature increase and pressure drop significantly modify the helium density and consequently the dimensioning.

The temperature $T_{0,x}$ and the pressure $p_{0,x}$ upstream of the PRD are calculated simultaneously by applying mass conservation, momentum and energy balance. The steady and one-dimensional flow is assumed to be fully developed. A heat flow from ambience is considered at constant outer wall temperature for each section. The potential energy of and the axial heat conduction inside the fluid are neglected.

The mass conservation for the helium flow in the upstream piping is calculated as

$$\frac{\partial \dot{M}_0}{\partial x} = 0. \tag{4.48}$$

With the assumption made above, the energy balance in the vertical upstream piping yields

$$\frac{\partial h_{0,x}}{\partial x} = \underbrace{\frac{\dot{q}_{\mathrm{up}} \cdot P_{\mathrm{pipe}}}{\dot{M}_0}}_{\text{heat input from ambient}} - \underbrace{\frac{1}{\partial \mathrm{x}} \left[\frac{\dot{m}_0^2}{2 \cdot \rho_{0,x}^2}\right]}_{\text{kinetic energy}} \tag{4.49}$$

where $\dot{q}_{\mathrm{up}}$ is the heat flux between the wall of the upstream pipe and the helium, P_{pipe} is the circumference of the pipe and $\dot{m}_0$ is the mass flux inside the pipe. Applying the total derivative for enthalpy and density as a function of temperature and pressure and taking

the following definition into account (cf. [76, p.92ff])

$$\text{Isothermal bulk compressibility:} \quad \chi = \frac{1}{\rho} \cdot \left(\frac{\partial \rho}{\partial p}\right)_T \tag{4.50}$$

$$\text{Volume expansivity:} \quad \beta = -\frac{1}{\rho} \cdot \left(\frac{\partial \rho}{\partial T}\right)_p \tag{4.51}$$

$$\text{Isenthalpic Joule Thomson coefficient:} \quad \mu = -\frac{1}{c_p} \cdot \left(\frac{\partial h}{\partial p}\right)_T \tag{4.52}$$

$$\text{Isobaric heat capacity:} \quad c_p = \left(\frac{\partial h}{\partial T}\right)_p \tag{4.53}$$

the equation for the temperature increase in the piping upstream of the PRD results in

$$\frac{\partial T_{0,x}}{\partial x} = \frac{\frac{\dot{q}_{\text{up}} \cdot P_{\text{pipe}}}{\dot{M}_0} + \left(\mu \cdot c_p + \frac{\dot{m}_0^2}{\rho_{0,x}^2} \cdot \chi\right) \cdot \frac{\partial p_{0,x}}{\partial x}}{c_p - \frac{\dot{m}_0^2}{\rho_{0,x}^2} \cdot \beta} \tag{4.54}$$

The heat flux from ambient to helium inside the upstream piping is defined to

$$\dot{q}_{\text{up}} = k \cdot (T_{\text{pipe}} - T_{0,x}) \tag{4.55}$$

with

$$\frac{1}{k \cdot P_{\text{pipe}}} = \frac{1}{\pi} \cdot \left(\frac{1}{\alpha_{0,x} \cdot d_{\text{i}}} + \frac{\log\left(\frac{d_{\text{o}}}{d_{\text{i}}}\right)}{2 \cdot \lambda_{\text{pipe}}}\right) \tag{4.56}$$

where T_{pipe} is the wall temperature of the pipe, k is the overall heat transfer coefficient, λ_{pipe} is the thermal conductivity of the wall and d_{o} and d_{i} are the outer respectively inner diameters of the piping. The convective heat transfer coefficient $\alpha_{0,x}$ is calculated with an empirical Nusselt-correlation Nu for supercritical helium as a function of Reynolds-number Re and Prandtl-number Pr according to [76, p.148f]

$$Nu = 0.0259 \cdot Re^{4/5} \cdot Pr^{2/5} = \frac{\alpha_{0,x} \cdot d_{\text{i}}}{\lambda_{0,x}} \tag{4.57}$$

where d_{i} is the characteristic length of the heat transfer problem. All fluid properties are evaluated at $T_{0,x}$.

For the definition of the wall temperature, two cases are distinguished: (i) the pipe inside and (ii) the pipe outside of the vacuum vessel. Inside the vacuum vessel, a linear axial wall temperature profile is assumed. Outside the vacuum vessel, the wall temperature equals the constant ambient temperature.

The momentum conservation yields the overall pressure drop for a compressible fluid in vertical piping

$$\frac{\partial p}{\partial x} = -\underbrace{\zeta \cdot \frac{\dot{m}_0^2}{2 \cdot d_{\text{i}} \cdot \rho}}_{\text{friction}} - \underbrace{\dot{m}_0 \cdot \frac{1}{\partial x}\left[\frac{1}{\rho}\right]}_{\text{acceleration}} - \underbrace{\rho_{0,x} \cdot g}_{\text{hydrostatic}} \ . \tag{4.58}$$

With the total derivative for ρ as a function of T and p and Equations 4.50 to 4.51 the overall pressure drop inside the vertical upstream piping is calculated as

$$\frac{\partial p_{0,x}}{\partial x} = \frac{-\zeta \cdot \frac{\dot{m}_0^2}{2 \cdot d_\mathrm{i} \cdot \rho_{0,x}} - \frac{\dot{m}_0^2}{\rho_{0,x}} \cdot \beta \cdot \frac{\partial T_{0,x}}{\partial x} - \rho_{0,x} \cdot g}{1 - \frac{\dot{m}_0^2}{\rho_{0,x}} \cdot \chi} \tag{4.59}$$

where the Darcy friction factor ζ is calculated with empirical correlations for smooth surfaces as a function of the Reynolds-number according to e.g. [23, p.1223]

$$\zeta = \begin{cases} \text{Hagen Poiseuille law} & Re \leq 2320 \\ \text{Blasius correlation} & 2320 < Re < 10^4 \\ \text{Konakov correlation} & 10^4 < Re < 10^6 \\ \text{Filonenko correlation} & 10^6 < Re < 5 \cdot 10^7 \end{cases} \tag{4.60}$$

The frictional pressure drop in piping components, such as a venturi tube for flow measurement, is included with a constant zeta value $\zeta_{\text{components}}$, yielding a mass flux dependent pressure drop according to

$$\Delta p_{\text{f,components}} = \zeta_{\text{components}} \cdot \frac{\dot{m}_0^2}{2 \cdot d_\mathrm{i} \cdot \rho} \tag{4.61}$$

$\zeta_{\text{components}}$ values for piping components are tabulated for example in [62, p.212f].

Equations 4.54 and 4.58 form a system of two ODEs for the two gradients $\frac{\partial T_{0,x}}{\partial x}$ and $\frac{\partial p_{0,x}}{\partial x}$, which can be solved numerically.

4.7 Numerical implementation

This section describes the implementation of the systems of ODEs presented in previous sections into a numerical solver. This includes the introduction of a flow chart that visualises the dependencies of the different variables and parameters, of the physical properties and of a mathematical approach to create continuously differentiable functions.

4.7.1 Flow chart of the numerical model

Figures 4.6 and 4.7 depict a flow chart of the numerical model. For better overview, this flow chart is divided into two parts. Part 1 illustrates the dependencies of mathematical operations inside the vacuum vessel and through the vessel wall, while part 2 focuses on the helium vessel and the upstream piping. The link between part 1 and part 2 is the heat flow transferred to helium. In the last step of part 2 - definition of PRD - the numerical model is linked to the calculation rules for the dimensioning of PRVs of the new European Standard EN 17527 that will be published in 2021 (cf. [30] and Figure 3.2). For consistency reasons, same colours are used in Figures 4.1, 4.6 and 4.7.

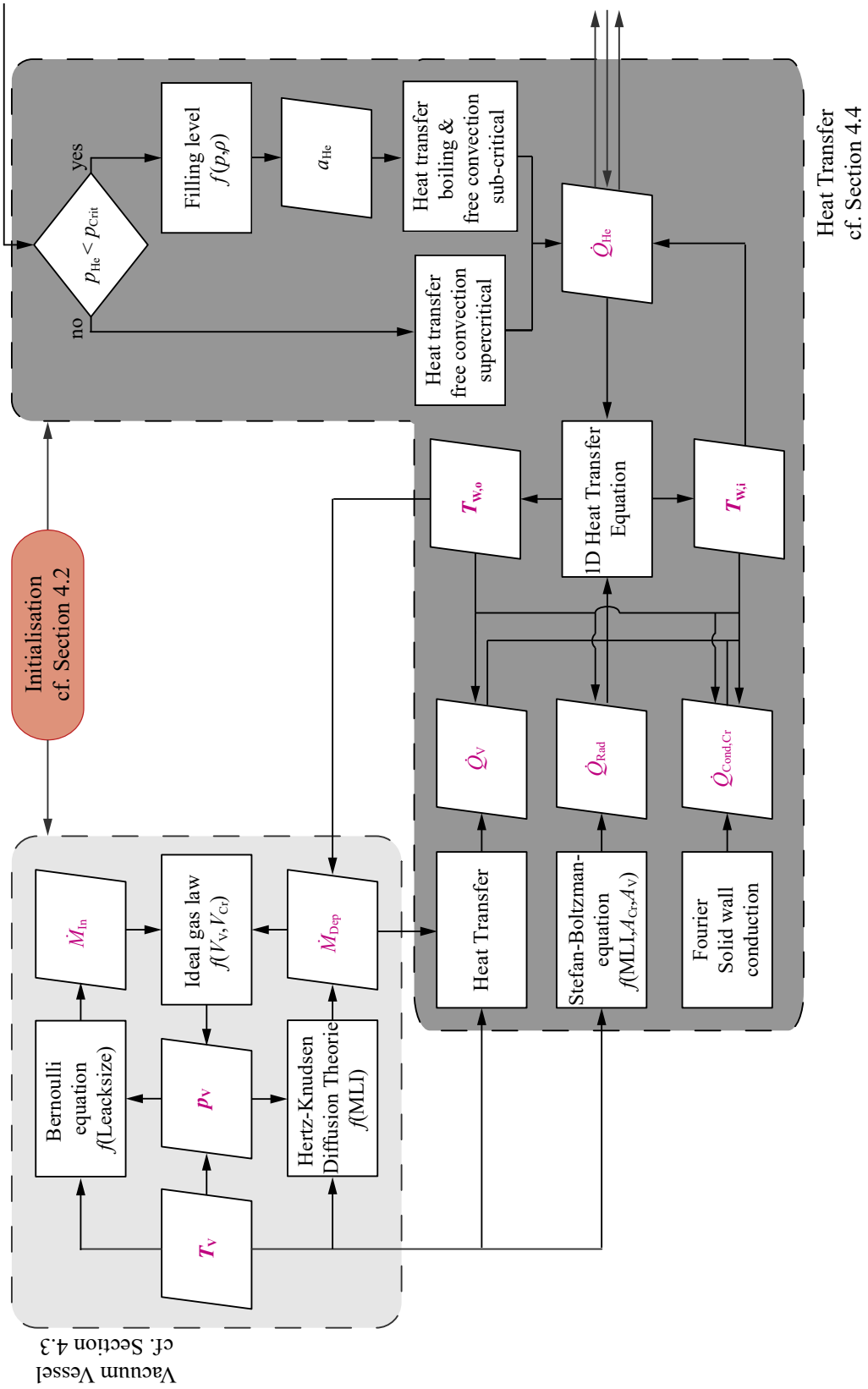

Figure 4.6: Part 1 of a flow chart of the numerical model for dimensioning of PRDs developed in the course of this work. Part 1 considers the processes inside the vacuum vessel and the heat transfer through the vessel wall. The cut is made at the transition to the helium vessel. Part 2 can be found in Figure 4.7.

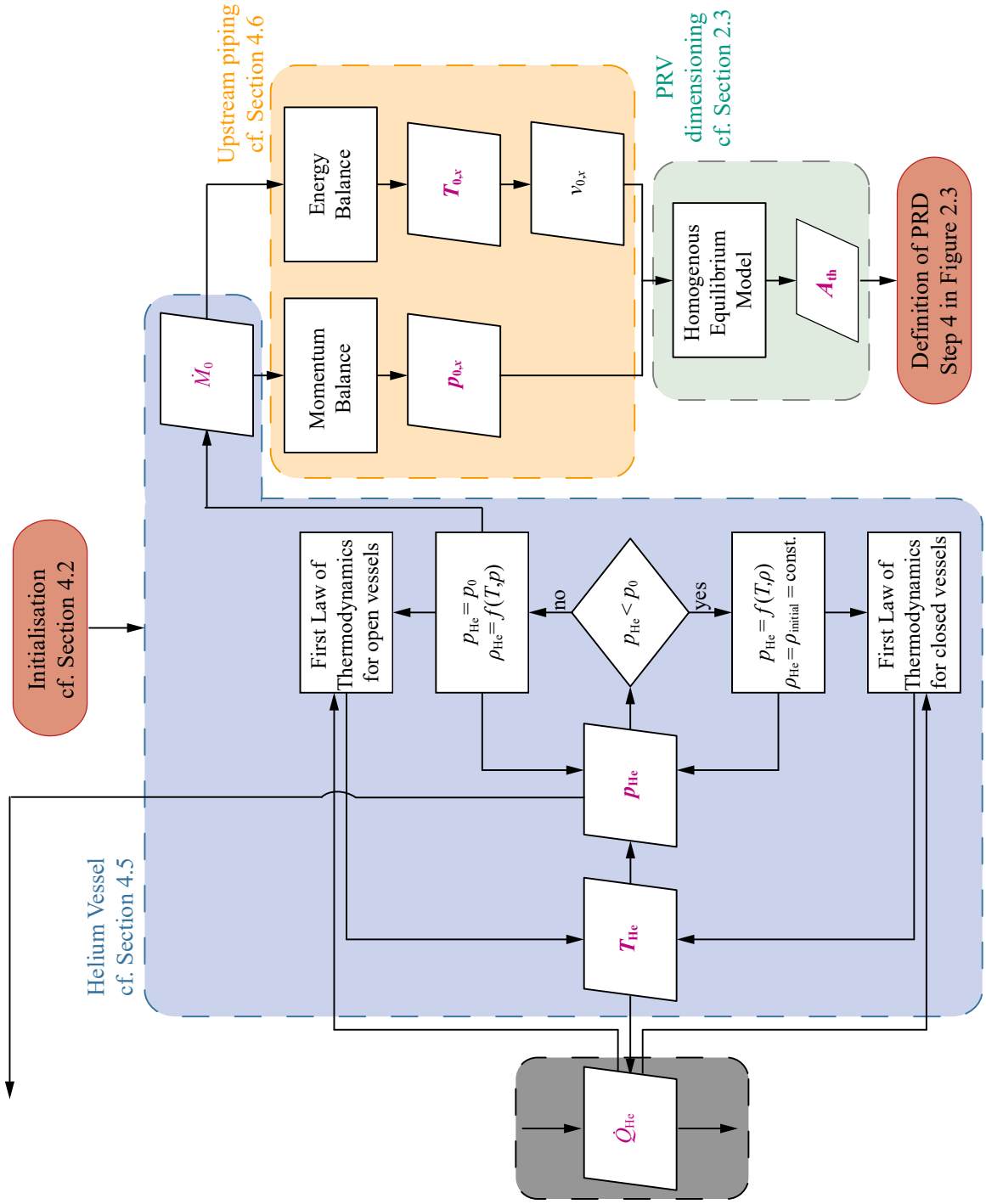

Figure 4.7: Part 2 of a flow chart of the numerical model for dimensioning of PRDs developed in the course of this work. Part 2 considers the processes inside the helium vessel and the upstream piping as well as the PRD dimensioning process. The cut is made at the transition to the helium vessel. Part 1 can be found in Figure 4.6.

4.7.2 Physical properties

For the evaluation of the present model, several physical properties and their derivatives are required. Material data for the cryogenic vessel such as the thermal conductivity λ and specific heat capacity c are taken from Cryocomp [73]. Fluid properties of the venting fluid (dry air as pseudo-pure fluid[7]) and the cryogenic fluid (helium) are implemented via the REFPROP database (Version 10) [53, 54, 58, 67, 71, 75].

Taking into account the humidity of air in the enthalpy for the evaluation of the deposited heat flux according to Equation 4.18 increases the resulting value by up to 11 %, depending on the humidity of air. Consequently, the humidity is considered in the property data as follows.

At wall temperatures above the triple point of pseudo-pure dry air ($T_{\mathrm{trip,air}} = 59.75\,\mathrm{K}$, [53]), humid air is considered as a gas-steam mixture, where the gaseous phase consists of the inert dry air and the condensible water, while the liquid phase consists of water only [57]. In this approach, the interaction between the air and water molecules through the use of interaction parameters is neglected to simplify the evaluation of the numerical solver. In Section 6.2 it is shown that this assumption is sufficient due to its low impact on the heat transfer process. The state changes of such a humid air mixture are defined for many technical applications and processes at ambient pressure and a temperature range of $20 \ldots 100\,^{\circ}\mathrm{C}$, but can also be applied to cryogenic conditions relevant to this work. Available databases such as REFPROP, however, do not provide fluid property data below the triple point. Thus, at $T < 59.75\,\mathrm{K}$, an ideal mixture of the air components nitrogen, oxygen, argon and water is assumed, considering the sensible and latent heat of all humid air components with the solid enthalpies and/or heat capacities according to [19, 33, 48]. An overview of the property data of solid air is given in Appendix C.

Based on the aforementioned assumptions, the enthalpy of humid air h_{amb} is defined as a function of temperature, pressure and water load of air, i.e. the mass water per mass of dry air $Y_{\mathrm{H_2O}}$

$$h_{\mathrm{amb}} = h_{\mathrm{air}} + (Y \cdot h)_{\mathrm{H_2O}} \tag{4.62}$$

where h_{air} is the enthalpy of dry air and $(Y \cdot h)_{\mathrm{H_2O}}$ is the weighted water enthalpy defined to

$$(Y \cdot h)_{\mathrm{H_2O}} = \begin{cases} Y_{\mathrm{H_2O}} \cdot (\Delta h_{\mathrm{V}} + c_{p,\mathrm{vap}} \cdot (T - T_{\mathrm{trip,H_2O}})) & T \geq T_{\mathrm{trip,H_2O}} \\ Y_{\mathrm{S}} \cdot (\Delta h_{\mathrm{V}} + c_{p,\mathrm{vap}} \cdot (T - T_{\mathrm{trip,H_2O}})) & \\ \quad + (Y_{\mathrm{S}} - Y_{\mathrm{H_2O}}) \cdot (c_{p,\mathrm{solid}} \cdot (T - T_{\mathrm{trip,H_2O}}) - \Delta h_{\mathrm{melt}}) & T < T_{\mathrm{trip,H_2O}} \end{cases} \tag{4.63}$$

where Δh_{V} and Δh_{melt} are the heat of vaporization and melting, respectively. $c_{p,\mathrm{vap}}$ and $c_{p,\mathrm{solid}}$ are the isobaric heat capacity of the gaseous water dissolved in the air and the ice that is built at temperatures below the triple point of water due to decreasing solubility of gaseous water in the air, respectively. In order to add the enthalpy values of different

[7] A pseudo-pure fluid is a mixture that is treated like a pure fluid due to its constant composition. [50, p. 271]

fluids, all enthalpy data has been normalized to the same reference state, i.e. the triple point of water $T_{\mathrm{trip,H_2O}} = 273.15\,\mathrm{K} = 0\,^{\circ}\mathrm{C}$. The water load of air $Y_{\mathrm{H_2O}}$ is defined as a function of the relative humidity φ to

$$Y_{\mathrm{H_2O}} = \frac{\tilde{M}_{\mathrm{H_2O}}}{\tilde{M}_{\mathrm{air}}} \cdot \frac{\varphi \cdot p_{\mathrm{sat,H_2O}}\left(T\right)}{p_{\mathrm{amb}} - \varphi \cdot p_{\mathrm{sat,H_2O}}\left(T\right)}. \tag{4.64}$$

where $\tilde{M}$ is the molar mass of dry air respectively water, p_{amb} is the ambient pressure and $p_{\mathrm{sat,H_2O}}$ is the saturation pressure of water as a function of temperature. The saturation water load of air Y_{S} corresponds to $\varphi = 1$.

The enthalpy of dry air h_{air} in Equation 4.62 is calculated according to

$$h_{\mathrm{air}} = \begin{cases} h_{\mathrm{air.ppf}} & T \geq T_{\mathrm{trip,Ar}} \\ \sum\limits_{i=\{\mathrm{N_2,O_2,Ar}\}} \left(\xi_i \cdot h_{\mathrm{i}}\right) & T < T_{\mathrm{trip,Ar}} \end{cases} \tag{4.65}$$

where $h_{\mathrm{air.ppf}}$ is the enthalpy of the pseudo pure fluid from [53] and ξ_i are the mass fractions of the air components $\xi_{\mathrm{N2}} = 0.755$, $\xi_{\mathrm{O2}} = 0.232$ and $\xi_{\mathrm{Ar}} = 0.013$ [53]. Since argon has the highest triple point of the air components, its triple point temperature is set as the limit of the sectionally defined enthalpy.

Additionally, the density and the isobaric specific heat capacity are affected by the humidity. The density of humid air is calculated as

$$\rho_{\mathrm{amb}} = \begin{cases} \left(\frac{1}{\rho_{\mathrm{air}}} \cdot \left(1 + \frac{\tilde{M}_{\mathrm{air}}}{\tilde{M}_{\mathrm{H_2O}}} \cdot Y_{\mathrm{H_2O}}\right)\right)^{-1} & T \geq T_{\mathrm{trip,H_2O}} \\ \rho_{\mathrm{air}} & T < T_{\mathrm{trip,H_2O}} \end{cases} \tag{4.66}$$

and the specific isobaric heat capacity to

$$c_{p,\mathrm{amb}} = Y_{\mathrm{H_2O}} \cdot c_{p,\mathrm{H_2O}} + \begin{cases} c_{p\mathrm{air.ppf}} & T \geq T_{\mathrm{trip,Ar}} \\ \sum\limits_{i=\{\mathrm{N_2,O_2,Ar}\}} \left(\xi_i \cdot c_{p,i}\right) & T < T_{\mathrm{trip,Ar}} \end{cases} \tag{4.67}$$

Being a mixture, the pseudo-pure fluid air does not have a constant vaporization temperature. Thus, the fluid properties of the pseudo-pure fluid air as a function of temperature and pressure are not defined in the two phase region, i.e. between the saturation temperature of the liquid T_{liq} and the one of the vapour T_{vap} (cf. Figure 4.8a). REFPORP outputs *ComplexInfinity*. This discontinuity in the property function can lead to numerical problems during the evaluation of the ODE system. The simplifying mathematical approach of regularisation functions introduced in the next section is applied to overcome this problem.

4.7.3 Regularisation

Regularisation is a mathematical approach to create continuously differentiable functions [28]. In the presented dynamic process this is important, where derivatives of functions

are used. A discontinuity, a jump or a kink in e.g. the property data (cf. Figures 4.8a, c and e can yield unrealistic results and long computation times, since very small time steps are required to resolve the change or may even result in abort of the differential equation solver. In a predefined interval $-\epsilon < x - x_1 < +\epsilon$, regularisation functions can close discontinuities and smooth jumps and kinks.

The regularisation can be done with every function λ_R that has a value range of $0 \ldots 1$ in the regularisation interval $2 \cdot \epsilon$ using the following approach

$$f(x) = (1 - \lambda_\mathrm{R}) \cdot f(x)_{\mathrm{x<x_1}} + \lambda_\mathrm{R} \cdot f(x)_{\mathrm{x>x_1}} \tag{4.68}$$

Within the regularisation interval, Equation 4.68 replaces the values of $f(x)$, resulting in a continuously differentiable function.

In [83], different regularisation functions λ_R are compared for the application in air separation plant modelling. The following sinus period based equation is recommended

$$\lambda_\mathrm{R}(x) = 0.5 + 0.5 \sin\left[\frac{\pi}{2} \cdot \frac{x}{\epsilon}\right] \tag{4.69}$$

and applied in this work too. In Figure 4.8b, the result of Equation 4.69 applied to the discontinuous enthalpy profile of dry air with an interval of $\epsilon = \pm 0.02$ is shown. Figure 4.8d depicts the result for the smoothing of the jump in the enthalpy profile of helium at saturation temperature. Here, a smaller interval of $\epsilon = \pm 0.01$ is used. Equation 4.69 is applied for all fluid properties of dry air and helium as function of pressure and temperature to close the discontinuities or to smooth the jump functions at phase transition. This approach significantly reduces the size of the interpolation functions and thus the computation time.

In [83], a phase shift of $\pi/2$ is used in the sinus function when two functions that intersect in the regularisation interval are considered

$$\lambda_\mathrm{R}(x) = 0.5 + 0.5 \sin\left[\frac{\pi}{2} \cdot \frac{x}{\epsilon} + \frac{\pi}{2}\right] \tag{4.70}$$

Equation 4.70 is applied to fluid property functions that evaluate data in the two phase region, e.g. as a function of density. In this case, there is no jump in the profile at phase transition, but rather a kink, which can be considered as an intersection of two independent functions. This is exemplary depicted for the internal energy of helium at 4 K as a function of density in Figures 4.8e and f with a regularisation interval of $2 \cdot \epsilon = 0.01$.

4.7.4 Numerical solver

In Sections 4.3 to 4.6, two systems of ODEs have been presented that have to be numerically evaluated one after the other in order to dimension a PRV for helium cryostats. System 1 includes the processes inside the helium cryostat induced by LIV and system 2 covers the state changes of helium inside the piping upstream of the PRV, i.e. from the

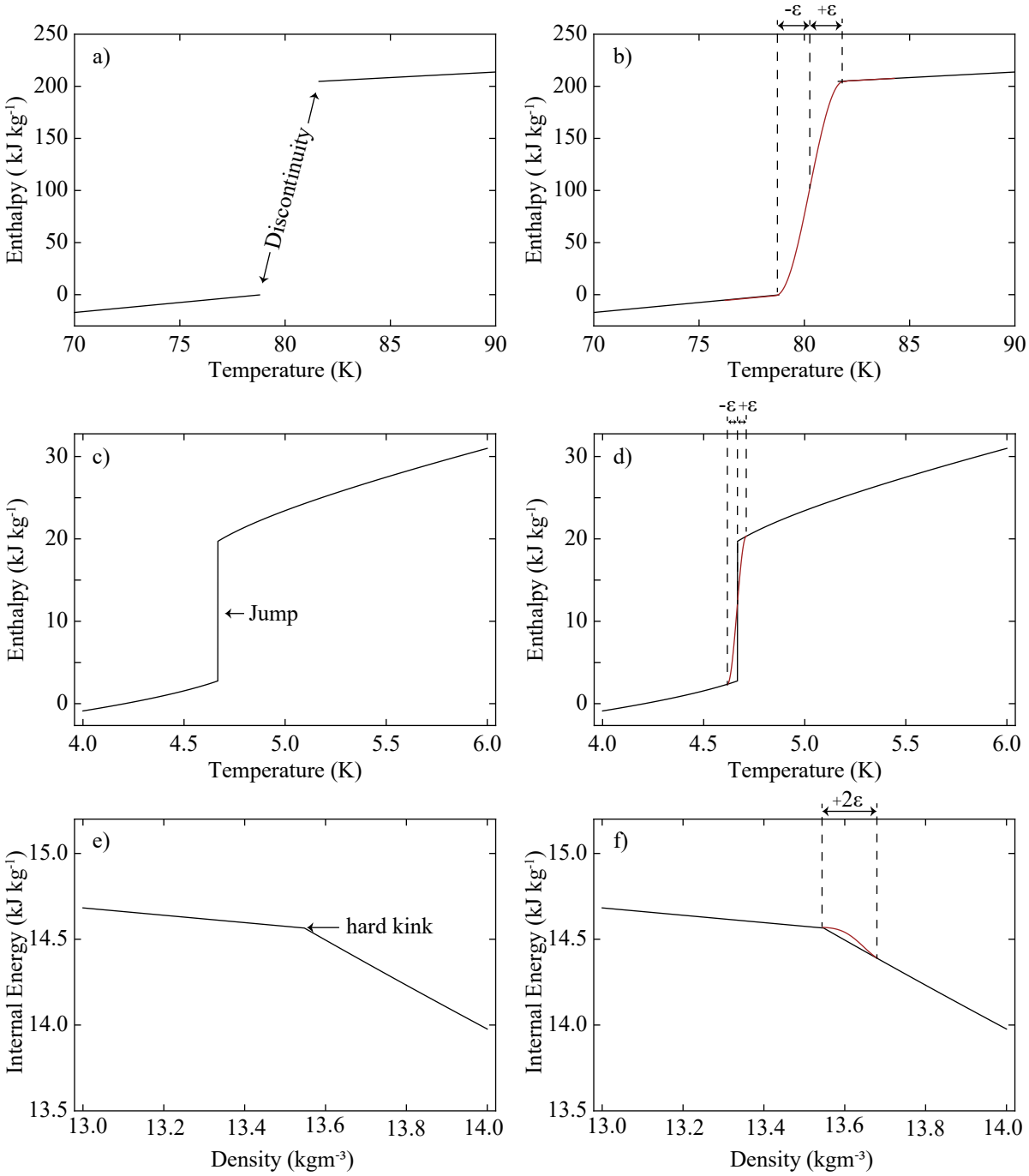

Figure 4.8: Examples of regularisation functions applied to fluid property data. a) Enthalpy profile of dry air as a function of temperature at 1 bar with a discontinuity between $T_{\mathrm{liq}} < T < T_{\mathrm{vap}}$. b) Enthalpy profile of Figure 4.8a including a regularisation at $x = (T_{\mathrm{liq}}+T_{\mathrm{vap}}/2)_{\mathrm{air}}$ with a regularisation interval of $\epsilon = \pm 0.02$. c) Enthalpy profile of helium at 1.5 bar as a function of temperature showing the jump at saturation temperature. d) Enthalpy profile of Figure 4.8c including a regularisation at $x = T_{\mathrm{Sat}}$ with a regularisation interval of $\epsilon = \pm 0.01$. e) Profile of the internal energy of helium at 4 K as a function of density focusing on the hart kink at the density of saturated liquid ρ_{liq}. f) Profile of Figure 4.8e including a regularisation at $x = \rho_{\mathrm{liq}}$ with phase shift and an interval of $2 \cdot \epsilon = 0.01$.

exit of the cryogenic vessel to the inlet of the PRV. System 2 requires the results of the time-dependent helium temperature and pressure profiles and the relieving mass flow rate of system 1 as boundary conditions. Table 4.1 summarizes the differential equations of both systems that have to be solved simultaneously. Besides the differential equations describing the main time-dependent variables, several other parameters are defined by polynomial equations as a function of the time-dependent variables (e.g. $f(T, p, ...)$). The corresponding equations can be found in the respective sections and the dependencies are visualised in the flow chart in Figures 4.6 and 4.7.

Both systems of ODEs are evaluated in the computer algebra system Mathematica [42]. Mathematica includes the framework *NDSolve* to solve ordinary, partial, algebraic and even delay differential equation systems. During numerical solving of such systems, *NDSolve* runs through three phases. First, the equations are processed into a function that represents the right-hand side of the equations in normal form. Second, a numerical solution is found iteratively starting from the initial conditions. Third, the resulting data is processed into interpolating functions, one for each time-dependent variable.

In the first step, as per default configuration, *NDSolve* tries to transfer the system symbolically into the normal form $x' = F(t, x)$. Due to the complexity of the presented systems of ODEs, however, Mathematica is not able to perform this step by default configuration, but *NDSolve* offers a treatment to simplify such equation systems. The *EquationSimplification* stage with the method *Solve* forces Mathematica to transfer the system symbolically into the normal form [70]. The application of this treatment solves the issue for the presented systems.

The second step includes the numerical time integration of the ODE system. Before starting the numerical integration, the system is initialised by the values introduced in Section 4.2. The following time integration methods are implemented in *NDSolve*

"Adams"	predictor-corrector Adams method with orders $1 \ldots 12$
"BDF"	implicit backward differentiation formulas with orders $1 \ldots 5$
"ExplicitRungeKutta"	adaptive embedded pairs of $2 \pm 1 \ldots 9 \pm 8$
"ImplicitRungeKutta"	families of arbitrary-order implicit Runge-Kutta methods

Further information about numerical methods and numerical differential equation solving in Mathematica can be found in [70]. In what follows, the applicability of the available time integration methods to system 1 of ODEs is discussed.

Table 4.2 compares the solving time, the numerical steps[8] and the evaluation steps[9] necessary to solve system 1 of ODEs with the four numerical time integration methods available in Mathematica. The values can only be compared relatively to each other, since the absolute values also depends on the performance of the computer used. The resulting time-dependent profiles are independent of the numerical model used. Thus, the solver comparison is done with a focus on the optimization of the evaluation time. With

[8] Numerical steps indicate how often a step is taken by the numerical method used.
[9] Evaluation steps indicate how often the functions derived from the input are evaluated numerically.

the default automatic setting, Mathematica will choose a method that should be appropriate to solve the system of ODEs, resulting in a solving time of 705 s using 783 numerical and 1868 evaluation steps. However, it is not possible to get the information of the solver used as an output. By trial and error, it is deduced that the results have been produced using the *Adams*-method. The solving time with the *BDF*-method exceeded all other methods by far and is therefore not taken into account. The *RungeKutta*-methods, both explicit and implicit, lead to the same results more efficiently, i.e. in less than 315 s. The implicit method converges faster but requires significantly more numerical and evaluation steps.

For the *ExplicitRungeKutta*-method several additional parameters, such as the differential pair or step-size control parameter, can be set. Table 4.3 compares the results for the available differential pairs using a discrete proportional integrate (PI) step-size controller as described in [35] in order to overcome the problem of oscillating step-size sequences that typically appear when stiffness is encountered. The presented system tends to be stiff at the transition between closed and open helium vessel.

After further testing, it can be concluded that a differential pair of 3(2) explicit Runge-Kutta formula yields in 7.5 s the most time efficient results even compared to the *ImplicitRungeKutta*-formula. To further optimize the solver, the *AccuracyGoal* is set to 4, the *PressicionGoal* is set to 6, all interpolation orders are allowed and the initial step size is limited to 0.001. *AccuracyGoal* determines the absolute error to be allowed in the solution, while *PressicionGoal* determines the relative error.

The same solver is applied for the evaluation of the temperature and pressure increase in the piping upstream of the PRV (System 2).

Table 4.1: Overview of the systems of ODEs that have to be solved for the dimensioning of PRVs for helium cryostats.

Section	Variable	Equation	Conditions
System 1 Cryostat			
4.3	p_{V}	4.16	
	T_{V}	4.15	
4.4	$T_{\mathrm{W,o}}$	4.26	
	$T_{\mathrm{W,i}}$	4.27	
4.5.1	p_{He}	4.41	$p_{\mathrm{He}} < p_0$
4.5.2		4.43	$p_{\mathrm{He}} \geq p_0$
4.5.1	T_{He}	4.40	$p_{\mathrm{He}} < p_0$
4.5.2		4.45	$p_{\mathrm{He}} \geq p_0$
4.5.1	M_{He}	4.37	$p_{\mathrm{He}} < p_0$
4.5.2		4.46	$p_{\mathrm{He}} \geq p_0$
4.5.1	ρ_{He}	4.37	$p_{\mathrm{He}} < p_0$
4.5.2		4.47	$p_{\mathrm{He}} \geq p_0$
System 2 Upstream Piping			
4.6	$T_{\mathrm{He},x}$	4.54	$p_{\mathrm{He}} \geq p_0$
	$p_{\mathrm{He},x}$	4.58	$p_{\mathrm{He}} \geq p_0$

Table 4.2: Comparison of the solving time, the numerical steps and the evaluation steps of different numerical methods for the calculation of the wall temperature increase during experiments exemplary for E1.

Method	Solving time (s)	Numerical steps	Evaluation steps
Automatic	704.67	783	1868
Adams	713.11	783	1868
BDF	2015.02	1443	2398
Explicit Runge Kutta	314.95	306	920
Implicit Runge Kutta	19.64	2322	12806

Table 4.3: Comparison of the solving time, the numerical steps and the evaluation steps of the *RungeKutta*-pairs $2 \pm 1 \ldots 9 \pm 8$, available in Mathematica, for the calculation of the wall temperature increase during experiments exemplary for E1.

Pair	Solving time (s)	Numerical steps	Evaluation steps
2(1) [69]	2059.84	3082	6165
3(2) [69]	7.48	352	1076
4(3) [69]	7.97	326	1641
5(4) [14]	590.11	166	1640
6(5) [78]	3744.97	684	9505
7(6) [78]	869.08	122	2441
8(7) [78]	3932.39	367	10261
9(8) [78]	8773.14	619	22838

5 PICARD - A cryogenic safety test facility

In this chapter, the cryogenic safety test facility PICARD, used to experimentally investigate LIV, is presented. In addition, design and functionality of pressure relief valves (PRVs) in helium cryostats, installation of multi-layer insulation (MLI), instrumentation and data evaluation are covered. Furthermore, constraints of the test facility regarding data evaluation are discussed.

5.1 The test facility

The cryogenic safety test facility PICARD, which stands for **P**ressure **I**ncrease in **C**ryostats and **A**nalysis of **R**elief **D**evcies, has been designed, constructed and commissioned at the Institute for Technical Physics (ITEP) at Karlsruhe Institute of Technology (KIT) in the course of a previous work [85], in order to analyse the dynamic process induced by LIV to helium cryostats. Figure 5.1 provides an overview of the test facility that consists of a cryostat with a cryogenic volume of 100 L and a maximum allowable pressure $p_S = 16\,\text{bar}\,(\text{g})$, a vacuum pumping station, a venting section, a water bath heater and piping. The vacuum pumping station enables insulation vacua of up to $10^{-6}\,\text{mbar}$, thus limiting the thermal conduction inside the vacuum vessel. Additionally, a radiation shield made of aluminium is mounted inside the vacuum vessel to reduce the heat input due to thermal radiation. As it is only cooled by conduction to the helium filling line, it has an average temperature barely below 0 °C. During LIV, the air can pass the shield through holes, three at the bottom and two at the top. An orifice measurement section closed with a ball valve installed at the vacuum vessel allows to break the insulation vacuum. The cryogenic pressure vessel is protected against excessive pressure with a bursting disc (BD) at p_S according to the PED. In order to analyse the behaviour of PRVs, a second protection stage is realized with replaceable PRVs at set pressures $p_{set} \leq 12\,\text{bar(g)}$ with respect to the opening tolerances of both PRV and BD. While the helium circuit would be opened to atmosphere when the BD responds, after an activation of the PRV, helium is guided through a quench gas line to a recovery system. The cryostat can be filled with liquid helium via an external filling line from a helium dewar with a liquid level of up to 80 %. The helium that evaporates during filling and normal operation is warmed up in a water bath heater to prevent air condensation on the piping, and then guided into the recovery system. The bypass line allows to pre-cool the pipe upstream of the PRV.

① Quench line downstream
② Bypass
③ Exhaust line
④ Water bath heater
⑤ Vacuum pump
⑥ Venting section
⑦ BD vacuum vessel
⑧ PRV
⑨ Quench line upstream
⑩ Venturi tube
⑪ BD cryogenic vessel
⑫ Cryostat
⑬ Filling line
⑭ Helium dewar

Figure 5.1: Photographic overview of the cryogenic safety test facility PICARD.

More detailed information on the design and commissioning of the test facility is given in [85].

In preparation of venting experiments, the PRV is first dimensioned according to the required conditions, then adjusted to its set pressure by the manufacturer or in-house according to the initial audible discharge test [85] and finally mounted on the test facility. If MLI is required, it is installed on the cryogenic surface according to Section 5.3. When an insulating vacuum of below 10^{-4} mbar has been generated by the vacuum pumping station, the cryogenic vessel is filled with liquid helium from the external dewar by applying an overpressure of up to 180 mbar to the dewar with pressurized gaseous helium. In order to monitor the filling and cooling-down process, data is recorded at a rate of 5 Hz. When the required liquid level is reached, the filling line is disconnected manually and the vacuum pumps are switched off in order to protect the turbo-pump from pressure waves. Furthermore, the valves connecting the cryogenic vessel to the helium recovery system via the exhaust gas line are closed and the one to the quench gas system is opened. The time resolution of data acquisition is changed to a rate of 1 kHz to account for the short and highly dynamic process. Once the set-up is complete, the actual safety experiment is initiated by opening the ball-valve connecting the vacuum vessel to the venting orifice section.

Table 5.1: Settings and PRV dimensioning parameter of all experiments conducted in the course of this work.

Exp. No.	PRV	Insulation	N_{Layer}	p_{set} (bar(g))	d_{Orifice} (mm)	a_0 (%)	φ (%)
E1	PRV2	-	-	3.0	37.5	59.9	37.5
E2	PRV2	Shield	-	3.0	37.5	61.4	37.7
E3	PRV1	Shield	-	6.0	30	64.1	26.4
E4	PRV1	Shield	-	5.0	30	60.7	31.9
E5	PRV1	Shield	-	4.5	30	59.3	22.5
E6	PRV1	Shield	-	8.0	30	61.5	28.5
E7	PRV1	Shield	-	8.0	30	60.4	35.9
E8	PRV2	MLI2	1	6.0	37.5	61.2	33.4
E9	PRV2	MLI1	12	2.2	37.5	58.3	55.6
E10	PRV2	MLI1	12	4.5	37.5	61.2	18.5
E11	PRV2	MLI1	24	6.0	37.5	61.2	44.3
E12	PRV2	MLI1	24	3.0	37.5	60.7	25.5
E13	PRV2	MLI3	10	4.5	37.5	56.2	25.1
E14	PRV2	MLI3	10	3.1	37.5	56.8	28.5
E15	PRV3	Shield	-	4.0	12.5	82.3	38.3
E16	PRV3	Shield	-	2.0	5	84.9	41.6
E17	PRV3	Shield	-	1.0	3	84.7	50.2
E18	PRV3	Shield	-	1.0	3	83.6	45.0
E19	PRV3	Shield	-	1.0	3.8	83.2	60.9

Table 5.1 summarizes the settings and PRV dimensioning parameters of all experiments conducted in the course of this work. E8, E9 and E11 were conducted in the course of a master thesis [66] supervised by the author.

5.2 Pressure relief valves

PRVs are commonly used for immediate pressure limitation in pressure equipment. Full-lift, direct acting spring-loaded PRVs are preferred in helium cryostat, as they automatically close if the system pressure drops below the closing pressure, avoiding the risk of air leaking back into the cryogenic system. In addition, the defined opening and closing functions of full-lift valves reduce the risk of floating valve disks and thus unstable operation and helium leaks. Spring-loaded PRVs mainly consist of a spindle with a valve disk installed at one end and a helical spring to adjust the required pressure. In case of an incident, the pressure inside the cryostat increases until the force applied by the

fluid pressure on the effective surface of the valve disk exceeds the spring force. Beyond this pressure, referred to as set pressure p_{Set}, the PRV starts to open. Full-lift PRVs are designed to be fully open within 5 % of the set pressure and re-closed within 15 % below the set pressure. The pressure at full lift is defined as the relieving pressure p_0 to be used for dimensioning. Furthermore, PRVs are commonly equipped with balancing bellows to compensate back pressure influences. For helium applications, PRVs with balancing bellows have the added benefit of sealing the helium flow area from the spring housing. The spring constant is temperature-dependent, hence a contact with cold helium during release would influence the opening characteristic of the PRV.

It is not possible to adjust the set pressure over the entire pressure range investigated at PICARD with only one spring as the pressure and flow forces during the release have to be in a specific ratio to the spring force to maintain the standardized opening and closing pressure differences. As a results, springs with different spring constants are used. In the course of this work, three full-lift, direct-acting, spring-loaded PRVs from different manufacturers and with different minimum discharge diameters d_{th} are applied. The housing of all three is made of austenitic stainless steel according to EN 13445-2:2014 [29].

PRV1 Spring loaded, bellow balanced PRV with $d_{\mathrm{th}} = 17.5\,\mathrm{mm}$, $K_{\mathrm{dr,gas}} = 0.79$, lift = 4.1 mm

PRV2 Spring loaded, bellow balanced PRV with $d_{\mathrm{th}} = 22\,\mathrm{mm}$, $K_{\mathrm{dr,gas}} = 0.845$, lift = 9.1 mm

PRV3 Spring loaded PRV with $d_{\mathrm{th}} = 10\,\mathrm{mm}$, $K_{\mathrm{dr,gas}} = 0.76$, lift = 4 mm

Figure 5.2 shows a photograph of PRV2 on the left and the corresponding technical drawing on the right exemplary for the used PRVs. Unlike PRV1 and PRV3, PRV2 is equipped with friction dampers to avoid oscillations and thus support stable release.

The relieving mass flux depends on the system pressure and the lift of the PRV and thus the discharge coefficient. To cover a wider range of experimental parameters, lift restriction can be installed according to [44]. Therefore, detailed knowledge of valve design, actual K_{dr} and lift is essential. However, data sheets usually provide only average values of both the discharge coefficient and the lift. Hence, in cooperation with the manufacturer, the actual K_{dr} and the lift of PRV2 have been measured. The red profile in Figure 5.3a depicts the dependence of the lift of PRV2 on the system pressure.

A characteristic opening profile of a full-lift PRV is shown, where the valve starts to open at the set pressure ($p_{\mathrm{Set}} = 6.5\,\mathrm{bar\,(g)}$) with a short proportional increase of the lift at pressures up to 5 % of the set pressure ($p_0 = 6.83\,\mathrm{bar\,(g)}$). This is followed by a sharp increase of the lift of up to 100 % at relieving pressure. PRV2 is completely closed again at $p_{\mathrm{close}} = 5.85\,\mathrm{bar\,(g)}$, which is in the required closing difference of 15 % below the set pressure. In addition, the manufacturer has provided a dependence of the discharge function on the lift in Figure 5.3b, which is needed for the correct restriction of the lift.

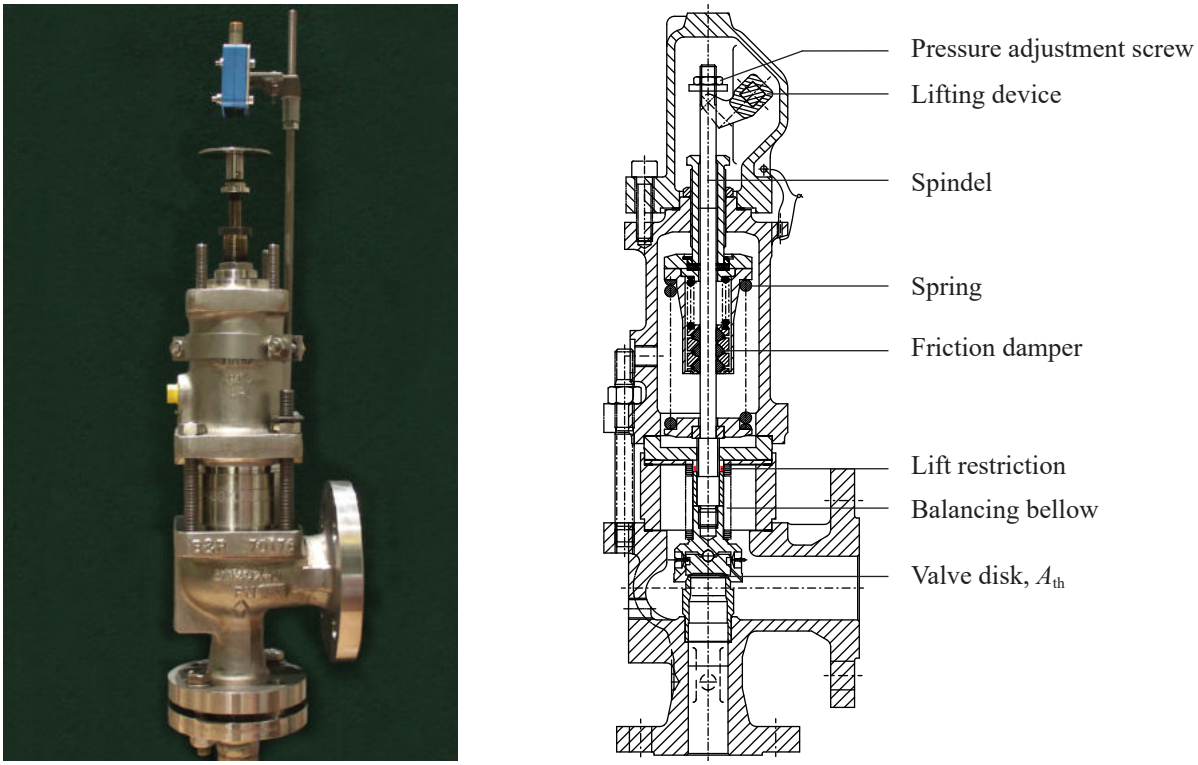

Figure 5.2: *Left*: Photograph of PRV2 including the lift measurement installation (GI31). *Right*: Technical drawing of PRV2 ©with kind permission for publication from the manufacturer.

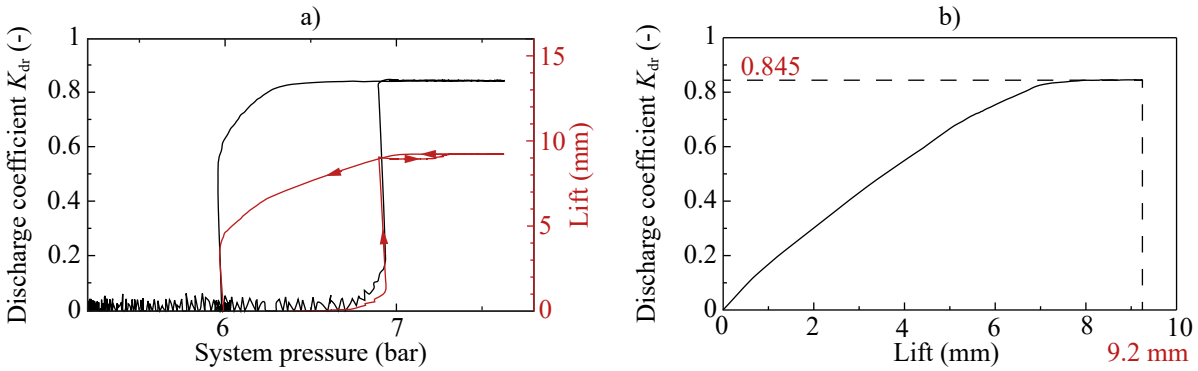

Figure 5.3: a) Discharge coefficient and lift of PRV2 as a function of the system pressure for $p_{Set} = 6.5\,\text{bar}\,(g)$. b) Discharge coefficient of PRV2 measured as a function of the lift.

5.3 Multi-layer insulation

In addition to a radiation shield, multiple radiation reflection, i.e. the installation of multi-layer insulation (MLI) on the cryogenic surface and/or thermal radiation shield, can reduce the heat input to helium cryostats due to thermal radiation. Generally, two forms of MLI are distinguished, blankets and reflector-spacer units. The blankets consist of 10 . . . 12 reflector layers, which are separated by spacer elements that prevent thermal conduction between layers. They are usually perforated to allow for proper evacuation inside the blankets. The layers, i.e. one reflector together with one spacer, have staggered perforations to avoid thermal short cuts. The schematic structure of a blanket is depicted on the left side in Figure 5.4. The reflector-spacer units are metallized plastic foils, which are folded or embossed to reduce the number of contact points and thus the thermal conductivity. [82]

The reduction of the thermal load in standard operation is thoroughly assessed for different types of MLI, cf. [74]. However, for the influence of MLI on the heat input to helium cryostats following LIV, where the MLI acts as diffusive barrier for the air to reach the cryogenic surface, only few constant heat flux values are proposed in the literature [52].

In order to investigate the influence of MLI on the heat transfer to helium after LIV, multiple experiments have been conducted, where the surface of PICARD's cryogenic vessel has been equipped with three different types of MLI and different layer numbers.

MLI1 consists of 12 layers of 6 µm thick perforated polyester film aluminized on either side with a thickness of 40 nm and separated by polyester tulle. The films are perforated with 2 mm diameter holes in a grid of 50 mm distance. Films and tulle are assembled together.

MLI2 is a single-layer aluminium film of 6 µm thickness, bonded to a 12 µm thick aluminized polyester film, which is perforated manually prior to installation with 6 mm holes in a grid of 200 mm. The matt aluminium side faces the warm surface and the glossy polyester side faces the cold surface.

MLI3 is composed of 10 layers of 12 µm thick polyester foil, double-side aluminized with a thickness of 40 nm and interleaved with 10 layers of non-woven polyester spacer material. The perforations have a diameter of 4 mm in a grid of 150 mm.

On the right in Figure 5.4, the dimensions of the MLI pieces used for the insulation are shown, exemplary for 10 layers of MLI3. A photograph of the insulated cryogenic vessel of PICARD can be found in Appendix B. The following precautions are taken for the installation of MLI on the cryogenic vessel [82]:

- The whole cryogenic vessel is covered in MLI, gaps of any size are avoided,
- the MLI is packed loosely with $\approx$ 10 layers/cm in order to reduce thermal conduction,
- contact between the warm outer layer and the cold inner layer is avoided,

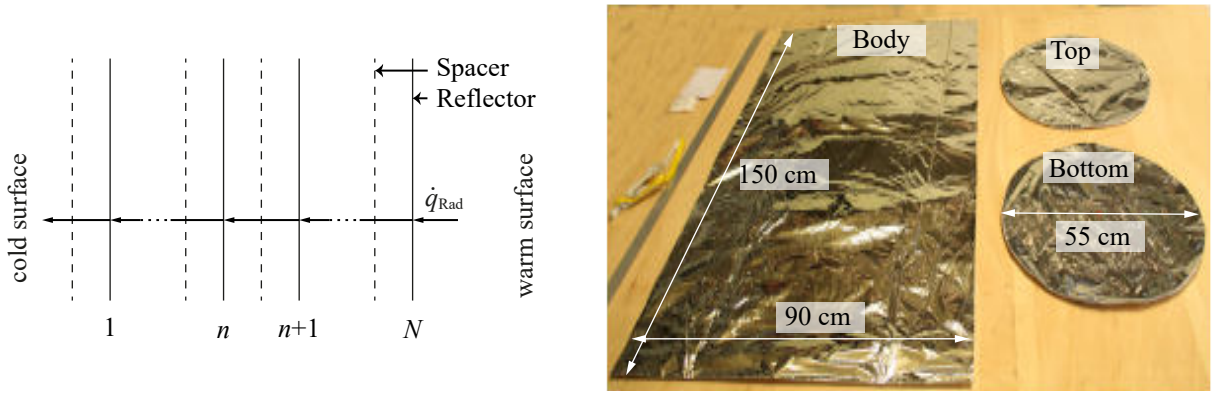

Figure 5.4: *Left*: Schematic structure of MLI-blankets. *Right*: Dimensions of the MLI pieces used for the insulation.

- wherever blankets meet at corners, cold layers are overlaid, tacked, folded and attached with aluminium adhesive tape,
- for straight overlaps, layers of the same temperature are stacked on top of each other.

5.4 Instrumentation upgrade

Figure 5.5 depicts the current piping and instrumentation diagram (P&ID) of the PICARD test facility with the temperature sensors (TI)[1], the pressure transmitters (PI), the differential pressure transmitter (PDI), the liquid level probe (LI), the humidity probe (MI) and the proximity probe (GI). Symbols in circles indicate an analogue display on site, while those in hexagons specify a recording by the data acquisition system. Beyond the detailed descriptions in [85], the following updates are made in the course of this work.

First, the differential pressure transmitter at the orifice measurement section, which is needed to define the venting mass flow rate of humid air, is replaced by faster and more accurate relative pressure transmitters PI24 and PI25 with a calibration uncertainty of less than $\pm 0.05\,\%$, because [85] showed that the response time of the differential pressure transmitter is too long to sufficiently evaluate the venting mass flow rate.

Second, the PICARD instrumentation is extended by a proximity sensor (GI31), emitting pulsed laser light to measure the lift of PRVs during discharge with a calibration uncertainty of $\pm 0.5\,\%$ of the range. In experiment E1 to E7, the proximity sensor is installed outside of the moving system, whereby a zero offset is obtained from the first opening to the closing of the PRV by the additional shrinkage of the pipeline. Therefore, only a qualitative statement about the opening process can be made for the aforementioned

[1] TI11-TI19, TI21-TI28 and TI31-TI32 are TVO-sensors, which are carbon ceramic temperature sensors produced in Russia, commonly used for the measurement of cryogenic temperatures [21] and calibrated in house with an calibration uncertainty of $\pm 1\,\%$. TI33 is a resistance temperature sensor.

experiments. From experiment E8 onwards, the proximity sensor is installed directly on the valve, i.e. in the moving system, to improve the measurement accuracy.

Third, an additional temperature sensor (TI19) is installed in the piping upstream of the PRV directly in front of the tapering in order to measure the influence of the upstream piping on the relieving temperature.

In addition, before experiment E15, pressure transmitters are installed up- (PI13) and downstream (PI32) of the PRV to investigate the influence of the pressure drop and the back pressure on the relieving process. Both have a calibration uncertainty of $\pm 0.5\,\%$ of the range, but different pressure ranges (PI13: $0 \ldots 16\,\mathrm{bar}$, PI31: $0 \ldots 4\,\mathrm{bar}$).

Finally, the orifice measurement section is upgraded to an in- and outlet diameter of $D_{\mathrm{Orifice}} = 49.25\,\mathrm{mm}$ (DN50) and an orifice diameter of $d_{\mathrm{Orifice}} = 37.5\,\mathrm{mm}$ since [85] showed that the pressure increase in the vacuum space is still constrained by the venting mass flow rate and thus by the former orifice diameter of $d_{\mathrm{Orifice}} = 30\,\mathrm{mm}$.

5.5 Data evaluation

In addition to directly measured temperatures, pressures, liquid level, humidity of air and lift of the PRV, the following quantities are derived from measured data:

- the venting mass flow rate $\dot{M}_{\mathrm{In,Exp}}$,
- the deposited mass flow rate $\dot{M}_{\mathrm{Dep,Exp}}$,
- the heat flux caused by the venting fluid $\dot{q}_{\mathrm{V,Exp}}$ and
- the relieving mass flow rate $\dot{M}_{\mathrm{0,Exp}}$

Data evaluation is based on the detailed descriptions in [85]. The fluid property data relevant for the data evaluation has been introduced in Subsection 4.7.2.

5.5.1 Venting mass flow rate

The venting mass flow rate occurring during an experiment $\dot{M}_{\mathrm{In,Exp}}$ is measured with an orifice section from *Tetratec* and calculated applying the following calibration polynomial based on a standardized formula according to [25]

$$\begin{aligned} \dot{M}_{\mathrm{In,Exp}} \quad & (T_{\mathrm{amb}}, p_{\mathrm{amb}}, \Delta p_{\mathrm{Orifice}}) \\ = \quad & \frac{\pi}{4} \cdot d_{\mathrm{Orifice}}^2 \cdot \sqrt{2 \cdot \rho_{\mathrm{vent}}\,(T_{\mathrm{amb}}, p_{\mathrm{amb}}, \varphi)} \\ \cdot \quad & \left(C_{\mathrm{A}} \cdot \Delta p_{\mathrm{Orifice}}^{0.5} + C_{\mathrm{B}} \cdot \Delta p_{\mathrm{Orifice}} + C_{\mathrm{C}} \cdot \Delta p_{\mathrm{Orifice}}^{1.5} + C_{\mathrm{D}} \cdot \Delta p_{\mathrm{Orifice}}^{2} + C_{\mathrm{E}} \cdot \Delta p_{\mathrm{Orifice}}^{2.5} \right) \end{aligned} \tag{5.1}$$

where d_{Orifice} is the diameter of the orifice, ρ_{vent} is the density of the venting fluid at ambient temperature T_{amb}, at ambient pressure p_{amb} and at the humidity φ, $\Delta p_{\mathrm{Orifice}}$ is the pressure difference at the orifice and $C_{\mathrm{A}} ... C_{\mathrm{E}}$ are the calibration coefficients according to Table 5.2.

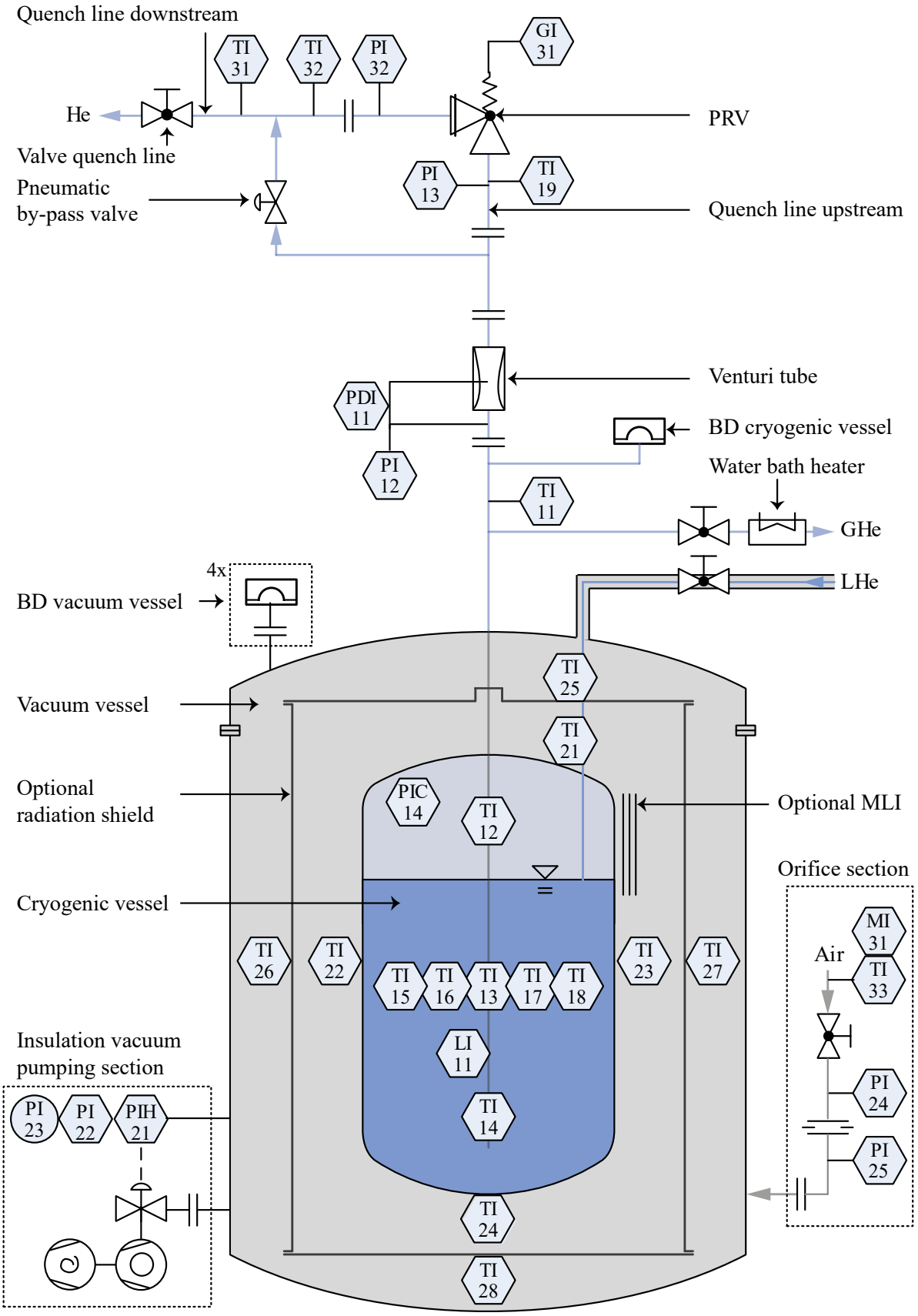

Figure 5.5: Simplified P&ID chart of the PICARD test facility. Updated from [81, 85].

Table 5.2: Calibration coefficients of the orifice measurement sections for three differently sized orifices by TetraTec. The orifice with $d_{\text{Orifice}} = 37.5\,\text{mm}$ can only be installed in the DN50 measurement section due to design constraints.

d_{Orifice} mm	$C_{\text{A}} \cdot 10^{5}$ mbar$^{0.5}$	$C_{\text{B}} \cdot 10^{3}$ -	$C_{\text{C}} \cdot 10^{2}$ mbar$^{-0.5}$	$C_{\text{D}} \cdot 10^{1}$ mbar^{-1}	$C_{\text{D}} \cdot 10^{-1}$ mbar$^{-1.5}$
12.5	3.760 724	−3.279 373	2.549 724	−1.724 653	2.762 988
30	4.381 178	−2.424 191	1.011 681	−1.344 474	2.157 243
37.5	4.626 943	−4.069 011	2.353 767	−1.986 69	3.266 313

5.5.2 Deposited mass flow rate

The deposited mass flow rate occurring during an experiment $\dot{M}_{\text{Dep,Exp}}$ is calculated by the time derivative of the ideal gas law

$$\dot{M}_{\text{Dep,Exp}} = \dot{M}_{\text{In,Exp}} - \frac{\frac{\mathrm{d}p_{\text{V}}}{\mathrm{d}t} \cdot (V_{\text{V}} - V_{\text{Cr}})}{T_{\text{V}} \cdot R_{\text{vent}}} \tag{5.2}$$

where p_{V} is the pressure and $T_{\text{V}} = T_{\text{amb}}$ the temperature of the venting fluid inside the vacuum vessel, V_{V} and V_{Cr} are the volumes of the vacuum and the cryogenic vessel, respectively and R_{vent} is the specific gas constant of the venting fluid.

5.5.3 Heat flux caused by the venting fluid

The experimentally derived heat flux caused by the venting fluid at $T_{\text{W,o}} \leq T_{\text{Vap,O}_2}$ is calculated by multiplying the experimentally derived deposited mass flow rate $\dot{M}_{\text{Dep,exp}}$ with the enthalpy difference of the venting fluid from ambient to the outer wall surface conditions according to Equation 4.29

$$(\dot{q}_{\text{V,Exp}})_{T_{\text{W,o}} \leq T_{\text{Vap,O}_2}} = \frac{\dot{M}_{\text{Dep,Exp}}}{A_{\text{Cr}}} \cdot \Delta h\,(T_{\text{amb}} \rightarrow T_{\text{W,o}}, p_{\text{V}}, \varphi) \tag{5.3}$$

5.5.4 Relieving mass flow rate

The helium relieving mass flow rate occurring during an experiment $\dot{M}_{0,\text{Exp}}$ is measured with a venturi tube according to [26]

$$\dot{M}_{0,\text{Exp}} = \frac{C_{\text{Venturi}}}{1 - (\beta_{\text{Venturi}})^4} \cdot \epsilon_{\text{Venturi}} \cdot A_{\text{Venturi}} \cdot \sqrt{2 \cdot \Delta p_{\text{Venturi}} \cdot \rho_{\text{He}}\,(T_{\text{Venturi}}, p_{\text{Venturi}})} \tag{5.4}$$

where $C_{\text{Venturi}} = 1.00$ is the flow coefficient for classical Venturi tubes, $\beta_{\text{Venturi}} = {}^{d_{\text{Venturi}}}/_{D_{\text{Venturi}}}$ is the diameter ratio, $\Delta p_{\text{Venturi}}$ is the pressure difference at the Venturi, T_{Venturi} and p_{Venturi} are the temperature respectively pressure of the flow in the piping upstream of the venturi tube and $\epsilon_{\text{Venturi}}$ is the expansion coefficient that is a function of the isentropic exponent κ, $\Delta p_{\text{Venturi}}$, p_{Venturi} and β_{Venturi}.

5.5.5 Sensor-to-variable assignment

Table 5.3 summarizes the sensor-to-variable assignment needed for the evaluation of Equations 5.1 to 5.4.

Table 5.3: Assignment of sensors to variables for the evaluation of experiments.

Variable	Sensor	Variable	Sensor
T_{amb}	TI33(t)	$\Delta p_{\mathrm{Venturi}}$	PDI11(t)
p_{amb}	PI25(t_{end})	$T_{\mathrm{He,liq}}$	$\frac{\mathrm{TI13}(t)+\mathrm{TI14}(t)}{2}$
φ	MI31(t)	$T_{\mathrm{He,gas}}$	TI12(t)
$\Delta p_{\mathrm{Orifice}}$	PI24 (t) − PI25 (t)	p_{He}	PI12(t)
p_{V}	PI22(t)	$T_{0,x}$	TI19(t)
T_{Venturi}	TI11(t)	$p_{0,x}$	PI13(t)
p_{Venturi}	PI12(t)		

5.5.6 Data smoothing

For the experimental data evaluation, the measured data points are spline-interpolated using cubic splines. As discussed in [85], the measured data are subjected to noise due to high sampling rates, although the interpolation functions look fairly smooth. However, short term fluctuations result in large changes of slope in the interpolation functions and thus render the numerical derivation of e.g. the vacuum pressure increase impossible. Furthermore, short term fluctuation can cause instabilities in the numerical calculation of the wall temperature (cf. Section 5.6). Hence, the data received by the sensors PI22, PI12, TI11...TI14 as well as the derivation of PI22 are smoothed by the simple moving average method (SMA).

To perform the SMA, the arithmetic mean value of n subsequent data points of the original dataset $\{a_i\}_{i=1}^{N}$ are calculated to create a new smooth dataset $\{s_i\}_{i=1}^{N-n+1}$ following

$$\{s_i\}_{i=1} = \frac{1}{n} \sum_{j=1}^{i-n+1} a_j \tag{5.5}$$

where the so-called moving average factor n is defined as a function of the sampling rate to

$$n\,(t) = \begin{cases} \frac{\mathrm{rate}}{100} & 0 \leq t \leq t_1 \\ \frac{\mathrm{rate}}{10} & t_1 \leq t \leq t_2 \\ \mathrm{rate} & t_2 \leq t \leq t_{\mathrm{LIV}} \end{cases} \tag{5.6}$$

taking into account the fast changes in slope in the beginning of the venting experiments. The time steps $(t_1, t_2, t_{\mathrm{LIV}})$ have to be defined individually for each sensor and experiment. The smoothed dataset is spline-interpolated before the evaluation. Figure 5.6 visualizes

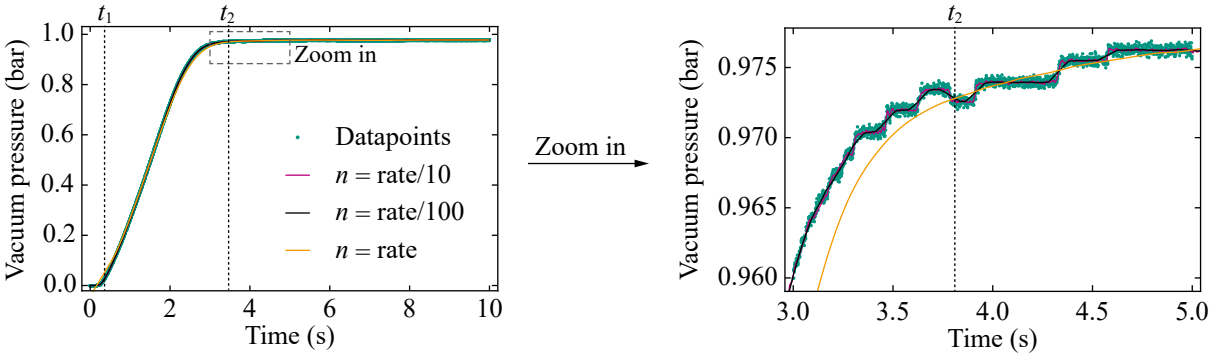

Figure 5.6: Result of the smoothing process according to Equation 5.5 and 5.6 at the example of the vacuum pressure increase measured in experiment E1.

the result of the smoothing process exemplary for the vacuum pressure increase measured in experiment E1. Further information on signal processing, the use of filters and the definition of sampling rates is given in [60].

5.6 Experimental constraints

An inconsistency was observed during the evaluation of experimentally obtained data. Following Equation 5.7, the outer wall temperature, which is measured with cast TVO sensors inserted into a copper block with aluminium radiation shield, and the corresponding heat flux transferred onto the outer surface of the cryogenic system, i.e. the deposited heat flux, are related by

$$\dot{q}_{\mathrm{W,o}} = \frac{\frac{dT_{\mathrm{W,o}}}{dt} \cdot c_{\mathrm{Cr}} \cdot M_{\mathrm{Cr}}}{A_{\mathrm{Cr}}} + \frac{\lambda_{\mathrm{Cr}}}{s_{\mathrm{Cr}}} \cdot (T_{\mathrm{W,o}} - T_{\mathrm{W,i}}) \tag{5.7}$$

where $T_{\mathrm{W,o}}$ and $T_{\mathrm{W,i}}$ are the wall temperature at the outer and the inner surface of the vessel, respectively, A_{Cr} is the outer surface and M_{Cr} the mass of the cryogenic vessel. c_{Cr} denotes the specific heat capacity and λ_{Cr} the thermal conductivity of the vessel material both at the mean wall temperature $T_{\mathrm{W}} = 1/2 \cdot (T_{\mathrm{W,o}} + T_{\mathrm{W,i}})$.

However, Figure 5.7 shows a discrepancy between the deposited heat flux according to Equation 5.3 and the heat flux that is required to match the measured wall temperature according to Equation 5.7. Specifically, the heat flux considering the measured outer wall temperature increase shows a differently shaped profile compared to the deposited heat flux. Additionally, the energy that is required by the black profile in the first 20 s is 30 % higher compared to the energy that is transferred to the wall by the red profile due to deposition. This suggests that the evaluation of direct wall temperature measurements in the set-up yields thermodynamically inconsistent results due to the sensor response time, sensor size and insufficient thermal contact and shielding, respectively. In the course of this work, the experimental data is evaluated applying the one-dimensional heat transfer model for the calculation of the outer wall temperature according to Section 4.4. The

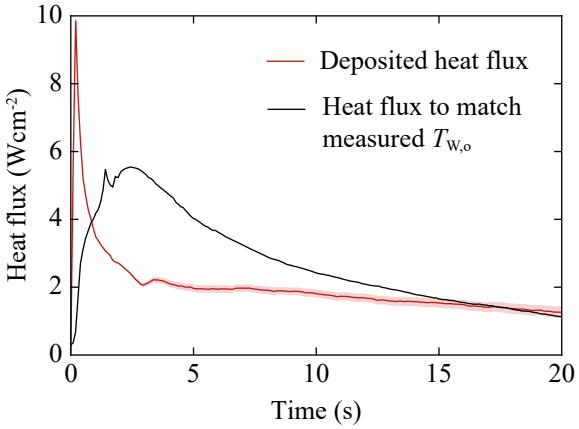

Figure 5.7: Deposited heat flux according to Equation 5.3 (red) and the heat flux required to match the measured wall temperature profile according to Equation 5.7 (black).

measured data of vacuum pressure and temperature, helium temperature and pressure, humidity and liquid level are used as initial and boundary values. In the next section, the calculation of the inner and outer wall temperatures based on the experiments is described.

5.7 Experimental model adaptations

In this section, the evaluation of the one-dimensional heat transfer model through the cryogenic vessel wall based on experimental data is introduced. Furthermore, an alternative approach for modelling the venting mass flow rate is presented to improve the comparability between model and experiment.

5.7.1 Heat transfer model evaluation based on experimental data

As described in Section 5.6, both the inner and outer wall temperature profiles occurring during experiments have to be evaluated with the heat transfer model introduced in Section 4.4 due to inconsistencies in the wall temperature measurement. Equations 4.26 and 4.27 have to be solved simultaneously taking into account the sensor-to-variable assignment according to Table 5.3 and the experimentally derived heat flux due to the venting fluid according to Equation 5.3.

In addition to the inconsistent wall temperature measurement, Figure 5.8 shows that the measured helium temperatures are subject to stratifications over the height of the cryostat. Thus, the equilibrium assumption for the helium bulk temperature made in the model cannot be transferred to the evaluation of measured data. Accordingly, the helium bulk temperature T_{He} in Equation 4.33 - calculation of the heat flux transferred to helium - is separated into a temperature for the liquid phase $T_{\mathrm{He,liq}}$ and a temperature for the gaseous phase $T_{\mathrm{He,gas}}$ at sub-critical pressure and as long as a liquid level exits. For

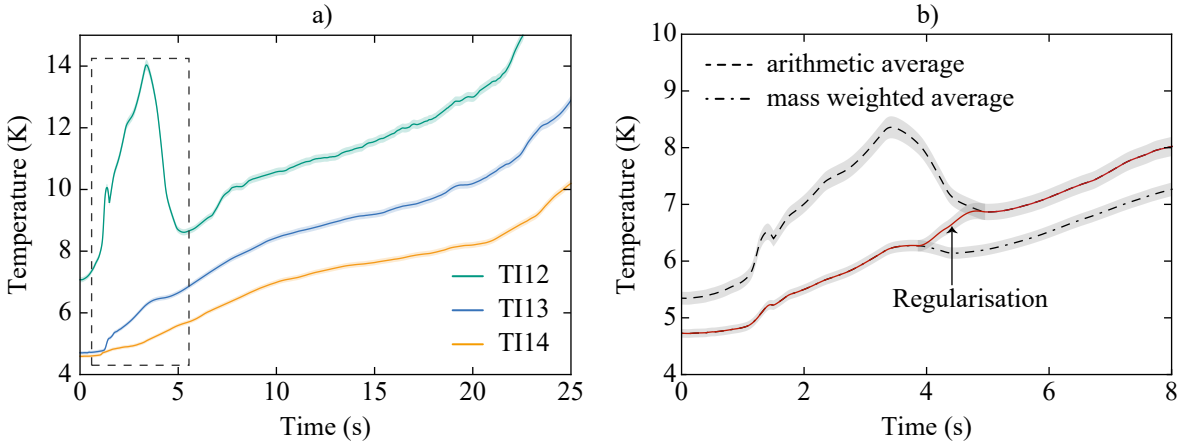

Figure 5.8: a) Helium temperature increase over time inside the helium over the vessel hight for the first 25 s after the start of the venting process exemplary during experiment E1. b) Mass weighted average and arithmetic average helium temperature profiles for the first 8 s after the start of the venting process combined to an average helium temperature for supercritical heat flux calculation via regularisation exemplary during experiment E1.

the experimentally analysed liquid levels $a_0 \geq 55\,\%$, the temperature sensors TI13 and TI14 are covered with liquid while TI12 is in the gaseous phase. Thus, the liquid helium temperature $\bar{T}_{\mathrm{He,liq}}$ is calculated as the arithmetic average of TI13 and TI14

$$\bar{T}_{\mathrm{He,liq}} = \frac{(\mathrm{TI13} + \mathrm{TI14})}{2} \tag{5.8}$$

and the temperature of the gaseous phase is set to

$$\bar{T}_{\mathrm{He,gas}} = \mathrm{TI12}. \tag{5.9}$$

At supercritical pressure and before the opening of the PRV, the helium temperature is calculated as the mass-weighted average of the initial sub-critical liquid and gaseous phases

$$\bar{T}_{\mathrm{He,mass}} = \frac{M_{\mathrm{gas},0}}{M_{\mathrm{total},0}} \cdot T_{\mathrm{He,gas}} + \frac{M_{\mathrm{liq},0}}{M_{\mathrm{total},0}} \cdot \bar{T}_{\mathrm{He,liq}}. \tag{5.10}$$

After the superheated former gaseous phase in the upper part of the vessel is released, the temperature distribution converges and the helium temperature is calculated as the arithmetic average value of the three temperature sensors over height TI12, TI13 and TI14

$$\bar{T}_{\mathrm{He,hight}} = \frac{(\ \mathrm{TI12} + \mathrm{TI13} + \mathrm{TI14}\ )}{3}. \tag{5.11}$$

The gap between the mass weighted average and the arithmetic average temperature profiles is closed via regularisation functions as shown in Figure 5.8b. The regularisation method is explained in Subsection 4.7.3. This approach ensures a continuous increase of the overall helium temperature, which is required in the context of Equation 4.33. Since the heat and mass transfer between the liquid and gaseous helium phase is neglected in the current model, a negative slope would result in a non-physical reversal of the direction of the overall heat flux.

5.7.2 Alternative modelling of the venting mass flow rate

For reasonable comparison of the model with experimental data obtained at PICARD in Chapter 6, other than introduced in Subsection 4.3.3, the venting mass flow rate $\dot{M}_{\mathrm{In}}$ is modelled as a flow through standard orifice measurement sections according to DIN EN ISO 5167-2:2003 [26]

$$\dot{M}_{\mathrm{In}}\left(p_{\mathrm{V}}\right) = \frac{C_{\mathrm{Orifice}}}{1-\left(\beta_{\mathrm{Orifice}}\right)^4} \cdot \epsilon_{\mathrm{Orifice}} \cdot A_{\mathrm{Orifice}} \cdot \sqrt{\left(p_{\mathrm{amb}} - p_{\mathrm{V}}\right) \cdot \rho_{\mathrm{V}}} \tag{5.12}$$

where A_{Orifice} is the free cross-section of the orifice, β_{Orifice} is the ratio between the orifice diameter d_{Orifice} and the pipe diameter D_{Orifice}, $\epsilon_{\mathrm{Orifice}}$ is an empirical expansion value depending on β_{Orifice} and κ_{vent}, which is the isentropic expansion coefficient of the venting fluid. C_{Orifice} is an empirical flow coefficient according to [61] dependent on the Reynolds-number Re_{D} related to the pipe diameter and β_{Orifice}

$$\begin{aligned} C_{\mathrm{Orifice}} =& 0.5961 + 0.0261 \cdot \beta_{\mathrm{Orifice}}^2 - 0.216 \cdot \beta_{\mathrm{Orifice}}^8 + 0.000521 \cdot \left(\frac{\beta_{\mathrm{Orifice}}}{Re_{\mathrm{D}}}\right)^{0.7} \\ &+ \left(0.0188 + 0.0063 \cdot \left(\frac{1900 \cdot \beta_{\mathrm{Orifice}}}{Re_{\mathrm{D}}}\right)^{0.8}\right) \cdot \beta_{\mathrm{Orifice}}^{3.5} \cdot \left(\frac{10^6}{Re_{\mathrm{D}}}\right)^{0.3} \\ &+ \left(0.043 + 0.080 \cdot e^{-10 \cdot L_1} - 0.123 \cdot e^{-7 \cdot L_1}\right) \\ &\cdot \left(1 - 0.11 \cdot \left(\frac{1900 \cdot \beta_{\mathrm{Orifice}}}{Re_{\mathrm{D}}}\right)^{0.8}\right) \cdot \frac{\beta_{\mathrm{Orifice}}^4}{1-\beta_{\mathrm{Orifice}}^4} \\ &- 0.031 \cdot \frac{2 \cdot L_2'}{1-\beta_{\mathrm{Orifice}}} - 0.8 \cdot \left(\frac{2 \cdot L_2'}{1-\beta_{\mathrm{Orifice}}}\right)^{1.1} \cdot \beta_{\mathrm{Orifice}}^{1.3} \end{aligned} \tag{5.13}$$

where $L_1 = 1$ and $L_2' = 0.47$ are geometry factors for the present design of pressure transmission. The pipe diameter D_{Orifice} has to be inserted in mm. The expansion coefficient $\epsilon_{\mathrm{Orifice}}$ is calculated as

$$\epsilon = 1 - \left(0.351 + 0.256 \cdot \beta_{\mathrm{Orifice}}^4 + 0.93 \cdot \beta_{\mathrm{Orifice}}^8\right) \cdot \left(1 - \left(\frac{p_{\mathrm{V}}}{p_{\mathrm{amb}}}\right)^{1/\kappa_{\mathrm{vent}}}\right). \tag{5.14}$$

The presented formulas are valid for orifice measurement sections with $d_{\mathrm{Orifice}} \geq 12.5\,\mathrm{mm}$ and $0.1 \leq \beta_{\mathrm{Orifice}} \leq 0.75$, which is fulfilled by the measurement sections used at PICARD. Due to design constraints, however, the present measurement sections do not have standard configurations regarding inlet and outlet lengths. Thus, each orifice is individually calibrated by the manufacturer (cf. Sections 5.4 and 5.5).

To evaluate the presented modelling approach of the venting mass flow rate, Figure 5.9 compares the profile calculated with the calibration polynomial of the manufacturer to the one obtained by DIN EN ISO 5167-2:2003 and by the equation for ideal nozzles using a correction factor $K_{\mathrm{Orifice}} = 0.85$ according to [85]. An orifice diameter of $d_{\mathrm{Orifice}} = 37.5\,\mathrm{mm}$ is applied. Calculating the venting mass flow rate with Equations 5.12 to 5.14 improves

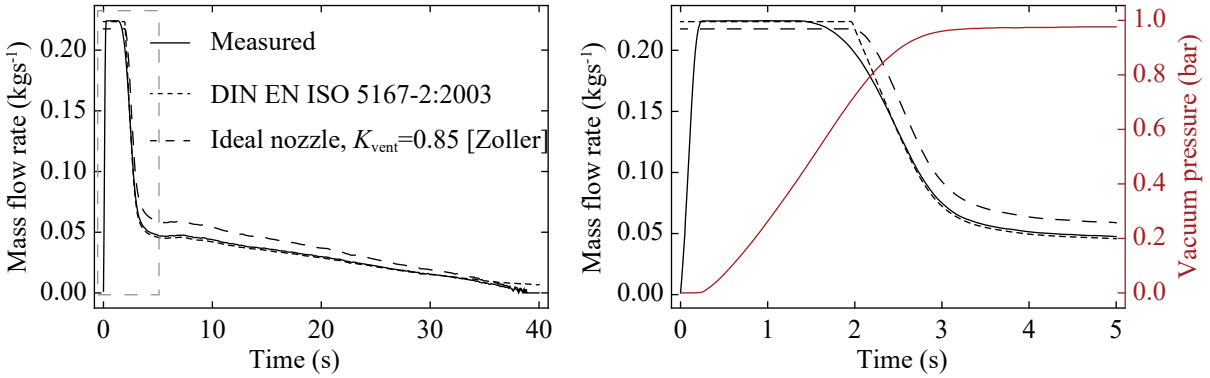

Figure 5.9: Venting mass flow rate profiles calculated with the calibration polynomial of the manufacturer (full line), with DIN EN ISO 5167-2:2003 (dotted line) and with the equation for ideal nozzle using a correction factor $K_{\mathrm{Orifice}} = 0.85$ according to [85] (dashed line) at the example of experiment E1 with $d_{\mathrm{Orifice}} = 37.5\,\mathrm{mm}$. *Left*: Profiles for the first 40 s after the start of the venting process. *Right*: Zoom into the first 5 s after the start of the venting process including the related vacuum pressure increase.

the accordance of the measured and modelled profiles compared to the calculation as an ideal nozzle according to [85], especially at sub-critical flow and venting times $t \geq 2.5\,\mathrm{s}$. In Figure 5.9, the relative error peaks with 11 % in the transition region between critical and sub-critical flow within 1.6 . . . 2.4 s. The influence of the different equations of the venting mass flow rate on the heat flux transferred to helium and thus on the PRV dimensioning is discussed in Section 6.4.

6 Experimental model validation

To ensure a general applicability of the LIV-model introduced in this work, a thorough validation against experimental results obtained at the PICARD-facility is documented in this chapter. In a first step, the model results are compared to experimental data at the example of a bare cryogenic vessel surface. This doubles as a discussion of the course of processes induced by LIV and the behaviour of all relevant values introduced in Chapter 4. In a second step, the model stability is tested for the range of initial liquid levels and humidities as defined in Subsection 4.2.1. In step three to five, the influence of the insulation, the leak size and the relieving pressure on the venting process with a focus on the safety relevant heat flux transferred to helium is discussed. These three parameters are defined as significant variables in this work. Finally, the influence of the PRV design is briefly addressed. Each section is concluded with a brief summary of the respective major outcomes.

A remark concerning graphical display As a large number of graphs is used in this chapter, each is displayed in a similar fashion to facilitate readability. Typically, the discussed value is plotted over a time window of $0 \ldots 20\,\mathrm{s}$, where $0\,\mathrm{s}$ represents the point in time where LIV is initiated. Beyond $10 \ldots 20\,\mathrm{s}$, depending on the process dynamics, the incident reaches steady state and values do not change significantly any more.

Uniform colouring is chosen in all graphs of this chapter that compare the model (red) to the experiment (black). Usually, the measurement uncertainties are depicted as error bars in grey. They are calculated according to the guide to the expression of uncertainty in measurement (GUM) [47] including Type B uncertainties with a coverage factor of $k = 2$. Type A uncertainties are not evaluated since the highly dynamic process disables a statistical repetition of measurements. As the first opening of the PRV marks the crucial point in the process that defines the values relevant for dimensioning, it is highlighted in yellow in graphs wherever relevant in this chapter. Since the results of model and experiment can deviate from each other, the first opening of the PRV is depicted as a time frame. Typically, the experiment shows the opening at an earlier time due to absence of equilibrium and temperature stratifications inside the helium. Both result in a faster pressure increase during experiments.

6.1 Results for a bare cryogenic vessel surface

In what follows, the experimental results obtained with a bare cryogenic surface (E1) are compared to the model. The initial values and boundary conditions of E1 are mirrored in the model to ensure comparability.

In experiment E1 the DN50 orifice measurement section with an orifice diameter of $d_{\mathrm{Orifice}} = 37.5\,\mathrm{mm}$ is used. PRV2 with a throat diameter of $d_{\mathrm{th}} = 22\,\mathrm{mm}$ is set to $3\,\mathrm{bar(g)}$ according to the initial audible discharge method. The lift is restricted to 4 mm corresponding to a discharge coefficient of $K_{\mathrm{dr}} = 0.55$ according to Figure 5.3b. The cryogenic vessel is filled with liquid helium up to 60 % and the humidity measured during E1 is $37.5 \pm 0.1\,\%$ at $300.1 \pm 0.2\,\mathrm{K}$ and $1.002 \pm 0.003\,\mathrm{bar}$.

6.1.1 Vacuum pressure increase

The pressure inside the vacuum vessel is expected to increase to ambient pressure after initiation of the venting process and to remain constant from that point onwards.

As can be seen in Figure 6.1a, ambient pressure is reached in the vacuum vessel over the course of 0.2 . . . 3.8 s. Thus, the pressure increases at a maximum rate of $0.48 \pm 0.03\,\mathrm{bar\,s^{-1}}$. The modelled profile and the maximum modelled vacuum pressure rise rate of $0.43\,\mathrm{bar\,s^{-1}}$ correspond to the results of the measurements.

Only within the first 0.25 s and 2 s prior to the first opening of the PRV, model and experiment show a slightly deviating profile. The model estimates a pressure increase right after the initiation of the venting followed by a short stagnation before the pressure increases to ambient. During experiment, the pressure starts to increase with a little delay at 0.25 s due to sensor response times and the venting section, which the air has to pass before entering the vacuum vessel. No further stagnation is observed in the further course. Within 2 . . . 3.7 s, the modelled profile increases slower than the measured vacuum pressure. In E1 ambient pressure is reached prior to the first opening of the PRV while the modelled profile rises for another half a second.

6.1.2 Venting mass flow rate

In principle, the behaviour of the venting mass flow rate can be divided into three consecutive steps. This can be seen in Figure 6.1b, where the profiles of the measured and modelled venting mass flow rate $\dot{M}_{\mathrm{In}}$ are compared.

In the first step right after the initiation of the venting process, the venting mass flow rates assume their critical value as the pressure ratio $p_{\mathrm{v}}/p_{\mathrm{amb}}$ is lower than the critical pressure ratio defined in Equation 2.21. The constant critical mass flow rate of $\dot{M}_{\mathrm{In}} = 0.224\,\mathrm{kg\,s^{-1}}$ is both measured and calculated. While the modelled profile starts directly at the critical rate, the measured mass flow rate increases from zero to the critical value within 0.2 s due

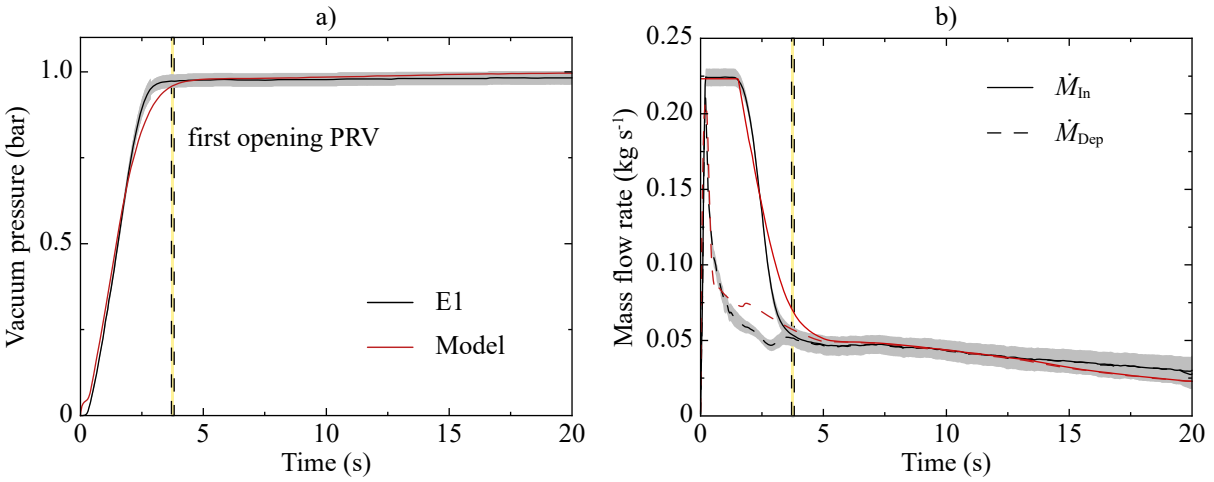

Figure 6.1: Modelled (red) and measured (black) a) vacuum pressure and b) venting (full line) and deposited (dashed line) mass flow rate for a bare cryogenic surface for the first 20 s after the start of the venting. The range of the first opening of the PRV is highlighted in yellow and the Type B measurement uncertainties according to GUM [47] are depicted in grey.

to sensor response times. Despite that, modelled and measured critical venting mass flow rate are congruent.

In the second step - beyond the critical pressure ratio - the venting mass flow rate is a function of p_v/p_{amb}, consequently it decreases with increasing vacuum pressure. In this sub-critical region, modelled and measured mass flow rates differ by a maximum of 30 %, which can be attributed to the non-ideal orifice measurement section used during experiments.

In the third step, ambient pressure is reached after 3.8 . . . 4.4 s and the remaining driving force of the venting mass flow rate is the deposition process. Thus, the venting mass flow rate equals the deposited mass flow rate as can be seen in Figure 6.1b.

In the safety relevant range of the first opening of the PRV, the modelled venting mass flow rate is 22 . . . 24 % higher than the measured one due to the explanations given above. Within 5 . . . 20 s after the start of the venting process, the modelled and measured venting mass flow rates overlap within the measurement uncertainty.

6.1.3 Deposited mass flow rate

The complex shape of the deposited mass flow rate $\dot{M}_{Dep}$, shown in Figure 6.1b, is a result of its dependency on the vacuum pressure and on the outer wall temperature as well as on α_C and on α_E (cf. [85] and Equations 4.18, 4.24 and 4.25).

The sharp peak at the beginning occurs due to the rapid increase of the vacuum pressure and the high sticking probability of molecules on the wall at temperatures $T_{W,o} < 20\,K$ ($\alpha_C = 1$). The measured peak value of $0.211 \pm 0.005\,kg\,s^{-1}$ is estimated by the model

with 1.4 % deviation within the measurement uncertainty. Since the outer wall temperature increases to temperatures $T_{\mathrm{W,o}} > 50\,\mathrm{K}$ within 0.5 s (cf. Figure 6.2b) α_{C} decreases and α_{E} increases exponentially, resulting in a decreasing deposited mass flow rate. In a short period of time within 3 . . . 3.5 s, $\dot{M}_{\mathrm{Dep}}$ increases again because the influence of the increasing vacuum pressure overshadows the influence of the coefficients. When ambient pressure is reached, the remaining driving force of the deposition process is the wall surface temperature. Since this value increases at a slow pace after 3.7 s, $\dot{M}_{\mathrm{Dep}}$ slowly declines in accordance with a decreasing α_{C} and an increasing α_{E}.

In the range of the first opening of the PRV, the model estimates the measured values of $0.052 \pm 0.005\,\mathrm{kg\,s^{-1}}$ with 9.6 % deviation, which is the maximum deviation within the measurement uncertainty. Higher deviations occur at outer wall surface temperatures in the range of 20 . . . 50 K where according to Section 4.3 α_{C} and α_{E} are fitted to the Clausius-Clapeyron-Equation due to lack of literature data. This time frame reflects also the region, where the modelled vacuum pressure increases less fast than the measured profile. However, this approach reflects well the general trend of the deposition process, which is confirmed within 3 . . . 10 s, where at wall temperatures above the triple point of oxygen and ambient vacuum pressure, the model estimates the measured deposited mass flow rate within the measurement uncertainty. Given the deviations in the vacuum pressure increase and the profile of the venting mass flow rate, the model slightly underestimates the deposited mass flow rate after 15 s.

6.1.4 Heat flux transferred to the outer surface

The total heat flux transferred to the outer surface of the cryogenic vessel shown in Figure 6.2a comprises the terms of the venting fluid and the thermal radiation.

As can be seen, the shape is similar to the one of the deposited mass flow rate depicted in Figure 6.1b, which indicates that the heat transfer via deposition overshadows other sources. Due to the almost constant outer wall surface temperature after 0.5 s the heat flux due to thermal radiation calculated according to the Stephan-Boltzmann Equation 4.32 assumes an almost constant value of $1.4 \cdot 10^{-3}\,\mathrm{W\,cm^{-2}}$. By this it can be confirmed that the deposition process is responsible for the complex shape of the heat flux transferred to the outer surface. Quantitatively, the total heat flux transferred onto the outer surface of the cryogenic vessel averages within the first 20 s of the experiment to 99.93 % deposition and 0.07 % thermal radiation. Since the outer wall temperature stays below $T_{\mathrm{W,o}} \leq T_{\mathrm{Vap,O_2}}$ convection does not occur in the first 20 s after initiation of LIV.

The peak heat flux value of $9.49 \pm 0.26\,\mathrm{W\,cm^{-2}}$ is calculated with 2.6 % deviation and the value in the range of the first opening $2.22 \pm 0.24 \ldots 2.23 \pm 0.23\,\mathrm{W\,cm^{-2}}$ with 6.8 . . . 7.6 % deviation. Except for the values in the transition region within 0.5 . . . 3.4 s, the modelled values are within the measurement uncertainty of the experiment.

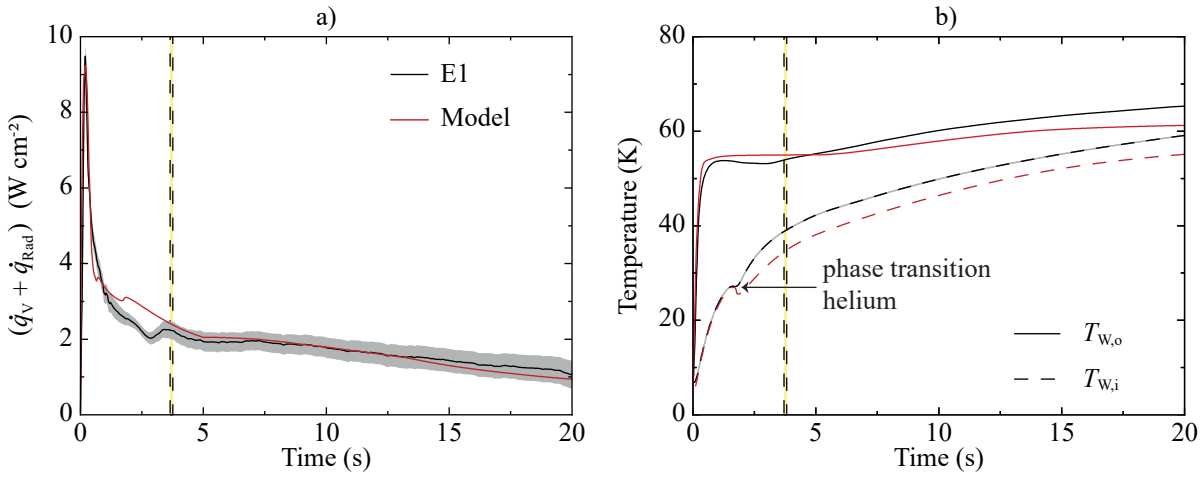

Figure 6.2: a) Modelled (red) and measured (black) heat flux transferred onto the outer surface of a bare cryogenic vessel. b) Modelled (red) and measured (black) inner and outer wall temperature increase, $T_{W,i}$ and $T_{W,o}$, for a bare cryogenic surface for the first 20 s after the start of the venting. The range of the first opening of the PRV is highlighted in yellow and the Type B measurement uncertainties according to GUM [47] are depicted in grey.

6.1.5 Inner and outer wall surface temperatures

Based on the in- and out-flowing heat fluxes (cf. Section 4.4), Figure 6.2 depicts the result of both the outer and the inner wall surface temperature profiles.

The outer wall temperature $T_{W,o}$ increases instantaneously after the initiation of the venting process to temperatures $T_{W,o} > 53.5\,K$ due to high initial heat fluxes onto the outer surface, low helium heat fluxes and a low heat capacity of stainless steel at cryogenic temperatures. It remains constant until the PRV opens and proceeds to rise slowly. Up to 5 s, the outer wall temperature profile of model and experiment are almost congruent. In the further course of time, the deviation between model and experiment increases because the model underestimates the deposited mass flow rate and therefore the transferred heat flux (cf. Figures 6.1b and 6.2a). At this time, however, the process has surpassed the safety relevant point, so that this deviation is acceptable.

The inner wall temperature $T_{W,i}$ starts to increase at a smaller slope directly after the start of the venting process due to the thermal resistance of the wall. The small jump at 1.8 s confirms that the heat transfer resistance to helium decreases in the vicinity of the critical point as will be explained below. After the first opening, the modelled and experimentally derived inner wall temperature profiles increase in parallel with a constant deviation. Based on a reduced heat flux transferred to helium, the inner wall temperature in E1 assumes higher values compared to the model.

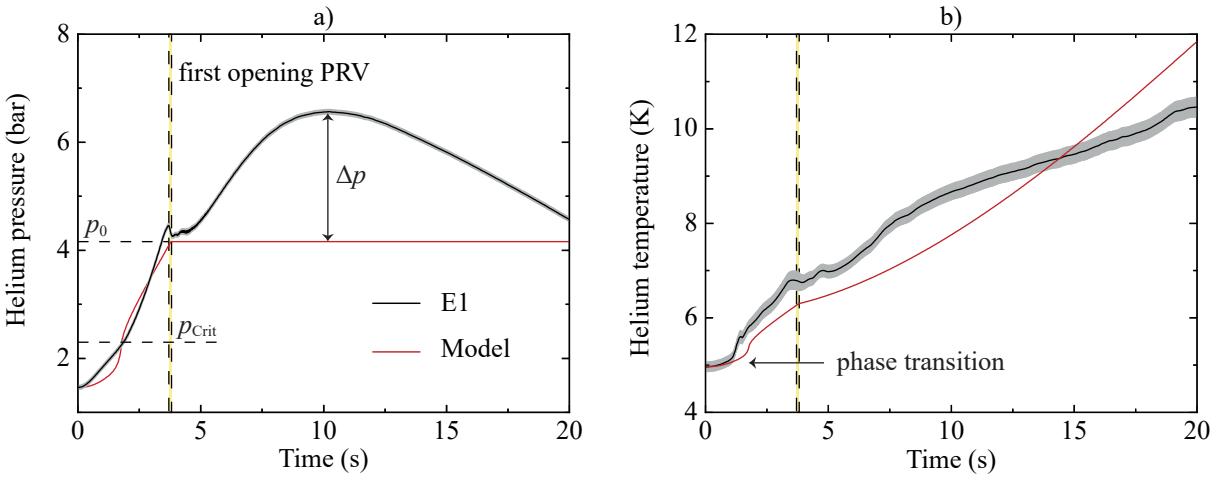

Figure 6.3: Modelled (red) and measured (black) a) helium pressure and b) helium temperature increase for a bare cryogenic surface for the first 20 s after the start of the venting. The range of the first opening of the PRV is highlighted in yellow and the Type B measurement uncertainties according to GUM [47] are depicted in grey.

6.1.6 Helium temperature and pressure increase

Due to the heat input to helium following LIV both helium pressure and temperature are supposed to increase during the venting process. Figures 6.3a and 6.3b depict the modelled and experimentally measured helium pressure and temperature increase, respectively.

While the model predicts the pressure increase up to the first opening of the PRV well, it can be seen that in the further course both the pressure and temperature profile of the model show substantial deviations from the experiment. This can be attributed to two reasons: First, contrary to the equilibrium assumption made in the model, during experiments neither are the gaseous and liquid helium phase at sub-critical pressure in equilibrium nor occurs a homogeneous temperature distribution (cf. Figure 5.8) inside the helium at supercritical pressure. Second, the PRV is undersized in experiment E1 resulting in a pressure increase of up to 77 % above p_{Set}. This higher pressure also results in higher temperatures as can be seen in Figure 6.3b.

However, the model reproduces the general trend well. Even if time-shifted, at the critical pressure and the first opening both measured and modelled pressure respectively temperature change their slope. The average helium pressure rise rate from the start of the venting to the first opening of the PRV ranges within $0.7 \ldots 0.8\,\mathrm{bar\,s^{-1}}$.

As a consequence of the overpressure, the model underestimated the measured helium temperature by a maximum of 11.8 % up to the maximum pressure of 6.27 ± 0.04 bar at 10.6 s. The delay in the relieving mass flow rate, which will be discussed below, leads to a lower measured than modelled helium temperature after 14.5 s.

6.1.7 Heat flux transferred to helium

The heat flux transferred to helium $\dot{q}_{\mathrm{He}}$ is the crucial parameter for the dimensioning of PRDs of helium cryostats. Therefore it is thoroughly discussed below. Figure 6.4a shows the heat flux transferred to helium of the model and derived from experimental data (cf. Section 4.4 and Subsection 5.7.1).

In the beginning, the heat flux transferred to helium increases slower than the heat flux transferred onto the outer surface (cf. Figure 6.2) since the heat transfer to helium is limited by film boiling and by the thermal resistance of the wall. However, with a Biot-number[1] in the range of $0.1 < Bi < 1$, the heat conduction in the wall is not negligible. For a short period of time in proximity to the peak at 1.7 s, the dominating heat transfer resistance changes, as the heat transfer coefficient α_{He} increases due to fluid property data in the vicinity of the critical point. Beyond that point in time, $\dot{q}_{\mathrm{He}}$ is at maximum 80 % lower than $\dot{q}_{\mathrm{V}}$ and the heat transfer resistance of helium is again higher than the thermal conduction resistance ($0.1 < Bi < 1$).

The measured peak value of $3.0 \pm 1.3\,\mathrm{W\,cm^{-2}}$ is estimated by the model to be twice as high due to property data. However, at this point the PRV is still closed and thus this value is not safety relevant.

Beyond the critical point of helium, the heat transfer coefficient and thus the heat flux drops due to the change in the heat transfer mechanism to free convection in supercritical helium. At this time, the deviation between model and experiment amounts to a maximum of 83.0 % due to temperature stratifications and an average helium temperature that is higher than the corresponding temperature in the case of equilibrium as assumed in the model. This effect is dominant in E1 since there is no further insulation besides the vacuum insulation. The higher heat input during cool-down leads to a higher evaporation rate, which disturbs the formation of the equilibrium significantly.

Reaching the relieving pressure, the modelled heat flux increases again to a maximum value of $1.40 \pm 0.07\,\mathrm{W\,cm^{-2}}$ since the relevant property data such as specific isobaric heat capacity, density, thermal conductivity and volume expansivity have a maximum at the present relieving pressure of 4.2 bar and at temperatures in the range of 5.5 . . . 6 K. In the further course, the modelled heat flux constantly decreases due to an increasing helium temperature and thus decreasing temperature difference to the inner wall temperature. Furthermore, the considered heat transfer coefficient declines with rising temperature.

Based on the resulting heat flux profile for a bare cryogenic surface, the statement made at the beginning of Chapter 6 that defines the point of the first PRV opening as safety relevant must be extended to include the peak value of $\dot{q}_{\mathrm{He}}$ value in the further course after the first opening of the PRV.

The experimentally derived heat flux profile increases over a wider time scale beyond the critical pressure. As a consequence of the inertia of the system, which is described in

[1] The Biot-number defines the ratio of the thermal conductive resistance to the thermal transfer resistance [12, p.134ff]. For $Bi < 0.1$ the thermal resistance of the wall can be neglected [12, p.202]

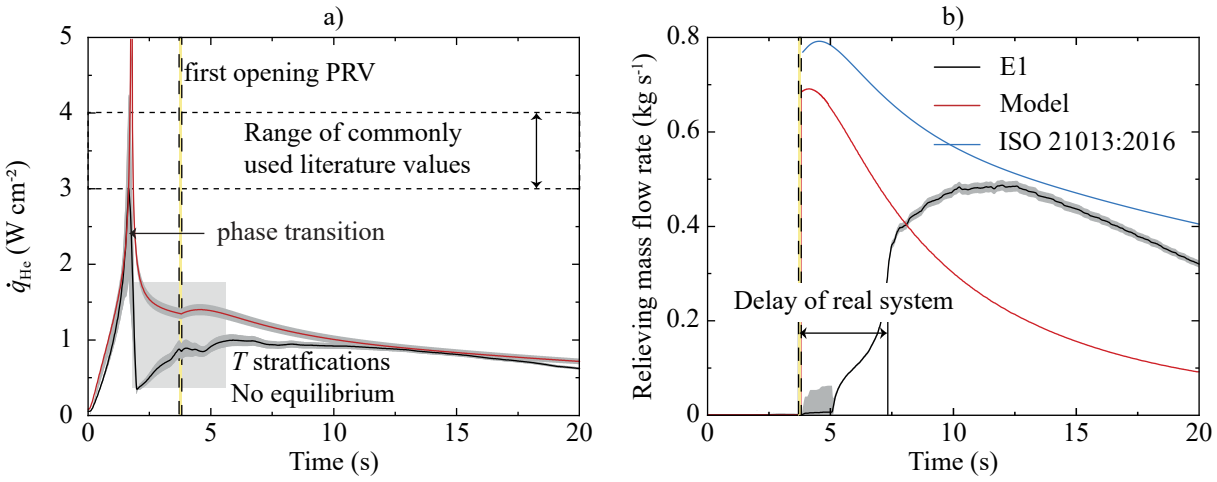

Figure 6.4: Modelled (red) and measured (black) a) heat flux transferred to helium and b) relieving mass flow rate and for a bare cryogenic surface for the first 20 s after the start of the venting. The range of the first opening of the PRV is highlighted in yellow and the Type B measurement uncertainties according to GUM [47] are depicted in grey.

the next subsection, and the resulting temperature and pressure profiles, the density in E1 changes slower and the heat transfer coefficient assumes lower values compared to the model calculation. Therefore, the safety relevant maximum value after the first opening of the PRV in E1 of $1.00 \pm 0.08\,\mathrm{W\,m^{-2}}$ is 28.6 % lower than the one predicted by the model. As time passes, modelled and experimentally derived heat flux profiles converge, especially due to the decreasing measured helium pressure.

In summary, the model does barely overestimate the safety relevant heat flux, therefore it can be concluded that the model provides a safe value for the dimensioning process.

Literature values that are commonly applied for the dimensioning of PRDs for helium cryostats are in the range of $3 \ldots 4\,\mathrm{W\,cm^{-2}}$ [17, 24, 52]. Comparing these literature values with the experimental data, the presented model produces more realistic heat flux profiles. The lower heat flux values result in a reduction of the required minimum discharge area by more than 50 % and in consequence cuts down the space needed for PRDs on helium cryostat and the possibility of instabilities during release.

6.1.8 Relieving mass flow rate

The mass flow rate released by a PRV, i.e. the relieving mass flow rate, should protect the cryostat against excessive pressure by compensating the heat input to the helium at constant relieving pressure.

Figure 6.4b depicts the modelled and measured relieving mass flow rates and compares both to the value estimated by established standards (cf. Equation 2.8). Both calculations (cf. blue and red line in Figure 6.4b) are based on the same value of heat flux

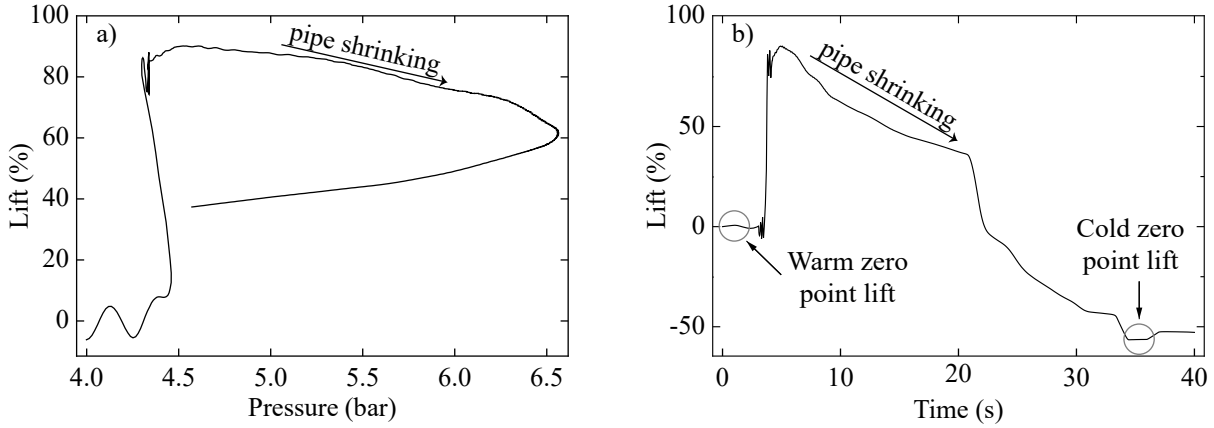

Figure 6.5: a) Lift as a function of pressure of PRV2 exemplary at E1. b) Lift of the PRV for the first 20 s after the start of the venting process.

transferred to helium obtained by the model, but barely deviate in their result. Although the overall profile of the modelled mass flow rate corresponds well to the result derived from *ISO21013:2016*, the modelled profile assumes at maximum 12 % lower values and decreases faster due to different relieving temperatures considered in the calculations. The model takes the further temperature increase after the first opening of the PRV into account, while the standardized procedure assumes a constant vessel temperature (cf. Equation 2.13).

The measured relieving mass flow rate, however, shows a completely different profile. The real system reacts in delay: Although the PRV opens already at 3.7 s, the mass flow rate peaks not before 12 s. The maximum value of $0.49 \pm 0.01\,\mathrm{kg\,s^{-1}}$ obtained in E1 is 29 . . . 38 % lower than the one required by both model and standardized calculation rules. The reduced measured relieving mass flow rate is one of the reasons for the 76 % overpressure in E1. In addition, the reduced relieving mass flow rate leads to a slower decrease in density and thus significantly influences the course of heat transfer to helium.

To further investigate the experimentally obtained mass flow rate profile, Figure 6.5a depicts the opening curve of the PRV during E1. In agreement with the characteristic opening curve of a PRV introduced in Section 5.2, the valve starts to open at relieving pressure. Contrary to the ideal profile, where the pressure stays constant, during the opening process in E1 the pressure slightly decreases during the opening process due to pressure drop in the pipe and the delay of the system. The further pressure increase at 90 % lift indicates an under-dimensioned PRV. In the further course, the lift decreases with increasing pressure due to a zero-point shift that is depicted in the time dependent profile of the lift in Figure 6.5b. The proximity sensor is installed outside of the moving system, thus, here the shrink of the upstream piping is measured. This zero-point shift is also responsible for not reaching 100 % lift.

Taking the behaviour of the valve into account, it can be concluded that the deviation between modelled and measured relieving mass flow rate occurs due to an under-sized PRV in combination with an inert reacting system and not due to model restrictions.

6.1.9 Temperature and pressure in upstream piping

As introduced in Chapter 3, both the temperature increase and the pressure drop in the piping upstream of the PRD have a significant influence on the relieving capacity, i.e. the mass flux, and thus on the required minimum discharge area of the PRD. In what follows, the results of a first approach to model the temperature increase and pressure drop inside the upstream piping according to Section 4.6 are discussed.

Figure 6.6a shows the modelled and measured temperature profile upstream of the PRV. Since the heat transfer in the upstream piping is highly dependent on the mass flow rate, the measured relieving mass flow rate is used in the model. Before the start of the venting, the piping is filled with a warm gas column at ambient temperature. When the PRV opens, cold helium from the cryogenic vessel displaces the warm gas and the temperature decreases rapidly. Given that the pipe lacks insulation to the environment and therefore represents a source of heat input, the minimum temperature measured at the entrance of the valve is 24.5 K. The model overestimates this influence and estimates a minimum temperature at the entrance of 45.9 K. The increase in temperature over the length of the pipe given at maximum mass flow rate amounts to 15.3 K. The presented approach already estimates the general trend of the temperature increase in the piping upstream of the PRV in good agreement. To improve the temperature calculation in the piping upstream of the PRV other heat transfer correlations can be tested and compared to further measurements in future work.

Figure 6.6b) depicts the modelled pressure drop over the length of the pipe at different points in time after the start of the venting, i.e. at different mass flow rates. The maximum pressure drop upstream of the PRV, which is less than 2.5 % of the set pressure, occurs at maximum mass flow rate. Established standards require a pressure drop less than 3 % of the set pressure to ensure a safe operation of the PRV, which is fulfilled in this experiment. Unfortunately, in experiment E1, no pressure transmitter is installed upstream of the PRV to compare the pressure drop calculations.

6.1.10 Required minimum discharge area

In the PRV dimensioning process of E1, the impact of the temperature increase in the upstream piping is not considered and the relieving temperature according to Equation 2.13 is applied, although the heat input into the upstream piping has already been identified as a crucial parameter in the dimensioning process. The purpose of this approach is to quantify the impact of this parameter experimentally and thereby set a comparison for the dimensioning of PRVs in subsequent experiment. Together with the relieving mass flow rate derived from *ISO 21013:2016*, the dimensioning of the PRV (cf. Chapter 3) yields exactly the throat diameter of PRV2, which is $d_{\mathrm{th}} = 22\,\mathrm{mm}$. The resulting time-dependent profile of the minimum throat diameter is depicted in Figure 6.7 (red dotted-dashed line).

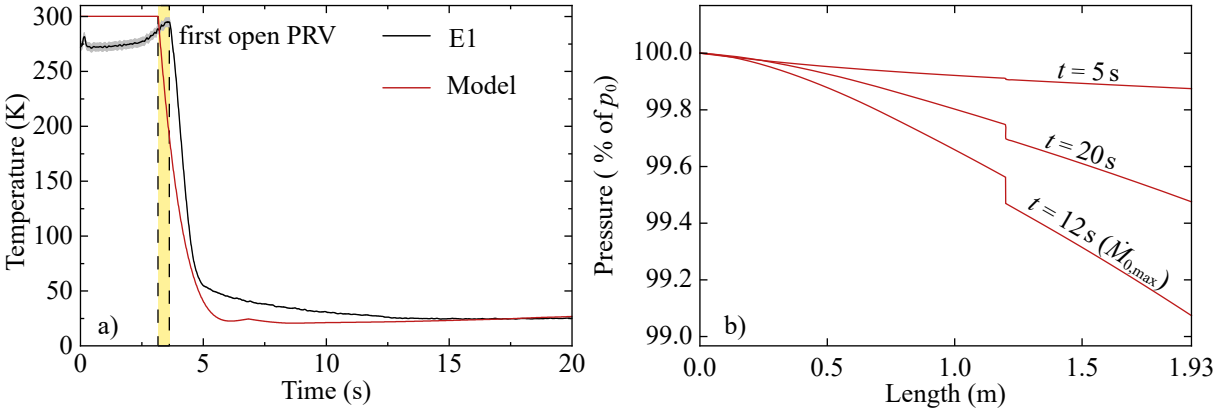

Figure 6.6: a) Measured and modelled temperature profile upstream of PRV for the first 20 s after the start of the venting process. For temperature modelling the measured relieving mass flow rate is applied. b) Modelled pressure drop over the length of the upstream piping at 5, 12 and 20 s based on the measured relieving mass flow rate. 12 s corresponds to the maximum mass flow rate.

Considering the temperature increase in the upstream piping would result in the red full line with a maximum required throat diameter of about $d_{\mathrm{th}} = 42\,\mathrm{mm}$. The higher diameter values before 6 s results from the lower density due to higher temperatures before the warm gas column is fully displaced, thus can be neglected to prevent over-sizing of the PRV. The black full line in Figure 6.7 represents the diameter required by the measured relieving mass flow rate and measured temperature upstream of the PRV (TI19). Confirming the pressure increase beyond the relieving pressure, after 7.4 s the used PRV2 with a throat diameter of $d_{\mathrm{th}} = 22\,\mathrm{mm}$ is too small to release the produced mass flow rate.

It can be concluded that the pressure increase beyond the relieving pressure in E1 could be avoided by taking the temperature increase inside the upstream piping into account.

6.1.11 Conclusions

In summary, the following conclusions can be drawn from this section:

- The model presented in Chapter 4 estimates the dynamic processes following LIV in a helium cryostat with a bare cryogenic vessel and the safety-relevant heat flux transferred to helium in very good agreement.
- The maximum heat flux to helium reaches more than 50 % lower values than commonly applied literature values.
- The investigated leak vs. cryogenic surface area ratio $A_{\mathrm{Orifice}}/A_{\mathrm{Cr}} = 8.84 \cdot 10^{-4}$ yields an instantaneous increase of the vacuum vessel pressure, thus the heat transfer is not limited by the leak size.

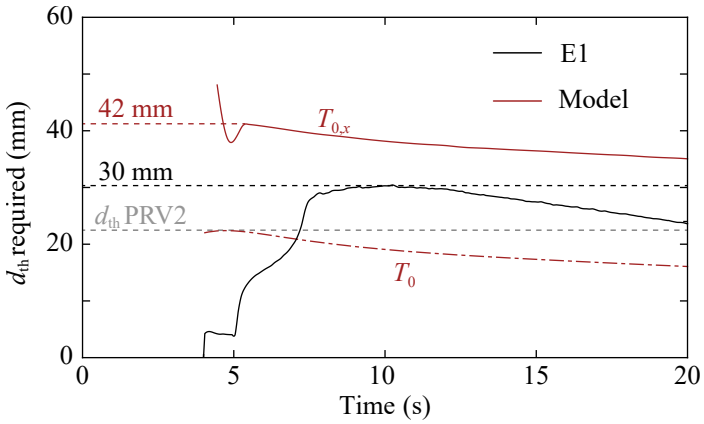

Figure 6.7: Time-dependent modelled (*red*) and based on experimental data (*black*) evaluated throat diameter of PRV according to the HEM (cf. Chapter 3) with considering the heat input in the upstream piping (full line) and based on the relieving temperature according to Equation 2.13 (dotted dashed line).

- The heat input in the upstream piping is a crucial parameter in the dimensioning process of PRVs.

Based on these results, the next sections discuss the influence of the following parameters on the venting process and in particular on the heat flux transferred to helium as the safety relevant value in the PRD-dimensioning process

- The influence of the initial liquid level and humidity,
- the influence of the insulation,
- the influence of the leak size and
- the influence of the relieving pressure.

6.2 Influence of initial values

In this section, the influence of the air humidity and the initial liquid helium level on the heat flux transferred on the outer surface and to helium are investigated by model calculations. Therefore, first, the initial liquid helium level is varied within 20 . . . 80 % at a set pressure of $p_{set} = 3\,\text{bar(g)}$ and at a humidity of $\varphi = 30\,\%$. In a second set, the air humidity is varied within 0 . . . 100 % at a set pressure of $p_{set} = 3\,\text{bar(g)}$ and at an initial liquid level of $a_{He} = 60\,\%$.

The resulting heat flux transferred to helium for 20, 40, 60 and 80 % initial liquid level respectively 40.4, 60.5, 80.6 and 100.6 kg m^{-3} initial density are compared in Figure 6.8a. The maximum heat flux transferred to helium after the first opening of the PRV varies within 0.8 . . . 1.7 W cm^{-2}. At sub-critical pressure, the heat flux increases with increasing liquid level since the wetted surface increases. This results in an increasing heat transfer coefficient due to film boiling. At supercritical pressure, a higher density respectively

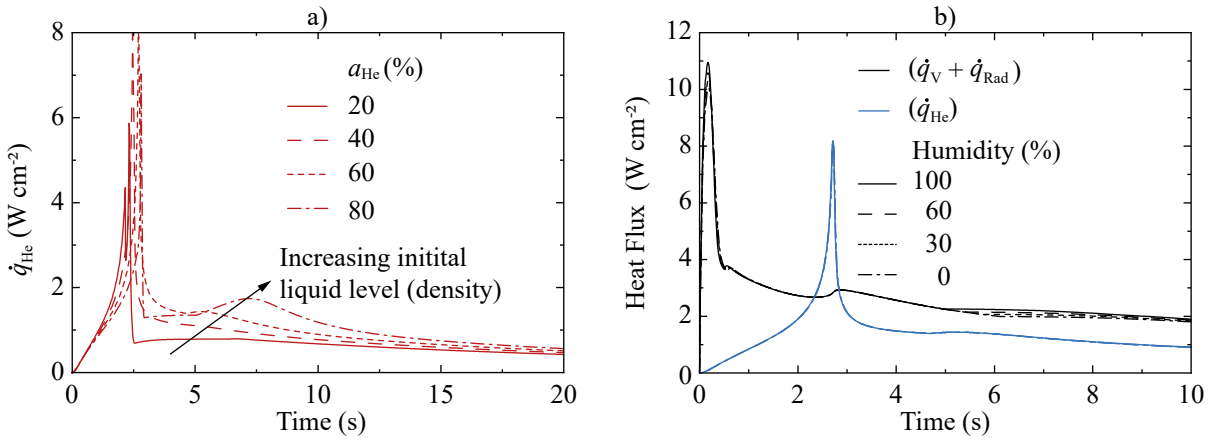

Figure 6.8: a) Modelled heat flux transferred to helium for 20, 40, 60 and 80 % initial liquid level for 20 s and b) modelled heat flux transferred to the outer surface and to helium for 0, 30, 60 and 100 % humidity for 10 s after the start of the venting, both at $p_{set} = 3$ bar(g).

initial liquid level also increases the heat transfer coefficient. The second peak, which grows in size with increasing density, occurs due to the influence of the property data in the vicinity of the critical point as explained in the former section.

In Figure 6.8b the resulting heat flux transferred to the outer surface of the cryogenic vessel and to helium for 0, 30, 60 and 100 % humidity are depicted. While the heat flux transferred to the outer surface increases by a maximum of 11 % with increasing humidity, the heat flux to helium is not as affected since the additional heat is buffered by the capacity of the wall only resulting in a marginally higher wall surface temperatures.

It can be concluded, that the initial liquid level of helium is another crucial parameter that has to be taken into account during the PRV dimensioning process. But, the humidity does not influence the safety relevant heat flux transferred to helium significantly. Furthermore, an important result of this section is that the model delivers stable results in the initial value ranges of humidity and initial liquid helium level introduced in Subsection 4.2.1.

6.3 Influence of insulation

As introduced in Section 5.1 and 5.3, helium cryostats are often equipped with thermal radiation shields and/or MLI in addition to the vacuum insulation in order to minimize the heat input to the system during normal operation. Due to space restriction at PICARD, the thermal radiation shield is never installed in conjunction with MLI.

In this section, first, the influence of the thermal radiation shield on the venting process following LIV is compared to the results of the bare surface and the model. Then the experimental results for different MLI configurations are compared to each other and to the results received with the radiation shield, including a reproducibility check. Thereafter,

the model is applied to an exemplary multi-layer insulated cryogenic surface and compared to the respective experimental data.

6.3.1 Influence of a thermal radiation shield

Below, the results of experiment E2 with the radiation shield are compared to the model and to the results of experiment E1 with the bare cryogenic surface. As mentioned in Section 5.1, the considered thermal radiation shield is only cooled by conduction to the helium filling line and therefore has an average temperature barely below 0 °C during the entire venting process. Its flow resistance during LIV is neglected in the model; i.e. the model assumes the same parameters as for LIV with a bare surface. In E2 the same venting orifice ($d_{\mathrm{Orifice}} = 37.5\,\mathrm{mm}$) and PRV with the same set pressure ($p_{\mathrm{Set}} = 3\,\mathrm{bar}$) as in E1 is used. The lift of PRV2 is not restricted in order to reduce the overpressure and thus the temperature stratifications during experiment. The initial liquid level and the humidity only differ by 1.5 % and 0.2 %, respectively. Especially the first value is identified as crucial for the heat flow transferred to helium in Section 6.2. To concentrate on the safety relevant values, the time frame of the plots is reduced to 10 s.

Venting mass flow rate and vacuum pressure

The resulting venting mass flow rates are depicted in Figure 6.9a. Compared to the experimental data for a bare cryogenic surface, the venting mass flow rate in E2 shows a little stagnation within 0.05 . . . 0.2 s. The ball valve, which is used to vent the insulation vacuum, could not be opened in one continuous movement because it was slightly blocked. Therefore, the venting cross section was not fully available immediately, causing the observed stagnation. The resulting time shift in the further course of the venting mass flow rate and consequently in the profiles of all other measured values is considered as an offset and not discussed for each profile separately.

The critical venting mass flow rate in E1 - predominantly dependent on the flow area - is reproduced in E2 with a deviation of only $0.003\,\mathrm{kg\,s^{-1}}$ due to little influences of the humidity and ambient temperature on the density of humid air. As the model calculations are based on the initial and boundary condition of E2 the modelled critical venting mass flow rate equals the one measured in E2. The value in the range of the first opening of the PRV within 4.1 . . . 4.7 s is estimated with a maximum deviation of 12 %, which is half of the deviation in E1. In E2 the PRV opens half a second later than in E1 due to a lower starting pressure. Based on this, the venting mass flow rate already reaches step 3 in its profile, where ambient pressure is reached and the deviation between model and experiment is within the measurement uncertainty.

This can be confirmed by the vacuum pressure increase shown in Figure 6.9b. The measured profiles during E1 and E2 are almost congruent and the model estimates the profile of E2 in very good agreement. At the first opening of the PRV, ambient pressure is already reached in both model and experiment.

Heat flux transferred to the outer surface and wall temperatures

The heat flux transferred to the outer surface of the cryogenic vessel shown in Figure 6.9c is affected by the installation of the thermal shield. The peak heat flux value in the beginning is reduced by 31.9 % to $6.46 \pm 0.26\,\mathrm{W\,cm^{-2}}$ compared to both the results of a bare cryogenic surface and the model. The local minimum occurring at the time where the vacuum pressure reaches ambient is more pronounced in E2 than in E1. Here, the deposition process depends only on the wall temperature, which assumes values in the proximity of the triple point of oxygen $T_{\mathrm{W,o}} \approx T_{\mathrm{trip},0_2}$. In the further course of E2 the heat flux amounts to 4.8 . . .32.1 % higher values compared to E1 due to lower outer surface temperatures (cf. Figure 6.9e). Apart from the differences in the time dependent profile, however, the integral value up to the first opening of the PRV of $11.4\,\mathrm{J\,cm^{-2}}$ in E1 is only 7.4 % higher in E2 since the PRV start to open 0.5 s later.

Passing the very fast transition region within the first 3 s, the model predicts the measured profile within the measurement uncertainty. At the first opening, the heat flux transferred to the outer surface amounts to $2.48 \pm 0.21\,\mathrm{W\,cm^{-2}}$.

It can be concluded, that certainly the thermal shield represents an additional flow resistance for the air to reach the cold surface explaining the peak reduction, the further time shift and the slightly different form of the heat flux profile within the first seconds. But it does not affect the integral amount of deposited air and thus the transferred energy.

In accordance with the agreement of modelled and experimentally derived heat flux transferred to helium and on the outer surface (cf. Figure 6.9 and 6.9c), both the inner and outer wall temperature profiles in Figure 6.9f show a slight overestimation by the model prior to the first opening of the PRV and a slight underestimation in the further course.

Helium pressure and temperature

Figure 6.9g depicts the helium pressure increase. In E2 the initial helium pressure is reduced from 1.46 bar to 1.19 bar compared to E1, since the radiation shield reduces the heat flux due to thermal radiation and thus the zero boil off rate during filling and operation by about 30 %. In the further course of time, the helium pressure in E2 increases in parallel to the profile of E1. As expected, the overpressure could be reduced by skipping the lift restriction, i.e. increasing the minimum discharge area. Comparing the results of E2 to the model, the general trend is again in good agreement although the model estimates a 11.4 % slower pressure increase up to the set pressure.

According to the reduced initial pressure, the initial helium temperature in E2 is also lower than in E1 (cf. Figure 6.9h). Additionally, the initial helium temperature of 4.54 K is only 0.14 K higher than the saturation temperature at initial pressure. Compared to a deviation of 6.2 % in E1, the system in E2 is closer to the equilibrium state, which is confirmed by the estimated model profile. Besides higher deviations around the critical point, where also the property data are affected by an increased uncertainty, the helium

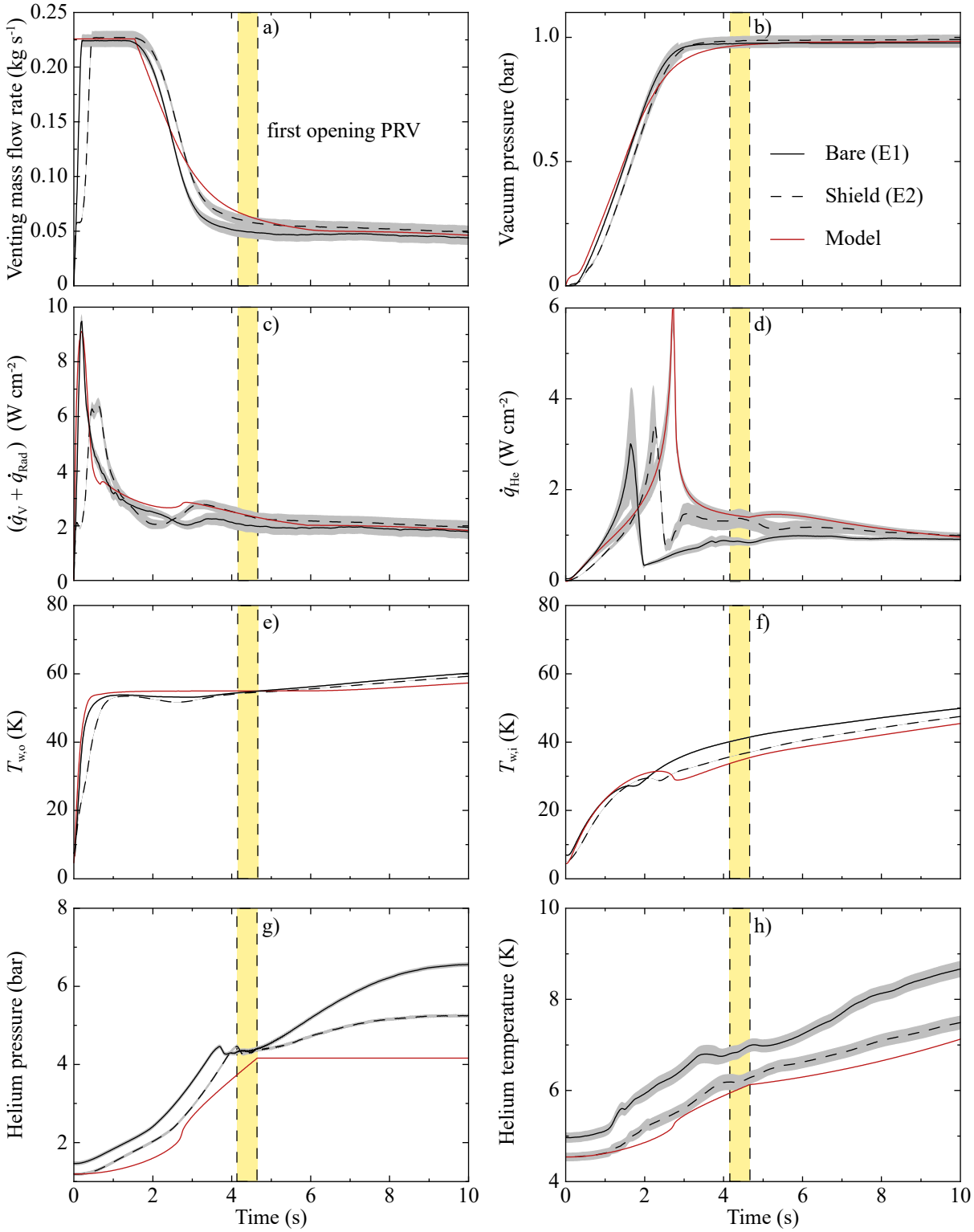

Figure 6.9: Modelled (red) and measured (black) a) venting mass flow rate, b) vacuum pressure increase, c) overall heat flux transferred to the cryogenic surface, d) heat flux transferred to helium, e) outer wall temperature increase f) inner wall temperature increase, g) helium pressure and h) helium temperature for a cryogenic surface insulated with a radiation shield during the first 10 s after the start of the venting process compared to the results for a bare cryogenic surface (full black). The first opening of the PRV is highlighted and the Type B measurement uncertainties according to GUM [47] are depicted in grey.

temperature profile measured in E2 is estimated by the model with less offset compared to the results of E1.

Heat flux transferred to helium

Together with the lower overpressure in E2, the reduced stratifications inside the helium result in a maximum heat flux transferred to helium of $1.38 \pm 0.15\,\mathrm{W\,cm^{-2}}$ after the first opening of the PRV. This represents a value about 27.5 % higher compared to the maximum value in E1 after the first opening of the PRV (cf. Figure 6.9d). Almost the same deviation occurs between the model and experimental results for the bare surface. Apart from again higher deviations around the critical point, the model overestimates the maximum heat flux transferred to helium after the first opening with a maximum deviation of 6.1 % to $1.47 \pm 0.08\,\mathrm{W\,cm^{-2}}$, which is within the measurement uncertainty. Thus, the safety relevant heat flux value transferred to helium is estimated in very good agreement and the model delivers a safe value for dimensioning.

6.3.2 Comparison of experimental data using MLI

In the course of this work 7 experiments are carried out in which the cryogenic surface is insulated with 3 different types of MLI and 4 different numbers of layers (cf. Table 5.1 and Section 5.3):

E8 MLI2 with 1 layer,

E9 & E10 MLI1 with 12 layers,

E11 & E12 MLI1 with 24 layers and

E13 & E14 MLI3 with 10 layers.

Some of the data presented here are already published by the author in [79]. The absolute values, however, may differ marginally due to an update of the heat transfer model in the course of this work.

In the following paragraphs, the influence of the four different MLI configurations in E8, E10, E12 and E14 on selected values of the venting process is discussed and compared to the results of E2 with the thermal shield.

Venting mass flow rate and vacuum pressure

Figure 6.10a shows the first 4 s of the vacuum pressure increase of all selected MLI experiments. It can be seen, that the vacuum pressure increases faster in all experiments conducted with MLI compared to E2 with the thermal shield. Considering the 1, 12 and 24 layers of MLI2 respectively MLI1 in E8, E10 and E12, the vacuum pressure rise rate is higher, the higher the number of layers. Notably, the profile of E14 with 10 layers of MLI3 is almost congruent to the one of E12 with 24 layers of MLI1.

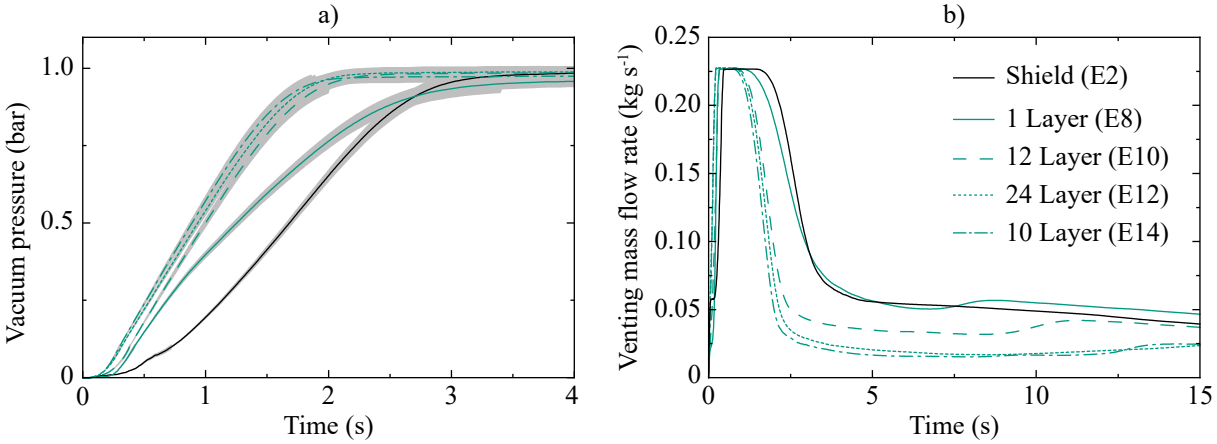

Figure 6.10: a) The first 4 s of the vacuum pressure increase during experiment E2 with the thermal shield (black) compared to experiment E8, E10, E12 and E14 using different MLI configurations (green). The measurement uncertainty according to GUM [47] is depicted in grey. b) Venting mass flow rate of experiment E2 with the thermal shield (black) compared to experiment E8, E10, E12 and E14 using different MLI configurations (green) for the first 15 s after the start of the venting process.

Accordingly, the venting mass flow rate, depicted in Figure 6.10b, decreases earlier with increasing layer number as p_v/p_{amb} increases faster above the critical pressure ratio. Again, 10 layers of MLI3 show the same impact as 24 layers of MLI1. In case of experiment E8 with 1 layer, the venting mass flow rate follows nearly the same trend as in E2 with the thermal shield. For the other configurations, the venting mass flow rate assumes lower values when ambient pressure is reached due to a lower deposited mass flow rate, which - at ambient pressure inside the vacuum vessel - is the only driving force of the venting mass flow rate. The influence of the MLI on the deposition process is explained below.

Heat flux transferred to the outer surface

In order to illustrate the influence of MLI on the deposition process, the overall heat flux transferred to the outer surface of the cryogenic vessel is shown in Figure 6.11a. Similar to the profile obtained with the thermal shield, the heat flux transferred to a multi-layer insulated surface exhibits a sharp peak within the first 0.3 s due to air molecules being able to penetrate the loosely wrapped MLI through the perforations and thus deposit on the cold surface. The peak value is reduced by 41 % with 1 layer and by 50.7 . . . 55.5 % for an increased number of layers, but without any defined trend. As the PRV is still closed at this point in time, however, this peak is not safety-relevant.

The zoom into the first 2 s of the heat flux transferred to the outer surface in Figure 6.11a shows that after 0.25 . . . 0.4 s, depending on the configuration, the heat flux drops sharply. At this point in time, the maximum venting mass flow rate is reached and the layers are compressed, building a diffusive barrier. For 1 layer, the heat flux drops to $0.40 \pm 0.27\,\mathrm{W\,cm^{-2}}$ consisting of 99.9 % deposition and 0.1 % thermal radiation. Followed

by a direct increase to a second peak of $3.82 \pm 0.19\,\mathrm{W\,cm^{-2}}$ reaching even higher values compared to the thermal shield. This is caused by lower wall temperature at this point in time. Beyond this peak, the heat flux profile is almost congruent to the one obtained during E2 with the thermal shield. In summary, applying 1 layer changes the shape of the heat flux on the outer surface but does not significantly reduce the energy that is integrally transferred to the outer surface.

In case of 12, 24 and 10 layers, between 0.4 . . . 0.7 s the air cannot reach the cold surface any more and thus the deposition stops. The remaining heat flux is almost zero and only caused by thermal radiation. The deposition process starts again after 0.7 . . . 1.4 s, when the venting mass flow rate decreases, resulting in a decompression of the layers. Experiment E10 with 12 layers of MLI1 shows a lower impact on the reduction of the deposition heat flux than experiment E14 with 10 layers of MLI3. The latter values correspond more to those of experiment E12 with 24 layers of MLI1. This is explained by the open perforation area, which in case of MLI1 is 2.3 times larger compared to MLI3.

Heat flux transferred to helium

Figure 6.11b shows the heat flux profiles to helium for all investigated MLI configurations during the first 15 s after the start of the venting process. Compared to Figure 6.12a, the differences in heat flux cause a wall temperature increase as a function of heat capacitance of the cryogenic vessel as already explained in previous sections. For the dimensioning of the PRV, only the heat flux values $\dot{q}_{\mathrm{He}}$ after the first opening of the PRV are relevant, thus this time is indicated with dots including their measurement uncertainty bars in Figure 6.11b.

The maximum heat flux of $1.38 \pm 0.15\,\mathrm{W\,cm^{-2}}$ after the first opening of the PRV in E2 is reduced by 10.9 % to $1.23 \pm 0.06\,\mathrm{W\,cm^{-2}}$ in experiment E8 conducted with the single layer. The difference results from the process dynamics, as the overall heat flux profiles are similar apart from the time shift within the first 3 s. The set pressure during E8 is higher than the one in E2; hence the PRV opens later and the heat flux has already decreased after the first opening of the PRV in E2.

The installation of 12 layers of MLI1 in E10 reduces the maximum heat flux at the first opening more significant by 24.6 % to $1.04 \pm 0.07\,\mathrm{W\,cm^{-2}}$. In contrast to E8, a reduction of the overall heat flux profile is observed. Doubling the number of layers in E12 further decreases the heat flux by 38 % to $0.64 \pm 0.13\,\mathrm{W\,cm^{-2}}$. A comparable result is obtain in experiment E14 with only 10 layers of MLI3. The value at first opening amounts to $0.51 \pm 0.09\,\mathrm{W\,cm^{-2}}$. Due to process dynamics and stratifications inside the helium, the heat flux in E12 and E14 increases at a stronger slope in the further course passing a maximum of $0.74 \pm 0.15\,\mathrm{W\,cm^{-2}}$ respectively $0.73 \pm 0.13\,\mathrm{W\,cm^{-2}}$, before they average to about $0.65\,\mathrm{W\,cm^{-2}}$. The main differences between MLI1 and MLI3 are the open perforation areas as well as the thickness of the reflective screens.

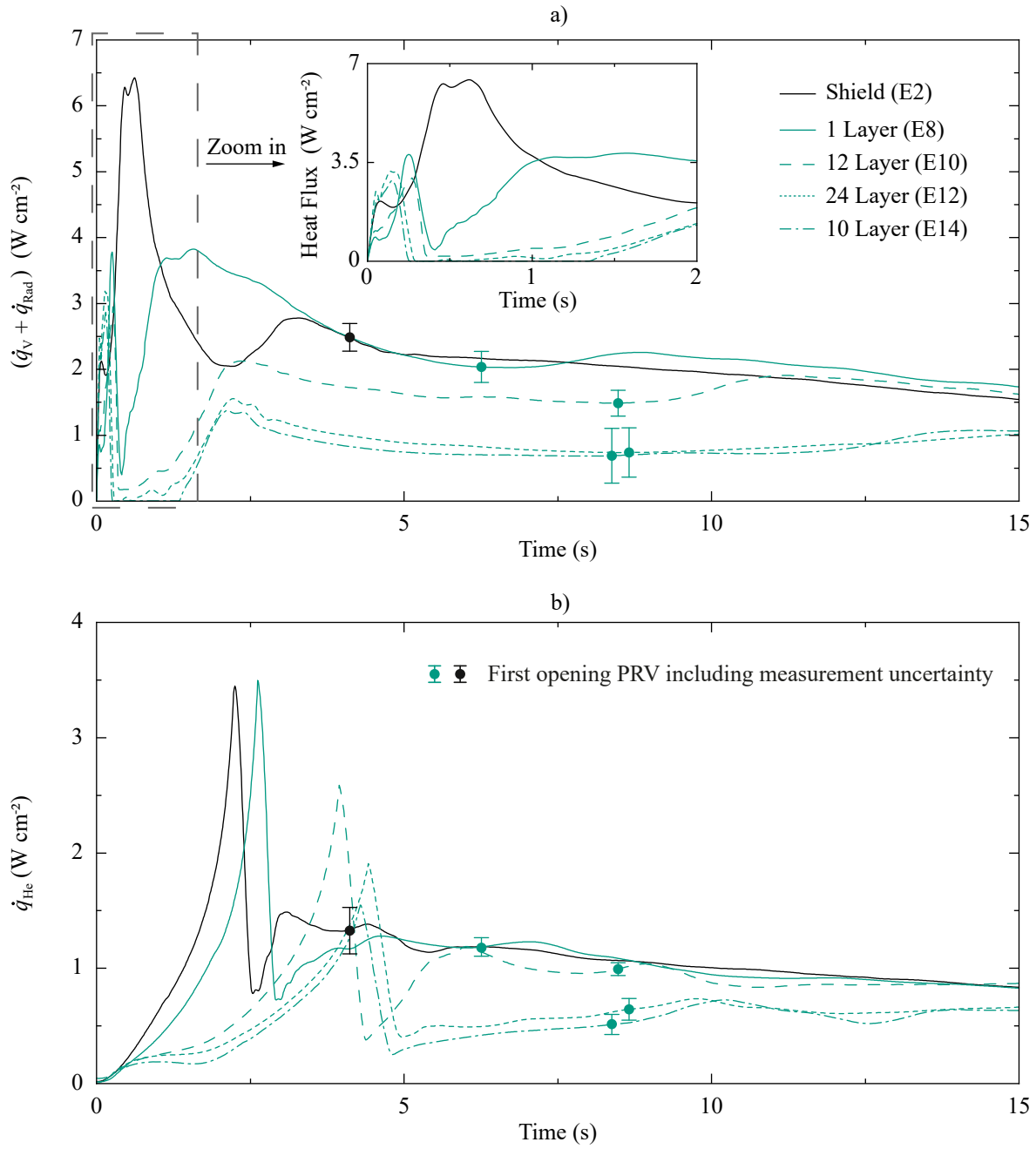

Figure 6.11: a) Heat flux transferred to the cryogenic surface, including a zoom into the first 2 s and b) heat flux transferred to helium for experiment E2 with a thermal shield (black) and experiment E8, E10, E12 and E14 using different MLI configurations (green) for the first 15 s after the start of the venting. The values relevant for dimensioning at the first opening of the PRV including their measurement uncertainty bars are highlighted with a dot.

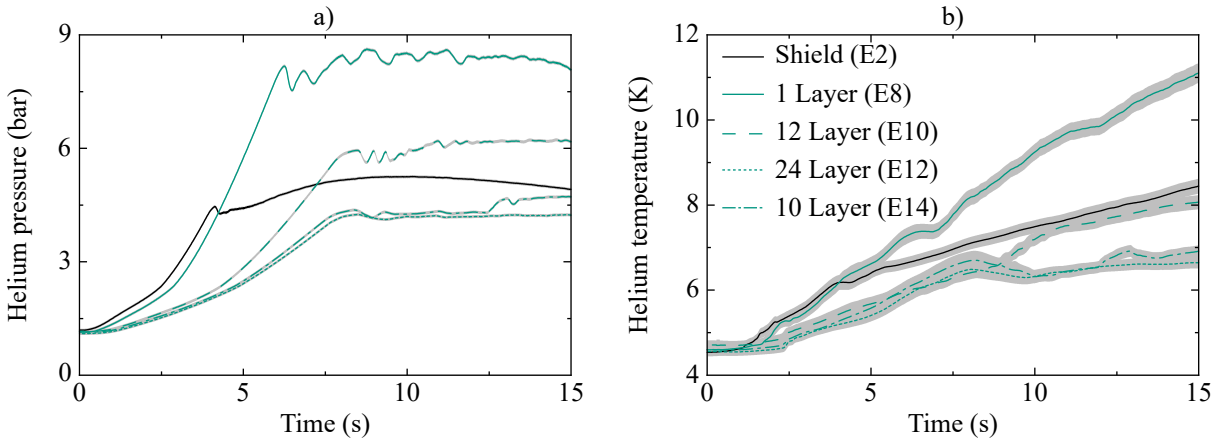

Figure 6.12: a) Helium pressure increase and b) helium temperature increase for experiment E2 with a thermal shield (black) and experiments E8, E10, E12 and E14 using different MLI configurations (green) for the first 15 s after the start of the venting process. The measurement uncertainty according to GUM [47] is depicted in grey.

Helium temperature and pressure

Given the similarity of the helium heat flux profiles of E2 and E8 Figure 6.11b, it can be assumed that the helium temperature and pressure most likely will follow the same trend as well. As can be seen in Figure 6.12, which compares the temperature and pressure increase over time of the various MLI experiments to E2, this hypothesis holds true for the first 4 s of the experiments until the PRV in E2 opens.

Due to the higher relieving pressure in E8, p_{He} and T_{He} increase further beyond this point in time. On the basis of the other experiments it can be concluded that an increasing number of layers and thus decreasing heat flux results in a reduction of the pressure and temperature rise rates. The temperature profiles of E2 and E10 assume the same value due to the random interplay of heat flux and relieving pressure.

6.3.3 Reproducibility

To confirm the validity of the experiments, the venting process is repeated for 12, 24 and 10 layers. Prior to each experiment, the MLI is installed new to ensure reproducible conditions and to exclude influences such as remaining humidity or destroyed layers after a previous venting process.

Figure 6.13 compares the heat flux profiles as well as the helium pressure and temperature increase of experiment E13 and E14 both with 10 layers of MLI3 for 40 s after the start of the venting process. Further experiments with different number of layers are conducted, but E13 and E14 are depicted here since both their input parameters overlap the most. In particular, the set pressure differs only by 1.4 bar, the liquid level by 0.4 % and the humidity by 3.4 %. A long time scale is chosen for these graphs to confirm the reproducibility by displaying the trend similarities maintained over a long period of time.

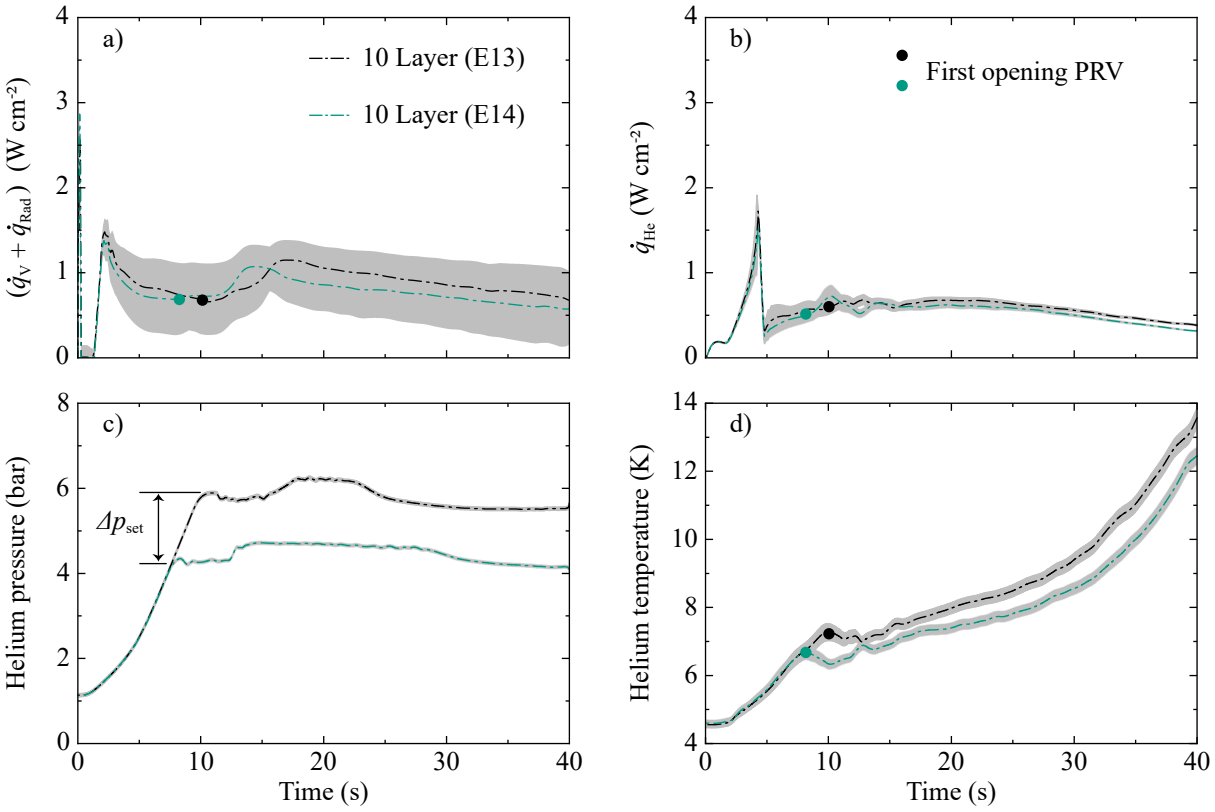

Figure 6.13: a) Heat flux transferred to the cryogenic surface, b) heat flux transferred to helium, c) helium pressure increase and d) helium temperature increase for experiment E13 (black) and E14 (green) with 10 layers of MLI3 for 40 s after the start of the venting process. The measurement uncertainty according to GUM [47] is depicted in grey and the first opening of the PRV is highlighted with a dot.

The heat flux transferred to the outer surface of the cryogenic vessel - depicted in Figure 6.13a - shows the same general profile in both experiments. The first drop down of the heat flux due to the compression of the MLI is reproduced very well. The second turning point is time shifted forward by a maximum of 3 s at the third peak. A possible reason is a varying packing density of the MLI, resulting in a less obstructed flow path of venting air in the vacuum vessel.

The quality of the packing density can be judged by the heat input under vacuum due to thermal radiation and conduction, referred to as static losses. Therefore, in preparation of the experiments the filling line is disconnected at the required initial liquid level and the change in liquid level is observed during a short duration of time. In E13 the static losses average to 2.1 W m^{-2} within a measuring period of 3.4 min and in E14 to 1.92 W m^{-2} within a measuring period of 6.1 min. The manufacturer specifies values in a range of $> 1.3 \ldots 1.5$ W m^{-2} from 300 ... 77 K for insulation vacua $< 10^{-3}$ Pa. In the presented experiments, the MLI is installed within 300 ... 4.2 K and the insulation vacuum is $> 10^{-4}$ Pa, thus the MLI packing quality can be evaluated as sufficient. The barely higher static losses in E13 may indicate a higher packing density resulting in a reduced insulation

capacity. For LIV this would result in less space for the air to pass the MLI, explaining the time shift in the heat flux profile.

The deviation between the heat flux transferred to the outer surface in E13 and E14, however, is within the range of measurement uncertainty, which is increased here due to low pressure differences at the orifice measurement section.

Figure 6.13b shows almost congruent profiles of the heat flux transferred to helium in E13 and E14. Up to the first opening of the PRV in E14, the deviation is within the measurement uncertainty. Some higher deviation in the further course can be explained by the temperature stratifications inside the helium and the higher relieving pressure in E13. The latter leads to a higher heat transfer coefficient.

Figure 6.13c and 6.13d show that both helium pressure and temperature in E13 and E14 increase with the same slope up to the relieving pressure of E14. As a lower set pressure is chosen for E14, the graphs diverge after the first opening of the PRV but continue to follow a similar trend nonetheless.

The highly comparable heat flux profiles as well as helium temperature and pressure curves proof the reproducibility of the venting experiments using MLI at PICARD. The comparison of E9 to E10 and E11 to E12, respectively, can be found in Appendix D.3.

6.3.4 Model adaptation for multi-layer insulated surfaces

The comparison of the experimental data obtained with MLI to those with a thermal shield or bare surface already indicates that the model with the same parameters of the deposition process as for the bare surface cannot adequately incorporate the processes occurring when MLI is used. Figure 6.14 visualizes that both the heat flux transferred to the outer surface of the cryogenic vessel and the one transferred to helium in E14 are highly overestimated. Neither the shape with the drop down of the deposited heat flux nor the absolute values at the first opening of the PRV can be predicted well. The modelling of the deposition process needs to be adjusted to allow for the estimation of the dynamic process following LIV with multi-layer insulated surfaces. The evaluation of the experimental data in the previous paragraphs show a strong dependence on not only the number of layers but especially on the type. Thus, the influence of MLI cannot be described analytically.

As introduced in [66], the additional flow restriction of the MLI can be described by the adaptation of the transmission coefficient α_T in Equation 4.18. Considering only the second increase in the heat flux transferred to the outer surface, varying α_T within $1 \cdot 10^{-4} \ldots 3 \cdot 10^{-4}$ shows promising results for the considered MLI configurations in [66]. However, the peak and the drop down in the beginning of the heat flux profile cannot be estimated in this way.

In order to improve the agreement between model and MLI experiments in the course of this work, α_T is adapted to the experimentally obtained deposited mass flow rate yielding

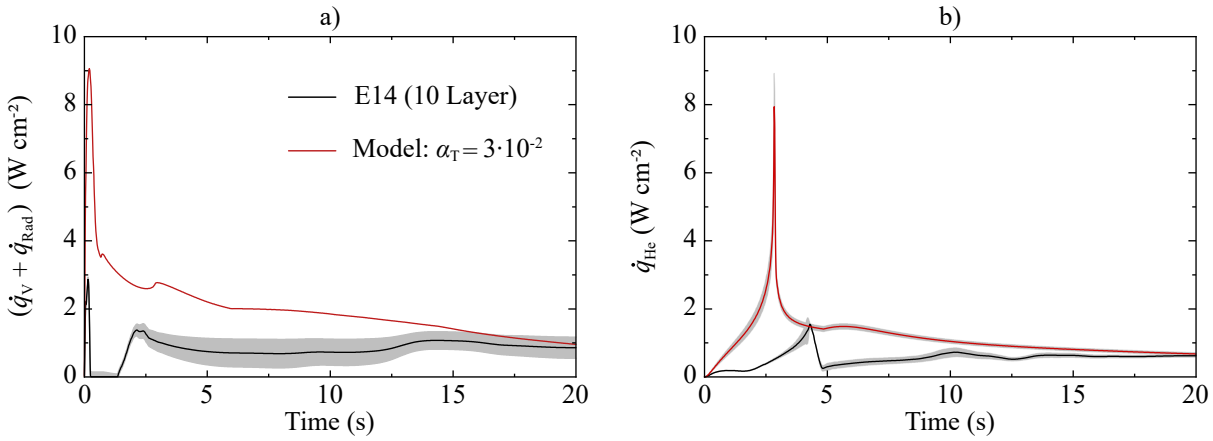

Figure 6.14: Modelled and measured a) heat flux transferred on the cryogenic surface, b) heat flux transferred to helium with 10 layers of Type 3 MLI for 20 s after the start of the venting process. The deposition process is modelled based on Subsection 4.3.4 for a bare surface. The measurement uncertainty according to GUM [47] is depicted in grey.

empirical functions for α_T dependent on the vacuum pressure for different layer numbers and MLI types. The respective equations are already introduced in Subsection 4.3.4.

At $p_v < 0.02$ bar the venting fluid is able to pass the loosely wrapped MLI unhindered, thus α_T of a bare surface is assumed. With increasing vacuum pressure the MLI is compressed and the air cannot reach the cryogenic vessel any more, resulting in an exponential drop of α_T to zero. Above a vacuum pressure of $p_v > 0.7 \ldots 0.8$ bar the MLI decompresses again, hence α_T logarithmically increases to $2.5 \cdot 10^{-4} \ldots 1.5 \cdot 10^{-4}$.

The experimental results show that although 1 layer influences the form of the deposited heat flux in the first seconds of the experiment, the transferred energy is not affected. Consequently, $\alpha_T = 3 \cdot 10^{-2}$ in that case.

In what follows, the adapted model is compared to the experimental results of E8 with 1 layer, E14 with 10 layers and E10 with 12 layers. The comparison to an experiment with 24 layers is shown in Appendix D.2.

Model results for 1 layer

Figure 6.15a depicts the modelled and experimentally derived heat flux transferred to the outer surface for 1 layer. As expected, the model overestimates the heat flux in the first second, followed by an underestimation within $1 \ldots 4$ s. Up to this point in time, the transferred energy differs only by 13 %. In the further course, the model estimates the measured profile with very good agreement. At the first opening of the PRV, the modelled heat flux transferred to the outer surface runs within the measurement uncertainty.

The modelled profile of the heat flux transferred to helium confirms the good agreement between model and experiment (cf. Figure 6.15b). The measured value at the first opening

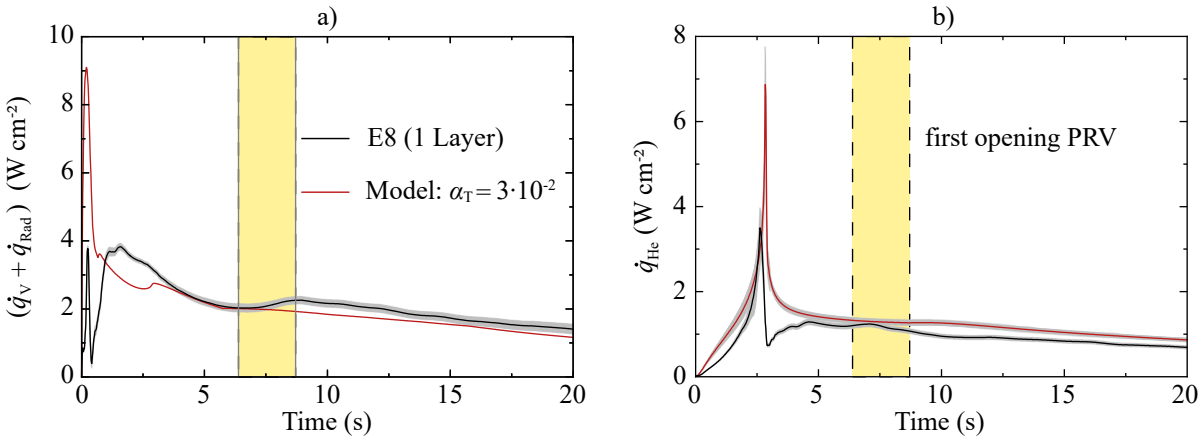

Figure 6.15: Unadapted modelled (red) and measured (black) a) heat flux transferred to the cryogenic surface, b) heat flux transferred to helium with 1 layer of MLI2 for 20 s after the start of the venting process. The first opening of the PRV is highlighted and the measurement uncertainty according to GUM [47] is depicted in grey.

of the PRV that amounts to $1.23 \pm 0.07\,\mathrm{W\,cm^{-2}}$ is predicted by the model with 2.4 % deviation, which is within the measurement uncertainty. This deviations is attributable to the deviation of the energy transferred to the outer surface at this time. The deviations in the further course of the experiment are marginal and can be explained by the overpressure that is measured during E8 leading to a slightly increased heat transfer coefficient.

Model results for 10 layers

In Figure 6.16, the experimental results of E14 for 10 layers of MLI3 are compared to the adapted model. In particular, Figure 6.16a shows that the vacuum pressure increase of the adapted model and the experiment are almost congruent. Likewise, the profile of the heat flux transferred to the outer surface of the cryogenic vessel - depicted in Figure 6.16b - is reproduced by the model within the measurement uncertainty. Solely, the first peak upon initiation of the venting is over-predicted by the model because α_T is possibly assumed to be too large.

The general trend of the heat flux transferred to helium, however, is well estimated by the updated model (cf. Figure 6.16c). The higher deviation between model and experiment beyond the critical pressure within 5 . . . 10.5 s can be explained again by the temperature stratifications and deviation to the equilibrium as depicted in the temperature profiles in Figure 6.16f. Additionally, the relieving mass flow rate (cf. Figure 6.16e) measured in E14 is again subject to a system inertia. Although the helium pressure profile in Figure 6.16d stagnates already after 8 s, the maximum relieving mass flow rate occurs not before 13 s after the start of the venting process. However, the maximum and therefore safety relevant heat flux value that occurs after the first opening of the PRV of $0.73 \pm 0.13\,\mathrm{W\,cm^{-2}}$ is estimated by the model within the uncertainty.

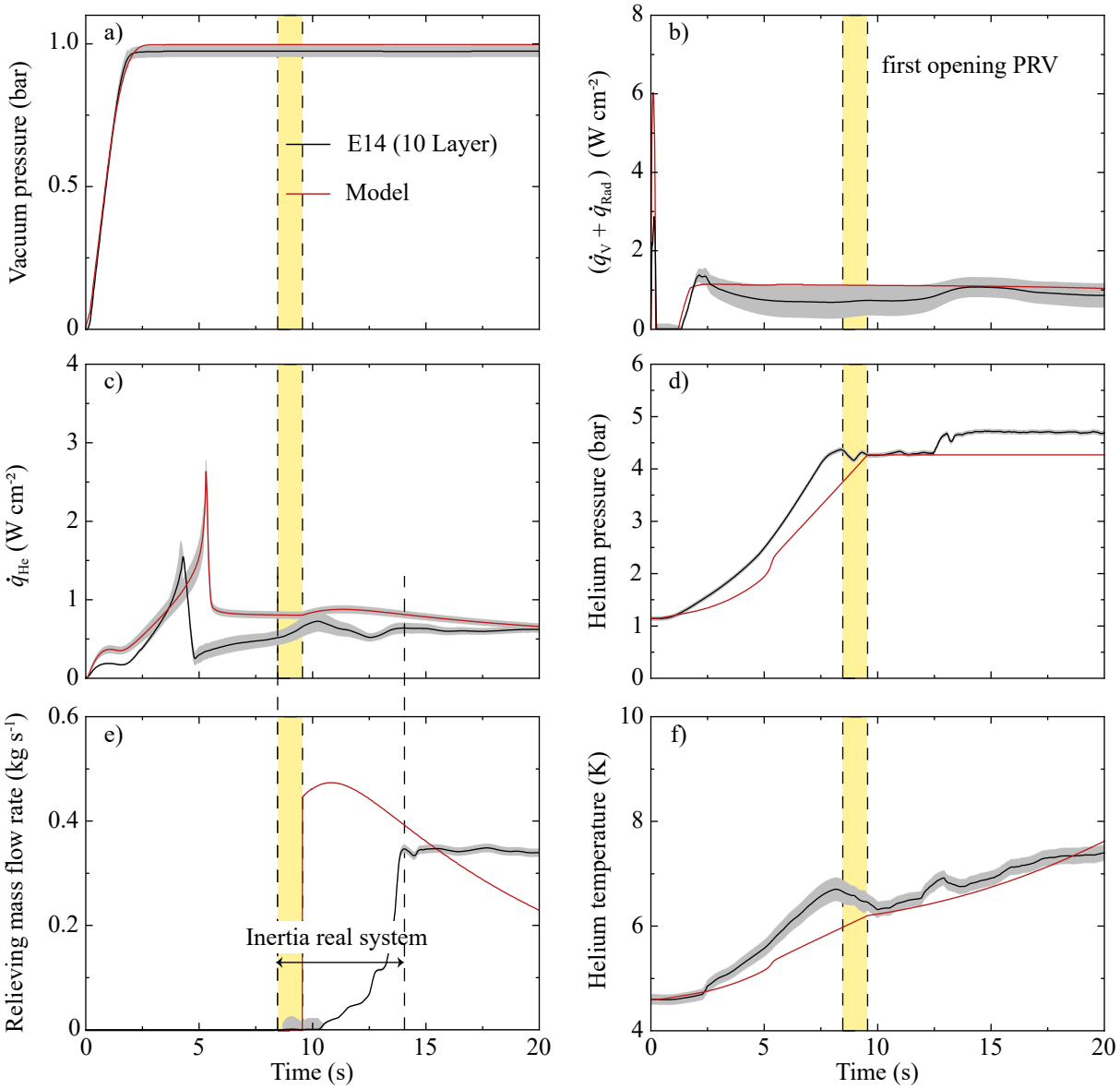

Figure 6.16: Adapted modelled (red) and measured (black) a) vacuum pressure increase, b) heat flux transferred on the cryogenic surface, c) heat flux transferred to helium, d) helium pressure increase, e) relieving mass flow rate and f) helium temperature increase with 10 layers of MLI3 for 20 s after the start of the venting process. The first opening of the PRV is highlighted and the measurement uncertainty according to GUM [47] is depicted in grey.

Model results for 12 layers

Figure 6.17a through 6.17f cover the comparison of the adapted model to the experiment E10 with 12 layers of MLI1 in the same fashion as E14 is covered in Figure 6.16 above. Both vacuum pressure increase and the heat flux transferred to the outer surface are well estimated by the model. Although the second peak in the profile of the heat flux transferred to the outer surface is underestimated, the value at the first opening of the PRV is predicted again within the measurement uncertainty.

Figure 6.17f shows that during experiment E10 the temperature stratifications are less developed. Additionally, based on the experience gained in previous experiments, the PRV is well dimensioned yielding an almost constant pressure during relieving (cf. Figure 6.17d). Figure 6.17e shows that the inertia of the system is reduced at the higher relieving pressure in E10 resulting in a comparable maximum modelled and measured relieving mass flow rate. In accordance, the heat flux transferred to helium of $1.04 \pm 0.07\,\mathrm{W\,cm^{-2}}$ is estimated by the model within the measurement uncertainty at the first opening of the PRV (cf. Figure 6.17c).

6.3.5 Conclusions

In summary, the following conclusions can be drawn from the experiments with different insulation:

- The deviation between the modelled and experimentally derived helium heat flux profiles for a bare surface occurs due to the strong temperature stratifications and the missing equilibrium state.
- The model presented in this work is applicable to helium cryostats containing both a not actively-cooled thermal shield and MLI.
- A not actively-cooled thermal shield and a single layer do not influence the heat flux transferred to helium during LIV significantly.
- The heat flux to helium is reduced by increasing the number of layers.
- The heat flux to helium depends on the type of MLI, influenced by the perforation area and the internal structure.
- The reduction of static losses due to insulation, reduces the temperature stratifications inside the helium and the deviation of the measured temperatures to the equilibrium state, which leads to an improved agreement between model and experiment.

In addition, the evaluation of several experiments confirm that an inertia of the system can delay the relieving mass flow rate. Since this effect is not considered in the model, higher deviations between predicted and measured behaviour occur, especially at low relieving pressures.

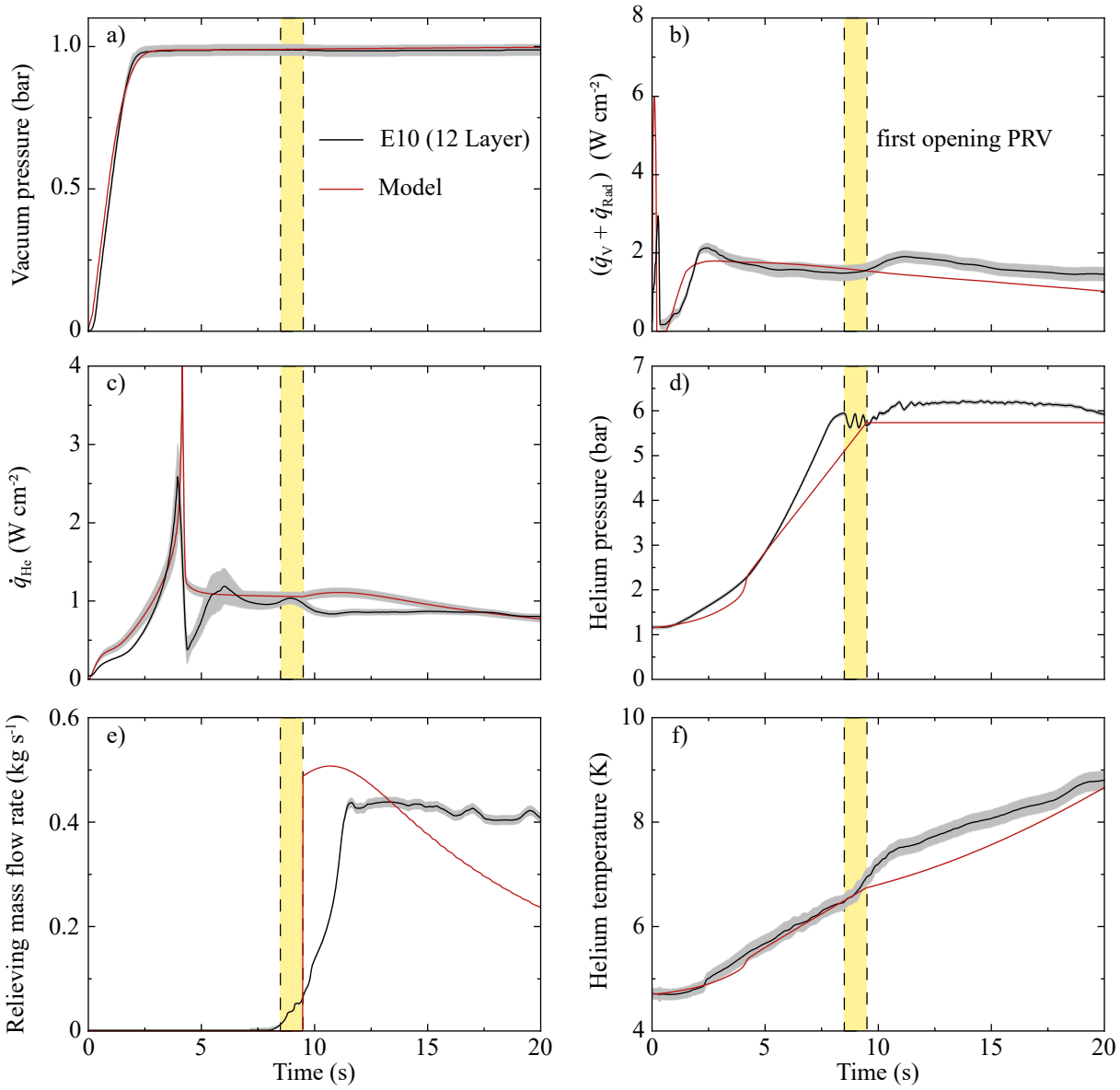

Figure 6.17: Adapted modelled (*red*) and measured (*black*) a) vacuum pressure increase, b) heat flux transferred on the cryogenic surface, c) heat flux transferred to helium, d) helium pressure increase, e) relieving mass flow rate and f) helium temperature increase with 12 layers of MLI1 for 20 s after the start of the venting process. The first opening of the PRV is highlighted and the measurement uncertainty according to GUM [47] is depicted in grey.

Table 6.1: Comparison of literature data from [52] with the experimental and modelled results obtained over the course of this work. Listed are the maximum heat flux values transferred to helium after the first opening of the PRV. All considered experiments are conducted at supercritical p_0.

Cryogenic vessel insulation	Literature data [52] ($\mathrm{W\,cm^{-2}}$)	Experimental results ($\mathrm{W\,cm^{-2}}$)	Model results ($\mathrm{W\,cm^{-2}}$)
Bare vessel (Shield)	3.8	1.0 . . . 1.4	1.4 . . . 1.5
Single MLI layer	2.0	1.2	1.3
10 (12) MLI layers	0.6	0.7 . . . 1.0	0.8 . . . 1.3
24 MLI layers	-	0.6 . . . 0.7	0.8 . . . 0.9

In Table 6.1 the experimental results are compared to commonly applied literature data. Experiments with a bare surface or with a not actively-cooled thermal shield show significantly lower heat flux values (−74 %) after the first opening of the PRV than commonly referred to in the literature. In this work, only a range of resulting heat flux values can be defined since different initial liquid levels, relieving pressures and general process dynamics influence the absolute values. This applies also for the insulation with a single layer, whereby its insulation effect is marginal compared to the thermal shield. The model well predicts the heat flux profiles in both cases.

In contrast, both the measured and modelled heat flux value for 12 layers of MLI in experiment E10 are up to 80 % higher than the value for 10 layers in [52], whereby the values in E14 is up to 33 % higher, again depending on the stratifications, the initial liquid level and further process dynamics. This illustrates that the type of MLI is a sensitive parameter, which is not documented in [52].

Remark If the thermal shield is cooled to $T \leq 90\,\mathrm{K}$, which is the saturation temperature of oxygen, air ingredients might also condensate and/or sublimates on the surface of the thermal shield. The reduction of the heat flux transferred on the cryogenic surface has to be considered accordingly.

6.4 Influence of leak size

In this section, the influence of the leak size on the heat transfer process to helium following LIV is investigated. First, the experimental data for three different leak sizes are compared. Second, the model is applied to medium and minor leak size and compared to the respective experimental data.

6.4.1 Comparison of experimental data

The leak size has a direct influence on the amount of air entering the vacuum space and thus on the vacuum pressure increase and deposited mass flow rate. In Section 6.1 and

6.3 is shown that a leak with a diameter of $d_{\text{Orifice}} = 37.5\,\text{mm}$ results in a direct vacuum pressure increase to ambient without without any stagnation for a bare surface (E1) and with radiation shield (E2). Hence, in these cases the heat transfer to helium is not limited by venting mass flow rate. In order to quantitatively investigate the influence of a leak size variation on the heat transfer mechanism, the results of E2 with the 37.5 mm orifice, referred to as major LIV, are compared to the results of E7 with the 30 mm orifice, referred to as medium LIV, and of E15 with the 12.5 mm orifice, referred to as minor LIV in this section. Further experimental conditions and parameters are summarized in Table 5.1.

Venting mass flow rate and vacuum pressure

The evaluation of the venting mass flow rate, depicted in Figure 6.18a, shows that a reduction of the leak size reduces the critical venting mass flow rate almost linearly. This follows the Bernoulli equation, where the ideal critical mass flow rate is directly proportional to the flow area. Minor deviations are caused by the non-ideal orifices used. Compared to major LIV, the critical mass flow rate is reduced by 90 % in minor LIV and by 36 % in medium LIV.

During major and medium LIV, the venting mass flow rate decreases after 3 . . . 4 s because the critical pressure ratio is exceeded. During minor LIV, however, the pressure ratio between ambient and vacuum space does not exceed the critical value within the first 20 s after the start of the venting, thus the mass flow rate still assumes its constant critical value. Ambient pressure is not reached at this point in time of minor LIV, thus the vacuum space is not yet completely filled with air (cf. Figure 6.18b). Consequently, the total amount of ambient air that enters the vacuum space within the first 20 s is $1.3 \pm 0.4\,\text{kg}$ for medium and major LIV, but only 0.5 kg in case of minor LIV.

Figure 6.18b depicts the vacuum pressure increase during major, medium and minor LIV. As already explained in the former paragraph, the vacuum pressure measured during major LIV increases to ambient pressure without any stagnation within the first 3 s after the start of the venting. In accordance with the amount of air entering the vacuum space, the slope of the vacuum pressure is reduced in medium LIV compared to major LIV, including a stagnation within 0.2 . . . 0.6 s. In minor LIV, a significant stagnation of the vacuum pressure at $6.0 \pm 0.1\,\text{mbar}$ during the first 20 s after the start of the venting can be observed. While, in medium LIV ambient pressure is already reached at the first opening of the PRV, in minor LIV the PRV opens at reduced vacuum pressure.

Heat flux transferred to outer surface and wall temperatures

Figure 6.18c shows the heat flux transferred to the outer surface for minor, medium and major LIV. It can be seen that the peak value in medium LIV is reduced by 13.4 % compared to major LIV. In accordance with the vacuum pressure increase and the total amount of ambient air entering the vacuum space, the profiles of major and medium LIV converge within the measurement uncertainty to the same value at 5.5 s. The value at

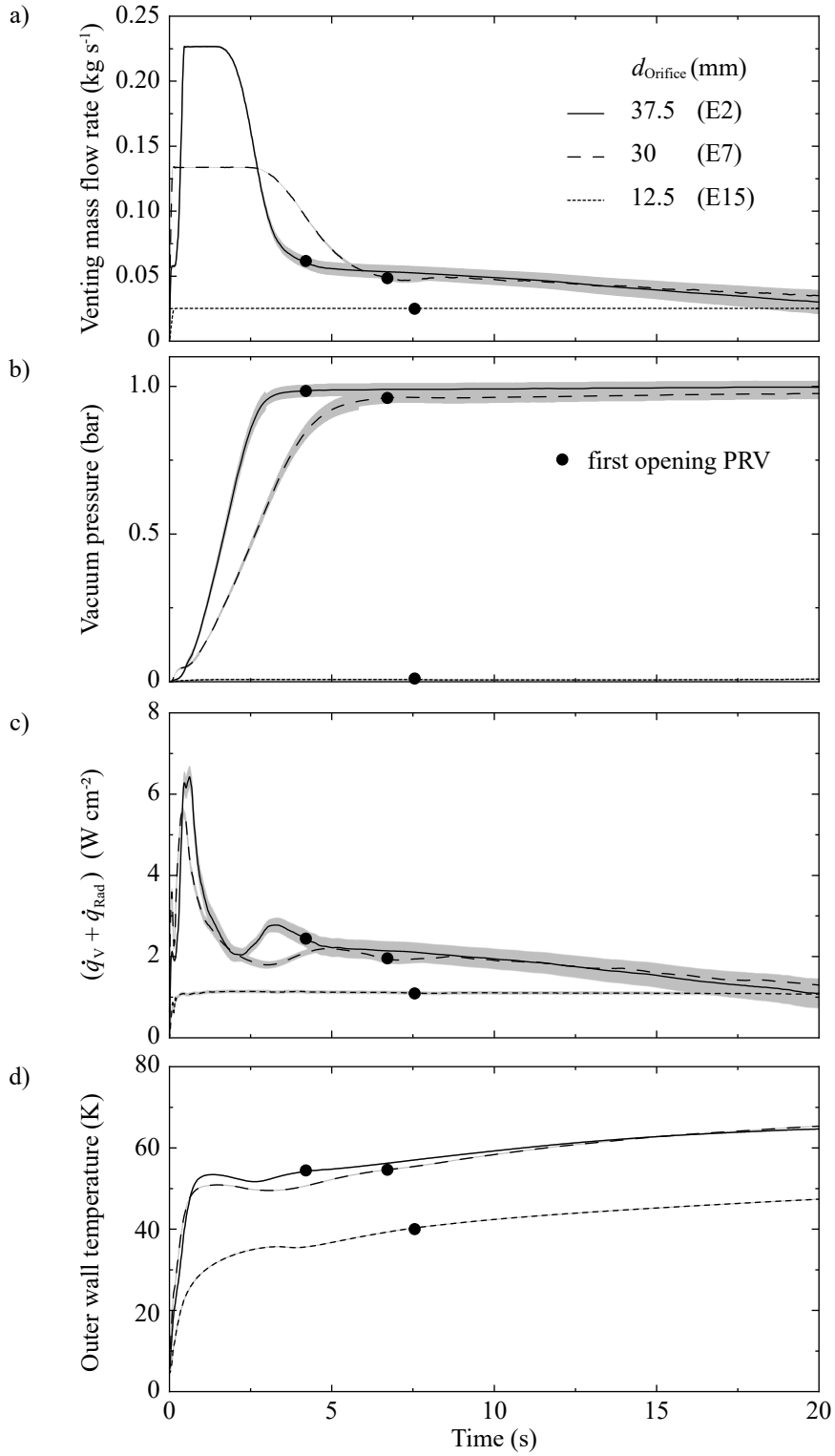

Figure 6.18: a) Profile of the venting mass flow rate, b) vacuum pressure increase, b c) profile of the heat flux transferred to the cryogenic surface including deposition, convection, thermal conduction and radiation, d) outer wall temperature increase for the first 20 s after the start of the venting process for major, medium and minor LIV. The first opening of the PRV is highlighted and the Type B measurement uncertainties according to GUM [47] are depicted in grey.

the first opening of the PRV is reduced by 22 % to $1.94 \pm 0.09\,\mathrm{W\,cm^{-2}}$ for medium LIV due to process dynamics only. A higher relieving pressure in medium LIV causes a later opening of the PRV.

In minor LIV, the characteristic shape of the deposition process is replaced by a constant value of $1.11 \pm 0.02\,\mathrm{W\,cm^{-2}}$. In accordance with the constant vacuum pressure, the deposited mass flow rate equals the venting mass flow rate, thus the heat flux transferred to the outer surface of the cryogenic vessel is limited by the amount of air entering the vacuum space.

A similar trend of the outer wall temperature profiles during major, medium and minor LIV is shown in Figure 6.18d. Compared to major LIV, the wall temperature in medium LIV is reduced by a maximum of 4 K within the first 15 s. In minor LIV, the limitation of the heat flux transferred to the outer surface averages in a 17 K lower wall temperature compared to the values measured during major LIV.

The inner wall temperature profiles in Figure 6.19c are in accordance with the considerations made for the outer wall temperature. The profiles in major and medium LIV are almost congruent. In comparison to that, the inner wall temperature in minor LIV assumes 14 . . . 20 K lower values.

The minimum observed in all three inner wall temperature profiles within 2.5 . . . 4 s is caused by the peak value of the heat flux transferred to helium at the critical point. Here, the temperature difference between inner and outer wall temperature increases up to 20 K.

Processes inside helium

Figure 6.19a shows that in major and medium LIV, the helium pressure increases almost congruent up to the lower relieving pressure of the PRV in major LIV. The helium pressure rise rate in minor LIV is reduced compared to the result of medium and major experiments. Since the PRVs are adjusted to different set pressures in the three experiments, the helium pressure increase culminates in different pressures.

The helium pressure profile of medium LIV shows an unstable behaviour of the PRV due to over-sizing. Beyond the set pressure, the PRV opens and closes in repeated intervals, the so called *pumping*. The helium temperature profiles shown in Figure 6.19b correlate to the pressure increase.

The heat flux transferred to helium during major, medium and minor LIV, which is the crucial value for the dimensioning of the PRV, is depicted in Figure 6.19d. All profiles show the characteristic shape that is explained in Section 6.1. The peak value of $3.6 \pm 0.2\,\mathrm{W\,cm^{-2}}$ at the critical point in major and medium LIV is almost twice as high as the one occurring during minor LIV. The latter amounts to $2.0 \pm 0.4\,\mathrm{W\,cm^{-2}}$. Due to the lower heat flux on the outer surface and the resulting lower inner wall temperature the peak in minor LIV is time-shifted additionally. Beyond the critical point, the heat flux of minor LIV is lower compared to the value of major and medium LIV due to the

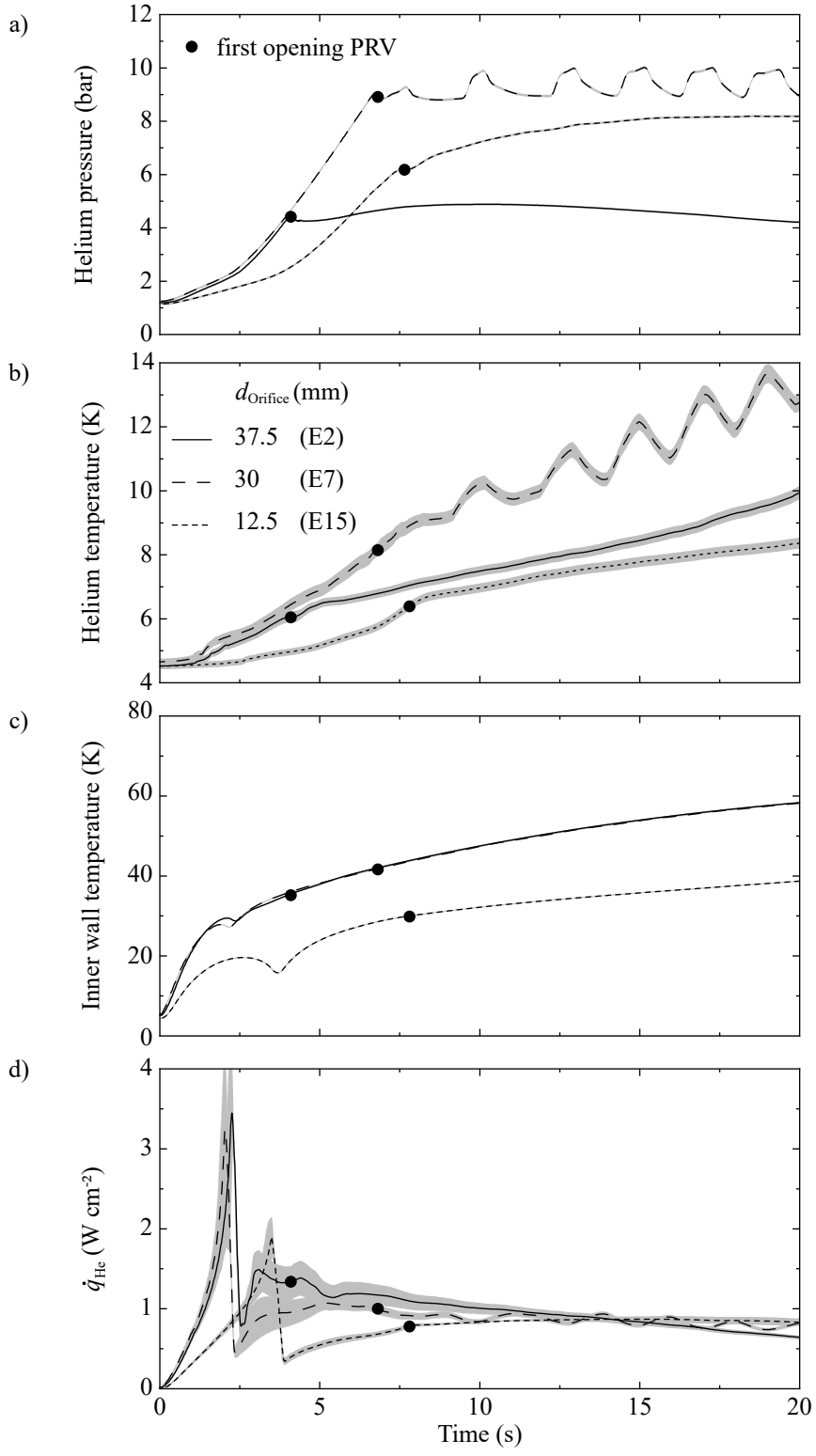

Figure 6.19: a) Helium pressure increase, b) helium temperature increase, c) inner wall temperature increase d) heat flux transferred to helium for the first 20 s after the start of the venting process for three different leak sizes. The first opening of the PRV is highlighted and the Type B measurement uncertainties according to GUM [47] are depicted in grey.

reduced temperature difference between inner surface and helium. In the further course of the experiment, the heat flux profiles approach.

Beyond the critical point, the Biot number in all considered experiments is between $0 < Bi < 1$. Thus, the heat transfer resistance of helium is still higher than the thermal conduction resistance, although the heat flux on the outer surface is limited by the venting mass flow rate in minor LIV.

The heat flux at the first opening of the PRV amounts to $1.31 \pm 0.01\,\mathrm{W\,cm^{-2}}$ in major LIV, $1.06 \pm 0.04\,\mathrm{W\,cm^{-2}}$ in medium PRV and $0.78 \pm 0.02\,\mathrm{W\,cm^{-2}}$ in minor LIV. Other than in major and medium LIV, during minor LIV the heat flux increases further after the first opening of the PRV up to $0.90 \pm 0.03\,\mathrm{W\,cm^{-2}}$ due to process dynamics and temperature stratifications.

Different leak sizes influence the deposited heat flux to a larger degree than the heat flow transferred to helium. The wall functions as a buffer due to its heat capacity that increases with increasing temperature.

6.4.2 Model evaluation for medium LIV

To approve the applicability of the presented model to medium LIV, Figure 6.20 shows both the model and the results measured in experiment E7 for the first 20 s after the start of the venting process.

Processes inside vacuum space

In Figure 6.20a the measured and modelled vacuum pressures are compared. The model predicts the measured profile well. Especially, the little stagnation between 0.2 . . .0.8 s, where the heat transfer is limited by the venting mass flow rate for a short period of time is very well estimated by the model. Higher deviation only arise within 2 . . .7 s, where the model slightly under-predicts the slope of the vacuum pressure. At the first opening of the PRV, both model and experiment have already reached ambient pressure.

Figure 6.20b depicts the modelled and measured venting mass flow rate. The model estimates the measured critical mass flow rate of $0.134 \pm 0.002\,\mathrm{kg\,s^{-1}}$ within the measurement uncertainty. Except for some higher deviations when the critical pressure ratio in the model is exceeded with a short delay in time, the modelled and experimentally measured venting mass flow rates are in very good agreement to each other and also with the vacuum pressure increase and the profile of the deposited mass flow rate. The latter profiles are also shown on Figure 6.20b.

Similar to major LIV, the model overestimates the measured peak value of the deposited mass flow rate of $0.126 \pm 0.002\,\mathrm{kg\,s^{-1}}$ in medium LIV by 4.0 %. Some higher deviations occur in the same time frame as for the venting mass flow rate, where the vacuum pressure is increasing to ambient pressure and both the outer wall temperature and the vacuum pressure influence the deposition process and α_C and α_E are fitted to the equation of

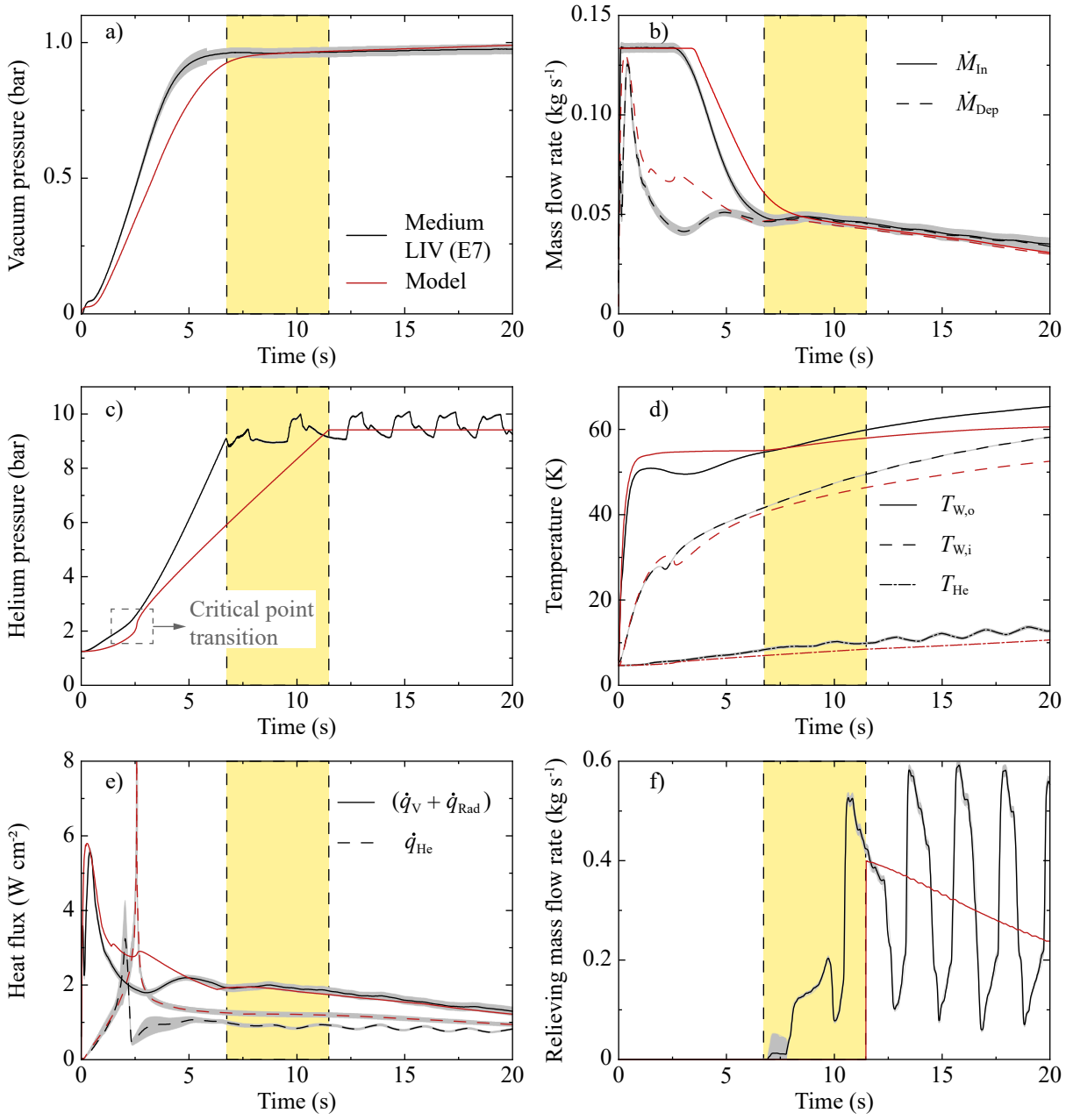

Figure 6.20: Modelled (*red*) and measured (*black*) results of medium LIV for the first 20 s after the start of the venting process. The initial values of E7 are used for modelling. a) Vacuum pressure increase, b) profile of venting and deposited mass flow rate, c) helium pressure increase, d) increase of outer, inner and helium temperature, e) profile of both the heat flux transferred on the outer surface of the cryogenic vessel and to helium and f) relieving mass flow rate. The range of the first opening of the PRV is highlighted in yellow and the Type B measurement uncertainties according to GUM [47] are depicted in grey.

Clausius-Clapeyron. Apart from that, the model predicts the measured profile within the measurement uncertainty.

The profile of the heat flux transferred to the outer surface of the cryogenic vessel (cf. Figure 6.20e) follows the same train of logic because the deposition process again dominates the heat transfer on the outer surface. The value at the first opening of $1.92 \pm 0.09\,\mathrm{W\,cm^{-2}}$ is estimated by the model within the measurement uncertainty of 4.9 %.

Processes inside helium and wall temperatures

Figures 6.20c and 6.20d show the modelled and measured helium pressure and temperature, respectively. The model estimated the general trend of both helium pressure and temperature well. Some higher deviations occur at the transition around the critical point and during the experimentally observed pumping steps of the PRV, where the pressure increases and decreases at a defined frequency. Pumping of a PRV typically occurs when it is oversized. Since the PRV in E7 is dimensioned according to literature heat flux values, i.e. $4\,\mathrm{W\,cm^{-2}}$, this behaviour is comprehensible. However, these points are not safety relevant because, first, the set pressure is far above the critical pressure and, second, pumping is to be prevented. Furthermore, the model estimates a significantly (40 %) lower pressure rise rate up to the first opening of the PRV. The comparatively high set pressure of 8 bar(g) in this experiment together with the slightly reduced process dynamics due to the use of a smaller orifice seem to enhance this trend, which is observed in all experiments.

When comparing the modelled and experimentally derived profiles of the heat flux transferred to helium in Figure 6.20e, it can be concluded that the model approach provides a good estimation of the actual behaviour since both are in good agreement. Higher deviations occur only at pressures directly beyond the critical point where the stratifications inside the cryostat influence the measured heat flux. The model, however, overestimates the measured value at the first opening of $0.99 \pm 0.05\,\mathrm{W\,cm^{-2}}$ by about 17.5 %. This can be explained by the pumping of the PRV: During each pumping step, heat is transferred from the warm end of the piping upstream of the PRV to the helium vessel, which results in higher helium temperatures and thus a smaller temperature differences to the wall (cf. Figure 6.20d). Consequently, the heat transfer to helium is reduced. Due to the higher relieving pressure of medium LIV compared to major LIV, the heat flux profile does not show a second peak.

In accordance with the in- and out-flowing heat fluxes, the modelled and measured profiles of the outer and inner wall surface temperatures compared in Figure 6.20d are of similar shape. While the model overestimates the outer wall temperature up to the first opening of the PRV, in the further course this changes to an underestimation as the deposited heat flux is underestimated by the model.

Figure 6.20f compares the modelled and measured relieving mass flow rate. The latter shows also the pumping of the PRV. The model estimates a maximum required relieving mass flow rate of $0.40\,\mathrm{kg\,s^{-1}}$, while during one pumping step in E7 up to $0.59 \pm 0.01\,\mathrm{kg\,s^{-1}}$

are released. When the pressure inside the helium vessel drops below the reseating pressure because of the over-sized mass flow rate the PRV closes. Thus, also the measured mass flow rate drops to almost zero. Due to the remaining heat flux, the pressure increases again and a new pumping step is induced.

6.4.3 Model evaluation for minor LIV

To show the applicability of the model introduced in Chapter 4 to minor LIV, in Figure 6.21 the experimental results of E15 are compared to the according model results for the first 30 s after the start of the venting process. The higher evaluation time is chosen because the small leak size reduces the process dynamics.

Processes inside vacuum space

In Figure 6.21a both the modelled and measured vacuum pressure increase are depicted. Within the first second, the modelled value increases faster than the measured one due to sensor response times. The experiment shows a pressure profile that starts by increasing to 7.5 ± 0.7 mbar, followed by a decrease at the first opening of the PRV to 6.0 ± 0.6 mbar. After that, it starts to increase to ambient with an average slope of $12\,\mathrm{mbar\,s^{-1}}$. Contrary, the modelled vacuum pressure stagnates at 5 mbar up to 22 s after the start of the venting and increases to ambient pressure at an average slope of $15\,\mathrm{mbar\,s^{-1}}$. However, considering the highly dynamic process and the extremely different conditions in minor and major LIV, the presented model depicts the experimental results very well.

This is underlined by the comparison of the modelled and measured venting and deposited mass flow rate, respectively, depicted in Figure 6.21b. The critical venting mass flow rate is estimated by the model within the measurement uncertainty and also in the further course the model predicts the measured values over a wide time range within the measurement uncertainty. Higher deviations occur only within the first 2 s, where the model slightly overestimates the deposited mass flow rate and after 25 s, where the experimentally derived deposited mass flow rate decreases faster compared to the model results. Since the deposition process again dominates the heat transfer process on the cryogenic surface (99.9 %), the heat flux transferred to the outer surface depicted in Figure 6.21e shows the same dependencies as the deposited mass flow rate.

Processes inside helium and wall temperatures

The modelled and in E15 experimentally derived heat fluxes transferred to helium are depicted in Figure 6.21e. The heat flux transferred to helium is modelled with a time shift of about 1 s due to a later opening of the PRV in the model calculations. This results in higher deviations between model and experiment around the critical pressure. At the first opening of the PRV, however, the model estimates the measured data with a smallest deviation of 3 %, which is within the measurement uncertainty. The slightly

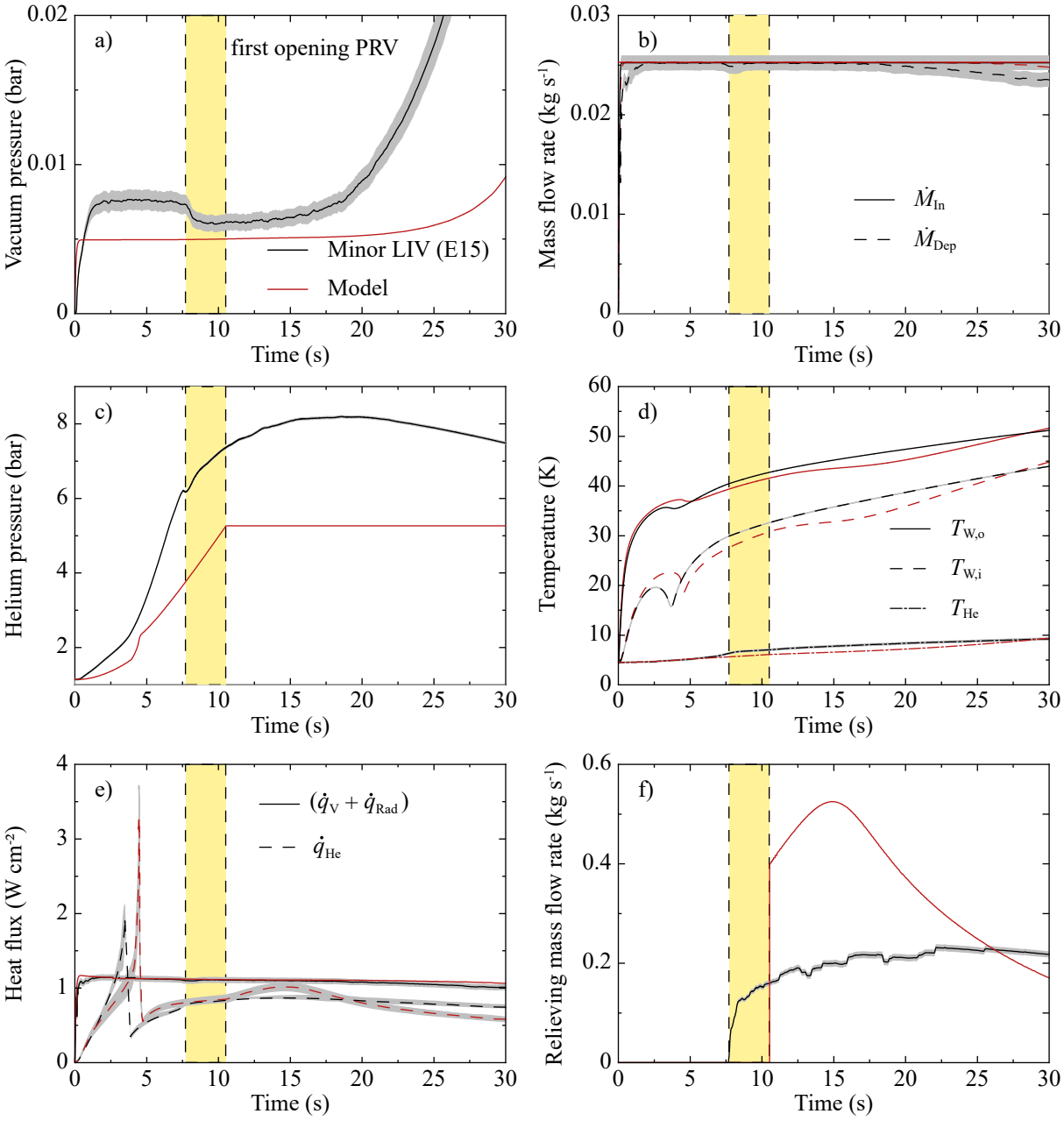

Figure 6.21: Modelled (*red*) and measured (*black*) results of minor LIV for the first 30 s after the start of the venting process. The initial values of E15 are used for modelling. a) Vacuum pressure increase, b) profile of venting and deposited mass flow rate, c) helium pressure increase, d) increase of outer, inner and helium temperature, e) profile of both the heat flux transferred on the outer surface of the cryogenic vessel and to helium and f) relieving mass flow rate. The range of the first opening of the PRV is highlighted in yellow and the Type B measurement uncertainties according to GUM [47] are depicted in grey.

increased deviation between model and experiment in the further course of time can be explained by the overpressure occurring during the experiment (cf. Figure 6.21c)). The higher pressure measured within 7.5 . . . 15 s results in a lower heat transfer coefficient and thus in a lower heat flux. The reason why heat transfer temporarily decreases with increasing pressure is explained in Subsection 6.5.1. While the measured heat flux remains almost constant, the modelled one decreases. This effect can be explained by a higher modelled relieving mass flow rate that results in a faster decrease in density and therefore in a reduced heat transfer coefficient.

In accordance with the in- and out-flowing heat fluxes, the modelled and measured profiles of the inner and outer wall surface temperatures compared in Figure 6.21d are almost coinciding.

The PRV in experiment E15 is under-sized on purpose to guarantee that it fully opens during release. Thus, both the occurring overpressure and the deviation between modelled and measured relieving mass flow rate - depicted in Figure 6.21f - can be explained.

6.4.4 Calculation of the venting mass flow rate

To enable a reasonable comparison of modelled and measured results, the venting mass flow rate is modelled according to *DIN EN ISO 5167-2:2003* [26] (cf. Equation 5.12) for real orifice measurement sections. However, during a risk assessment according to Chapter 3 only a maximum leak size is defined. Other parameters required in Equation 5.12 such as the expansion coefficient cannot be defined in the risk assessment. Thus, the venting mass flow rate can only be considered as a flow through ideal short nozzles (Bernoulli equation, cf. Equation 3.5) in a model that should be generally applicable for PRV dimensioning.

Figure 6.22a depicts the profiles of the resulting venting mass flow rates for all considered leak sizes calculated for real orifices and for ideal nozzles at a set pressure of 3 bar(g), an initial liquid level of 60 % and a humidity of 30 %. The critical mass flow rate through an ideal orifice is 11 . . . 16 % higher than the one through the real orifice measurement section of the same diameter. This results in a 11 . . . 16 % higher peak heat flux value transferred to the outer surface of the cryogenic vessel as shown in Figure 6.22b since the heat flux transferred on the outer surface is apart from the portion due to thermal radiation direct proportional to the venting mass flow rate. The faster decrease of the ideal venting mass flow rate after exceeding the critical pressure ratio at major and medium LIV results in a delay over the further course of the heat flux profiles.

The heat flux transferred to helium (cf. Figure 6.22c) is less affected by the differences in the venting mass flow rates. The maximum deviation between ideal and real calculation is less than 1 % in the safety relevant time frame after the first opening of the PRV for major and medium LIV. Concerning the case of minor LIV, the heat transfer is limited by the venting mass flow rate. In comparison to major and medium LIV, the influence of the venting mass flow rate increases and the difference between the heat fluxes transferred to the outer surface amounts up to 5 % in the safety relevant time frame. The deviation

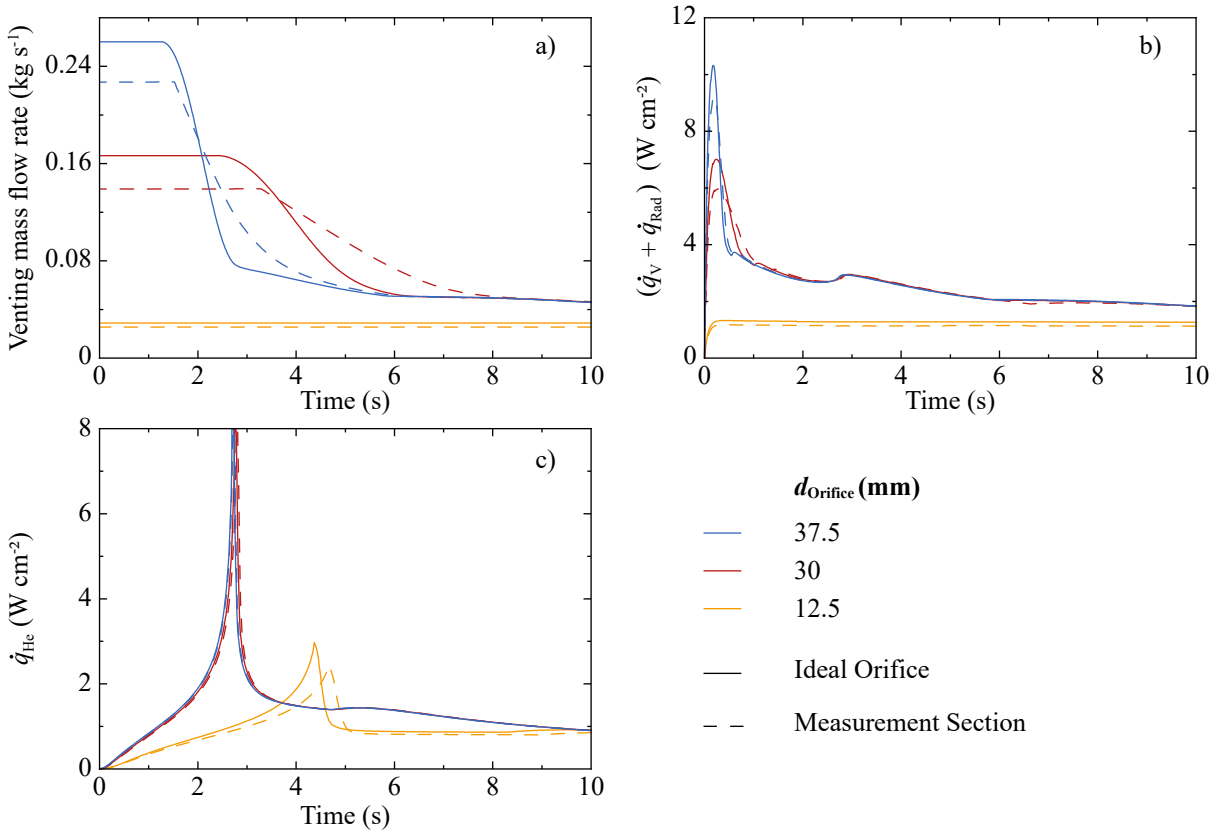

Figure 6.22: Modelled results considering the leak as an ideal nozzle compared to the real orifice measurement section for different leak sizes within the first 10 s after the start of the venting process. a) Profile of the venting mass flow rate, b) heat flux transferred on the outer surface of the cryogenic vessel and c) heat flux transferred to helium.

between the heat fluxes transferred to helium is reduced again, since a portion of the additional heat on the outer surface is buffered by the capacity of the wall.

It can be concluded, that the consideration of the venting mass flow rate as a flow through an ideal nozzle always yields a conservative solution and does not effect the general trend of the safety relevant heat flux transferred to helium. Thus, for general applicability of the model for dimensioning of PRDs, the venting mass flow will be calculated as a flow through an ideal nozzle. Is the heat transfer limited by the venting mass flow rate, however, the influence of the venting mass flow rate on the safety relevant heat flux increases and so a careful definition of the leak size is recommended to ensure a reasonable dimensioning of the PRD.

Conclusions

Table 6.2 summarises the safety relevant values of different leak sizes following LIV. It can be summarized that

- the venting mass flow rates scales linearly with the leak size area.

Table 6.2: Summary of the maximum venting mass flow rate, the heat flux value transferred on the outer surface of the cryogenic vessel ($\dot{q}_{\mathrm{V}} + \dot{q}_{\mathrm{Rad}}$) and the heat flux transferred to helium, both at the first opening of the PRV for minor, medium and major LIV.

d_{orifice} (mm)	$\dot{M}_{\mathrm{In,max}}$ ($\mathrm{kg\,s^{-1}}$)	$(\dot{q}_{\mathrm{V}} + \dot{q}_{\mathrm{Rad}})_{\tau\mathrm{open}}$ ($\mathrm{W\,cm^{-2}}$)	$(\dot{q}_{\mathrm{He}})_{\tau\mathrm{open}}$ ($\mathrm{W\,cm^{-2}}$)
12.5	0.025 ± 0.001	1.10 ± 0.03	0.75 ± 0.02
30	0.134 ± 0.002	1.92 ± 0.09	0.99 ± 0.05
37.5	0.227 ± 0.006	2.48 ± 0.21	1.33 ± 0.20

- the heat transfer is limited by the venting mass flow rate at ratios ${}^{A_{\mathrm{Leak}}}/_{A_{\mathrm{Cr}}} > 9 \cdot 10^4$. During limitation, the deposited mass flow rate equals the venting mass flow rate at constant vacuum pressure. Thus, the reduction of heat flux transferred on the outer surface is directly proportional to the reduction of the venting mass flow rate.
- the influence on the heat flux transferred to helium that is the safety relevant value, however, is less significant. Specifically, a reduction of the venting mass flow rate by more than 90 % from medium to minor LIV reduces the dimensioning relevant heat flux by only 25 %. It can be assumed that a further increase of the heat flux transferred on the outer surface of the cryogenic vessel is buffered by the specific heat capacity of the material of the wall, i.e. stainless steel. At e.g. 4.2 K the specific heat capacity of stainless steel is only $1.97\,\mathrm{J\,kg^{-1}\,K^{-1}}$, while at 60 K it is already increased to $128\,\mathrm{J\,kg^{-1}\,K^{-1}}$.
- Besides major LIV, the presented model is able to estimate processes induced by medium and minor LIV in very good agreement with the experimental data.

6.5 Influence of relieving pressure

So far, only experiments with supercritical relieving pressure have been discussed and compared to the model. However, the influence of the relieving pressure itself has not yet been discussed separately. Hence, in this section, first, the influence of an increasing supercritical relieving pressure is investigated by model calculations. Second, an experiment with sub-critical relieving pressure is presented and compared to the model. The section concludes with a comparison of the resulting heat flux values at sub- and supercritical relieving pressure.

6.5.1 Supercritical relieving pressure

In previous sections, the model is successfully validated at supercritical relieving pressures and various other input parameters. This enables the influence of an increasing supercritical relieving pressure to be investigated by the model. Other initial and boundary conditions, such as venting area and initial liquid level are kept constant. Figure 6.23a

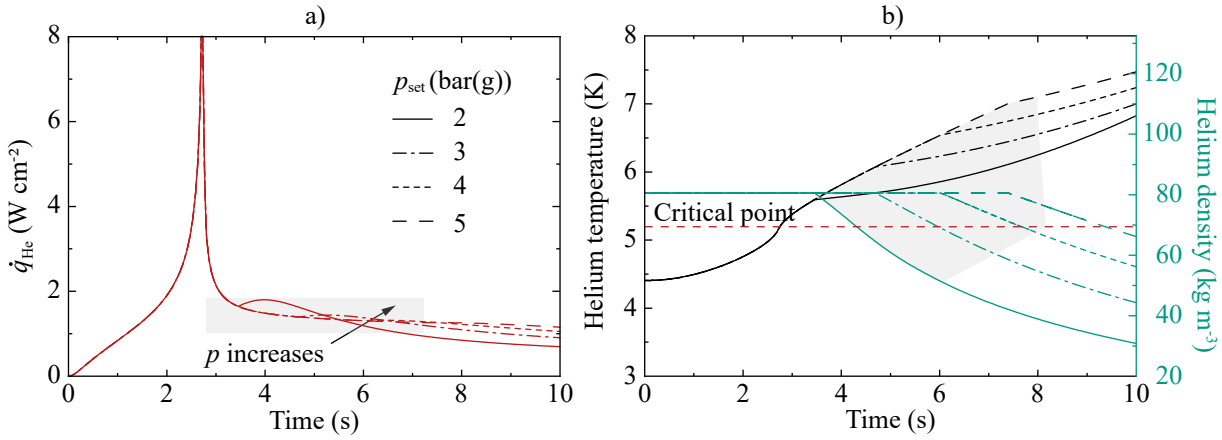

Figure 6.23: a) Modelled heat flux transferred to helium for set pressures of 2, 3, 4 and 5 bar(g) and b) corresponding temperature and density increase for the 10 s after the start of the venting process.

depicts the resulting heat flux profiles transferred to helium for set pressures of 2, 3, 4 and 5 bar(g) at 60 % initial liquid level, a humidity of 30 % and a venting diameter of $d_{\text{Orifice}} = 37.5$ mm.

It can bee seen that the heat flux profiles of the considered set pressures are congruent up to the first opening of the PRV due to the same boundary and initial values. In the further course, the heat flux profiles run differently. They all increase after the first opening of the PRV passing a second maximum but at different absolute values. The lower the pressure, the more pronounced is the maximum and the profile of the lower pressure assumes higher heat flux values. Initially, it was expected that the heat transfer always increases with pressure. However, results show that this is achieved only after about 6 s.

The reason can be found in the combination of temperature and density during the release at different pressures depicted in Figure 6.23b. With lower pressure, the helium approaches the critical point and with it the critical temperature and density of 5.19 K and 69.5 kg m^{-3}, respectively, are approximated (cf. red line in Figure 6.23b). In the vicinity of the critical point, the property data relevant for the calculation of the heat transfer coefficient take maximum values. This results in an increase of the heat flux. The grey area in Figure 6.23b depicts those combinations of temperature and density that cause this unexpected behaviour of the heat flux. Beyond this critical region (20 % beyond critical temperature and density), the heat transfer improves with increasing pressure, as expected.

Together with the investigation of the influence of the initial liquid level on the heat flux transferred to helium in Section 6.2, it can be concluded that at supercritical relieving pressures, the highest heat flux values occur at high initial densities and low relieving pressures due to the vicinity to the critical point.

6.5.2 Sub-critical relieving pressure

In the literature, maximum heat flux values transferred to helium at sub-critical relieving pressure are defined in a range of $3 \ldots 4.5\,\mathrm{W\,cm^{-2}}$ [24, 32, 52], cf. Table 3.1. To compare these literature values with the presented model, Figure 6.24a depicts the profile of the heat flux transferred to helium obtained by an exemplary model calculation with a sub-critical relieving pressure of $p_0 = 1.75\,\mathrm{bar}$, an initial liquid level of $a_{\mathrm{He},0} = 60\,\%$ and a leak diameter of $d_{\mathrm{Orifice}} = 37.5\,\mathrm{mm}$. The maximum heat flux amounts to $3.3\,\mathrm{W\,cm^{-2}}$, which confirms the higher maximum heat flux values at sub-critical release in the literature. The corresponding temperature increase depicted in Figure 6.24b illustrates that the maximum value occurs at the condensation line, where the last liquid evaporates.

Dimensioning the PRV based on these high heat flux values at sub-critical relieving pressure according to Chapter 3 yields required throat diameters of the PRV in a range of $38 \ldots 53\,\mathrm{mm}$ even when the heat input in the upstream piping is neglected. Taking the density upstream of the PRV into account further increases the required diameter. The higher diameter values in the aforementioned range correspond to a specific volume at pressure vessel relieving conditions of $v_0 = v_{\mathrm{liq}}$ and the lower one to $v_0 = v_{\mathrm{vap}}$, cf. Equation 3.1.

However, the PRVs used in the course of this work have a throat diameter of maximum 22 mm. Therefore, currently an experiment with sub-critical relieving pressure at maximum heat load cannot be conducted. Generally, the throat diameter is limited by the diameter of the upstream pipe that amounts to $d_{\mathrm{Upstream\ Pipe}} = 54.5\,\mathrm{mm}$ at PICARD. In order to match the constraints of the facility, the heat input to helium is reduced by reducing the orifice diameter to a value of $d_{\mathrm{Orifice}} = 3\,\mathrm{mm}$. Since this orifice plate is manufactured in house, it is not calibrated. However, in this way experiment E18 can be carried out with a set pressure of $p_{\mathrm{Set}} = 1\,\mathrm{bar(g)}$ and an initial liquid level of 83.6 %[2]. Figure 6.25 depicts the results of E18 compared to the respective model calculations.

The vacuum pressure, whose course is depicted in Figure 6.25a, does not significantly increase before $450 \ldots 500\,\mathrm{s}$ due to the very small orifice diameter. As a consequence of the low heat input, the overall venting time is increased to more than 650 s. The model estimates the measured stagnation pressure of $0.3 \pm 0.2\,\mathrm{mbar}$ within the measurement uncertainty up to 250 s. In the further course of time, the modelled vacuum pressure profile is shifted backwards in time by 100 s before it increases to ambient at a higher rate compared to the experiment, which increases with less slope over a longer period.

The heat flux transferred on the outer surface averages to an almost constant value of $0.070 \pm 0.002\,\mathrm{W\,cm^{-2}}$ during the entire venting time, cf. Figure 6.25b. It does not assume the typical profile due to deposition as the heat transfer process is highly limited by the venting mass flow rate. The model overestimates the heat flux by only 1.4 % within the first 250 s after the start of the venting process. In the further course of time, the modelled profile decreases barely below the measured heat flux.

[2] The results of experiment E17 with the same parameters could not be evaluated, because the PRV blocked at the first opening and thus no relieving mass flow rate could be measured.

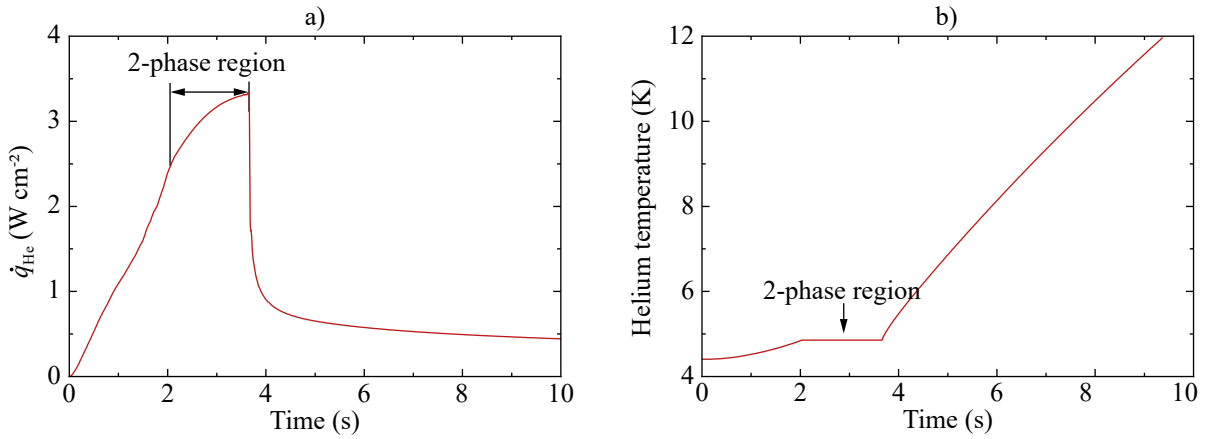

Figure 6.24: a) Modelled heat flux transferred to helium for sub-critical set pressures of 0.7 bar(g) and b) the corresponding temperature increase for the 10 s after the start of major LIV.

Due to the low heat flux transferred on the outer surface of the cryogenic vessel both the outer and inner wall temperature shown in Figure 6.25e increase only little to about 11 K and 6 K, respectively. Then, they remain constant until all liquid helium is evaporated. Due to the negligible thermal resistance of the wall at low temperatures, the heat flux transferred to helium is more or less equal to the one transferred to the outer surface, cf. Figure 6.25c.

All presented profiles confirm that the absolute values are well estimated by the model, however, the modelled profiles inside the helium are shifted forward in time. The reason for this time shift can be found in the profiles of the modelled and measured relieving mass flow rates depicted in Figure 6.25d. While the model estimates a direct increase to the maximum relieving mass flow rate, during experiments the system reacts inert again. Hence, the evaporation of the liquid takes more time during experiment and the relieving time is longer.

The measured helium pressure increase in Figure 6.25f) shows a periodic de- and increase in pressure after the first opening of the PRV. The PRV is pumping after its first opening. After 80 s the pumping stops and the pressure stagnates at 1.87 ± 0.04 bar, which is 13 % below the set pressure. Thus, the PRV is almost closed. Within 100 . . . 380 s, the released mass flow rate passes only a small gap created by the floating of the spring plate on the flow. The increasing helium temperature profile indicates that at 380 s the last liquid evaporates. The transition to gas results in another *pumping* sequence of the PRV due to volume expansion of the helium. The unstable operation of the PRV and the stagnation pressure smaller than the set pressure indicate an over-sized PRV, although the throat diameter of the PRV used is already 30 % lower than required by the dimensioning process.

Based on Equation 3.1, the PRV is dimensioned applying the specific volume of the saturated liquid due to a high initial liquid level. The heat input in the upstream piping is taken into account. The maximum relieving mass flow rate for dimensioning of 0.11 kg s^{-1}

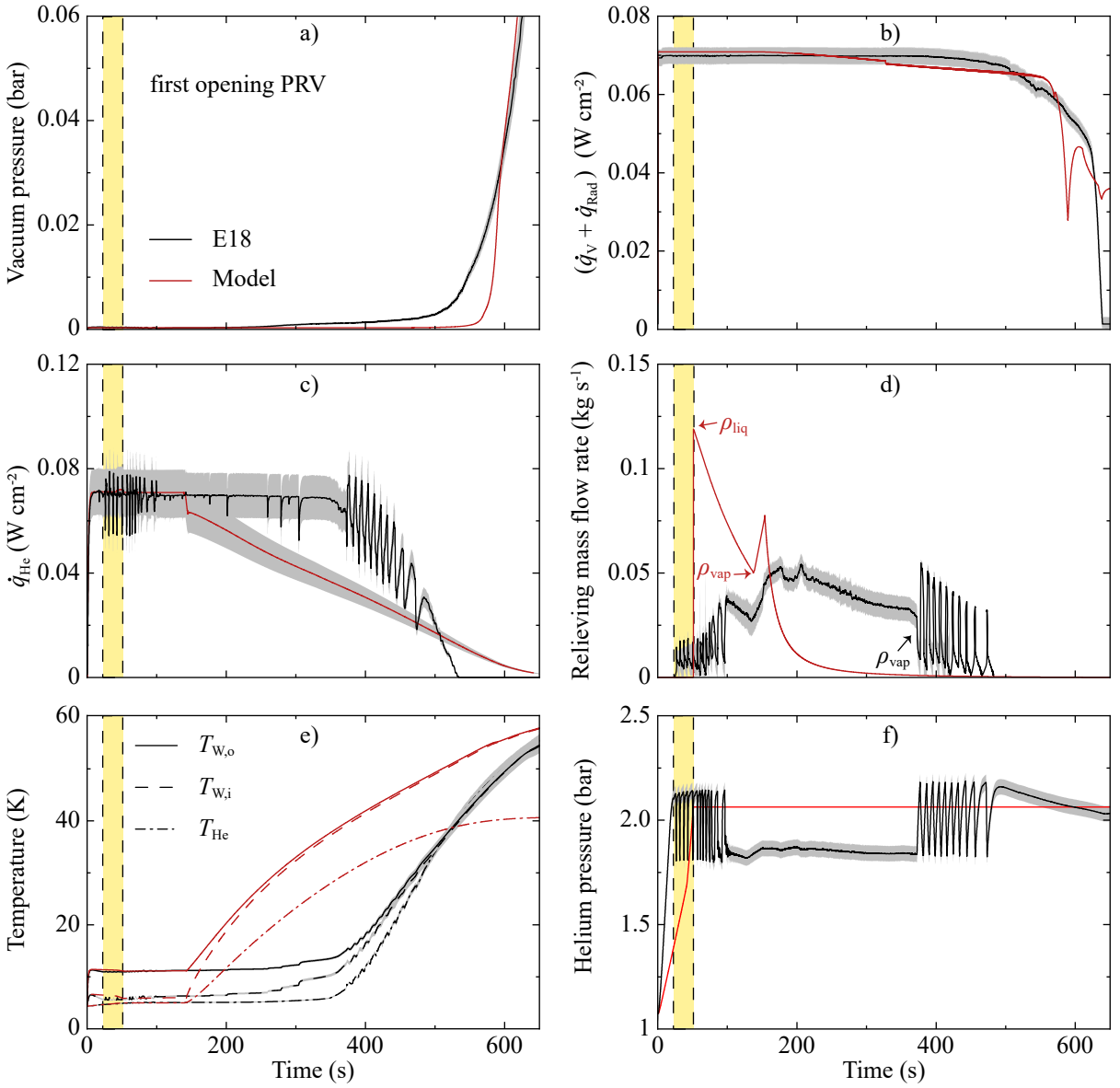

Figure 6.25: Modelled (*red*) and measured (*black*) results (E18) of a minor LIV at sub-critical relieving pressure for 650 s after the start of the venting process. a) Vacuum pressure increase, b) profile of the heat flux transferred on the outer surface, c) heat flux transferred to helium, d) relieving mass flow rate, e) helium temperature increase and f) helium pressure increase. The range of the first opening of the PRV is highlighted in yellow and the Type B measurement uncertainties according to GUM [47] are depicted in grey.

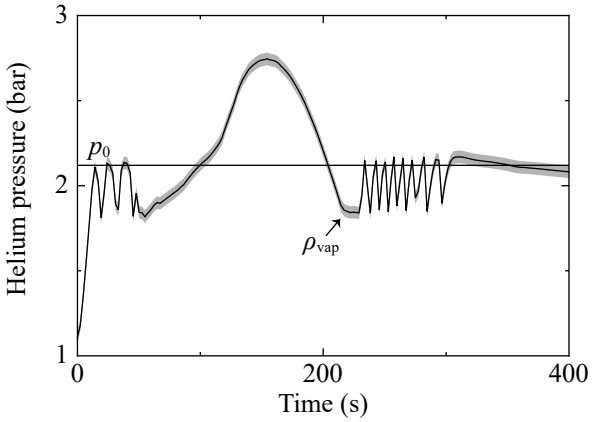

Figure 6.26: Helium pressure increases during E19 for 400 s after the start of the venting process. The Type B measurement uncertainties according to GUM [47] are depicted in grey.

according to *ISO21013-3:2016* corresponds well to the maximum value of the model at saturated liquid. Although the valve has been stringently dimensioned, the experimental data suggest an over-sizing.

To further investigate this effect, in E19 the PRV is dimensioned using the specific volume of the saturated gas at pressure vessel relieving conditions since that approach is recommended in *ISO21013-3:2016*. To match the required heat input, an orifice with a diameter of $d_{\mathrm{Orifice}} = 3.8\,\mathrm{mm}$ is manufactured in house. The dimensioning process results in a required diameter of $d_{\mathrm{th}} = 11.9\,\mathrm{mm}$. To ensure that the PRV fully opens during E19, pressure increase in cryostats and analysis of relief devices (PICARD) is equipped with PRV3 although its throat diameter of $d_{\mathrm{th,PRV2}} = 10\,\mathrm{mm}$ is smaller than required. Figure 6.26 shows the helium pressure increase measured in E19. Due to the inertia of the system the PRV *pumps* again after the first opening. In the further course of time, the pressure increases beyond the relieving pressure, with an overpressure of up to 27.8 % of the set pressure due to the under-dimensioned PRV. The results of E19 indicate that the dimensioning based on the specific volume at saturated gas provides more reasonable results compared to the dimensioning based on the specific volume at saturated liquid in E18.

6.5.3 Conclusions

The following conclusions can be drawn from this section:

- Commonly used literature values for the heat flux transferred to helium at subcritical relieving pressure are confirmed by the presented model.
- The helium heat flux takes values that can be more than twice as high as at supercritical relieving pressure.
- At supercritical relieving pressure the highest heat flux values occur in the vicinity of the critical point due to property data and at high initial liquid levels.

- At temperatures and densities of about 20 % above the critical value, the heat flux transferred to helium initially decreases with increasing pressure. Beyond this range, the heat flux increases with increasing pressure.

6.6 Influence of PRV design

In the course of this work, three different spring-loaded PRVs with different throat diameters and partly different design are applied at PICARD, cf. Section 5.2. Since they exhibit a different behaviour during the experiments, their application is briefly compared in the following paragraphs.

Both, PRV1 and PRV2 have a balancing bellow, separating the helium flow area from the spring. The friction damper of PRV2 actually reduces the tendency of unstable release, even if the relieving capacity is not fully reached due to inertia of the system, for example.

PRV3 does not have a balancing bellow. Furthermore, the spindle of PRV3 is not sealed to the flow area, thus cold helium can flow around the spring during release. To investigate the influence of the reduction of the spring temperature on the behaviour of PRV3 during release three temperature sensors are installed over the hight of the spring, one at the bottom, one in the middle and one at the top.

In experiment E15, where PRV3 is applied at a set pressure of $p_{\mathrm{Set}} = 4\,\mathrm{bar(g)}$, it is observed that though the PRV responds correctly, it does not close completely. The temperature sensors show a cool-down of the spring to a minimum temperature of about 130 K at the bottom of the spring. It can be assumed that the stiffness of the spring increases in such a way that the spring is stuck in the compressed position after the first opening preventing the valve from fully closing again. In this case, the essential feature of a PRV in cryogenic applications to close the system after release is not fulfilled.

It can be concluded that a PRV without a balancing bellow is not applicable to helium cryostats. Friction damper are recommended as they support stable behaviour during release.

7 Conclusion and outlook

The aim of this work is to improve the dimensioning of pressure relief devices (PRDs) for helium cryostats. A dynamic model of the heat transfer to helium following loss of insulating vacuum (LIV) - as a representative maximum credible incident (MCI) - is developed and validated with experimental data. In order to ensure a reasonable calculation of the required minimum discharge area, different models for the dimensioning of PRDs are compared with a focus on the applicability to helium cryostats. From the model comparison, it can be concluded that the homogeneous equilibrium model (HEM) is most suitable for the dimensioning of PRDs for helium cryostats since it is valid in the entire range of both operating temperatures and pressures.

According to the HEM, the heat flow to helium is the main design criterion for the dimensioning of PRDs for helium cryostats. However, HEM is based on the assumption of constant heat flux values that may result in oversized PRDs. To allow for a dynamic calculation of the heat input during LIV, in this work the heat transfer from the vacuum space through the wall to helium is incorporated in an existing basic dynamic model of LIV by adding one-dimensional heat transfer equations. Thermal resistances due to possibly installed multi-layer insulation (MLI) are also included in the presented approach. Furthermore, the heat input to the upstream piping, which significantly influences the density at the throat and thus the discharge area of the PRD, can be calculated by the extended model. The new dynamic calculation of the heat flux according to the presented model does not require experimentally based temperature corrections and is therefore transferable to any application.

To enable the experimental model validation, the safety test facility PICARD is upgraded with further temperature and pressure sensors and a proximity sensor to measure the lift of the PRV used. The model is validated based on the results of a venting experiment conducted at PICARD with a bare cryogenic surface at supercritical relieving pressure. The general trends and dependencies of the heat flux transferred to helium on pressure, temperature and mass flow rates are discussed. The influence of sensitive parameters on the heat flux calculation, specifically the initial liquid level, the insulation of the cryogenic vessel, the leak size and the relieving pressure is further investigated.

Regarding various types of insulation, the applicability of the model is successfully tested for the use of a thermal shield at temperatures $T > 200\,\mathrm{K}$, where a deposition of the venting fluid on the surface of the shield can be excluded. Furthermore, experiments with 1, 10, 12 and 24 layers of MLI are used to adapt the model applicability when cryogenic surface are multi-layer insulated. The model suggests that a single layer and the thermal shield do not reduce the heat flux during LIV significantly, but that increasing the number

of layers decreases the heat flux noticeably. A noteworthy result is that the heat flux to helium depends to a higher degree on the type of MLI, i.e. on the perforation area and the internal structure, than on the number of layers.

By varying the leak size, specifically of the ratio of the leak cross section to the surface of the cryogenic vessel ${}^{A_{\mathrm{Leak}}}/_{A_{\mathrm{Cr}}} = 10^5 \ldots 9 \cdot 10^4$, the applicability of the model to extremely different initial heat loads to the outer surface of the cryogenic vessel is confirmed. Furthermore, the results indicate that at ratios ${}^{A_{\mathrm{Leak}}}/_{A_{\mathrm{Cr}}} > 9 \cdot 10^4$ the heat transfer is not limited by the leak size, thus maximum heat flux values are transferred to helium.

Experiments are performed at both sub-critical and supercritical relieving pressure. At sub-critical relieving pressures, the observed heat flux values are twice as high as at supercritical relieving pressures. The maximum heat flux values of $3 \ldots 4\,\mathrm{W\,cm^{-2}}$ described in the literature are confirmed at sub-critical relieving pressure in the present work. At supercritical relieving pressure, however, the presented results show significantly lower heat flux values ($-74\,\%$) after the first opening of the PRV. They range between $0.7 \ldots 1.75\,\mathrm{W\,cm^{-2}}$ and are predominantly dependent on the initial liquid level, respectively the initial density, and the relieving pressure. The highest values occur at high initial densities and low supercritical relieving pressures. Since a lower heat flux reduces the required minimum discharge area and thus the size of the overall PRD, space and costs can be saved. Both space and costs represent very important parameters in cryogenic applications. Hence, for dimensioning of PRDs it is essential to distinguish between sub- and supercritical relieving pressure. Based on the present work, this novel finding is already included in the New European Standard *"Helium cryostats – protection against excessive pressure"* (Publication by CEN/TC 268/WG6 forthcoming), where two different maximum heat flux values for the dimensioning of PRDs at sub- or supercritical relieving pressures are introduced.

Though the model predicts the dynamic processes following LIV for various input parameters well, it has to be noted that temperature stratifications and delayed reaction of the real system influence the correspondence of modelled and experimentally derived heat flux substantially. Both the stratifications and the delayed reaction result from design constraints of the facility. This effect is most visible at low set pressures and low initial liquid helium levels.

Overall, the present work considerably improves the dimensioning of PRDs in helium cryosats compared to conventional approaches by introducing a dynamic helium cryostat safety model. It provides a solid foundation for further studies.

Future work should aim to advance the present model into a robust dynamic helium cryostat safety model for example applying a probabilistic modelling approach [9, 34]. This would require additional experiments in PICARD to enlarge the current data basis, especially at sub-critical pressure and for the whole range of possible initial liquid levels. To confirm the model tuning for multi-layer insulated surfaces, the investigation of further types of MLI and layer numbers is necessary. The model provides the opportunity to implement other possible MCI besides LIV, as the heat transfer to helium is similar. Although the option of numerical modelling is already incorporated in the New European

Standard (cf. Chapter 3), the possibility of a normative dynamic algorithm and a normative solution strategy would be beneficial to a future update of this standard.

Bibliography

[1] *Cryogenics Safety Manual: A Guide to Good Practice*. British Cryogenics Council, Safety, 5th edition, 2018.

[2] ISO 4126-2:2003. Safety devices for protection against excessive pressure – Part 2: Bursting disc safety devices.

[3] ISO 4126-3:2006. Safety devices for protection against excessive pressure – Part 3: Safety valves and bursting disc safety devices in combination.

[4] ISO 4126-4:2013. Safety devices for protection against excessive pressure – Part 4: Pilot operated safety valves.

[5] ISO 4126-5:2013. Safety devices for protection against excessive pressure – Part 5: Controlled safety pressure relief systems.

[6] ISO 4126-6:2014. Safety devices for protection against excessive pressure – Part 6: Application, selection and installation of bursting disc safety devices.

[7] AD 2000-A1:2006. Safety devices against excessive pressure – bursting discs. german version.

[8] AD 2000-A2:2012. Safety devices against excessive pressure – safety reliev devices. german version.

[9] Marco Andreini, Paolo Gardoni, Stefano Pagliara, and Mauro Sassu. Probabilistic models for erosion parameters and reliability analysis of earth dams and levees. *ASCE-ASME Journal of Risk and Uncertainty in Engineering Systems, Part A: Civil Engineering*, 2(4):04016006, 2016. doi:10.1061/AJRUA6.0000878.

[10] API250-1:2014. Sizing, Selection, and Installation of Pressure-Relieving Devices.

[11] Hans Dieter Baehr. *Thermodynamik : Grundlagen und technische Anwendungen*. SpringerLink. Springer Vieweg, Berlin, Heidelberg, 16. aufl. 2016 edition, 2016. doi:10.1007/978-3-662-49568-1.

[12] Hans Dieter Baehr and Karl Stephan, editors. *Wärme- und Stoffübertragung*. Springer eBooks. Springer Vieweg, Berlin, 10. edition, 2019. doi:10.1007/978-3-662-58441-5.

[13] Randall F. Barron. *Cryogenic heat transfer*. Series in chemical and mechanical engineering. Taylor and Francis, Philadelphia, Pa. [u.a.], 1999. ISBN = 1560325518.

[14] Przemyslaw Bogacki and Lawrence F. Shampine. An efficient runge-kutta (4,5) pair. *Computers Mathematic Application*, 32(6):15–28, 1996. doi:10.1016/0898-1221(96)00141-1.

[15] Maurice Bond and Henning Struchtrup. Mean evaporation and condensation coefficients based on energy dependent condensation probability. *Phys. Rev. E*, 70:061605, Dec 2004. doi:10.1103/PhysRevE.70.061605.

[16] B.P. Breen and J.W. Westwater. Effect of diameter of horizontal tubes on film boiling heat transfer. *Chemical Engineering Progress*, 58:67–72, 1962.

[17] G. Cavallari, I. Gorine, D. Güsewell, and R. Stierlin. Pressure protection against vacuum failures on the cryostats for lep sc. cavities. *Proceedings 4th Workshop on RF Superconductivity*, 1:781–803, 1989.

[18] Stuart W. Churchill and Humbert H.S. Chu. Correlating equations for laminar and turbulent free convection from a horizontal cylinder. *International Journal of Heat and Mass Transfer*, 18(9):1049–1053, 1975. doi:10.1016/0017-9310(75)90222-7.

[19] J.R. Cooper. Representation of the ideal-gas thermodynamic properties of water. *International Journal of Thermophysics*, 3(1):35–43, 1982. doi:10.1007/BF00503957.

[20] Ron Darby. On two-phase frozen and flashing flows in safety relief values. *Journal of Loss Prevention in the Process Industries*, 17(4):255–259, 2004. doi:10.1016/j.jlp.2004.04.001.

[21] V.I. Datskov and J.G. Weisend. Characteristics of russian carbon resistance (TVO) cryogenic thermometers. *Cryogenics*, 34:425 – 428, 1994. Fifteenth International Cryogenic Engineering Conference. doi:10.1016/S0011-2275(05)80097-9.

[22] S.H.M. Deng, D.B. Cassidy, R.G. Greaves, and A.P. Mills. Sticking coefficient of nitrogen on solid nsub 2 at low temperatures, Oct 2007. doi:10.1016/j.apsusc.2007.06.025.

[23] Verein deutscher Ingenieure. *VDI-Wärmeatlas*. VDI-BuchSpringerLink. Springer Vieweg, Berlin, Heidelberg, 11. bearb. und erw. edition, 2013. doi:10.1007/978-3-642-19981-3.

[24] R.C. Dhuley and S.W. van Sciver. Sudden vacuum loss in long liquid helium cooled tubes. *IEEE Transactions on Applied Superconductivity*, 25(3):1–5, 2015. doi:10.1109/TASC.2014.2367156.

[25] DIN EN 5167-2:2003. Measurement of fluid flow by means of pressure differential devices inserted in circular cross-section conduits running full – Part 2: Orifice plates. German version.

[26] DIN EN 5167-4:2004. Measurement of fluid flow by means of pressure differential devices inserted in circular cross-section conduits running full – Part 4: Venturi tubes. German version.

[27] Directive 2014/68/EU, Pressure Equipment Directive . European Parliament.

[28] M.A. Duran and I.E. Grossmann. Simultaneous optimization and heat integration of chemical processes. *AIChE Journal*, 32(1), 1986. doi:10.1002/aic.690320114.

[29] EN 13445-2:2014. Unfired pressure vessels - Part 2: Materials.

[30] EN 17527:2020. Helium Cryostats – Protection against excessive pressure, Draft.

[31] EN ISO 21013-3:2016. Cryogenic vessels – pressure relief accessories for cryogenic service - Part 3: Sizing and capacity determination.

[32] E. Ercolani, A. Gauthier, P. Gully, and J.M. Poncet. Quantification of heatflux in supercritical helium. Presentation at the 1st Cryogenic Safety - HSE Seminar at CERN, "https://indico.cern.ch/event/495194/contributions/2181322/", 2016.

[33] C.-H. Fagerstroem and A.C. Hollis Hallett. The specific heat of solid oxygen. *Journal of Low Temperature Physics*, 1(1):3–12, 1969. doi:10.1007/BF00628329.

[34] Paolo Gardoni, Armen Der Kiureghian, and Khalid M. Mosalam. Probabilistic capacity models and fragility estimates for reinforced concrete columns based on experimental observations. *Journal of Engineering Mechanics*, 128(10):1024–1038, 2002. doi:10.1061/(ASCE)0733-9399(2002)128:10(1024).

[35] Kjell Gustafsson. Control theoretic techniques for stepsize selection in explicit runge-kutta methods. *ACM Transactions on Mathematical Software*, 17(4):533–554, 1991. doi:10.1145/210232.210242.

[36] R.A. Haefer. *Cryopumping: Theory and practice*. Clarendon Press, 4th edition, 1989. ISBN: 0198548125.

[37] S. Harisson. Loss of vacuum experiments on superfluid helium vessel. *IEEE Transactions on Applied Superconductivity*, 12:1343–1346, 2001. doi:10.1109/TASC.2002.1018651.

[38] C. Heidt, S. Grohmann, and M. Süser. Modeling the pressure increase in liquid helium cryostats after failure of the insulating vacuum. *Advances in Cryogenic Engineering*, 1573:1574–1580, 2014.

[39] C. Heidt, A. Henriques, M. Stamm, and S. Grohmann. First experimental data of the cryogenic safety test facility picard. *IOP Conference Series: Materials Science and Engineering*, 171:1757–8981, 2017.

[40] C. Heidt, H. Schön, M. Stamm, and S. Grohmann. Commissioning of the cryogenic safety test facility picard. *IOP Conference Series: Materials Science and Engineering*, 101:012161, 2015.

[41] M.A. Hilal and R.W. Boom. An experimental investigation of free convection heat transfer in supercritical helium. *International Journal of Heat and Mass Transfer*, 23(5):697 – 705, 1980. doi:10.1016/0017-9310(80)90014-9.

[42] Inc., Wolfram Research. Mathematica. Version 12, 2018.

[43] ISO 4126-10:2010. Safety devices for protection against excessive pressure – Part 10: Sizing of safety valves for gas/liquid two-phase flow.

[44] ISO 4126-1:2013. Safety devices for protection against excessive pressure – Part 1: Safety Valves.

[45] ISO 4126-7:2013. Safety devices for protection against excessive pressure – Part 7: Common Data.

[46] ISO 4126-9:2008. Safety devices for protection against excessive pressure – Part 9: Application and installation of safety devices excluding stand-alone bursting disc safety devices.

[47] ISO/IEC Guide 98-3:2008. Uncertainty of measurement – Part 3: Guide to the expression of uncertainty in measurement.

[48] Yukikazu Iwasa. *Case Studies in Superconducting Magnets: Design and Operational Issues*. Springer-Verlag US, Boston, MA, 2 edition, 2009. doi:10.1007/b112047.

[49] Richard W. Johnson, editor. *The handbook of fluid dynamics*. Springer, Heidelberg, 1998. ISBN: 0-8493-2509-9.

[50] S.A. Klein and G. Nellis. *Thermodynamics*. Cambridge University Press, New York, 2012. ISBN: 978-0-521-19570-6.

[51] S.S. Kutateladze. A hydrodynamic theory of changes in a boiling process under free convection. *Izvestia Akademia Nauk Otdelenie Tekhnicheski Nauk*, 4(529):529–536, 1951.

[52] W. Lehmann and G. Zahn. Safety aspects for lhe cryostats and lhe transport containers. *IOP Conference Series: Materials Science and Engineering*, 7:569–579, 1978.

[53] E. W. Lemmon, M. L. Huber, and M. O. McLinden. Refprop. Version 10, 2018.

[54] E.W. Lemmon, R.T. Jacobson, S.G. Penoncello, and D.G. Friend. Thermodynamic properties of air and mixtures of nitrogen, argon, and oxygen from 60 to 2000 k at pressures to 2000 mpa. *Journal of Physical and Chemical Reference Data*, 29(3):331–385, 2000. doi:10.1063/1.1285884.

[55] T. Lenzing, L. Friedel, J. Cremers, and M. Alhusein. Prediction of the maximum full lift safety valve two-phase flow capacity. *Journal of Loss Prevention in the Process Industries*, 11(5):307–321, 1998. doi:10.1016/S0950-4230(98)00014-X.

[56] J. C. Leung. A theory on the discharge coefficient for safety relief valve. *Journal of Loss Prevention in the Process Industries*, 17(4):301–313, 2004. doi:10.1016/j.jlp.2004.04.002.

[57] Siegfried Lück and Hartmut Hermann. *Das Mollier-h, x-Diagramm zur graphisch-analytischen Praxis: Aufbaubeschreibung und Anwendungsanleitung*. Wärme - Kälte - Klima - Prozeß - Luft - Technik. PP, Publico Publ, Essen, revised and extended edition, 2012. ISBN: 978-3-934736-21-4.

[58] D.O. Ortiz Vega. *A new wide range equation of state for helium-4*. Ph.D. Thesis, A&M University, Texas, US, 2013.

[59] T.J. Peterson, J.G. Weisend, and J.M. Jurns. *Cryogenic safety: A guide to best practice in the lab and workplace*. International Cryogenics Monograph Series. Springer Nature Switzerland AG, 2019. ISBN: 978-3-030-16506-2.

[60] Fernando Puente León, Holger Jäkel, and Uwe Kiencke. *Signale und Systeme*. De Gruyter Studium. De Gruyter Oldenbourg, Berlin and Boston, 6th revised edition, 2015. ISBN:978-3-11-040385-5.

[61] M.J. Reader-Harris and J.A. Sattary. The orifice plate discharge coefficient equation - the equation for iso 5167-1. *Internal report of the National Engineering Laboratory, East Kilbride, Glasgow*, 1998.

[62] Sprenger Recknagel. *Taschenbuch für Heizung und Klimatechnik*. R. Oldenbourg München Wien, 58th edition, 1974. ISNB: 3-486-35918-5.

[63] Dr. Torsten Richter. Latex-template. 1.0.2, 2013. URL: http://www.tortools.de/.

[64] Robert C Sallash. Cen/tc 268/wg 6 questions on iso 21013-3:2016, 2019.

[65] D. W. Sallet. Thermal hydraulics of valves for nuclear application. *Nuclear Science and Engineering*, 88(3):220–244, 1984. doi:10.13182/NSE84-A18579.

[66] Sabrina Schirle. *Experimentelle Untersuchung des Vakuumzusammenbruchs in Helium-Kryostaten mit Superisolation*. Master Thesis, Karlsruhe Institute of Technology, Karlsruhe, 2018.

[67] R. Schmidt and W. Wagner. A new form of the equation of state for pure substances and its application to oxygen. *Fluid Phase Equilibria*, 19(3):175 –200, 1985. doi:10.1016/0378-3812(85)87016-3.

[68] Herbert Sigloch. *Technische Fluidmechanik: Mit 40 Tabellen, sowie 114 gelosten Berechnungsbeispielen*. Springer-Verlag, Berlin, Heidelberg, 6., neu bearb. aufl. edition, 2008. doi:10.1007/978-3-540-44635-4.

[69] Marc Sofroniou and Giulia Spaletta. Construction of explicit runge-kutta pairs with stiffness detection. *Mathematical and Computer Modelling*, 40(11-12):1157–1169, 2004. doi:10.1016/j.mcm.2005.01.010.

[70] Mark Sofroniou and Rob Knapp. Mathematica tutorial: Advanced numerical differential equation solving, https://library.wolfram.com/infocenter/Books/8503/AdvancedNumericalDifferentialEquationSolvingInMathematicaPart1.pdf, 2019.

[71] R. Span, E.W. Lemmon, R.T. Jacobson, W. Wagner, and A. Yokozeki. A reference equation of state for the thermodynamic properties of nitrogen for temperatures from 63.151 to 1000 k and pressures to 2200 mpa. *Journal of Physical and Chemical Reference Data*, 29(6):1361–1433, 2000. doi:10.1063/1.1349047.

[72] E. S. Starkman, V. E. Schrock, K. F. Neusen, and D. J. Maneely. Expansion of a very low quality two-phase fluid through a convergent-divergent nozzle. *Journal of Basic Engineering*, 86(2):247–254, 1964. doi:10.1115/1.3653047.

[73] R. Stewart and Eckels. Cryocomp for windows ver. 5.3, 1993 – 2017.

[74] P. M. Sutheesh and A. Chollackal. Thermal performance of multilayer insulation: A review. *IOP Conference Series: Materials Science and Engineering*, 396:012061, aug 2018. doi:10.1088/1757-899x/396/1/012061.

[75] C. Tegeler, R. Span, and W. Wagner. A new equation of state for argon covering the fluid region for temperatures from the melting line to 700 k at pressures up to 1000 mpa. *Journal of Physical and Chemical Reference Data*, 28(3):779–850, 1999. doi:10.1063/1.556037.

[76] Steven W. Van Sciver. *Helium Cryogenics*. Springer, 2nd edition, 2012. doi:10.1007/978-1-4419-9979-5.

[77] A.P. Varghese and B.X. Zhang. Capacity requirements for pressure relief devices on cryogenic containers. *Advances in Cryogenic Engineering Materials*, 37:1487–1492, 1992. doi:10.1007/978-1-4615-3368-9_85.

[78] J. H. Verner. Numerically optimal runge–kutta pairs with interpolants. *Numerical Algorithms*, 53(2-3):383–396, 2010. doi:10.1007/s11075-009-9290-3.

[79] C. Weber, A. Henriques, and S. Grohmann. Study on the heat transfer of helium cryostats following loss of insulating vacuum. In *IOP Conference Series: Materials Science and Engineering*, volume 502.1, page 012170, 2019. doi:10.1088/1757-899x/502/1/012170.

[80] C. Weber, A. Henriques, S. Schirle, and S. Grohmann. Measurement of heat flux in multi-layer insulated helium cryostats after loss of insulating vacuum. *IOP Conference Series: Materials Science and Engineering*, 755:012155, 2020. doi:10.1088/1757-899x/755/1/012155.

[81] C. Weber, A. Henriques, C. Zoller, and S. Grohmann. Safety studies on vacuum insulated liquid helium cryostats. *IOP Conference Series: Materials Science and Engineering*, 278:012169, 2017. doi:10.1088/1757-899X/278/1/012169.

[82] J.G. Weisend II, editor. *Cryostat Design: Case Studies, Principles and Engineering*. International Cryogenics Monograph Series. Springer, Cham, 2016. ISBN: 978-3-319-31150-0. doi:10.1007/978-3-319-31150-0.

[83] Bernd Wunderlich. *Entwicklung eines druckgetriebenen dynamischen Kolonnenmodells zur Erhöhung der Flexibilität von kryogenen Luftzerlegungsanlagen*. Dissertation, Karlsruher Institut für Technologie, Karlsruhe, 2017. doi:10.5445/KSP/1000080378.

[84] G.F. Xie, X.D. Li, and R.S. Wang. Study on the heat transfer of high-vacuum-multilayer-insulation tank after sudden, catastrophic loss of insulating vacuum. *Cryogenics*, 50(10):682–687, 2010. doi:10.1016/j.cryogenics.2010.06.020.

[85] C. Zoller. *Experimental Investigation and Modeling of Incidents in Liquid Helium Cryostats*. Dissertation, Karlsruhe Institute of Technology, Karlsruhe, 2018. doi:10.5445/IR/1000082999.

A Dimensioning of pressure relief devices

In Section 2.2, the PRD dimensioning process according to established standard is introduced. For clarity, no unit-dependent input values are used in the calculations. Here, all unit conversion and the equality of the presented formulas are presented.

A.1 Unit conversion

In ISO 4126-7:2013 and in ISO 21013-3:2016 the minimum discharge area A_{th} for gaseous fluids and sonic flow is calculated according to

$$A_{\mathrm{th}} = \frac{\dot{M}}{p_0 \cdot C \cdot K_{\mathrm{dr}} \cdot \sqrt{\frac{\tilde{M}}{Z \cdot T_0}}} \tag{A.1}$$

$$= \frac{\dot{M}}{0.2883 \cdot C \cdot K_{\mathrm{dr}} \cdot \sqrt{\frac{p_0}{v_0}}} \tag{A.2}$$

where $\dot{M}$ is the relieving mass flow rate in $\mathrm{kg\,h^{-1}}$, p_0 is the relieving pressure in bar, K_{dr} the dimensionless discharge coefficient, $\tilde{M}$ is the molar mass in $\mathrm{kg\,kmol^{-1}}$, Z is the dimensionless real gas factor, T_0 is the relieving temperature in K and v_0 the specific volume at relieving conditions in $\mathrm{m^3\,kg^{-1}}$. The dimensionless discharge function C is defined to

$$C = 3.948 \cdot \sqrt{\kappa \cdot \left(\frac{2}{\kappa+1}\right)^{\frac{\kappa+1}{\kappa-1}}} = 3.948 \cdot f(\kappa) \tag{A.3}$$

and the factor $3.948 = \frac{3600}{\sqrt{10^5} \cdot \sqrt{R}}$ with the ideal gas constant R. As the ideal gas constant has the unit $\mathrm{J\,mol^{-1}\,K^{-1}}$ but the discharge coefficient is dimensionless, this definition is mathematically wrong. The same contradiction occurs in the definition of the factor $0.2883 = \frac{\sqrt{R}}{10}$. However, in Equation A.2 $\sqrt{R}$ is cancelled out again as both factors are multiplied.

To derive Equation A.2 from Equation A.1 four steps are needed. First, Equation A.3 is inserted into Equation A.1

$$A_{\mathrm{th}} = \frac{\dot{M}}{\frac{3600}{\sqrt{10^5}} \cdot f(\kappa) \cdot K_{\mathrm{dr}} \cdot \sqrt{\frac{\tilde{M} \cdot p_0^2}{Z \cdot T_0 \cdot R}}}. \tag{A.4}$$

Second, the root expression is transformed with the ideal gas law $p_0 \cdot v_0 = \frac{R \cdot Z \cdot T_0}{\tilde{M}}$

$$A_{\mathrm{th}} = \frac{\dot{M}}{\frac{3600}{\sqrt{10^5}} \cdot f\left(\kappa\right) \cdot K_{\mathrm{dr}} \cdot \sqrt{\frac{p_0}{v_0}}}. \tag{A.5}$$

In a third step, the dominator is expanded with $\sqrt{R}$:

$$A_{\mathrm{th}} = \frac{\dot{M}}{\sqrt{R} \cdot \underbrace{\frac{3600}{\sqrt{10^5} \cdot \sqrt{R}} \cdot f\left(\kappa\right)}_{C} \cdot K_{\mathrm{dr}} \cdot \sqrt{\frac{p_0}{v_0}}}. \tag{A.6}$$

The missing factor of 10 is derived in the forth step: the dimension analysis. Starting with the units given in ISO 4126-7:2013:

$$\mathrm{mm}^2 = \frac{\mathrm{kg}}{\mathrm{h} \cdot \sqrt{\frac{\mathrm{bar}}{\mathrm{m}^3\,\mathrm{kg}^{-1}}}} \tag{A.7}$$

$$\mathrm{mm}^2 = \frac{\mathrm{kg}}{3600\,\mathrm{s} \cdot \sqrt{\frac{10^5\,\mathrm{Pa}}{\mathrm{m}^3\,\mathrm{kg}^{-1}}}} \cdot 10^6 \tag{A.8}$$

$$\mathrm{mm}^2 = \frac{\mathrm{kg}}{3600\,\mathrm{s} \cdot \frac{\sqrt{10^5}}{\sqrt{10^{12}}} \cdot \sqrt{\frac{\mathrm{Pa}}{\mathrm{m}^3\,\mathrm{kg}^{-1}}}} \tag{A.9}$$

$$\mathrm{mm}^2 = \frac{\mathrm{kg}}{3600\,\mathrm{s} \cdot \frac{1}{10 \cdot \sqrt{10^5}} \cdot \sqrt{\frac{\mathrm{Pa}}{\mathrm{m}^3\,\mathrm{kg}^{-1}}}} \tag{A.10}$$

Expanding the dominator with $\sqrt{R}$ again yields the factors 3.948 and 0.2883:

$$\mathrm{mm}^2 = \frac{\mathrm{kg}}{\underbrace{\frac{3600\,\mathrm{s}}{\sqrt{10^5} \cdot \sqrt{R}}}_{3.948 \text{ in } C} \cdot \underbrace{\frac{\sqrt{R}}{10}}_{0.2883 \text{ in } A_{\mathrm{th}}} \cdot \sqrt{\frac{\mathrm{Pa}}{\mathrm{m}^3\,\mathrm{kg}^{-1}}}} \tag{A.11}$$

The dimensional analysis confirms that Equation A.1 equals A.2. However, the approach with unit dependent input values always causes uncertainty in the evaluation process and confuses the users. To the opinion of the author, thus, the SI-unit based approach in the new European Standard is more handy.

A.2 Discharge function

Equation A.3 defines the maximum discharge function for sonic flow according to ISO 4126-7:2013 as well as in API 520-1:2014 Formula 9. In AD2000-A2:2012 Formula 12, however, it is defined to

$$C = \sqrt{\frac{\kappa}{\kappa + 1}} \cdot \left(\frac{2}{\kappa + 1}\right)^{\frac{1}{\kappa - 1}} \tag{A.12}$$

The conversion between the two forms is shown below, starting with Equation A.3:

$$\frac{C}{3.948} = \sqrt{\kappa \cdot \left(\frac{2}{\kappa+1}\right)^{\frac{\kappa+1}{\kappa-1}}} \tag{A.13}$$

First, the square root expression is divided into two terms. The resulting first term is expanded by $\kappa + 1$

$$\frac{C}{3.948} = \sqrt{\frac{\kappa \cdot (\kappa+1)}{(\kappa+1)}} \cdot \left(\frac{2}{\kappa+1}\right)^{\frac{\kappa+1}{2\cdot(\kappa-1)}} . \tag{A.14}$$

Second, the expression $\sqrt{\frac{\kappa}{(\kappa+1)}}$ is isolated from the first term and the remaining part is expanded by 2.

$$\frac{C}{3.948} = \sqrt{\frac{\kappa}{(\kappa+1)}} \cdot \sqrt{\frac{2\cdot(\kappa+1)}{2}} \cdot \left(\frac{2}{\kappa+1}\right)^{\frac{\kappa+1}{2\cdot(\kappa-1)}} . \tag{A.15}$$

Third, $\sqrt{2}$ is isolated from the second expression, and this expression is converted to its reciprocal to the power of $-1/2$.

$$\frac{C}{3.948} = \sqrt{2} \cdot \sqrt{\frac{\kappa}{(\kappa+1)}} \cdot \left(\frac{2}{(\kappa+1)}\right)^{-\frac{1}{2}} \cdot \left(\frac{2}{\kappa+1}\right)^{\frac{\kappa+1}{2\cdot(\kappa-1)}} \tag{A.16}$$

As a last step, exponents of the same basis are merged and the expressions are further simplified yielding:

$$\frac{C}{3.948} = \sqrt{2} \cdot \sqrt{\frac{\kappa}{(\kappa+1)}} \cdot \left(\frac{2}{\kappa+1}\right)^{\frac{\kappa+1}{2\cdot(\kappa-1)}-\frac{1}{2}} \tag{A.17}$$

$$\frac{C}{3.948} = \sqrt{2} \cdot \sqrt{\frac{\kappa}{(\kappa+1)}} \cdot \left(\frac{2}{\kappa+1}\right)^{\frac{\kappa+1}{2\cdot(\kappa-1)}-\frac{1\cdot(\kappa-1)}{2\cdot(\kappa-1)}} \tag{A.18}$$

$$\frac{C}{3.948} = \sqrt{2} \cdot \sqrt{\frac{\kappa}{(\kappa+1)}} \cdot \left(\frac{2}{\kappa+1}\right)^{\frac{1}{(\kappa-1)}} . \tag{A.19}$$

The remaining factor $\sqrt{2}$ comes from the different definition of the square root expression in the equation of the minimum discharge area respectively mass flux in Section 2.2, (cf. Equation A.2 and 2.19).

B Installation of MLI

A detailed description of the installation of MLI at PICARD is given in [66] including an instruction manual for the removal of the cryogenic vessel. As an example, Figure B.1 shows a photograph of the multi-layer insulated cryogenic vessel with one blanket of MLI3 consisting of 10 layers.

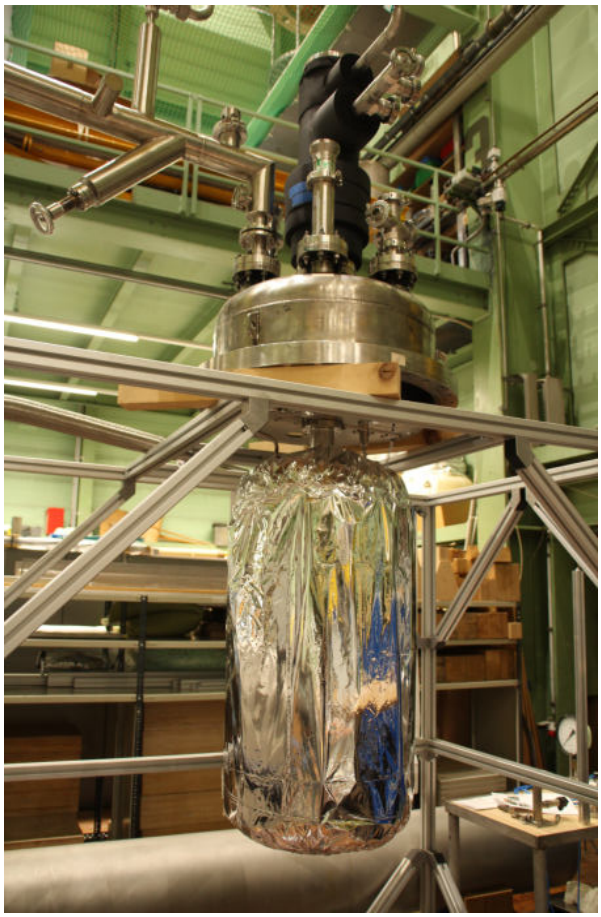

Figure B.1: Photograph of the multi-layer insulated cryogenic vessel exemplary for one blanket of MLI3.

C Property data of solid air

The specific enthalpy of the air components nitrogen, oxygen, argon and water are calculated based on the data summarized in Table C.1. With the isobaric heat capacity, the specific enthalpy is calculated according to $\mathrm{d}h = c_p\,(T)\,\mathrm{d}T$.

Table C.1: Enthalpy data of solid nitrogen and argon [48] and heat capacity data of solid oxygen [33] and water [19].

Nitrogen		Argon		Oxygen		Water	
T (K)	h ($\mathrm{kJ\,kg^{-1}}$)	T (K)	h ($\mathrm{kJ\,kg^{-1}}$)	T (K)	c_p ($\mathrm{J\,mol^{-1}\,K^{-1}}$)	T (K)	$\frac{c_p}{R}$ -
4	0.008	4	0.01	2	0.0139	10	2.952 27
5	0.021	5	0.015	3	0.0476	20	3.430 43
6	0.044	6	0.024	4	0.116	30	3.681 97
8	0.15	8	0.08	5	0.237	40	3.829 47
10	0.38	10	0.2	6	0.43	50	3.918 03
12	0.8	12	0.42	7	0.72	60	3.965 53
15	1.85	15	0.96	8	1.12	70	3.988 47
20	4.74	20	2.2	9	1.65	80	3.998 78
22	6.29	22	2.8	10	2.3	90	4.003 23
24.56	8.51	24.56	3.9	11	3.1	100	4.005 17
30	14.4	30	6.12	12	4	110	4.006 11
35.61	22.7	35.61	8.9	13	5	120	4.006 67
35.611	30.8	40	11.3	14	6	130	4.007 09
40	37.1	45	14.2	15	7.1	140	4.007 49
45	44.3	50	17.3	16	8.3	150	4.0079
50	52.1	60	23.9	17	9.6	160	4.008 35
60	68.9	63.16	25.5	18	11.1	170	4.008 87
63.16	74.3	70	31.1	19	12.5	180	4.009 48
		80	39.1	20	14	190	4.010 22
		83.81	42.3	30	28	200	4.011 14
				35	34	210	4.0123
				40	41	220	4.013 73
				50	46	230	4.015 49
						240	4.017 63
						250	4.020 22
						270	4.026 82

D Further results

In this Appendix, additional experimental and modelled results are discussed. First, the results of model calculation using the internal energy in the first Law of Thermodynamics for closed systems are compared to those applying the enthalpy. Second, the measured and modelled results for 24 Layer of MLI1 are introduced and compared to each other. Third, the reproducibility of the measurements with 12 and 24 layers of MLI1 is presented.

D.1 1st Law of Thermodynamics for closed systems - Internal energy vs. enthalpy

Other than in commonly applied literature, in this work the First Law of Thermodynamics for closed vessels and open vessels with changing mass in Subsection 4.5.1 and 4.5.2, respectively, is expressed by the change of the enthalpy instead of the change of the internal energy. While for the open vessels with changing mass a transformation into a closed system that performs work due to volume change is a common approach, for closed vessels such a transformation is not shown in the literature. However, due to the explanations given in Subsection 4.5.1 the specific enthalpy change is applied also for the closed helium vessels in this work. To discuss the influence of the expression of the First Law of Thermodynamics via internal energy and enthalpy and to justify the approach of using the enthalpy, Figure D.1 compares the modelled results fore a bare surface with internal energy to those with enthalpy and to the corresponding experimental results of E1.

The vacuum pressure increase of the model expressed by the internal energy shown in Figure D.1a) is congruent with the result for the enthalpy, except for a small time frame within 2 . . . 4 s, where the PRV opens. Here, the profile for the internal energy estimates a faster pressure increases compared to the profile for the enthalpy. A reason for this is a slightly lower deposited mass flow rate in the internal energy calculation. The corresponding heat flux transferred on the outer surface is shown in Figure D.1b). The profile for the internal energy again assumes slightly lower values. Compared to the experimental data, however, both modelled profiles estimated the measured values within the measurement uncertainty, except for the time frame of 2 . . . 4 s, where the deposition process depends on both vacuum pressure and wall temperature increase.

As expected, the influence of the use of the internal energy instead of the enthalpy has a more significant influence on the processes inside the helium vessel. Especially helium temperature and helium pressure in Figure D.1c) and D.1d), respectively, increase faster when calculated with the internal energy since the additional energy since the energy

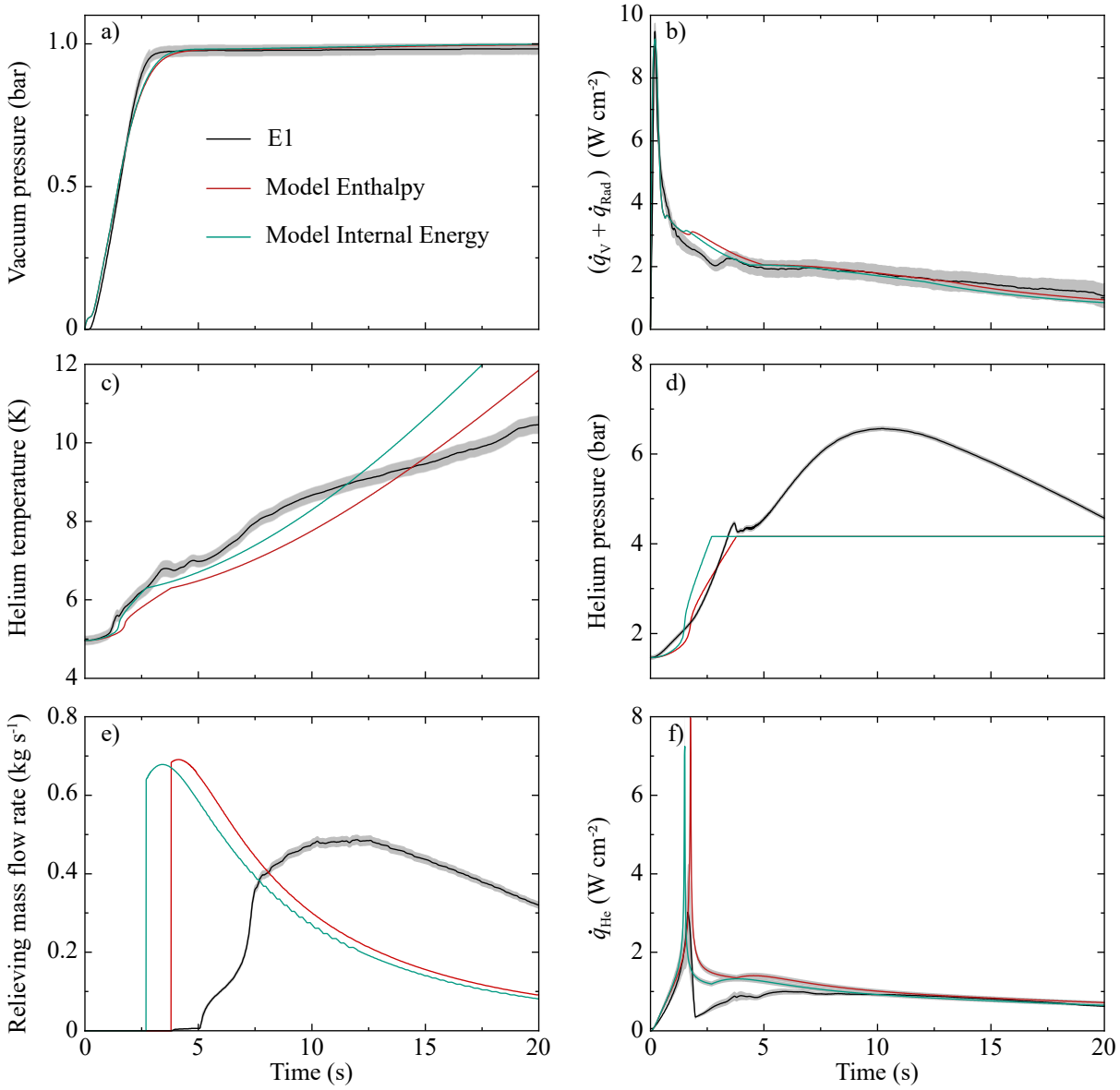

Figure D.1: Modelled and measured a) vacuum pressure increase, b) heat flux transferred on the cryogenic surface, c) helium temperature increase, d) helium pressure increase, e) relieving mass flow rate and f) heat flux transferred to helium with a bare cryogenic surface for 20 s after the start of the venting process. The model is evaluated two times, first with the internal energy in the First Law of Thermodynamics (green) and second with the enthalpy (red).

due to the pressure change is not considered and therefore does not need to be applied to cause a temperature or pressure increase. The PRV opens 1 s earlier in the calculation with the internal energy. While the measured pressure increase is in better agreement with the enthalpy calculation, the measured temperature increase fits better to the internal energy calculation. However, due to the stratifications and missing equilibrium occurring during experiment, it is more realistic that the calculated temperatures are lower and the temperature increase is slower than during E1 as valid for the enthalpy calculation. After the first opening, the calculated profiles run in parallel. The difference slightly increases over the venting time due to process dynamics.

Given the lower modelled helium temperatures, the safety relevant heat flux values transferred to helium are up to 10 % higher in the enthalpy calculation due to a higher temperature difference between helium and the wall. However, both modelled results follow the same trend.

Except for the time shift and a slightly lower maximum value, the modelled relieving mass flow rates in Figure D.1e) also follow the same trend.

It can be concluded, that the calculations with the enthalpy results in more conservative solutions. Furthermore, the result of the helium temperature increase in the enthalpy expression is more reasonable with respect to the experimental constrains. Hence, all model calculations are performed using the enthalpy in the First Law of Thermodynamics.

D.2 Model comparison for 24 layers of MLI1

Figure D.2 compares the results of experiment E12 with 24 layers of MLI1 to those of the tuned model. The vacuum pressure increase that is depict in Figure D.2a is estimated by the model within the measurement uncertainty. At the first opening of the PRV in both model and experiment ambient pressure is already reached inside the vacuum space.

The modelled and experimentally derived heat flux transferred on the outer surface of the cryogenic vessel is depicted in Figure D.2a. The model predicts the general trend well. Only the peak value in the very first second is estimated by the model to be twice as high as in E12. However, this time frame is not safety relevant, since the PRV is still closed. The second increase of the heat flux transferred on the outer surface that occurs when ambient pressure is reached and the MLI decompresses, has a slightly higher rate in the model calculation and the second peak value is not reflected in the model. In the further course of time, the heat flux is modelled within the measurement uncertainty.

The heat flux profile transferred to helium is well estimated by the tuned model, even though the peak value at the critical point is estimated to be 29 % higher. Again, here the PRV is still closed, thus the value is not safety-relevant. Beyond the critical point, up to the first opening of the PRV, the model still overestimates the experimentally derived heat flux due to the stratification and a delay of the measured relieving mass flow rate, which is shown in Figure D.2e. The maximum and safety relevant value that occurs in the course of experiment and model differs by 17 % only. Although this value does not occur at the same time, the model well estimates the safety relevant value.

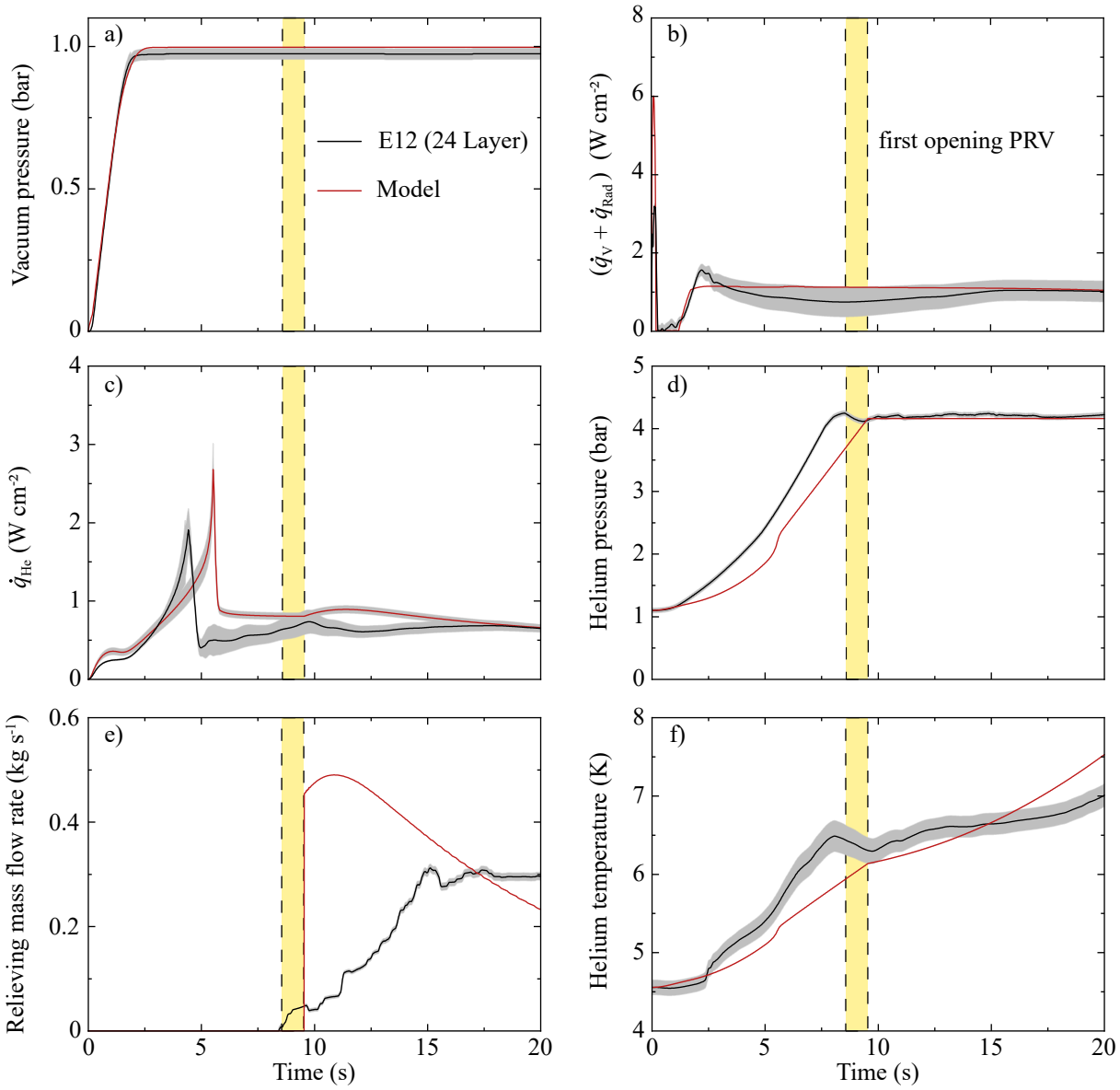

Figure D.2: Modelled and measured a) vacuum pressure increase, b) heat flux transferred on the cryogenic surface, c) heat flux transferred to helium, d) helium pressure increase, e) relieving mass flow rate and f) helium temperature increase with 24 layers of MLI1 for 20 s after the start of the venting process. The first opening of the PRV is highlighted and the measurement uncertainty according to GUM is depicted in grey.

Figure D.2d and D.2e show the measure and modelled pressure and temperature increase, respectively. The model estimates an average pressure rise rate that is 21.5 % slower than the during experiment, due to the temperature stratification and absence of equilibrium in the experiments. A remarkable observation in E12 is, however, the very constant and stable pressure after the first opening of the PRV. This indicates a well dimensioned PRV based on the experience gained in former experiments. The model underestimates the helium temperature increase up to 15 s after the initiation of the venting process due to temperature stratification inside PICARD. In the further course, the modelled temperature increases faster than the measured value. This is the point in time, where the measured relieving mass flow rate reaches its maximum while the model shows an already decreases flow rate. It can be assumed that the higher helium mass and thus higher capacity remaining in the system buffers the heat flux that is transferred to helium in E14 and the stratifications are reduced. The real system shows again a delayed reaction to the heat transfer.

In summary, based on the presented results it can be concluded that the tuned model is applicable to a cryogenic surface insulated with 24 layers of MLI1.

D.3 Reproducibility check with 12 and 24 layers of MLI1

Figure D.3a and D.3b compare the heat flux transferred on the outer surface and to helium, respectively, of E9 to those of E10. Both, E9 and E10 are conducted with 12 layers of MLI1. The set pressure in E9 is 2.2 bar(g) and in E10 4.5 bar(g). The initial liquid level differs by only 2.9 % between E9 and E10. The results are plotted over 40 s after the start of the venting process to confirm reproducibility by displaying the trend over a long time scale.

The aspects discussed in Section 6.3 in the main part can be transferred to the experimental results with 12 layers of MLI1. The general trend of the heat flux transferred to the outer surface of the cryogenic vessel is reproducible within the measurement uncertainty of E9 and E10 over a wide period in time. Only the peak value in the first second and the slope of the second increase when the MLI decompresses are slightly different. Furthermore, the third increase is more pronounced in E10 than in E9. Possible reasons are deviations in the packing density and quality that always occur in a certain measure between two installations. The heat fluxes transferred to helium measured in E9 and E10 are almost congruent. Little deviations occur beyond the critical point up to 10 s after the start of the venting process due to stratifications inside the helium and the different reaction of the system in release of the helium mass flow rate. However, the maximum value after the first opening of the PRV of $1.19 \pm 0.23\,\mathrm{W\,cm^{-2}}$ is reproduced within a deviation of 30 %. This deviation is 50 % as high as the measurement uncertainty, however, it occurs under the influence of stratification, time delay and different set pressures.

Figure D.3c and D.3d compare the heat flux transferred on the outer surface and to helium, respectively, of E11 to those of E12. Both, E11 and E12 are conducted with 24 layers of MLI1. The set pressure in E11 is 6.0 bar(g) and in E12 3.0 bar(g). The initial liquid level differs by only 0.5 % between E11 and E12. The results are again plotted over 40 s after

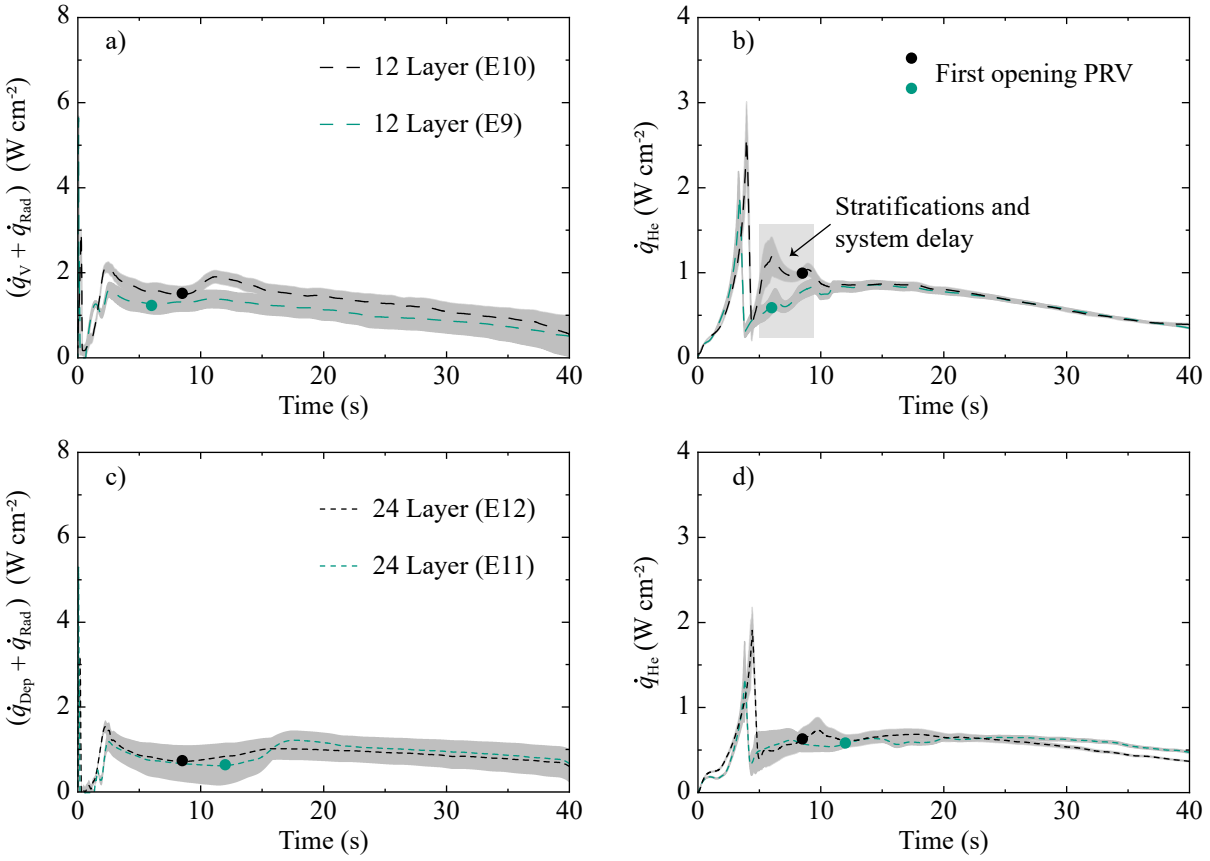

Figure D.3: a) Heat flux transferred to the cryogenic surface and b) heat flux transferred to helium for experiment E9 (green) and E10 (black) with 12 layers of MLI1. c) Heat flux transferred to the cryogenic surface and d) heat flux transferred to helium for experiment E11 (green) and E12 (black) with 24 layers of MLI1. All for 40 s after the start of the venting process. The measurement uncertainty according to GUM is depicted in grey and the first opening of the PRV is highlighted with a dot.

the start of the venting process to confirm reproducibility by displaying the trend over a long time scale. The heat flux transferred on the outer surface of the cryogenic vessel is again reproduced within the measurement uncertainty, besides the peak value in the beginning and the increase after decompression (cf. Figure D.3c). Since the deviations are less pronounced, it can be assumed that doubling the layer number reduces the effect of different packing density. The heat flux transferred to helium experimentally derived in E11 and E12 are almost congruent. The value of E12 is higher in the beginning since the lower set pressure results in higher heat flux values. After 20 s this effect chances as explained in cf. Section 6.5, thus the heat flux of E11 at higher set pressure increases above the value of E11.

In summary, the six experiments with 10, 12 and 24 layers MLI show a very good reproducibility of the experiments conducted on PICARD.

List of publications

Reviewed journal papers

[1] N. Merkel, **C. Weber**, M. Faust, K. Schaber, K. Influence of anion and cation on the vapor pressure of binary mixtures of water + ionic liquid and on the thermal stability of the ionic liquid. *Fluid Phase Equilibria. volume 349 page 27-32*, DOI: http://dx.doi.org/10.1016/j.fluid.2015.03.001.

Reviewed conference papers

[2] **C. Weber**, C. Heidt, A. Henriques, and S. Grohmann. Safety studies on vacuum insulated liquid helium cryostats. In *IOP Conference Series: Materials Science and Engineering*, volume 278.1, page 012169, 2017.
DOI: https://doi.org/10.1088/1757-899X/278/1/012169.

[3] **C. Weber**, A. Henriques, and S. Grohmann. Study on the heat transfer of helium cryostats following loss of insulating vacuum. In *IOP Conference Series: Materials Science and Engineering*, volume 502.1, page 012170, 2019.
DOI: https://doi.org/10.1088/1757-899x/502/1/012170

[4] **C. Weber**, A. Henriques, S. Schirle and S. Grohmann. Measurement of heat flux in multi-layer insulated helium cryostats after loss of insulating vacuum. In *IOP Conference Series: Materials Science and Engineering*, volume 755, page 012155, 2020.
DOI: https://doi.org/10.1088/1757-899x/755/1/012155.

Presentations

[5] **C. Weber**. Status of a European Standard for the protection of helium cryostats against excessive pressure. In *REMBE Process Safety Days: Process Pressure Safety and Relief*. Brilon, Germany, September, 2019.

[6] **C. Weber** and S. Grohmann. Status of a European Standard for the protection of helium cryostats against excessive pressure. In *DKV-Tagung*, Aachen, Germany, November 2018.

[7] **C. Weber**, S. Schirle, and S. Grohmann. Untersuchungen zur Wärmeübertragung in Helium-Kryostaten nach Bruch des Isolationsvakuums. In *DKV-Tagung*, Aachen, Germany, November 2018.

[8] **C. Weber**, A. Henriques, and S. Grohmann. Study on the heat transfer of helium cryostats following loss of insulating vacuum. In *27th International Cryogenic Engineering Conference (ICEC27-ICMC2018)*, Oxford, UK, September 2018.

[9] **C.Weber**. Herausforderungen an die Auslegung von Druckentlastungseinrichtungen in Tieftemperaturanlagen. In *4. CSE Sicherheitstage*, Wangerooge, Germany, April 2018.

[10] **C.Weber** and S. Grohmann. Europaeisches Normungsprojekt zum Schutz von Helium-Kryostaten gegen Druckueberschreitung. In *DKV-Tagung*, Bremen, Germany, November 2017.

[11] **C. Weber**, C. Heidt, A. Henriques, and S. Grohmann. Safety studies on vacuum insulated liquid helium cryostats. In *26th International Cryogenic Engineering Conference (ICEC27-ICMC2018)*, Madison, USA, July 2017.

[12] **C.Weber**, C. Heidt, A. Henriques, J. Schwenzer, and S. Grohmann. Study on set pressure adjustment methods of cryogenic spring loaded safety relief valves. In *17. Cryogenics*, Dresden, Germany, May 2017.

[13] **C. Weber**, C. Heidt, S. Grohmann. Betriebsverhalten federbelasteter Sicherheitsventile bei kryogenen Bedingungen. In *DKV - Tagung*, Kassel, Germany, November 2016.

[14] C. Heidt, A. Henriques, M. Stamm, **C. Weber**, S. Grohmann. The PICARD Test Facility - KIT/CERN Collaboration on Cryogenic Pressure Relief Experiment. In *Cryogenic Safety - HSE seminar*, CERN, Meyrin, Switzerland, September 2016. https://indico.cern.ch/event/495194/contributions/2216811/.

[15] **C.Weber**, C. Heidt, A. Henriques, and S. Grohmann. Investigation of Two-Phase Flow in Cryogenic Pressure Relief Devices. In *Cryogenic Safety - HSE seminar*, CERN, Meyrin, Switzerland, September 2016. https://indico.cern.ch/event/495194/contributions/2216812/.

Posters

[16] A. Henriques, **C. Weber** and S. Grohmann. Cryogenic pressure relief valve sizing tool. *27th International Cryogenic Engineering Conference (ICEC27-ICMC2018)*, Oxford, UK, September 2018.